Development of aminoquinoline-benzimidazole hybrids and their organometallic complexes as antimicrobial agents against *Plasmodium falciparum* and *Mycobacterium tuberculosis*

Nadia Baartzes

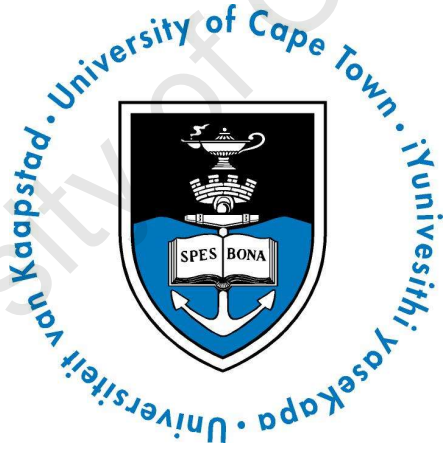

University of Cape Town

December 2019

Development of aminoquinoline-benzimidazole hybrids and their organometallic complexes as antimicrobial agents against *Plasmodium falciparum* and *Mycobacterium tuberculosis*

Thesis presented for the Degree of

DOCTOR OF PHILOSOPHY

by

Nadia Baartzes

Department of Chemistry

University of Cape Town

Supervisor: Associate Professor Gregory S. Smith

Co-supervisor: Professor Kelly Chibale

December 2019

Declaration

I declare that "**Development of aminoquinoline-benzimidazole hybrids and their organometallic complexes as antimicrobial agents against *Plasmodium falciparum* and *Mycobacterium tuberculosis***" is my own work and has never been submitted for examination for any degree at any university. All sources of information used are acknowledged, cited and completely referenced at the end of each chapter.

Signed by candidate

.....

Nadia Baartzes

December 2019

Acknowledgements

Firstly, I would like to gratefully acknowledge my supervisors, Associate Professor Gregory Smith and Professor Kelly Chibale, for their guidance and encouragement throughout this project. I would like to thank Dr Siyabonga Ngubane for his helpful input during group meetings. Special thanks to past and present members of the Organometallic Research Group and Lab 7A, for the support, meaningful discussions and laughter. Thank you to the Medicinal Chemistry Research Group for their positive contribution to this project. A heartfelt thanks to my colleagues/friends, Dr Marwaan Rylands, Mr Shepherd Siangwata and Ms Nikechukwu Omosun, for their friendship and support on our shared scientific journeys over the past few years.

I would like to acknowledge the following people for their assistance; Mr Pete Roberts for recording NMR spectra, Dr Hong Su for Single-crystal X-ray diffraction analyses, Mr Gianpiero Benincasa for Electron Impact Mass Spectral analyses and Dr Marietjie Stander (Stellenbosch University) for Electrospray Ionisation Mass Spectral analyses.

Sincere thanks to Dr Tameryn Stringer, Dr Dale Taylor, Dr Jill Combrinck and Ms Somila Mateza (UCT, Division of Clinical Pharmacology) for conducting *in vitro* antiplasmodium screenings, as well as Dr Sergio Wittlin (Swiss Tropical and Public Health Institute) for performing *in vivo* antimalarial studies. Thank you to Professor Digby Warner, Ms Ronnett Seldon and Ms Audrey Jordaan (UCT, Division of Medical Microbiology) for antimycobacterial screenings. Thanks to Professor Orde Munro and Dr Cathryn Slabber at the University of Witwatersrand for conducting reactive oxygen species studies. Thank you to Ms Diana Melis for assistance with transfer hydrogenation studies.

For funding, I would like to thank the National Research Foundation (NRF), Ernst and Ethel Eriksen Trust, K. W. Johnstone Bursary Programme and the University of Cape Town.

Finally, I would like to express my sincerest gratitude to my family. Thank you to my parents, Waleed and Aziza Baartzes, for the encouragement, support and patience. To my brothers, Imrhan and Rafeeq, thank you for always believing in me. A very special shout-out to Blu, for being by my side through the long writing process.

Abstract

Malaria and tuberculosis (TB) are infectious microbial diseases contributing to a major global health problem and remain a high priority. The problem is further compounded by the emergence of drug resistant strains of the respective causative agents. New therapies and drug design strategies are thus continually required to overcome this resistance. A unique approach in tackling rising resistance is the use of hybrid chemotherapy, which involves the combination of two or more pharmacophores into a single compound. This study investigated the synthesis, characterisation and pharmacological properties of new organic and ferrocenyl aminoquinoline-benzimidazole hybrid compounds, as well as the corresponding Platinum Group Metal (PGM)-containing complexes. The compounds were screened for their activity against *Plasmodium falciparum*, and for their cytotoxicity against the Chinese hamster ovarian (CHO) cell-line. In addition, the compounds were also evaluated against *Mycobacterium tuberculosis*.

A series of aminoquinoline-benzimidazole hybrid compounds were prepared. The 2-position of the benzimidazole was substituted with an organic phenyl or pyridyl group, or an organometallic ferrocenyl group. The 5-position of the benzimidazole was varied using substituents with varying hydrophobic and electron-withdrawing or -donating properties, in order to probe the effect on biological activity. These compounds were fully characterised using ^{1}H, $^{13}C\{^{1}H\}$, COSY and HSQC NMR spectroscopy, IR spectroscopy and electrospray ionisation mass spectrometry.

The organic and ferrocenyl aminoquinoline-benzimidazole hybrids were screened *in vitro* against the chloroquine-sensitive (CQS) NF54 strain and multidrug-resistant (MDR) K1 strain of *P. falciparum*. Most compounds displayed good activity against the sensitive NF54 strain, with IC_{50} values in the low to sub-micromolar range. With the exception of the pyridyl analogues, most compounds were more potent in the resistant K1 strain. Resistance indices lower than one (RI < 1) were observed in most cases, indicating greater applicability in the resistant strain. The individual aminoquinoline and benzimidazole components were also evaluated in order to determine the value in the use of hybrid agents in comparison to the individual components. In the K1 strain, the

hybrid proved more potent than either of the individual components. Using isobologram analysis in the NF54 strain, additive and antagonistic relationships were revealed for the co-administration of the aminoquinoline and benzimidazole components in different relative concentrations.

All of the tested hybrids displayed low or no cytotoxicity towards CHO cells and consequent selectivity towards *Plasmodium* strains. The most active phenyl and ferrocenyl hybrids were subsequently screened for *in vivo* efficacy against *P. berghei*-infected mice. Treatment with the ferrocenyl hybrid resulted in a 92% reduction in parasitemia, proving a more potent inhibitor than the phenyl hybrid (58%).

The haem degradation pathway is a known target of many antimalarials, and thus haemozoin inhibition was investigated as a possible mechanism of action of these hybrid compounds. All screened hybrids were found to inhibit synthetic haemozoin (β-haematin) formation in a cell-free assay. A cellular haem fractionation assay was performed on the most active ferrocenyl hybrid, confirming haemozoin inhibition in the parasite. In addition, reactive oxygen species (ROS) generation by this ferrocenyl hybrid was explored using a DNA-cleavage assay, revealing insignificant ROS-generating ability.

Furthermore, the aminoquinoline-benzimidazole hybrids were evaluated *in vitro* against the H37Rv strain of *M. tuberculosis*. For the phenyl and ferrocenyl hybrids, those with the less hydrophobic 5-position substituents were inactive, while those with the more hydrophobic substituents showed moderate to good activity. Based on logP values, there was a positive correlation between lipophilicity and antimycobacterial activity. In line with this, the more lipophilic ferrocenyl hybrids were consistently more active than their corresponding less lipophilic phenyl analogues. Additionally, in an evaluation of the individual aminoquinoline and benzimidazole components, the hybrid compound was more potent than either component administered individually.

The active phenyl hybrid ligands were reacted with $[Ir(Cp^*)Cl_2]_2$ and $[Rh(Cp^*)Cl_2]_2$ to yield neutral *C^N*-coordinated and *N*-coordinated hybrid complexes. Furthermore, the pyridyl hybrid ligands were reacted with $[Ir(Cp^*)Cl_2]_2$, $[Rh(Cp^*)Cl_2]_2$, as well as $[Rh(ppy)_2Cl]_2$ to afford cationic *N^N*-coordinated hybrid complexes. The complexes were fully characterised using the aforementioned spectroscopic and analytical techniques.

The *C*^*N*- and *N*^*N*-coordinated PGM-containing complexes were screened against the NF54 and K1 strains of *P*. *falciparum*, generally displaying low to sub-micromolar IC_{50} values across both strains. In the sensitive NF54 strain, the cationic Rh(III)-ppy complexes were most potent, outperforming the neutral and cationic M-Cp* complexes. The selected complexes (NF54 $IC_{50} \leq 2$ μM) tested in the resistant K1 strain, generally had activity comparable to or lower than that in the NF54 strain (RI ≥ 1). The active hybrid complexes were evaluated against the non-tumorigenic CHO cell-line, displaying low or no cytotoxicity overall. With regards to a possible mechanism of action, the hybrid complexes were found to be potent inhibitors of β-haematin formation.

The catalytic ability of selected Ir(III) and Rh(III) *C*^*N*-coordinated hybrid complexes, in the transfer hydrogenation of NAD^+ to NADH, was also investigated. Using sodium formate as the hydride source, both complexes demonstrated the ability to catalyse the conversion under cell-free assay conditions. However, co-administration of the Ir(III) complex with sodium formate did not have a significant effect on parasite viability.

When evaluated against the H37Rv strain of *M*. *tuberculosis*, the hybrid complexes generally displayed moderate to good activity. The neutral M-Cp* and cationic Rh(III)-ppy complexes significantly outperformed the cationic M-Cp* complexes. Overall, the neutral Ir(III)-Cp* complexes were most potent, displaying MIC_{90} values in the low to sub-micromolar range.

Publications

Journal Article

- ***Bioisosteric ferrocenyl aminoquinoline-benzimidazole hybrids: Antimicrobial evaluation and mechanistic insights.***
  N. Baartzes, T. Stringer, R. Seldon, D. F. Warner, D. Taylor, S. Wittlin, K. Chibale and G. S. Smith, *European Journal of Medicinal Chemistry*, 2019, **180**, 121-133.

Conferences and Symposia

- **South African Chemical Institute Inorganic Chemistry Conference (INORG2017)**: Hermanus, South Africa (25 – 29 June 2017), Poster presentation – Silver prize.
  Nadia Baartzes, Kelly Chibale and Gregory S. Smith – *Synthesis and antimicrobial evaluation of organometallic aminoquinoline-benzimidazole hybrids.*

- **XXVIII International Conference on Organometallic Chemistry (ICOMC)**: Florence, Italy (15 – 20 July 2018), Oral flash presentation.
  Nadia Baartzes, Kelly Chibale and Gregory S. Smith – *Development of antimicrobial organometallic aminoquinoline-benzimidazole hybrids.*

- **11th Annual Science Postgraduate Symposium**: University of Cape Town, South Africa (11 September 2018), Poster presentation.
  Nadia Baartzes, Kelly Chibale and Gregory S. Smith – *Development of antimicrobial organometallic aminoquinoline-benzimidazole hybrids.*

Abbreviations

%	Percent
2D	Two-dimensional
°C	Degrees Celsius
δ	Chemical shift
AA	Ascorbic acid
ACT	Artemisinin-based combination therapy
ADC	Albumin-dextrose complex
ADME	Absorption, distribution, metabolism and excretion
APAD	3-Acetylpyridine adenine dinucleotide
APADH	3-Acetylpyridine adenine dinucleotide reduced
ATR	Attenuated total reflectance
βHIA	β-haematin inhibition activity
br	Broad (NMR)
CAS	Casitone
CHO	Chinese hamster ovarian
cm^{-1}	Reciprocal centimeters
COD	1,5-cyclooctadiene
COSY	Correlation Spectroscopy
Cp	Cyclopentadienyl
Cp*	1,2,3,4,5-Pentamethylcyclopentadienyl
CQ	Chloroquine
CQDP	Chloroquine diphosphate
CQR	Chloroquine-resistant
CQS	Chloroquine-sensitive
d	Doublet (NMR)
DCM	Dichloromethane
dd	Doublet of doublets

Dd2	CQR *P. falciparum* strain
decomp.	Decomposition
DHPS	Dihydropteroate synthase
DHFR	Dihydrofolate reductase
DHODH	Dihydroorotate dehydrogenase
DMF	*N*,*N*-Dimethylformamide
DMSO	Dimethyl sulfoxide
DMSO-d_6	Deuterated dimethyl sulfoxide
DS-TB	Drug-susceptible tuberculosis
EDTA	Ethylenediaminetetraacetic acid
EI	Electron Impact
EMB	Ethambutol
EMSA	Electrophoretic mobility shift assay
eq.	Equivalents
ESI	Electrospray Ionisation
Fc	Ferrocene
FT-IR	Fourier transform-infrared
FQ	Ferroquine
GFP	Green fluorescent protein
h	Hour(s)
HPLC	High performance liquid chromatography
HR-MS	High resolution mass spectrometry
HSQC	Heteronuclear single quantum correlation spectroscopy
Hz	Hertz
IC_{50}	50% Inhibitory concentration
INH	Isoniazid
IR	Infrared
IRS	Indoor residual spraying
ITN	Insecticide-treated mosquito nets
J	Coupling constant

K1	MDR *P. falciparum* strain
KBr	Potassium bromide
LDH	Lactate dehydrogenase
Lin	Linear
Lit	Literature
m	Multiplet (NMR)
MDR	Multidrug-resistant
MDR-TB	Multidrug-resistant tuberculosis
MHz	Megahertz
MIC_{90}	90% Minimum inhibitory concentration
min	Minute(s)
mM	Millimolar
M.p.	Melting point
MS	Mass spectrometry
MTT	3-(4,5-dimethylthiazol-2-yl)-2,5-diphenyltetrazolium bromide
m/z	Mass-charge ratio
NAD^+	Nicotinamide adenine dinucleotide
NADH	Nicotinamide adenine dinucleotide reduced
NBT	Nitroblue tetrazolium
ND	Not determined
NF54	CQS *P. falciparum* strain
nM	Nanomolar
NMR	Nuclear Magnetic Resonance
NP-40	Nonidet P-40
p	Pentet (NMR)
*Pf*CRT	*Plasmodium falciparum* chloroquine resistance transporter
PGM	Platinum Group Metal
pLDH	*Plasmodium* lactate dehydrogenase
POA	Pyrazinoic acid
PPh_3	Triphenylphosphine

ppm	Parts per million
ppy	2-Phenylpyridyl
pRBC	Parasitised red blood cell
PZA	Pyrazinamide
q	Quartet (NMR)
RA	Reversal agent
RBC	Red blood cell
RI	Resistance index
RIF	Rifampicin
ROS	Reactive oxygen species
RNS	Reactive nitrogen species
s	Singlet (NMR)
SC	Super-coiled
SDS	Sodium dodecyl sulfate
SE	Standard error
sep	Septet (NMR)
SI	Selectivity index
t	Triplet (NMR)
TB	Tuberculosis
td	Triplet of doublets
TDR-TB	Totally drug-resistant tuberculosis
TFA	Trifluoroacetic acid
TMS	Tetramethylsilane
t_R	Retention time
µg	Microgram
µM	Micromolar
W2	CQR *P. falciparum* strain
WHO	World Health Organisation
w/o	Without
XDR-TB	Extensively drug-resistant tuberculosis

Table of Contents

Chapter 4: Synthesis and characterisation of neutral and cationic PGM-containing complexes of aminoquinoline-benzimidazole hybrids

Chapter 5: Pharmacological evaluation of PGM-containing aminoquinoline-benzimidazole hybrid complexes

Chapter 6: Conclusions and Future Outlook

Chapter 7: Experimental

Chapter 1:

Literature Review

1.1 Malaria

Malaria is a life-threatening infectious disease caused by parasites of the *Plasmodium* genus, and is transmitted through the bite of a female *Anopheles* mosquito vector. In humans, malaria is caused by five different species; *P. ovale*, *P. malariae*, *P. knowlesi*, as well as *P. vivax* and *P. falciparum*, which are the most severe and pose the greatest threat in South America and Africa, respectively.[1] According to the World Health Organisation (WHO), there were approximately 219 million new malaria cases and 435 000 deaths in 2017.[1] Figure 1.1 shows the global distribution of indigenous malaria cases in 2017.

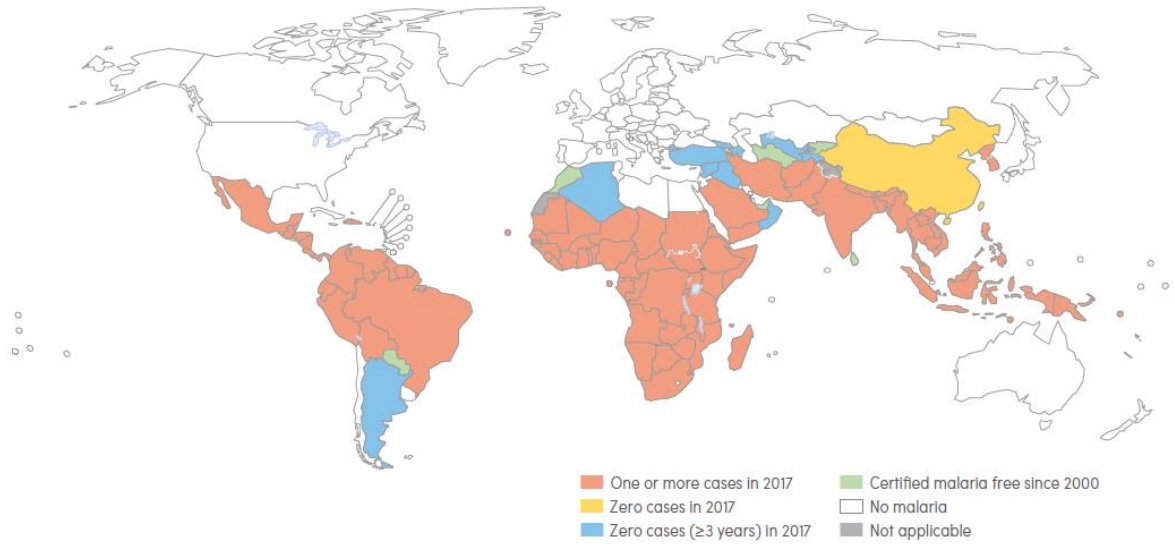

Figure 1.1 Countries with indigenous cases of malaria in 2017.[1]

Numerous factors related to the parasite, vector, host and environmental conditions affect the transmission of this infectious disease. The tropical and subtropical climates, densely-populated areas and the long lifespan of the African vector species lend itself well to the high transmission of malaria in the region.[2] WHO reports that in 2017, 92% of new malaria cases and 93% of malaria deaths occurred in Africa.[1]

Malaria is both preventable and curable. In terms of prevention of the disease, vector control is the main way to block transmission of malaria.[3] This takes the form of insecticide-treated mosquito nets (ITNs), as well as indoor residual spraying (IRS) of insecticides.[4] In addition, antimalarial drugs are used for travellers entering malaria-risk areas, which prevents malaria disease through chemoprophylaxis.[3, 4] With regards to both preventing and curing malaria, an understanding of the life cycle of the *Plasmodium* parasite is crucial.

1.1.1 Life cycle of the *Plasmodium* parasite

The malaria parasite life cycle involves two hosts, a mosquito and a human, as depicted in Figure 1.2.[5] The parasite is injected into the human host in the form of asexual sporozoites, through the bite of an infected mosquito vector. These sporozoites travel to the liver to invade hepatocytes, where they divide by schizogony, producing haploid merozoites. The merozoites are then released into the bloodstream. In some *Plasmodium* species, the sporozoites remain dormant (hypnozoites) in the hepatocytes, and may be activated at a later stage, leading to relapses of active infection in the bloodstream.[5]

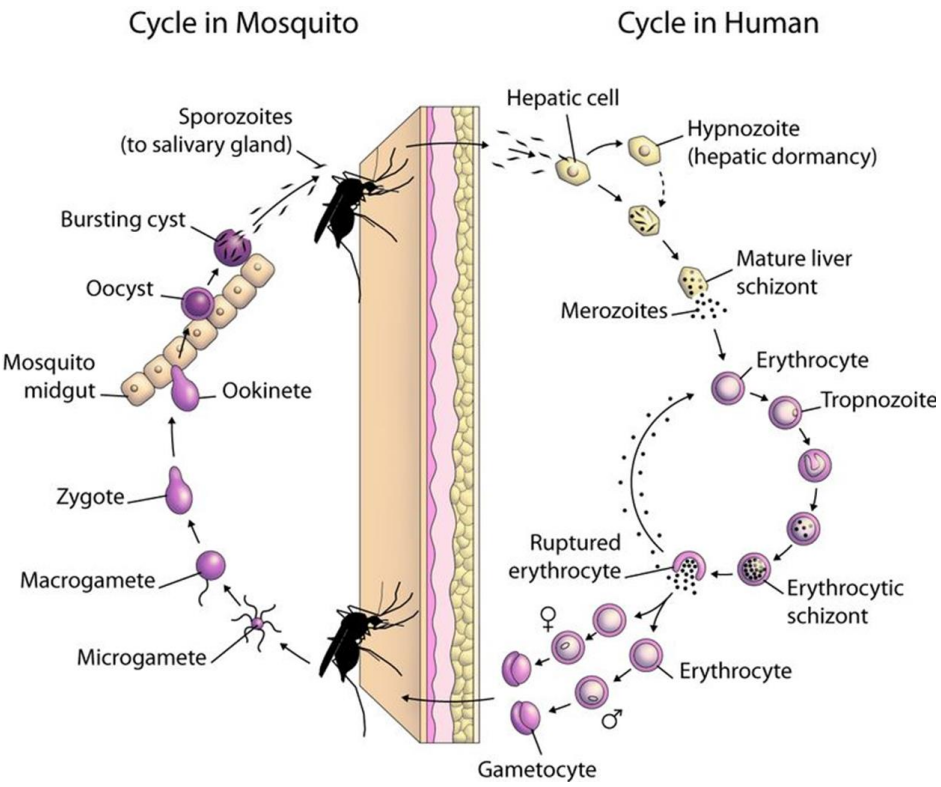

Figure 1.2 Life cycle of the malaria parasite.[5]

Once in the bloodstream, merozoites invade erythrocytes. This is the beginning of the blood stage, which is the only stage in which the parasite is pathogenic.[5] Inside the erythrocytes, the merozoites mature to form trophozoites. The nucleus of the trophozoite then divides asexually to produce a multinucleated schizont. Each schizont then divides further to form a new generation of mononucleated merozoites. The erythrocyte inevitably ruptures, releasing its contents, resulting in pathogenic symptoms in the human host. The released merozoites invade further erythrocytes as the erythrocytic stage undergoes multiple cycles. Alternatively, the merozoites develop sexually into gametocytes, which can be transmitted to a mosquito when it takes a blood meal from an infected human host. Once in the gut of the mosquito, the gametocytes develop into microgametes (male) and macrogametes (female) through gametogenesis. Fertilisation results in the formation of zygotes, which become ookinetes, penetrating the midgut wall of the mosquito, and then developing into oocysts. Within the oocyst, sporozoites develop by mitotic division. The oocysts eventually rupture, releasing sporozoites, which travel to the salivary gland of the mosquito, where the life cycle begins again.[5]

1.1.2 Haemozoin formation

Malaria pathogenesis begins once the parasite has entered the host erythrocytes. Parasites in the trophozoite and schizont stage ingest large quantities (60 – 80%) of host haemoglobin, transporting it to the parasitic digestive vacuole to be degraded.[6] This acidic organelle has a pH range of 5.2 – 5.6,[7] and contains a series of proteolytic enzymes, including plasmepsins (I, II and IV), histoaspartic protease, falcipains (2 and 3) and the metalloprotease falcilysin.[8-10] Once in the digestive vacuole, the catabolism of haemoglobin is catalysed by the aforementioned enzymes, to afford short peptides, which are further degraded to amino acids by aminopeptidases in the parasite cytoplasm.[11] These amino acids provide a source of nutrients, which is essential for parasite growth and maturation.

During the process of catabolism, the free haem by-product (Fe(II)PPIX) derived from haemoglobin is released into the digestive vacuole, as depicted in Figure 1.3. The iron centre of Fe(II)PPIX is oxidised from Fe(II) to Fe(III), likely through auto-oxidation by molecular oxygen (O_2), to produce haematin (ferriprotoporphyrin IX, Fe(III)PPIX).[6] This

free haem species has been demonstrated to induce free radical production,[12] peroxidation of lipid membranes,[13] as well as protein and DNA oxidation,[14, 15] and is thus toxic to the parasite. The *Plasmodium* parasite, however, employs a haem detoxification mechanism in order to overcome its harmful effects. In this process, the toxic haematin is converted to non-toxic haemozoin (malaria pigment), a highly insoluble microcrystalline substance, *via* biomineralization.[16] The chemically inert haemozoin accumulates in the digestive vacuole and is toxic to humans.

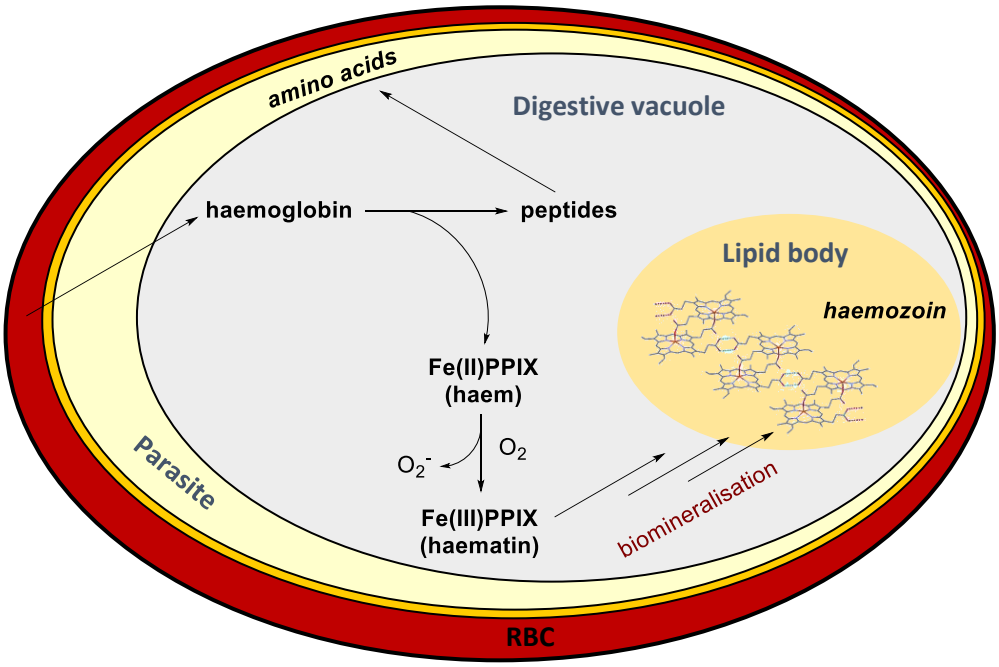

Figure 1.3 Haemoglobin degradation and haem detoxification.

1.1.3 Antimalarial therapies and modes of action

Quinoline-based antimalarials

The chemotherapeutic treatment of malaria has seen the use of a wide range of compounds with varying scaffolds and mechanisms of action. Perhaps the most highly efficacious of past antimalarials is the class of quinoline-based drugs (Figure 1.4). Drugs incorporating this heterocyclic scaffold have low toxicity, few side effects and low-cost preparation.[17] Successful drugs of this type include quinine (**1.1**), primaquine, amodiaquine, mefloquine (**1.2**) and the most prominent, chloroquine (**1.3**).[17]

Chloroquine (CQ) and other quinoline-based antimalarials are known to act against the pathogenic erythrocytic stage of the parasite life cycle, during which haemoglobin is ingested and transported to the digestive vacuole of the parasite.[18] CQ, a diprotic weak base, passes through the cell and parasite membranes unprotonated and accumulates in the acidic digestive vacuole.[18-20] Upon accumulation, CQ targets the parasite-induced host haem detoxification pathway, preventing the parasite from converting toxic haematin to the non-toxic haemozoin pigment.[18-20] The resulting build-up of toxic haem (Fe(III)PPIX) kills the parasite.[18-20]

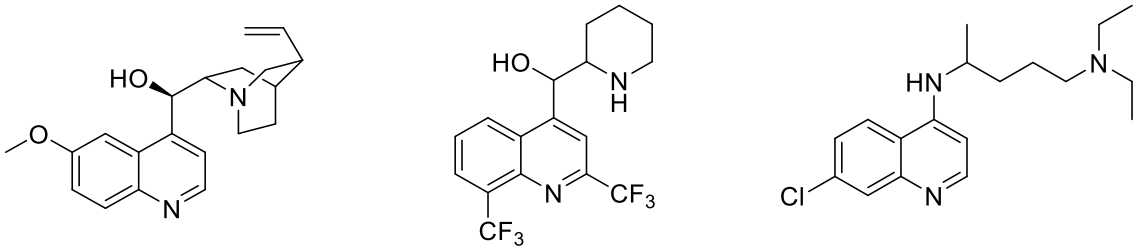

1.1 **1.2** **1.3**

Figure 1.4 Quinoline-based antimalarials; quinine (**1.1**), mefloquine (**1.2**) and chloroquine (**1.3**).

Microbes such as *P. falciparum* undergo mutations in order to survive, allowing them to develop resistance to previously effective treatments. CQ accumulates to a much lesser extent in resistant *Plasmodium falciparum* parasites, as a result of a point mutation in the *P. falciparum* CQ resistance transporter (*Pf*CRT).[21, 22] In the presence of the mutated form of this transporter, the protonated CQ present in the digestive vacuole is transported out, resulting in lower accumulation and thus a decrease in activity.[21, 22] As a result of widespread resistance, the use of quinoline-based drugs as monotherapies have been rendered largely ineffective. As part of combination therapies, certain quinoline-based drugs remain effective in specific parts of the world.

Antifolate drugs

Administering two or more drugs in combination reduces the risk of resistance and treatment failure. Antifolate drugs are a widely used class of antimalarials, acting by inhibition of enzymes involved in folate metabolism.[23, 24] This results in decreased pyrimidine synthesis, which is essential for DNA and other biomolecule synthesis. Antifolates are divided into two classes, dihydropteroate synthase (DHPS) inhibitors and

dihydrofolate reductase (DHFR) inhibitors, and are often administered in drug pairs.[24] Sulfadoxine (**1.4**) and pyrimethamine (**1.5**), depicted in Figure 1.5, are examples of DHPS and DHFR inhibitors, respectively.[24] Resistance to these antifolate drugs is brought about by point mutations in the key DHPS and DHFR targets.[25]

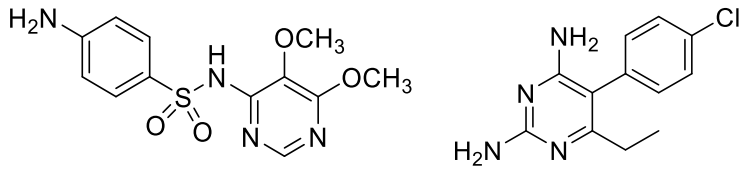

1.4 **1.5**

Figure 1.5 DHPS inhibitor, sulfadoxine (**1.4**) and DHFR inhibitor, pyrimethamine (**1.5**).

Artemisinin-based combination therapy

The current and most effective treatment against malaria infections is the artemisinin-based combination therapy (ACT).[26] Isolated from the Chinese sweet wormwood plant, artemisinin was traditionally used in the treatment of fever. Artemisinin and its derivatives, shown in Figure 1.6, were found to be highly effective antimalarials, capable of rapidly eliminating *Plasmodium* parasites from its human host.[27] ACT involves the use of two drugs, an artemisinin derivative together with another antimalarial of known efficacy and with a different mechanism of action.[28, 29] As a result of the short elimination half-life of artemisinin derivatives, a longer half-life partner drug is required.[28, 29] This combination gives enhanced activity, in addition to decreasing or delaying the development of drug resistance.

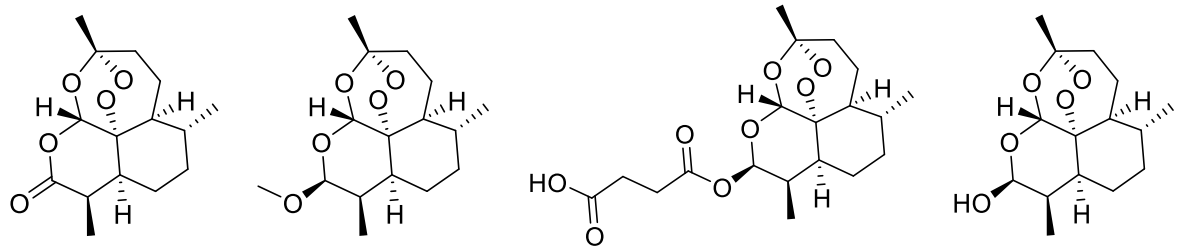

1.6 **1.7** **1.8** **1.9**

Figure 1.6 Artemisinin (**1.6**) and derivatives artemether (**1.7**), artesunate (**1.8**) and dihydroartemisinin (**1.9**).

Artemisinin derivatives show antiparasitic activity at multiple stages of the parasite life cycle, demonstrating activity against the asexual and sexual forms of the parasite.[29] The latter activity against sexual gametocytes, which are taken up by the mosquito vector, can thus lead to decreased transmission of malaria infection.[30] The exact mechanism of action of the artemisinins is not fully understood, however, the endoperoxide moiety of these compounds is thought to be essential for antimalarial activity.[31] Reactive oxygen species, generated through cleavage of the endoperoxide bridge, may result in parasite damage.[32] Although the ACT regimen is currently the most efficacious antimalarial treatment, there are recent reports of ACT-resistance in parts of Asia.[33, 34]

1.2 Tuberculosis

Tuberculosis (TB) is caused by a bacterial pathogen known as *Mycobacterium tuberculosis* and typically infects the lungs of its host, in the form of pulmonary TB. Tuberculosis remains a major global health problem, and is one of the top ten causes of death worldwide.[35] The WHO reports that in 2018, there were 10 million new cases of TB and 1.5 million deaths from the disease, with over 95% of cases and deaths occurring in developing countries.[36] Figure 1.7 shows the estimated TB incidence worldwide.

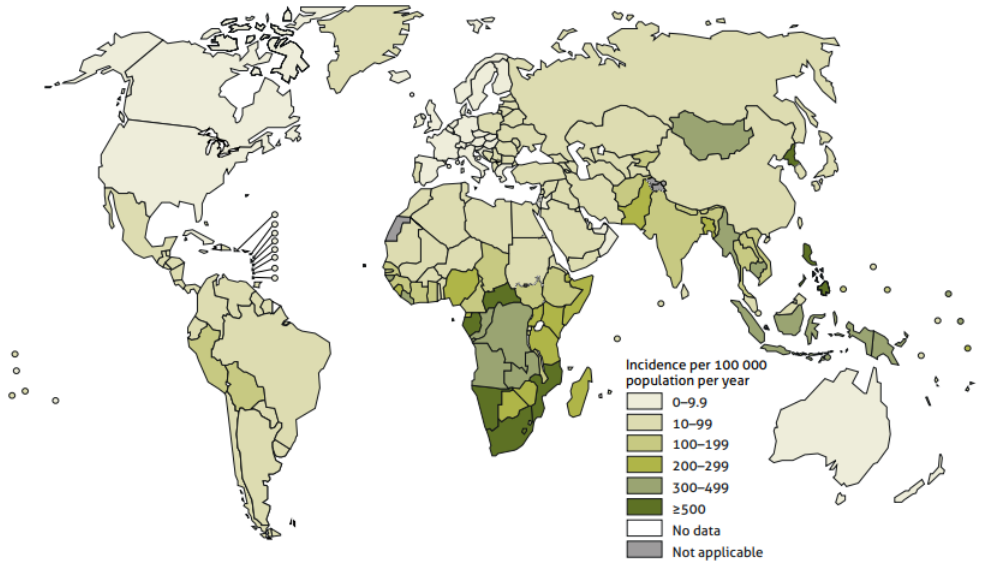

Figure 1.7 Estimated incidence of tuberculosis infection worldwide in 2018.[36]

1.2.1 Tuberculosis pathogenesis

Tuberculosis spreads through the air, when people who are infected with active pulmonary TB expel bacteria through coughing, sneezing or spitting. Inhalation of only a few tubercle bacilli is enough to result in the spread of TB infection. The pathogenic cycle of *M. tuberculosis* is depicted in Figure 1.8. Upon inhalation, TB infection begins once the tubercle bacilli bacteria reach the alveolar space in the lungs, where macrophages preferentially ingest the bacilli.[37] The macrophages proceed to eliminate the foreign bacteria by phagocytosis. Through this process, within the macrophage, the bacteria are stored in a phagosome, which combines with a lysosome to produce a phagolysosome. A combination of acidic pH, reactive oxygen species and lysosomal enzymes are employed to kill the bacteria.[37] Additional macrophages and other immune cells are recruited to the original infected macrophage, forming an aggregate called a granuloma.[37] The majority of the bacteria are inhibited by this innate immune response. Within the granuloma, the bacteria may remain alive and dormant, resulting in latent TB infection.[37] Approximately a quarter of the world's population are asymptomatically infected with latent TB, which can be reactivated at a later time.[35]

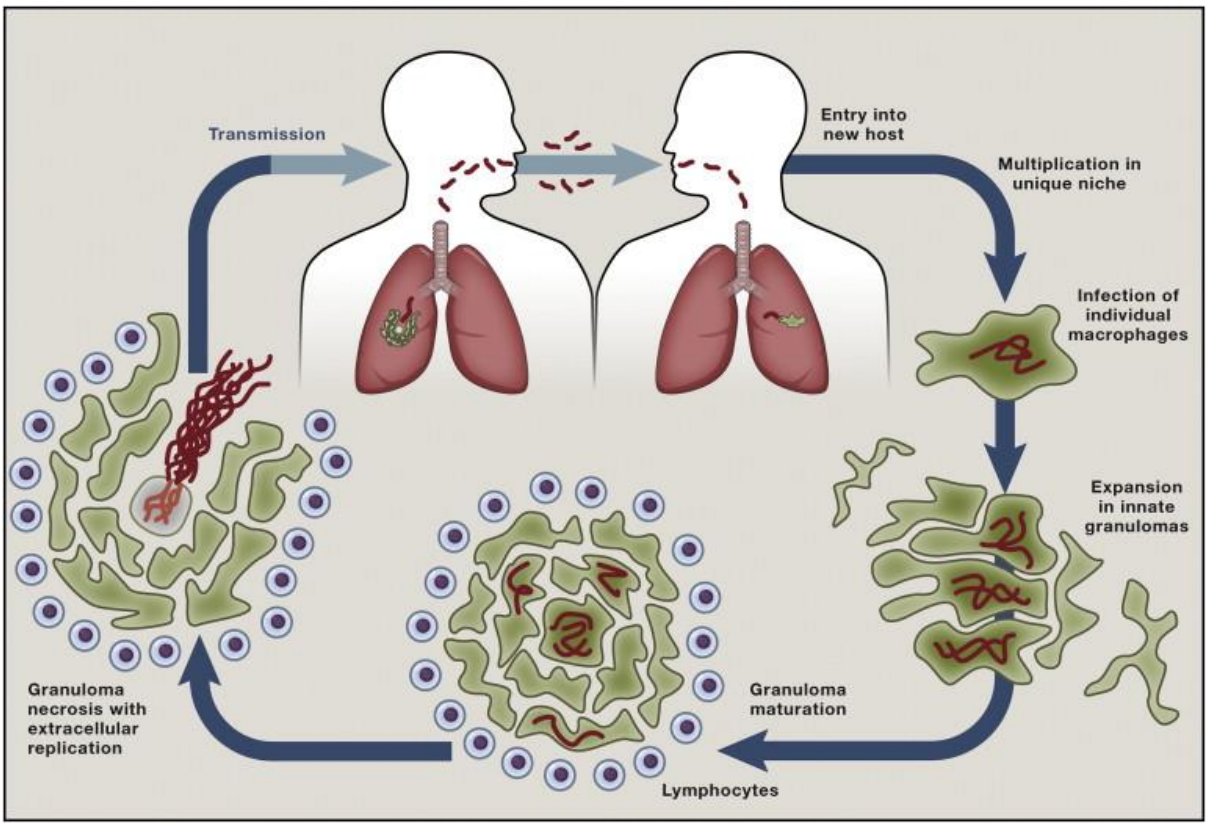

Figure 1.8 Pathogenic cycle of *M. tuberculosis*.[38]

On the other hand, *M*. *tuberculosis* is also able to resist antimicrobial mechanisms and disrupt macrophage signalling pathways in order to persist within the granuloma.[39] In this case, bacteria are able to evade or overcome the immune response, and bacterial replication takes place within the macrophage.[38] Under certain conditions, the infected granuloma may undergo necrosis, expelling the tubercle bacteria, where they replicate extracellularly.[38] Some bacteria can enter lymphatic channels or the bloodstream, and be further disseminated throughout the body. A further immune response is then triggered at the target tissues and organs.[38]

1.2.2 Anti-tuberculosis therapies and modes of action

The treatment of tuberculosis has involved the use of chemically diverse antimicrobial agents, with varying mechanisms of action. In the past, both monotherapies and combination therapies were utilised. Currently, however, long-term treatment with multiple drugs is required in order to cure the disease without relapse, and to prevent transmission and drug resistance.

Four-drug regimen

Current chemotherapy for drug susceptible TB (DS-TB) involves the use of isoniazid (INH, **1.10**), rifampicin (RIF, **1.11**), pyrazinamide (PZA, **1.12**) and ethambutol (EMB, **1.13**), known as the first-line drugs (Figure 1.9).[40] Used in a six-month regimen, all four drugs are administered for the first two months (intensive phase), followed by only INH and RIF for the remaining four months (continuation phase).[40]

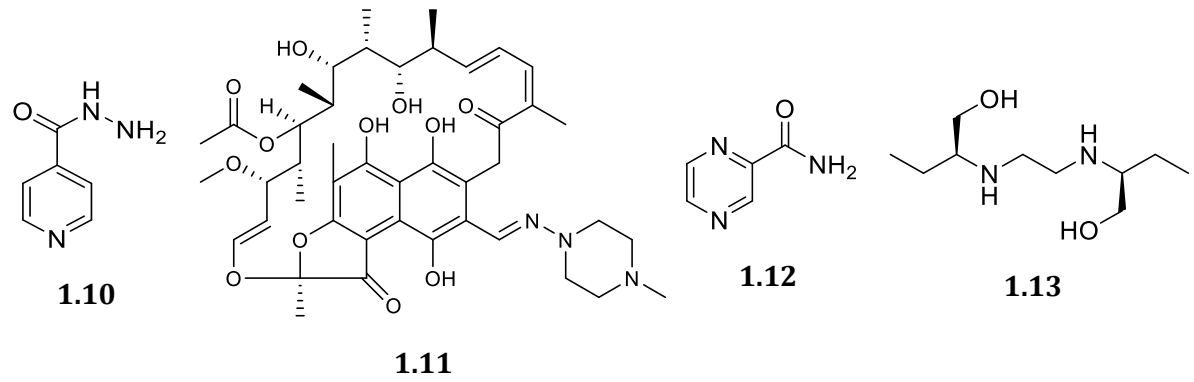

1.10 **1.11** **1.12** **1.13**

Figure 1.9 First-line drugs used against DS-TB; isoniazid (**1.10**), rifampicin (**1.11**), pyrazinamide (**1.12**) and ethambutol (**1.13**).

Isoniazid and pyrazinamide are pro-drugs, and are activated intracellularly through bacteria-specific metabolism. INH diffuses across the *M. tuberculosis* cell membrane through small water-filled pores.[41] It subsequently undergoes oxidative activation by the catalase-peroxidase katG to form an isonicotinyl radical.[42] Upon reaction with oxidised NAD^+ cofactors, several 4-isonicotinyl-NAD adducts are generated.[43] These active metabolites primarily inhibit the synthesis of mycolic acids, an essential component of the mycobacterial cell wall.[44, 45] RIF easily diffuses across the bacterial cell membrane as a result of its highly lipophilic nature.[46] The bactericidal properties of RIF are attributed to its ability to bind to mycobacterial DNA-dependent polymerases, resulting in the inhibition of mRNA synthesis.[47]

PZA enters the bacterium *via* ATP-dependent transport systems.[48] It is activated intracellularly by the bacterial pyrazinamidase pncA, to give the active pyrazinoic acid (POA).[49] The mechanism of action of PZA is poorly understood, however, it is hypothesised to act against non-replicating tubercle bacilli present in acidic compartments of the lungs during the early stages of TB infection.[50] This is consistent with the clinical observation that PZA is most active during the first two months of chemotherapy.[50] The mechanism of action of EMB is not fully understood and appears to be multifaceted. It is known to inhibit several mycobacterial cellular pathways, including RNA metabolism, phospholipid synthesis and mycolic acid transport.[50] The primary target of EMB, however, is the biosynthesis of arabinogalactan, an essential component of the mycobacterial cell wall.[51] Disruption of this pathway is achieved through inhibition of arabinan polymerisation.[52]

Through microbial mutations and the misuse of anti-TB treatments, drug-resistant mutant strains of *M. tuberculosis* have emerged. Multi-drug resistant TB (MDR-TB) is caused by strains that are resistant to INH and RIF, the most potent first-line drugs. Treatment for MDR-TB utilises second-line drugs, such as the fluoroquinolones.[40] Furthermore, extensively drug-resistant TB (XDR-TB) refers to strains of *M. tuberculosis* which are resistant to several first- and second-line drugs. Cases of totally drug-resistant TB (TDR-TB) have also been reported.[53]

Fluoroquinolones

Fluoroquinolones represent a class of bactericidal fluorine-substituted quinolone antibiotics which are active against Gram-positive and Gram-negative bacteria, and have been repurposed for their use as anti-TB agents. The WHO recommends the use of fluoroquinolones, such as levofloxacin (**1.14**), moxifloxacin (**1.15**) and ofloxacin (**1.16**), shown in Figure 1.10, as second-line drugs, in the treatment of MDR-TB.[40] This class of drugs have shown activity against both extracellular replicating bacteria and intracellular non-replicating bacteria.[54] Against *M*. *tuberculosis*, moxifloxacin (**1.15**) has bactericidal and sterilising activity similar to that of INH, and has thus been investigated as a potential first-line drug in the treatment of murine TB.[55]

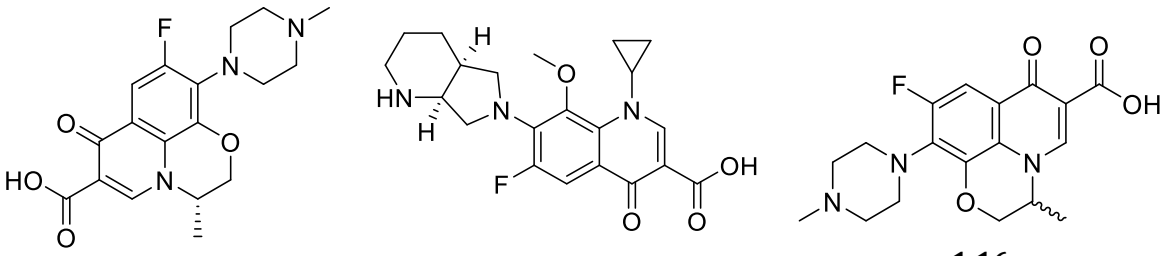

Figure 1.10 Second-line fluoroquinolone drugs; levofloxacin (**1.14**), moxifloxacin (**1.15**) and ofloxacin (**1.16**).

With regards to their mode of action, fluoroquinolones target two essential bacterial enzymes; DNA gyrase (topoisomerase II) and the closely related topoisomerase IV.[56] The drug traps the topoisomerase enzyme on DNA through formation of a complex containing the quinolone, DNA and the enzyme.[56] The ternary complex blocks the movement of transcription complexes and replication forks, thereby blocking DNA replication.[56]

1.3 Heterocyclic compounds

1.3.1 4-Aminoquinolines

Structure and chemotherapeutic application

Quinoline is a nitrogen-containing heterocyclic aromatic compound, comprising a benzene ring fused to a pyridine ring. The quinoline nucleus, depicted in Figure 1.11 (**1.17**), is present in many natural products, such as alkaloids extracted from Cinchona plants. The quinoline ring represents a popular scaffold in medicinal chemistry as a result of its diverse range biological properties,[57] which include anticancer,[58] antimycobacterial,[59, 60] antifungal[61] and anti-inflammatory activity.[62] However, quinoline derivatives have been most prominently applied in antimalarial chemotherapy,[63] as discussed earlier (Section 1.1.3).

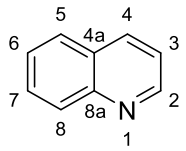

1.17

Figure 1.11 Structure of the quinoline nucleus.

The use of quinoline derivatives in the treatment of malaria began with quinine, an alkaloid consisting of a quinoline-alcohol group. Over the years, various other quinoline-containing drugs (Figure 1.12) were developed, as the result of drug toxicity, undesirable side-effects and drug-resistance.[63, 64] Pamaquine (**1.18**), an 8-aminoquinoline, represents the first synthetic antimalarial drug, however, its toxicity and multiple side-effects led to limited use. The less toxic analogue, primaquine (**1.19**), is known to eradicate hypnozoites of *P*. *vivax* and *P*. *ovale*.[65] The 4-aminoquinoline drug, chloroquine, was derived from an acridine-containing antimalarial, quinacrine (**1.20**), and became the most successful single drug in the treatment of malaria.[63, 64] Other 4-aminoquinoline drugs include amodiaquine (**1.21**) and piperaquine (**1.22**). The rise of chloroquine-resistant parasites led to the development of mefloquine, a potent 4-quinolinemethanol drug.[63, 64]

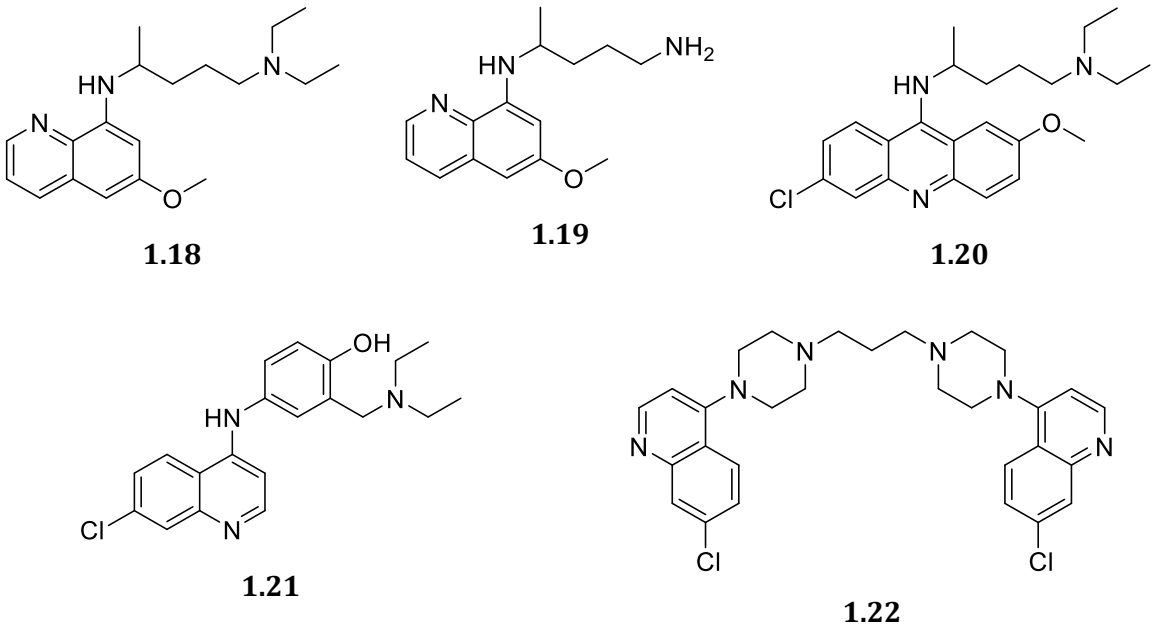

1.18 **1.19** **1.20**

1.21 **1.22**

Figure 1.12 Structures of 8-aminoquinoline drugs (**1.18** and **1.19**), an acridine-containing drug (**1.20**) and 4-aminoquinoline drugs (**1.21** and **1.22**).

Despite the presence of parasite resistance to some quinoline-based drugs, extensive studies to derivatise the scaffold continue to be done, to afford new and more effective treatments. Furthermore, the quinoline scaffold has also been repurposed for its use against other diseases.

4-Aminoquinolines against malaria and TB

Since the success of drugs such as chloroquine, amodiaquine and piperaquine, 4-aminoquinoline derivatives (Figure 1.13) have been further explored, with great potential in overcoming resistance.[66, 67] Ridley *et al*. reported the antimalarial activity of cyclohexane-linked bisquinoline analogues.[68] The S,S enantiomer, Ro 47-7737 (**1.23**) displayed low nanomolar *in vitro* activity against the chloroquine-sensitive (CQS) NF54 and chloroquine-resistant (CQR) K1 strains of *P*. *falciparum*, enhanced compared to chloroquine and mefloquine. In terms of a mode of action, Ro 47-7737 was a more potent inhibitor of haem polymerisation than CQ.[68] In addition, Ro 47-7737 was found to be a potent inhibitor of *P. vivax ex vivo* and *P. berghei in vivo*, however, its toxicity excluded the bisquinoline from further development. On the other hand, Delarue-Cochin *et al*. investigated the effect of shifting and modifying the 4'-phenolic group of amodiaquine in a series of related analogues.[69] The 5'-amino-substituted analogue (**1.24**) displayed *in*

vitro activity in the nanomolar range, against sensitive and resistant strains (Thai, FcB1R and K1) of *P. falciparum*. Compound **1.24** significantly inhibited *P. berghei in vivo* and displayed decreased cytotoxicity against MRC-5 cells compared to amodiaquine.[69]

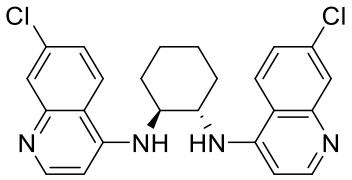

1.23

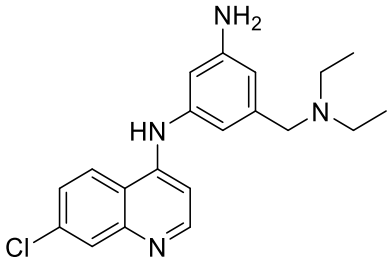

1.24

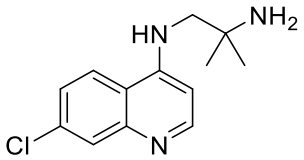

1.25

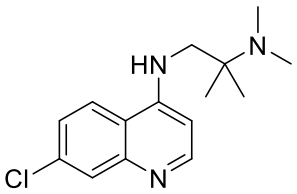

1.26

Figure 1.13 Antimalarial 4-aminoquinolines; bisquinoline Ro 47-7737 (**1.23**),[68] amodiaquine derivative (**1.24**)[69] and TDR 58845/6 (**1.25** and **1.26**)[70]

The antimalarial properties of two aminoquinoline derivatives, TDR 58845 (**1.25**) and TDR 58846 (**1.26**) were also reported.[70] Both analogues displayed potent *in vitro* activity (5.52 – 89.8 nM) against various sensitive and resistant *P. falciparum* strains, in addition to activity against early and late gametocyte stages. TDR 58845 and TDR58846 also cured *P. berghei* infected mice at 40 mg/kg. Furthermore, in combination studies, TDR 58845 (**1.25**) was synergistic with verapamil, desipramine and chlorpromazine, compounds known to reverse CQ resistance *in vitro*.[70]

Numerous aminoquinoline derivatives have been investigated for activity against *M. tuberculosis*, many displaying potency against drug-sensitive and MDR-TB strains.[59, 60, 71] Ngwane *et al*. screened a series of 2(5H)-furanone-aminoquinoline derivatives against strains of *M. tuberculosis*.[72] A biphenyl-containing analogue (**1.27**) was most potent, displaying comparable mycobacterial inhibition in both the H37Rv and MDR-TB strains. Additionally, when evaluated in two-drug combinations, compound **1.27** showed synergistic activity with RIF, and additive activity with INH and EMB.[72] With regards to

the mechanism of action of aminoquinolines against *M*. *tuberculosis*, recent research has shown various aminoquinoline derivatives to inhibit the mycobacterial DNA gyrase,[73, 74] in a similar way to the anti-TB fluoroquinolones. An anthranilamide-aminoquinoline derivative (**1.28**), displayed potent low micromolar activity (MIC = 1.56 μM) against the H37Rv strain, greater than pyrazinamide, a first-line anti-TB drug.[74] Furthermore, compound **1.28** inhibited *M*. *tuberculosis* DNA gyrase in a DNA supercoiling assay.

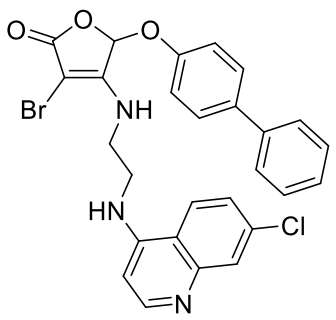

1.27

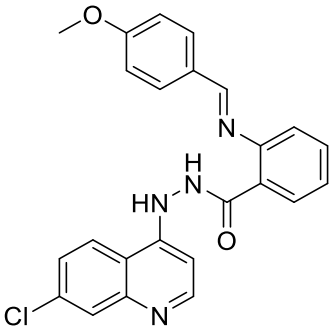

1.28

Figure 1.14 Furanone-aminoquinoline derivative (**1.27**)[72] and an anthranilamide-aminoquinoline derivative (**1.28**)[74] with activity against *M*. *tuberculosis*.

1.3.2 Benzimidazoles

Structure and synthesis

Benzimidazole is a nitrogen-containing heterocyclic compound, consisting of a benzene ring fused at the 4,5-positions of an imidazole ring. The structures and systematic numbering of the imidazole and benzimidazole ring systems are shown in Figure 1.15. These aromatic *N*-heterocycles are abundant in many natural products. The imidazole ring is present in many alkaloids and proteins, the α-amino acid histidine, the hormone histamine, as well as purine and biotin. The bicyclic benzimidazole occurs in *N*-ribosyl-dimethylbenzimidazole, an axial ligand of the cobalt metal atom in vitamin B_{12}.

1.29 **1.30**

Figure 1.15 Structures of imidazole (**1.29**) and benzimidazole (**1.30**).

Benzimidazole and its derivatives are most commonly synthesised by condensation of a 1,2-diaminobenzene with a carbonyl compound (aldehydes, carboxylic acids and derivatives), as shown in Scheme 1.1. The reaction is performed under dehydrating conditions and in the presence of a strong acid (e.g. hydrochloric acid or boric acid) or a milder acidifying reagent (Lewis acids or mineral acids). When condensing with an aldehyde, an oxidising reagent is required to achieve the benzimidazole core.[75]

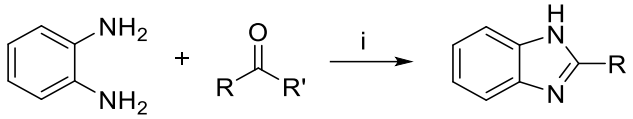

Scheme 1.1 General scheme for synthesis of a benzimidazole. (i) strong acid/milder reagents/oxidising agent; R' = aldehyde, carboxylic acid or derivatives.

Benzimidazoles in chemotherapy

The abundance of benzimidazoles in nature has led to the investigation into their potential as therapeutic agents. In the 1940s, Woolley[76] and Folkers[77] speculated that benzimidazoles may elicit similar biological responses or activity as purines and vitamin B_{12}, respectively. To date, extensive research has proven the benzimidazole nucleus to have a wide range of therapeutic applications owing to its presence in a host of biologically active compounds. These include anticancer and antihistaminic agents, as well as antiviral and antiparasitic (anthelmintic) agents.[75, 78] Examples of benzimidazole-based drugs are shown in Figure 1.16.

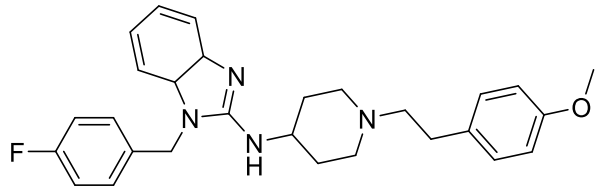

1.31

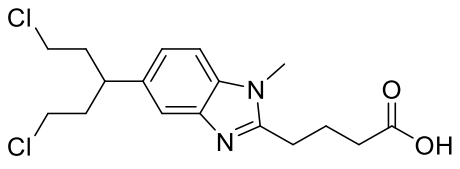

1.32

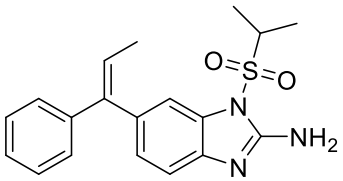

1.33

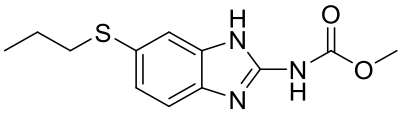

1.34

Figure 1.16 Benzimidazole-based pharmaceuticals; astemizole (**1.31**) – antihistaminic, bendamustine (**1.32**) – anticancer, enviradene (**1.33**) – antiviral, albendazole (**1.34**) – anthelmintic.

Benzimidazoles against malaria and TB

The antiplasmodium activity of various benzimidazole derivatives has been explored and in many cases, display potent *in vitro* activity against *P. falciparum,* as well as good *in vivo* efficacy in animal models.[75, 79, 80] Benzimidazoles may exert their antimalarial activity through various mechanisms. In a similar manner to the commercially-available omeprazole, benzimidazoles may inhibit proton pumps.[81] Artemisinin-derived benzimidazoles have been reported to exhibit *in vitro* and *in vivo* antimalarial activity, and may act accordingly.[82] Recent research has shown the β-haematin inhibition ability of some benzimidazole derivatives, exerting their antiparasitic activity in a manner similar to that of chloroquine.[83, 84] A 1,4-bis(3-aminopropyl)piperazine-derived benzimidazole, depicted in Figure 1.17 (**1.35**), has been shown to inhibit β-hematin formation.[84] On the other hand, a benzimidazole-thiophene-2-carboxamide derivative (Figure 1.17, **1.36**), reported by Skerlj *et al*., displayed significant inhibition of parasite dihydroorotate dehydrogenase (DHODH), as well as inhibition of parasite growth.[85]

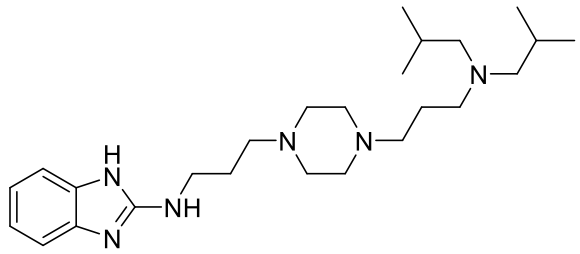

1.35

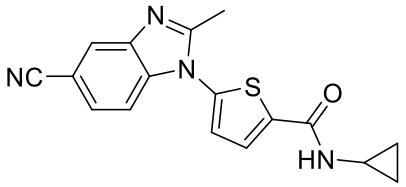

1.36

Figure 1.17 Antiparasitic benzimidazole derivatives; a β-haematin inhibitor (**1.35**)[84] and a dihydroorotate dehydrogenase inhibitor (**1.36**).[85]

In addition to antiplasmodium activity, the activity of benzimidazole-derived compounds against various strains of *Mycobacterium tuberculosis* has been explored. The *in vitro* antimycobacterial screenings of large libraries of benzimidazole derivatives have yielded promising results for the use of this scaffold.[75, 86, 87] The *in vivo* activities of some derivatives against TB in a murine model have also been investigated.[88] A pyrido[1,2-α]benzimidazole reported by Pieroni *et al.*, shown in Figure 1.18 (**1.37**), displayed good activity against five multidrug-resistant (MDR) and extensively drug-resistant (XDR) *M. tuberculosis* strains.[89] In another study, a nitrofuranyl benzimidazole (Figure 1.18, **1.38**), exhibited potent activity, high bactericidal selectivity and killed *M. tuberculosis* in primary human macrophages.[90]

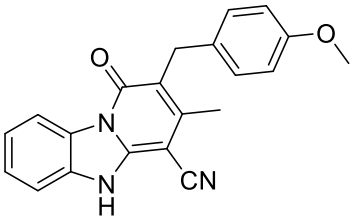

1.37

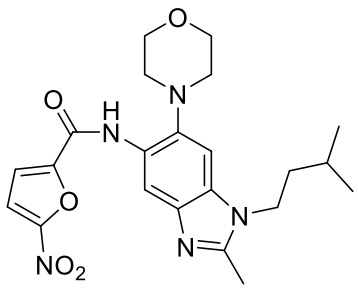

1.38

Figure 1.18 Benzimidazole-based antimycobacterial agents; A pyrido[1,2-α]benzimidazole derivative (**1.37**)[89] and a nitrofuranyl benzimidazole derivative (**1.38**).[90]

1.4 Metals in medicine

1.4.1 Background

The application of metal-based compounds in medicinal chemistry is a research field that has gained significant interest over the past fifty years and has reached many different therapeutic areas. Compared to organic drugs, metal complexes offer diverse biological and chemical properties, which can be tuned through the choice of metal, oxidation states, ligands and various geometries.[91] With this in mind, metal-based therapeutic agents are conferred unique redox properties, new biological targets and increased lipophilicity, which may result in enhanced biological activity.[91, 92]

The use of metal-containing complexes in chemotherapy is thought to have begun with Paul Ehrlich's discovery of an arsenic-based drug known as Salvarsan, which was used to treat syphilis.[93] Much attention was drawn to the field of metal-based chemotherapy following the success of the platinum-based anticancer drug cisplatin, shown in Figure 1.19 (**1.39**).[94] To date, cisplatin and its derivatives are still the most widely used drugs in the treatment of many cancers, but their high toxicity and side effects, as well as resistance shown in some cell lines, has led to the need for new drug therapies.[95]

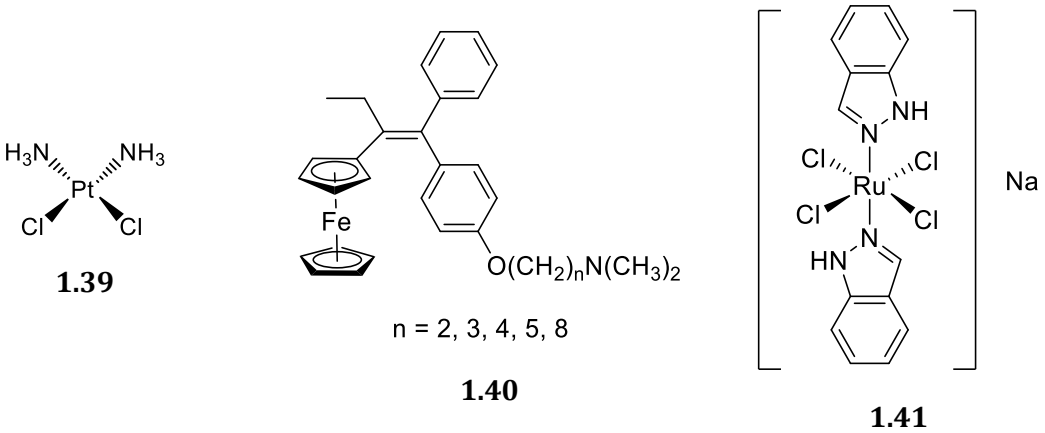

1.39 **1.40** **1.41**

Figure 1.19 Cisplatin (**1.39**),[94] ferrocifens (**1.40**)[97] and NKP-1339 (**1.41**).[99]

New drug design strategies continue to be explored in order to overcome the drawbacks of current chemotherapies, and numerous metal-based compounds (Figure 1.19) have been investigated.[92, 96] These strategies include the incorporation of metals into compounds of known therapeutic value. In this regard, Jaouen and co-workers reported

on the potent anticancer activity of ferrocifen-type compounds (**1.40**), which are ferrocenyl derivatives of the breast cancer drug, tamoxifen.[97] On the other hand, the use of alternative metals to platinum, which may reduce toxicity, and ligand modification have also been explored as important strategies for improving biological activity. Ruthenium complexes have featured prominently amongst metal-based anticancer agents, demonstrating much lower toxicity compared to platinum-based drugs.[98] Most notably, a Ru(III)-imidazole complex (NAMI-A) and Ru(III)-indazole complexes (KP1019 and NKP-1339) represent iconic anticancer drug candidates displaying potent activity, low general toxicity and tumour selectivity.[99] NKP-1339 (**1.41**) is the latest and most promising analogue to reach clinical trials.[100] Metal-based compounds are also being applied in antimalarial and antimycobacterial research.

1.4.2 Metal-containing antimalarial agents

Transition metal-based quinoline complexes

A range of transition metals have been incorporated into the quinoline scaffold with the aim of enhancing the activity and overcoming resistance of *P*. *falciparum* strains.[101, 102] The first application of metal-based complexes in antimalarial research is thought to have been initiated by Wasi *et al.*, who evaluated the antiplasmodium activity of transition metal-containing complexes of known antimalarial drugs, amodiaquine and primaquine.[103] This modification did not result in enhanced activity. Using a similar principal, Sanchez-Delgado *et al.* incorporated rhodium and ruthenium into the CQ scaffold (Figure 1.20), to afford metal-CQ conjugates which were evaluated against *P*. *berghei in vitro* and *in vivo*.[104] The Rh-CQ conjugate [RhCl(COD)CQ] (**1.42**) exhibited nanomolar activity, comparable to that of CQ, while the Ru-CQ conjugate $[RuCl_2(CQ)]_2$ (**1.43**) was 5 times more active. However, [RhCl(COD)CQ] and $[RuCl_2(CQ)]_2$ were both more potent than CQ *in vivo*, reducing parasitemia by 73 and 94%, respectively, at low doses (1 mg/kg). $[RuCl_2(CQ)]_2$ was further screened *in vitro* against CQR FcB1 and FcB2 strains of *P*. *falciparum* and was found to be 2-5 times more active than CQ.[104]

Gold-CQ complexes have also been investigated, with varying degrees of antimalarial activity.[105, 106] Most notably, the antimalarial properties of a cationic gold(I)-CQ complex

were investigated. [Au(PPh$_3$)(CQ)]PF$_6$ (**1.44**) displayed IC$_{50}$ values in the nanomolar range against the CQR FcB1 and FcB2 strains of *P. falciparum*.[106] Screened *in vivo* against *P. berghei* infected mice, [Au(PPh$_3$)(CQ)]PF$_6$ (**1.44**) inhibited parasitemia by 84% at a low dose of 1 mg/kg, at which CQ only afforded a 44% reduction in parasitemia.[106] A series of organometallic Ru(II)-arene complexes of CQ was evaluated against various sensitive and resistant strains of *P. falciparum*.[107] The dicationic quinoline *N*-coordinated complex (**1.45**) presented the highest activity in the series, displaying significantly enhanced activity compared to CQ in the resistant Dd2, K1 and W2 strains.[107] The antiplasmodium activity of CQ conjugates of other transition metals, such as iridium, manganese, cobalt, copper and platinum have since also been explored.[108, 109]

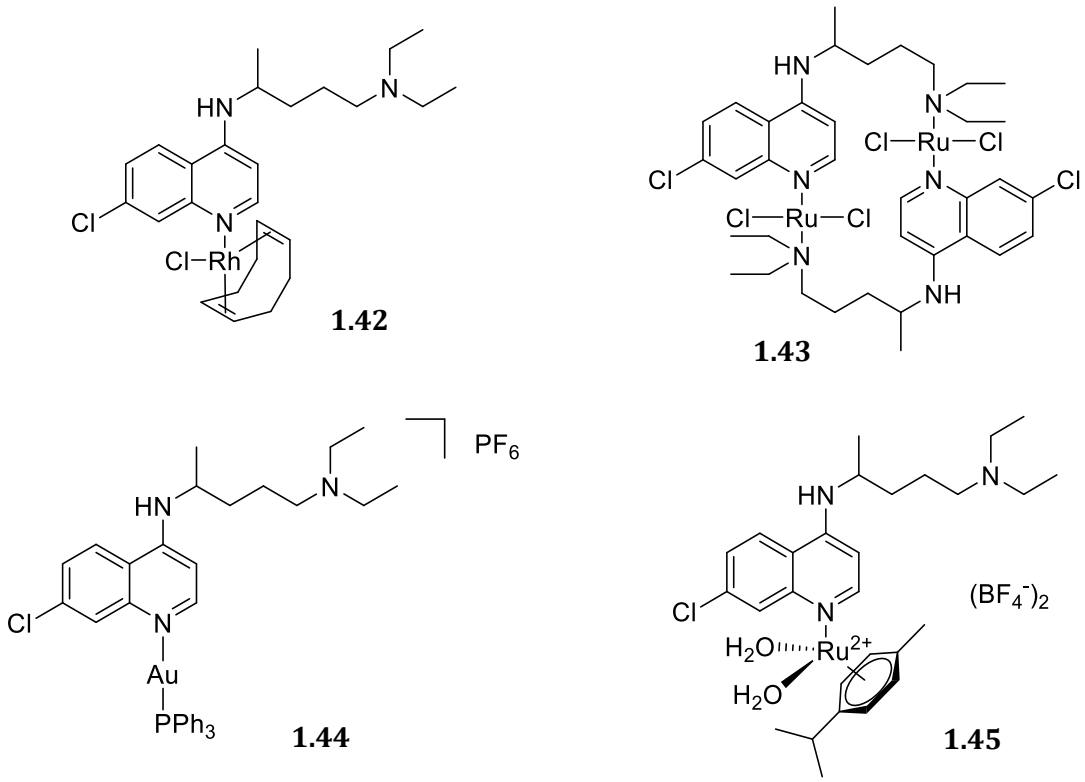

Figure 1.20 Rhodium-, ruthenium- and gold-CQ conjugates with antimalarial activity.[104, 106, 107]

On the other hand, extensive work has also been done in exploring the antiplasmodium activity of metal-based complexes in which the aminoquinoline ligands are bound in a bidentate chelating mode.[110-112] Stringer *et al*. investigated the activity of mono- and polynuclear *N^O*-coordinated Rh(I) aminoquinoline-salicylaldimine complexes against the sensitive NF54 and resistant K1 strain of *P. falciparum*.[113] In general, the aminoquinoline-salicylaldimine ligands were more active than the corresponding

complexes. The mononuclear Rh(I) complex **1.46**, shown in Figure 1.21, was the most potent complex in the series, displaying IC_{50} values of 98 and 866 nM against the NF54 and K1 strains, respectively.[113]

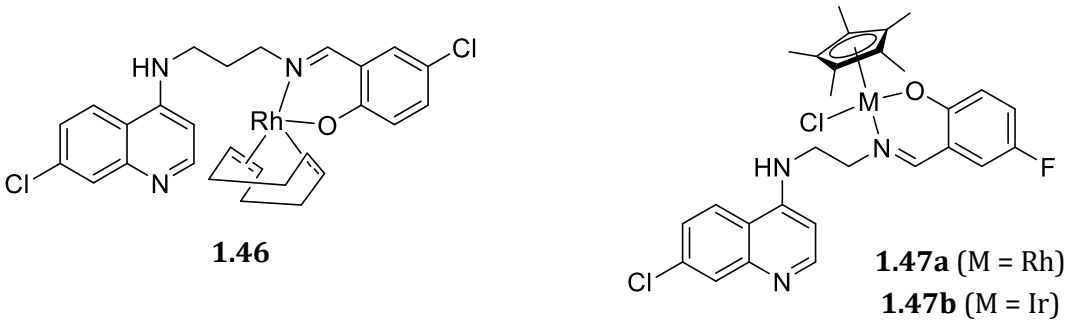

1.46

1.47a (M = Rh)
1.47b (M = Ir)

Figure 1.21 Rhodium and iridium aminoquinoline complexes with *in vitro* antiplasmodium activity.[113, 114]

A series of *N^N*- and *N^O*-coordinated Rh(III) and Ir(III) aminoquinoline complexes were evaluated for their *in vitro* activity against the CQS NF54 and CQR Dd2 strains of *P. falciparum*.[114] All complexes displayed nanomolar activity, with the Rh(III) complexes proving more potent than their Ir(III) analogues in all cases.[114] The fluoro-substituted Rh(III) and Ir(III) complexes (**1.47a** and **1.47b**) were most active overall. Complex **1.47a** (0.016 and 0.20 μM) and **1.47b** (0.030 and 0.26 μM) displayed IC_{50} values lower than and comparable to that of CQ (0.027 and 0.22 μM) in the NF54 and Dd2 strains, respectively.[114] In both of the aforementioned series, the complexes were less active in the resistant strains, suggesting cross-resistance with CQ.[113, 114]

The use of ferrocene, an organometallic sandwich compound, in potential therapeutic agents has garnered attention as a result of its favourable properties.[115] The chemical stability, low toxicity, ease of derivatisation and redox accessibility of the metallocene are useful for biological application. The ferrocenyl derivatisation of known drugs (Figure 1.22) is a popular strategy for enhancing efficacy and overcoming drug-resistance, however, it should be noted that this strategy may not be effective in all cases.[115] The incorporation of a ferrocenyl moiety into antimalarial drugs such as quinine (**1.48**), mefloquine and artemisinin (**1.49**) did not lead to improved antimalarial activity compared to the parent compounds.[116, 117]

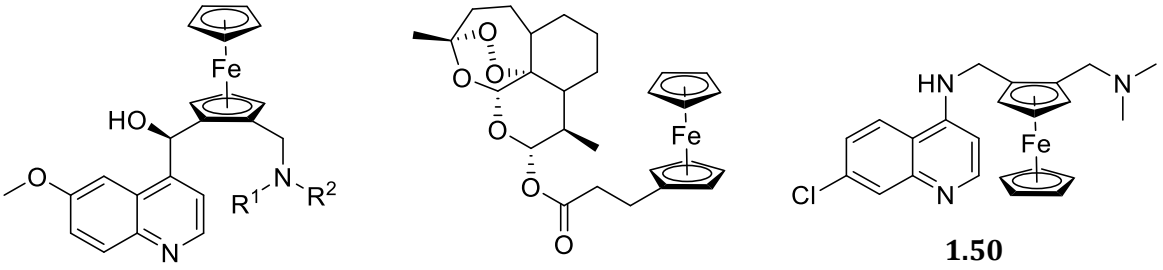

1.48 **1.49** **1.50**

Figure 1.22 Ferrocenyl conjugates of known antimalarials (**1.48 – 1.50**).[116-118]

The incorporation of ferrocene into the lateral side chain of chloroquine by Biot *et al*., to afford ferroquine (FQ, **1.50**), represents the most promising organometallic derivatisation in antimalarial research to date.[118] In the *in vitro* antiplasmodium screening against various CQ-sensitive and CQ-resistant strains of *P*. *falciparum*, FQ displayed comparable activity to CQ in the sensitive strains, and was 22-times more potent than CQ in the resistant strains.[118] FQ was also potent *in vivo* against *P*. *berghei*, *P*. *yoelii* and *P*. *vinckei vinckei* infected mice, most significantly curing *P*. *berghei* and *P*. *vinckei* infections at low doses (8.3 mg/kg) compared to CQ.[118, 119] FQ is thought to exert its antimalarial activity through a dual mode of action. In a similar manner to CQ, FQ accumulates in the parasite digestive vacuole, where it inhibits haemozoin formation.[120, 121] In addition, FQ generates reactive oxygen species (ROS) under oxidising conditions, *via* Fenton-like reactions, which cause parasite damage.[122] FQ is currently in Phase IIb clinical trials in combination with artefenomel, a synthetic trioxolane.[123]

Transition metal-based benzimidazole complexes

Metal-based benzimidazole complexes have been applied in antifungal studies[124] and anticancer studies,[125] however, their application as antiplasmodium agents is limited. The *in vitro* activity of a series of ferrocenyl and cyrhetrenyl benzimidazole complexes against the 3D7 (CQS) and W2 (CQR) strains of *P. falciparum* was reported by Toro *et al*.[126] All complexes displayed moderate micromolar antiplasmodium activity, with the nitro-substituted cyrhetrenyl complex (Figure 1.23, **1.51**) proving most active.[126] The *in vitro* activity of ferrocenylmethyl-substituted benzimidazoles and benzimidazolium iodide salts in the CQS NF54 strain of *P. falciparum* was investigated.[127] In all cases, the ferrocenyl benzimidazolium iodides were significantly more potent than their neutral

counterparts, displaying IC_{50} values in the nanomolar range. The thiophene-substituted analogue (Figure 1.23, **1.52**) was most active, displaying an IC_{50} value of 40 nM.[127]

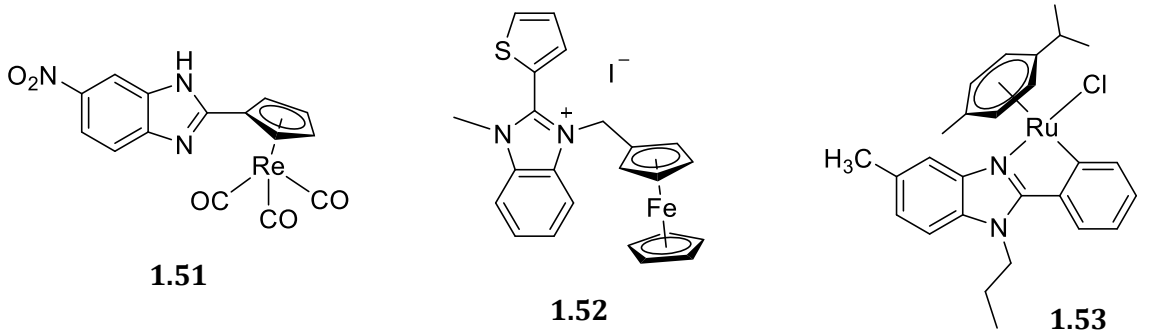

1.51 **1.52** **1.53**

Figure 1.23 Cyrhetrenyl and ferrocenyl benzimidazole complexes (**1.51** and **1.52**),[126,127] and a PGM-containing benzimidazole complex (**1.53**).[128]

More recently, Rylands *et al*. investigated the antiplasmodium activity of cyclometalated ruthenium(II), iridium(III) and rhodium(III) benzimidazole complexes against the CQS NF54 and CQR K1 strains.[128] These PGM-containing complexes displayed good activity in the low micromolar range, improved compared to the respective ligands. Overall, the Ru(II) and Ir(III) complexes proved more active than the Rh(III) complexes, and the methyl-substituted Ru(II) complex (**1.53**) was most potent, displaying an IC_{50} value of 0.97 μM in the resistant K1 strain.[128]

1.4.3 Metal-containing anti-tuberculosis agents

There are numerous examples of metal-based and organometallic complexes applied in antimycobacterial screenings, incorporating metals such as gold,[129] silver,[130] platinum,[131] palladium,[132] ruthenium[133] and iron in the form of ferrocene.[134-136] Based on the success of ferroquine, the strategy of ferrocenyl derivatisation of therapeutic compounds has also been applied in the search for new antimycobacterial agents. Pelinski and co-workers reported on the antimycobacterial activity of a series of ferrocenyl analogues of ethambutol (EMB) and isoniazid (INH), two first-line anti-TB drugs.[137-139] The ferrocenyl-INH analogues, shown in Figure 1.24 (**1.54**), were most potent, displaying sub-micromolar MIC values (0.75 and 0.72 μM), better than that of EMB (9.8 μM), against the H37Rv strain of *M. tuberculosis*.[139]

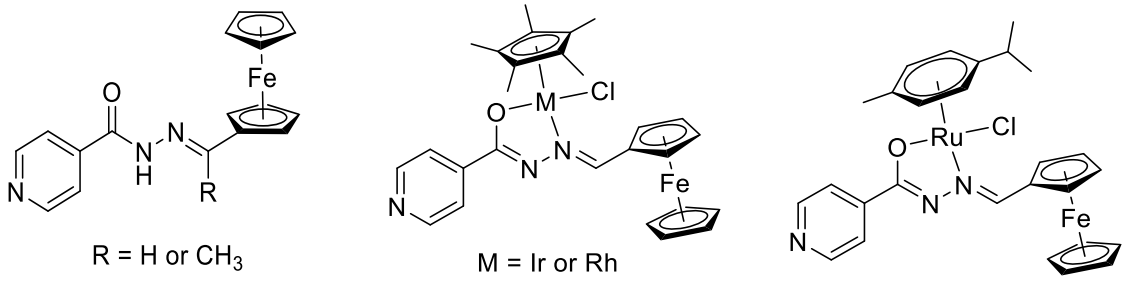

1.54 **1.55** **1.56**

Figure 1.24 Ferrocenyl-INH analogue (**1.54**)[139] and heterobimetallic PGM-containing ferrocenyl-INH complexes (**1.55** and **1.56**).[140]

Recently, *N^O*-coordinated iridium-, rhodium- and ruthenium-arene derivatives of a ferrocenyl-INH analogue were prepared and evaluated against the H37Rv strain of *M. tuberculosis*.[140] These heterobimetallic PGM-containing complexes, which are shown in Figure 1.24 (**1.55** and **1.56**), displayed moderate glycerol-dependent inhibitory activity.[140]

1.5 Hybrid chemotherapies

1.5.1 History and motivation

The current and most effective treatment for malaria and tuberculosis makes use of combination therapies or multi-drug regimens. The strategy is brought about by the emergence of drug-resistant microbes, and are utilised in order to overcome this resistance, reduce the risk of treatment failure and shorten treatment periods. Monotherapies, previously used in the treatment of both malaria and tuberculosis, are no longer a viable option due to the selection for resistant mutants of microbes and the speed with which this arises. A unique approach to achieving combination therapies is through molecular hybridisation or the use of hybrid chemotherapy. This strategy involves the combination of two or more bioactive moieties or pharmacophores into a single chemical compound, a 'hybrid'.[141] The combination of entities to form the hybrid agent may confer enhanced biological activity compared to the individual parent compounds, through multiple possible modes of action and enhanced uptake.[141-143] The hybrid is also afforded new physical and chemical properties, which may attribute interesting biological

properties to these systems. Optimisation of these properties may lead to improved solubility, pharmacokinetics and metabolic stability.[141-143] In addition, drug resistance may be bypassed or overcome through the attachment of known therapeutic compounds to inhibitors of antimicrobial resistance mechanisms.[141, 143]

1.5.2 Hybrid compounds against *P. falciparum* and *M. tuberculosis*

Molecular hybridisation is an emerging strategy in drug design and discovery and has been well applied in numerous therapeutic areas. The field of hybrid chemotherapy has been dominated by hybrids designed to target nitric oxide and cyclooxygenase-mediated inflammatory events.[144, 145] Other literature examples include hybrid agents targeting events mediated by histamine,[146] as well as hybrids designed to inhibit enzymes such as metalloproteinase-1 and cathepsin L.[147] With regards to infectious diseases, hybrid compounds have been applied in antimalarial and anti-tuberculosis research. To date, almost all classes of antimalarial drugs have been combined to produce hybrid compounds, the quinoline scaffold featuring prominently in many of these combinations.[143, 148-151] These hybrids (Figure 1.25), combining known antimalarial and repurposed pharmacophores, exhibit good *in vitro* activity against *P. falciparum*, and many have *in vivo* efficacy in animal models.

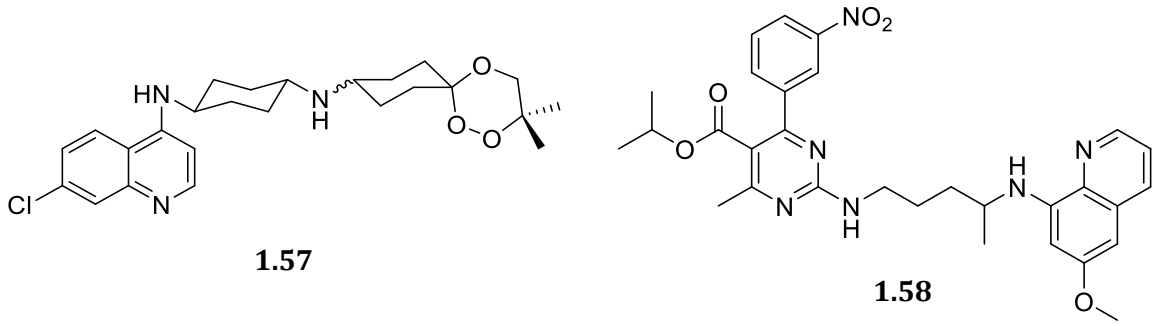

1.57 **1.58**

Figure 1.25 Antimalarial hybrids; trioxaquine hybrid (**1.57**)[152] and primaquine-pyrimidine hybrid (**1.58**).[153]

Most significantly, Cosledan *et al*. investigated the antimalarial activity of a trioxaquine compound (PA1103/SAR116242), which combines a 1,2,4-trioxane moiety with the 4-aminoquinoline structure.[152] The 1,2,4-trioxane moiety is present in the antimalarial artemisinin derivatives. This trioxaquine hybrid, depicted in Figure 1.25 (**1.57**), was highly active against CQS and CQR strains of *P. falciparum in vitro*, exhibited good *in vivo*

efficacy in mouse models, as well as a good drug-like profile. The trioxaquine hybrid drug is the first antimalarial hybrid to reach clinical trials against *P. falciparum*.[152] More recently, Kaur *et al*. investigated the antimalarial properties of a novel class of hybrids combining a pyrimidine-5-carboxylate with the antimalarial primaquine.[153] One of the primaquine-pyrimidine hybrids (Figure 1.25, **1.58**) displayed good blood and liver stage activities, suggesting dual-stage antiplasmodium activity.[153] This is a promising result in terms of tackling resistant strains.

Antimycobacterial hybrids have been explored to a lesser extent. Cinnamic acid-guanylhydrazones[154] and quinoline coupled 1,2,3-triazoles[155] are among the hybrids displaying promising activity against the H37Rv strain of *M. tuberculosis*. A benzofuran-isatin hybrid (Figure 1.26, **1.59**) proved more potent than the first-line drug RIF against H37Rv and MDR-TB strains of *M. tuberculosis*.[156] Several fluoroquinolone-isatin hybrids have been investigated as anti-tuberculosis agents, showing great promise.[157] In a study by Sriram *et al*., a gatifloxacin-isatin hybrid (**1.60**) was 16- and 64-fold more potent than second-line drug gatifloxacin against DS-TB and MDR-TB strains, respectively.[158] Additionally, compound **1.60** was efficacious *in vivo*, showing a reduction in bacterial load in lung and spleen tissues in a mouse model.[158]

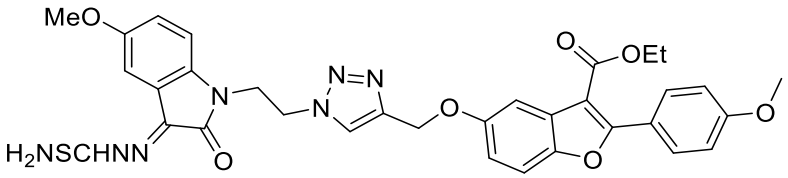

1.59

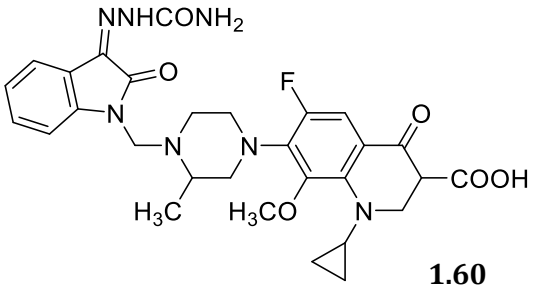

1.60

Figure 1.26 Antimycobacterial hybrid agents; Isatin-benzofuran hybrid (**1.59**)[156] and gatifloxacin-isatin hybrid (**1.60**).[158]

1.5.3 Metal-based hybrid complexes

Literature reports on the biological activity of metal-based hybrids complexes are largely limited to the use of ferrocene as the metal entity.[151] These include ferrocenyl carbohydrate-aminoquinoline conjugates,[159] ferroquine conjugates with glutathione-depletors and -reductase inhibitors,[160] ferrocenyl chalcone-aminoquinoline hybrids,[161] and ferroquine-thiosemicarbazone hybrids.[162] Bellot *et al*. investigated the antimalarial properties of trioxaferroquines, organometallic hybrid complexes incorporating a 1,2,4-trioxane group covalently linked to ferroquine as the bioactive moieties.[163] All of the trioxaferroquine compounds displayed potent activity in the nanomolar range against CQR strains of *P*. *falciparum*. The most active trioxaferroquine hybrid (Figure 1.27, **1.61**) displayed IC_{50} values of 20 and 17 nM against the CQR FcB1 and FcM29 strains, respectively. Compound **1.61** was efficacious *in vivo*, clearing parasitemia in *P*. *vinckei petteri* infected mice when administered orally at a low dose (10 mg/kg).[163]

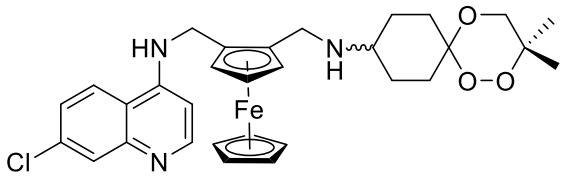

1.61

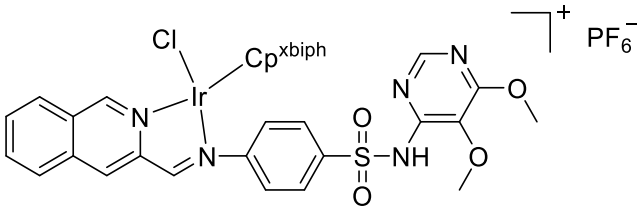

1.62

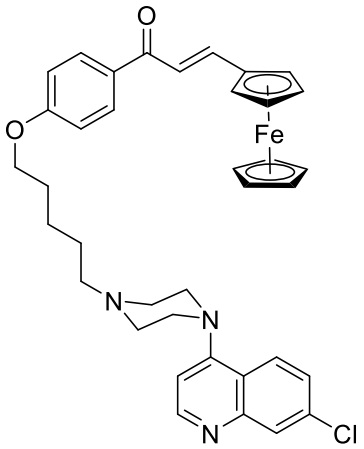

1.63

Figure 1.27 Metal-containing antimalarial hybrids; trioxaferroquine hybrid (**1.61**),[163] Ir(III)-containing quinoline-sulfadoxine hybrid complex (**1.62**)[164] and piperazine-linked aminoquinoline-ferrocenylchalcone (**1.63**).[165]

PGM-based hybrid complexes have also been investigated for their antimicrobial activity. Chellan *et al*. reported on the antiplasmodium and antimycobacterial activity of cationic ruthenium(II), iridium(III) and rhodium(III) complexes of hybrids incorporating a

quinoline moiety and the antimalarial sulfadoxine.[164] The *in vitro* screening against *P*. *falciparum* and *M*. *tuberculosis*, revealed that the Ru(II) hybrid complexes were inactive and in general, the Rh(III) complexes were more active than their Ir(III) analogues. However, an Ir(III) hybrid complex (**1.62**) had the best antimicrobial activity overall, displaying nanomolar IC_{50} values against the CQS 3D7 and CQR Dd2 strains of *P*. *falciparum*.[164] In a recent study, the antimycobacterial activity of piperazine-linked aminoquinoline-ferrocenylchalcone conjugates against the $mc^2$6230 strain of *M*. *tuberculosis* was evaluated.[165] Ferrocenyl derivatisation resulted in enhanced activities compared to the organic analogues and compound **1.63** was most active overall.[165]

There remains great scope for the preparation of metal-based hybrid complexes, and their application in biological studies. This is particularly true for antiplasmodium and antimycobacterial research. Thus, this project encompasses the combination of pharmacophores to prepare different series of hybrid compounds, and the incorporation of PGMs into these scaffolds to afford metal-containing hybrid complexes. These hybrids and their corresponding complexes were applied in pharmacological evaluations against *P*. *falciparum* and *M*. *tuberculosis* and contribute to the growing library of tested compounds to determine which structural components are important for biological activity.

1.6 Aims and Objectives

1.6.1 General aims

The incorporation of transition metals, specifically PGMs, into the structures of hybrid compounds is an emerging field, and is of great interest in the design and development of novel therapeutic agents. The purpose of this study was to prepare and develop hybrid ligands and their transition metal-containing complexes as potential antimicrobial agents. The proposed general structure of these hybrid compounds is shown in Figure 1.28.

Figure 1.28: Proposed general structure of hybrid compounds to be prepared.

The overall aims of the project were as follows:

i. To prepare organic and ferrocenyl aminoquinoline-benzimidazole hybrid compounds (Figure 1.29).
ii. To prepare neutral and cationic PGM-containing hybrid complexes of the most pharmacologically-active hybrid ligands (Figure 1.31).
iii. To evaluate the pharmacological properties of all hybrid ligands and complexes against microbial strains.
iv. To investigate potential mechanisms of antimicrobial action of the hybrid ligands and complexes.

1.6.2 Specific objectives

Synthetic objectives

- The rational design and synthesis of a series of organic and ferrocenyl aminoquinoline-benzimidazole hybrid compounds as shown in Figure 1.29. The 2-position of the benzimidazole was substituted with either an organic phenyl or pyridyl group, or an organometallic ferrocenyl group. The 5-position of the benzimidazole was varied using substituents from the Craig Plot (Figure 1.30), commonly used in rational drug design,

which categorises substituents based on hydrophobicity (π) and electron-withdrawing/donating nature (σ).

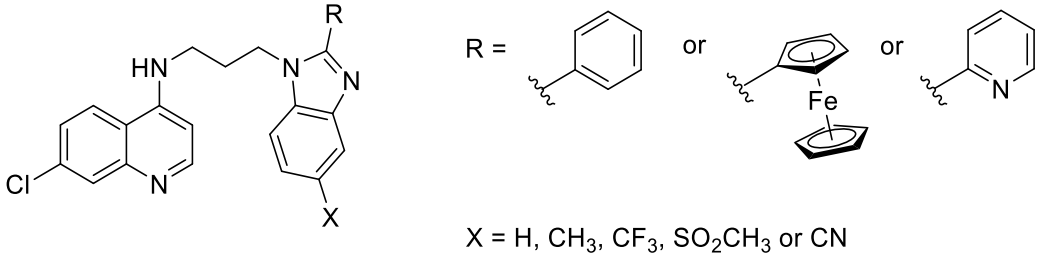

Figure 1.29 General structure of the organic and ferrocenyl aminoquinoline-benzimidazole hybrid compounds.

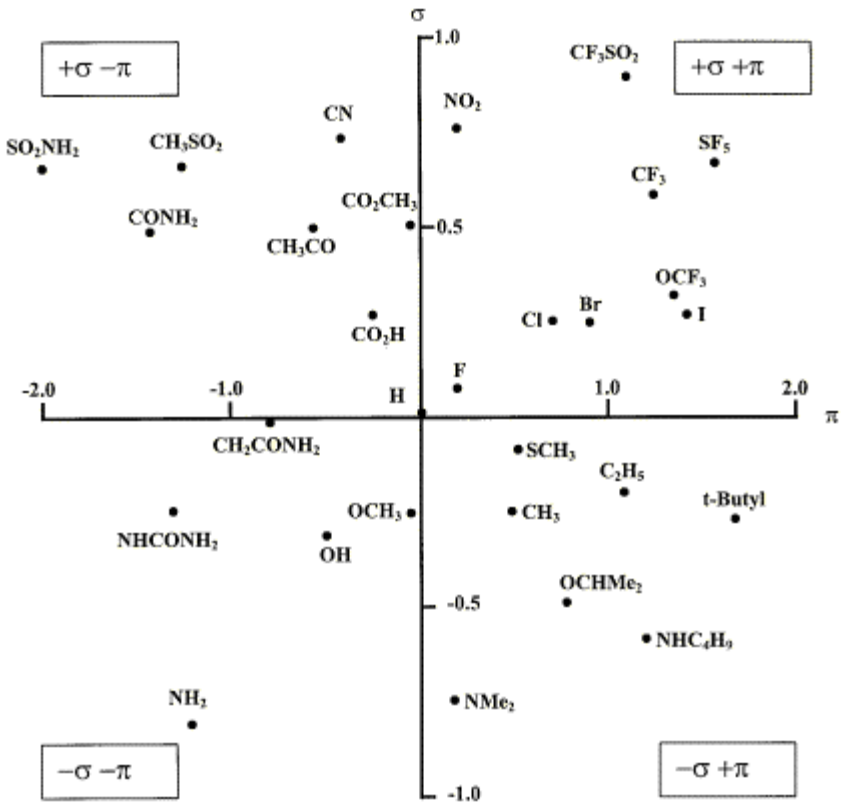

Figure 1.30 Craig Plot

- The synthesis of neutral and cationic iridium(III) and rhodium(III) complexes of selected 2-phenyl and 2-pyridyl aminoquinoline-benzimidazole ligands, as shown in Figure 1.31. Complexation was achieved through *C^N*- and *N^N*-coordination modes.

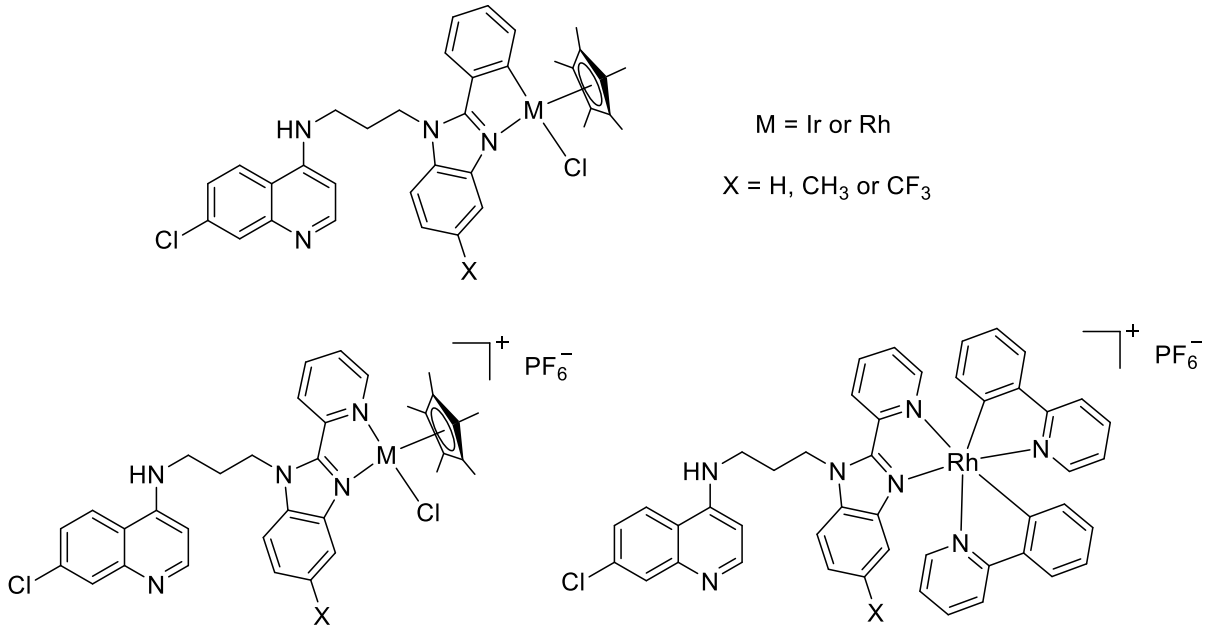

Figure 1.31 General structures of neutral and cationic PGM-containing aminoquinoline-benzimidazole hybrid complexes.

Characterisation

- The full characterisation of all compounds using ^{1}H, $^{13}C\{^{1}H\}$, $^{31}P\{^{1}H\}$, COSY and HSQC nuclear magnetic resonance (NMR) spectroscopy, infrared (IR) spectroscopy, and electron impact (EI) or electrospray ionisation (ESI) mass spectrometry. High-performance liquid chromatography (HPLC) was used to confirm purity and melting points were determined. The molecular structures of selected compounds were confirmed using single-crystal X-ray diffraction.

Pharmacological studies

- The evaluation of the hybrid ligands and PGM-containing complexes against the chloroquine-sensitive NF54 and multidrug-resistant K1 strains of *Plasmodium falciparum*. Cytotoxicity was determined against the non-tumorigenic Chinese hamster ovarian (CHO) cell-line. Selected compounds were screened for their *in vivo* efficacy against *Plasmodium berghei*-infected mice.

- The evaluation of their activity against the H37Rv strain of *Mycobacterium tuberculosis*, in the interest of drug repurposing and repositioning.

- Mechanistic studies of selected pharmacologically active hybrid compounds. Active compounds from each series were tested for their ability to inhibit β-haematin formation using the NP-40 detergent-mediated assay. A cellular haem fractionation assay was used to confirm haemozoin inhibition. A DNA cleavage assay was employed to determine reactive oxygen species (ROS) generation for a ferrocenyl hybrid compound.

- Investigation of the catalytic ability of selected Ir(III) and Rh(III) hybrid complexes in the transfer hydrogenation of NAD^+ to form NADH.

1.7 References

1. World Health Organisation, *World Malaria Report 2018*, WHO Press, Geneva, 2018.
2. https://www.who.int/news-room/fact-sheets/detail/malaria, (accessed October 2019).
3. World Health Organization, *Global malaria control and elimination: report of a technical review*, WHO Press, Geneva, 2008.
4. World Health Organization, *Malaria vector control and personal protection: report of a WHO study group*, World Health Organization, 2006.
5. Life cycle of the malaria parasite *http://www.malwest.gr/en-us/malaria/informationforhealthcareprofessionals/plasmodiumlifecycle.aspx* (accessed February 2016)
6. T. J. Egan, *Mol. Biochem. Parasit.*, 2008, **157**, 127-136.
7. S. M. Dzekunov, L. M. B. Ursos and P. D. Roepe, *Mol. Biochem. Parasit.*, 2000, **110**, 107-124.
8. R. Banerjee, J. Liu, W. Beatty, L. Pelosof, M. Klemba and D. E. Goldberg, *P. Natl. Acad. Sci. USA*, 2002, **99**, 990-995.
9. P. J. Rosenthal, P. S. Sijwali, A. Singh and B. R. Shenai, *Curr. Pharm. Des.*, 2002, **8**, 1659-1672.
10. K. K. Eggleson, K. L. Duffin and D. E. Goldberg, *J. Biol. Chem.*, 1999, **274**, 32411-32417.
11. C. S. Gavigan, J. P. Dalton and A. Bell, *Mol. Biochem. Parasit.*, 2001, **117**, 37-48.

12. J. Van Der Zee, D. P. Barr and R. P. Mason, *Free Radic. Biol. Med.*, 1996, **20**, 199-206.
13. J. Gutteridge and A. Smith, *Biochem. J.*, 1988, **256**, 861-865.
14. R. L. Aft and G. Mueller, *J. Biol. Chem.*, 1984, **259**, 301-305.
15. R. L. Aft and G. Mueller, *J. Biol. Chem.*, 1983, **258**, 12069-12072.
16. S. H. Abdalla and G. Pasvol, *Malaria: A hematological perspective*, Imperial college press, 2004.
17. T. J. Egan, *Expert Opin. Ther. Pat.*, 2001, **11**, 185-209.
18. M. Foley and L. Tilley, *Pharmacol. Ther.*, 1998, **79**, 55-87.
19. C. D. Fitch, *Life sciences*, 2004, **74**, 1957-1972.
20. H. Ginsburg, S. Ward and P. Bray, *Parasitol. Today*, 1999, **15**, 357-360.
21. A. Ecker, A. M. Lehane, J. Clain and D. A. Fidock, *Trends Parasitol.*, 2012, **28**, 504-514.
22. L. Tilley, P. Loria and M. Foley, *Antimalarial chemotherapy*, 2001, 87-121.
23. P. Olliaro, *Pharmacol. Ther.*, 2001, **89**, 207-219.
24. M. A. Avery, S.-R. Choi and P. Mukherjee, *Curr. Med. Chem.*, 2008, **15**, 161-171.
25. A. Dieckmann and A. Jung, *Parasitology*, 1986, **93**, 275-278.
26. W. H. Organization, *Guidelines for the treatment of malaria*, World Health Organization, 2015.
27. P. J. De Vries and T. K. Dien, *Drugs*, 1996, **52**, 818-836.
28. P. M. O'Neill and G. H. Posner, *J. Med. Chem.*, 2004, **47**, 2945-2964.
29. T. M. Davis, H. A. Karunajeewa and K. F. Ilett, *Med. J. Australia*, 2005, **182**, 181-185.
30. P. Chen, G. Li, X. Guo, K. He, Y. Fu, L. Fu and Y. Song, *Chinese Med. J. - Peking*, 1994, **107**, 709-711.
31. T. T. Hien and N. J. White, *The Lancet*, 1993, **341**, 603-608.
32. S. R. Meshnick, *Int. J. Parasitol.*, 2002, **32**, 1655-1660.
33. M. Enserink, *Journal*, 2010, 328, 844-846.
34. World Health Organization, *Global plan for artemisinin resistance containment (GPARC)*, WHO Press, Geneva, 2011.
35. *https://www.who.int/news-room/fact-sheets/detail/tuberculosis* (accessed October 2019).
36. World Health Organisation, *Global Tuberculosis Report 2019*, WHO Press, Geneva 2019.

37. I. Smith, *Clin. Microbiol. Rev.*, 2003, **16**, 463-496.
38. C. Cambier, S. Falkow and L. Ramakrishnan, *Cell*, 2014, **159**, 1497-1509.
39. D. F. Warner and V. Mizrahi, *Nat. Med.*, 2007, **13**, 282.
40. World Health Organization, *Treatment of Tuberculosis: Guidelines*, WHO Press, Geneva, 2010.
41. F. Bardou, C. Raynaud, C. Ramos, M. A. Laneelle and G. Lanŕelle, *Microbiology*, 1998, **144**, 2539-2544.
42. Y. Zhang, B. Heym, B. Allen, D. Young and S. Cole, *Nature*, 1992, **358**, 591.
43. M. Nguyen, C. Claparols, J. Bernadou and B. Meunier, *Chembiochem*, 2001, **2**, 877-883.
44. F. Winder and P. Collins, *Microbiology*, 1970, **63**, 41-48.
45. K. Takayama, H. K. Schnoes, E. L. Armstrong and R. W. Boyle, *J. Lipid Res.*, 1975, **16**, 308-317.
46. M. M. Wade and Y. Zhang, *Front. Biosci.*, 2004, **9**, 975-994.
47. G. Hartmann, *Biochem. Biophys. Acta*, 1967, **145**, 843-844.
48. C. Raynaud, M.-A. Lanéelle, R. H. Senaratne, P. Draper, G. Lanéelle and M. Daffé, *Microbiology*, 1999, **145**, 1359-1367.
49. A. Scorpio and Y. Zhang, *Nature medicine*, 1996, **2**, 662.
50. D. Mitchison, *Tubercle*, 1985, **66**, 219-225.
51. K. Takayama and J. O. Kilburn, *Antimicrob. Agents Ch.*, 1989, **33**, 1493-1499.
52. K. Mikusova, R. A. Slayden, G. S. Besra and P. J. Brennan, *Antimicrob. Agents Ch.*, 1995, **39**, 2484-2489.
53. A. A. Velayati, M. R. Masjedi, P. Farnia, P. Tabarsi, J. Ghanavi, A. H. ZiaZarifi and S. E. Hoffner, *Chest*, 2009, **136**, 420-425.
54. S. Gillespie and N. Kennedy, *Int. J. Tuberc. Lung D.*, 1998, **2**, 265-271.
55. E. L. Nuermberger, T. Yoshimatsu, S. Tyagi, R. J. O'Brien, A. N. Vernon, R. E. Chaisson, W. R. Bishai and J. H. Grosset, *Am. J. Resp. Crit. Care*, 2004, **169**, 421-426.
56. K. Drlica and M. Malik, *Curr. Top. Med. Chem.*, 2003, **3**, 249-282.
57. A. Marella, O. P. Tanwar, R. Saha, M. R. Ali, S. Srivastava, M. Akhter, M. Shaquiquzzaman and M. M. Alam, *Saudi Pharm. J.*, 2013, **21**, 1-12.
58. O. Afzal, S. Kumar, M. R. Haider, M. R. Ali, R. Kumar, M. Jaggi and S. Bawa, *Eur. J. Med. Chem.*, 2015, **97**, 871-910.

59. R. S. Keri and S. A. Patil, *Biomed. Pharmacother.*, 2014, **68**, 1161-1175.
60. S. Singh, G. Kaur, V. Mangla and M. K. Gupta, *J. Enzym. Inhib. Med. Ch.*, 2015, **30**, 492-504.
61. R. Musiol, M. Serda, S. Hensel-Bielowka and J. Polanski, *Curr. Med. Chem.*, 2010, **17**, 1960-1973.
62. S. Mukherjee and M. Pal, *Drug Discov. Today*, 2013, **18**, 389-398.
63. R. G. Ridley and A. T. Hudson, *Expert Opin. Ther. Pat.*, 1998, **8**, 121-136.
64. M. Schlitzer, *ChemMedChem*, 2007, **2**, 944-986.
65. N. Vale, R. Moreira and P. Gomes, *Eur. J. Med. Chem.*, 2009, **44**, 937-953.
66. P. M. O'Neill, S. A. Ward, N. G. Berry, J. P. Jeyadevan, G. A. Biagini, E. Asadollaly, B. K. Park and P. G. Bray, *Curr. Top. Med. Chem.*, 2006, **6**, 479-507.
67. M. Rudrapal and D. Chetia, *Der Pharma Lett*, 2011, **3**, 29-36.
68. R. G. Ridley, H. Matile, C. Jaquet, A. Dorn, W. Hofheinz, W. Leupin, R. Masciadri, F.-P. Theil, W. F. Richter and M.-A. Girometta, *Antimicrob. Agents Ch.*, 1997, **41**, 677-686.
69. S. Delarue-Cochin, E. Paunescu, L. Maes, E. Mouray, C. Sergheraert, P. Grellier and P. Melnyk, *Eur. J. Med. Chem.*, 2008, **43**, 252-260.
70. F. E. Sáenz, T. Mutka, K. Udenze, A. M. Oduola and D. E. Kyle, *Antimicrob. Agents Ch.*, 2012, **56**, 4685-4692.
71. B. Liu, F. Li, T. Zhou, X. Q. Tang and G. W. Hu, *J. Heterocyclic Chem.*, 2018, **55**, 1863-1873.
72. A. H. Ngwane, J. L. Panayides, F. Chouteau, L. Macingwana, A. Viljoen, B. Baker, E. Madikane, C. de Kock, L. Wiesner and K. Chibale, *IUBMB life*, 2016, **68**, 612-620.
73. B. Medapi, P. Suryadevara, J. Renuka, J. P. Sridevi, P. Yogeeswari and D. Sriram, *Eur. J. Med. Chem.*, 2015, **103**, 1-16.
74. P. S. Salve, S. G. Alegaon and D. Sriram, *Bioorg. Med. Chem. Lett.*, 2017, **27**, 1859-1866.
75. R. S. Keri, A. Hiremathad, S. Budagumpi and B. M. Nagaraja, *Chem Biol Drug Des*, 2015, **86**, 19-65.
76. D. Woolley, *J. Biol. Chem.*, 1944, **152**, 225-232.
77. G. Emerson, N. G. Brink, F. W. Holly, F. Koniuszy, D. Heyl and K. Folkers, *J. Am. Chem. Soc.*, 1950, **72**, 3084-3085.

78. Y. Bansal and O. Silakari, *Bioorg. Med. Chem.*, 2012, **20**, 6208-6236.
79. A. J. Ndakala, R. K. Gessner, P. W. Gitari, N. October, K. L. White, A. Hudson, F. Fakorede, D. M. Shackleford, M. Kaiser and C. Yeates, *J. Med. Chem.*, 2011, **54**, 4581-4589.
80. S. Thota and R. Yerra, *Curr. Protein Pept. Sci.*, 2016, **17**, 000-000.
81. T. S. Skinner-Adams, T. M. Davis, L. S. Manning and W. A. Johnston, *T. Roy. Soc. Trop. Med. H.*, 1997, **91**, 580-584.
82. X.-B. Liao, J.-Y. Han and Y. Li, *Tetrahedron Lett.*, 2001, **42**, 2843-2845.
83. J. Camacho, A. Barazarte, N. Gamboa, J. Rodrigues, R. Rojas, A. Vaisberg, R. Gilman and J. Charris, *Bioorg. Med. Chem.*, 2011, **19**, 2023-2029.
84. R. Deprez-Poulain and P. Melnyk, *Comb. Chem. High T. Scr.*, 2005, **8**, 39-48.
85. R. T. Skerlj, C. M. Bastos, M. L. Booker, M. L. Kramer, R. H. Barker Jr, C. A. Celatka, T. J. O'Shea, B. Munoz, A. B. Sidhu and J. F. Cortese, *ACS Med. Chem. Lett.*, 2011, **2**, 708-713.
86. F. Fei and Z. Zhou, *Expert Opin. Ther. Pat.*, 2013, **23**, 1157-1179.
87. G. Yadav and S. Ganguly, *Eur J Med Chem*, 2015, **97**, 419-443.
88. S. E. Knudson, K. Kumar, D. Awasthi, I. Ojima and R. A. Slayden, *Tuberculosis*, 2014, **94**, 271-276.
89. M. Pieroni, S. K. Tipparaju, S. Lun, Y. Song, A. W. Sturm, W. R. Bishai and A. P. Kozikowski, *ChemMedChem*, 2011, **6**, 334-342.
90. Y. Gong, S. S. Karakaya, X. Guo, P. Zheng, B. Gold, Y. Ma, D. Little, J. Roberts, T. Warrier and X. Jiang, *Eur. J. Med. Chem.*, 2014, **75**, 336-353.
91. N. P. Barry and P. J. Sadler, *ACS nano*, 2013, **7**, 5654-5659.
92. G. Gasser, I. Ott and N. Metzler-Nolte, *J. Med. Chem.*, 2010, **54**, 3-25.
93. K. Strebhardt and A. Ullrich, *Nat. Rev. Cancer*, 2008, **8**, 473.
94. B. Rosenberg and L. Vancamp, *Nature*, 1969, **222**, 385-386.
95. E. Wong and C. M. Giandomenico, *Chem. Rev.*, 1999, **99**, 2451-2466.
96. M. A. Jakupec, M. Galanski, V. B. Arion, C. G. Hartinger and B. K. Keppler, *Dalton Trans.*, 2008, 183-194.
97. G. Jaouen, A. Vessières and S. Top, *Chem. Soc. Rev.*, 2015, **44**, 8802-8817.
98. E. Alessio, G. Mestroni, A. Bergamo and G. Sava, *Metal ions in biological systems*, 2004, **42**, 323-352.

99. E. Alessio and L. Messori, *Molecules*, 2019, **24**, 1995.
100. R. Trondl, P. Heffeter, C. R. Kowol, M. A. Jakupec, W. Berger and B. K. Keppler, *Chem. Sci.*, 2014, **5**, 2925-2932.
101. M. Navarro, W. Castro and C. Biot, *Organometallics*, 2012, **31**, 5715-5727.
102. P. F. Salas, C. Herrmann and C. Orvig, *Chem. Rev.*, 2013, **113**, 3450-3492.
103. N. Wasi, H. Singh, A. Gajanana and A. Raichowdhary, *Inorg.Chim. Acta*, 1987, **135**, 133-137.
104. R. A. Sánchez-Delgado, M. Navarro, H. Pérez and J. A. Urbina, *J. Med. Chem.*, 1996, **39**, 1095-1099.
105. M. Navarro, F. Vasquez, R. A. Sánchez-Delgado, H. Pérez, V. Sinou and J. Schrével, *J. Med. Chem.*, 2004, **47**, 5204-5209.
106. M. Navarro, H. Pérez and R. A. Sánchez-Delgado, *J. Med. Chem.*, 1997, **40**, 1937-1939.
107. C. S. Rajapakse, A. Martinez, B. Naoulou, A. A. Jarzecki, L. Suarez, C. Deregnaucourt, V. Sinou, J. Schrevel, E. Musi and G. Ambrosini, *Inorg. Chem.*, 2009, **48**, 1122-1131.
108. M. Navarro, S. Pekerar and H. A. Pérez, *Polyhedron*, 2007, **26**, 2420-2424.
109. P. A. Ajibade and G. A. Kolawole, *Transit. Metal Chem.*, 2008, **33**, 493-497.
110. T. Stringer, M. A. S. Quintero, L. Wiesner, G. S. Smith and E. Nordlander, *J. Inorg. Biochem.*, 2019, **191**, 164-173.
111. L. Glans, A. Ehnbom, C. de Kock, A. Martínez, J. Estrada, P. J. Smith, M. Haukka, R. A. Sánchez-Delgado and E. Nordlander, *Dalton Trans.*, 2012, **41**, 2764-2773.
112. E. Ekengard, L. Glans, I. Cassells, T. Fogeron, P. Govender, T. Stringer, P. Chellan, G. C. Lisensky, W. H. Hersh and I. Doverbratt, *Dalton Trans.*, 2015, **44**, 19314-19329.
113. T. Stringer, D. Taylor, H. Guzgay, A. Shokar, A. Au, P. J. Smith, D. T. Hendricks, K. M. Land, T. J. Egan and G. S. Smith, *Dalton Trans.*, 2015, **44**, 14906-14917.
114. E. Ekengard, K. Kumar, T. Fogeron, C. de Kock, P. J. Smith, M. Haukka, M. Monari and E. Nordlander, *Dalton Trans.*, 2016, **45**, 3905-3917.
115. M. Patra and G. Gasser, *Nat. Rev. Chem.*, 2017, **1**, 0066.
116. C. Biot, L. Delhaes, L. A. Maciejewski, M. Mortuaire, D. Camus, D. Dive and J. S. Brocard, *Eur. J. Med. Chem.*, 2000, **35**, 707-714.
117. L. Delhaes, C. Biot, L. Berry, L. Maciejewski, D. Camus, J. Brocard and D. Dive, *Bioorg. Med. Chem.*, 2000, **8**, 2739-2745.

118. C. Biot, G. Glorian, L. A. Maciejewski, J. S. Brocard, O. Domarle, G. Blampain, P. Millet, A. J. Georges, H. Abessolo and D. Dive, *J. Med. Chem.*, 1997, **40**, 3715-3718.
119. L. Delhaes, H. Abessolo, C. Biot, L. Berry, P. Delcourt, L. Maciejewski, J. Brocard, D. Camus and D. Dive, *Parasitol. Res.*, 2001, **87**, 239-244.
120. C. Biot, D. Taramelli, I. Forfar-Bares, L. A. Maciejewski, M. Boyce, G. Nowogrocki, J. S. Brocard, N. Basilico, P. Olliaro and T. J. Egan, *Mol. Pharm.*, 2005, **2**, 185-193.
121. F. Dubar, T. J. Egan, B. Pradines, D. Kuter, K. K. Ncokazi, D. Forge, J.-F. Paul, C. Pierrot, H. Kalamou and J. Khalife, *ACS Chem. Biol.*, 2011, **6**, 275-287.
122. N. Chavain, H. Vezin, D. Dive, N. Touati, J.-F. Paul, E. Buisine and C. Biot, *Mol. Pharm.*, 2008, **5**, 710-716.
123. *https://clinicaltrials.gov/ct2/show/NCT03660839* (accessed May 2019).
124. R. J. Abdel-Jalil and W. Voelter, *J. Heterocyclic Chem.*, 2005, **42**, 67-71.
125. G. S. Yellol, A. Donaire, J. G. Yellol, V. Vasylyeva, C. Janiak and J. Ruiz, *ChemComm*, 2013, **49**, 11533-11535.
126. P. Toro, A. H. Klahn, B. Pradines, F. Lahoz, A. Pascual, C. Biot and R. Arancibia, *Inorg. Chem. Commun.*, 2013, **35**, 126-129.
127. J. Howarth and K. Hanlon, *Tetrahedron Lett.*, 2001, **42**, 751-754.
128. L. Rylands, A. Welsh, K. Maepa, T. Stringer, D. Taylor, K. Chibale and G. S. Smith, *Eur. J. Med. Chem.*, 2019, **161**, 11-21.
129. S. D. Khanye, B. Wan, S. G. Franzblau, J. Gut, P. J. Rosenthal, G. S. Smith and K. Chibale, *J. Organomet. Chem.*, 2011, **696**, 3392-3396.
130. I. L. Paiva, G. S. De Carvalho, A. D. Da Silva, P. P. Corbi, F. R. Bergamini, A. L. Formiga, R. Diniz, W. R. Do Carmo, C. Q. Leite and F. R. Pavan, *Polyhedron*, 2013, **62**, 104-109.
131. A. M. Carmo, F. M. Silva, P. A. Machado, A. P. Fontes, F. R. Pavan, C. Q. Leite, R. d. A. Sergio, E. S. Coimbra and A. D. Da Silva, *Biomed. Pharmacother.*, 2011, **65**, 204-209.
132. C. Da Silva, L. B. Ribeiro, C. C. Furuno, G. A. Da Cunha, R. F. De Souza, A. V. Netto, A. E. Mauro, R. C. Frem, J. A. Fernandes and F. A. A. Paz, *Polyhedron*, 2015, **100**, 10-16.
133. P. B. D. Silva, E. S. d. Freitas, M. C. Solcia, M. M. d. Silva, A. A. Batista, C. E. Eismann, A. M. C. M. Rolisola, A. A. Menegário, R. F. Cardoso and M. Chorilli, *Front. Microbiol.*, 2018, **9**, 2930.

134. P. Dandawate, K. Vemuri, E. M. Khan, M. Sritharan and S. Padhye, *Carbohyd. Polym.*, 2014, **108**, 135-144.
135. N. Baartzes, T. Stringer, R. Seldon, D. F. Warner, C. de Kock, P. J. Smith and G. S. Smith, *J. Organomet. Chem.*, 2016, **809**, 79-85.
136. N. Baartzes, T. Stringer, J. Okombo, R. Seldon, D. F. Warner, C. de Kock, P. J. Smith and G. S. Smith, *J. Organomet. Chem.*, 2016, **819**, 166-172.
137. D. Razafimahefa, D. A. Ralambomanana, L. Hammouche, L. Pélinski, S. Lauvagie, C. Bebear, J. Brocard and J. Maugein, *Bioorg. Med. Chem.*, 2005, **15**, 2301-2303.
138. D. A. Ralambomanana, D. Razafimahefa-Ramilison, A. C. Rakotohova, J. Maugein and L. Pelinski, *Bioorg. Med. Chem.*, 2008, **16**, 9546-9553.
139. G. M. Maguene, J. Jakhlal, M. Ladyman, A. Vallin, D. A. Ralambomanana, T. Bousquet, J. Maugein, J. Lebibi and L. Pélinski, *Eur. J. Med. Chem.*, 2011, **46**, 31-38.
140. T. Stringer, R. Seldon, N. Liu, D. F. Warner, C. Tam, L. W. Cheng, K. M. Land, P. J. Smith, K. Chibale and G. S. Smith, *Dalton Trans.*, 2017, **46**, 9875-9885.
141. B. Meunier, *Accounts of chemical research*, 2007, **41**, 69-77.
142. R. Morphy, C. Kay and Z. Rankovic, *Drug Discov. Today*, 2004, **9**, 641-651.
143. J. Walsh and A. Bell, *Curr. Pharm. Des.*, 2009, **15**, 2970-2985.
144. M. L. Lolli, C. Cena, C. Medana, L. Lazzarato, G. Morini, G. Coruzzi, S. Manarini, R. Fruttero and A. Gasco, *J. Med. Chem.*, 2001, **44**, 3463-3468.
145. C. Cena, M. L. Lolli, L. Lazzarato, E. Guaita, G. Morini, G. Coruzzi, S. P. McElroy, I. L. Megson, R. Fruttero and A. Gasco, *J. Med. Chem.*, 2003, **46**, 747-754.
146. R. Aslanian, M. wa Mutahi, N.-Y. Shih, J. J. Piwinski, R. West, S. M. Williams, S. She, R.-L. Wu and J. A. Hey, *Bioorg. Med. Chem. Lett.*, 2003, **13**, 1959-1961.
147. M. Yamamoto, S. Ikeda, H. Kondo and S. Inoue, *Bioorg. Med. Chem. Lett.*, 2002, **12**, 375-378.
148. F. W. Muregi and A. Ishih, *Drug Dev Res*, 2010, **71**, 20-32.
149. S. Vandekerckhove and M. D'Hooghe, *Bioorg. Med. Chem.*, 2015, **23**, 5098-5119.
150. R. Oliveira, D. Miranda, J. Magalhaes, R. Capela, M. J. Perry, P. M. O'Neill, R. Moreira and F. Lopes, *Bioorg. Med. Chem.*, 2015, **23**, 5120-5130.
151. X. Nqoro, N. Tobeka and B. A. Aderibigbe, *Molecules*, 2017, **22**, 2268.

152. F. Coslédan, L. Fraisse, A. Pellet, F. Guillou, B. Mordmüller, P. G. Kremsner, A. Moreno, D. Mazier, J.-P. Maffrand and B. Meunier, *P. Natl. Acad. Sci. USA*, 2008, **105**, 17579-17584.

153. H. Kaur, M. Machado, C. de Kock, P. Smith, K. Chibale, M. Prudêncio and K. Singh, *Eur. J. Med. Chem.*, 2015, **101**, 266-273.

154. R. Bairwa, M. Kakwani, N. R. Tawari, J. Lalchandani, M. K. Ray, M. G. Rajan and M. S. Degani, *Bioorg. Med. Chem. Lett.*, 2010, **20**, 1623-1625.

155. K. K. Kumar, S. P. Seenivasan, V. Kumar and T. M. Das, *Carbohyd. Res.*, 2011, **346**, 2084-2090.

156. F. Gao, H. Yang, T. Lu, Z. Chen, L. Ma, Z. Xu, P. Schaffer and G. Lu, *Eur. J. Med. Chem.*, 2018, **159**, 277-281.

157. Z. Xu, S. Zhang, C. Gao, J. Fan, F. Zhao, Z.-S. Lv and L.-S. Feng, *Chinese Chem. Lett.*, 2017, **28**, 159-167.

158. D. Sriram, A. Aubry, P. Yogeeswari and L. Fisher, *Bioorg. Med. Chem. Lett.*, 2006, **16**, 2982-2985.

159. C. Herrmann, P. F. Salas, B. O. Patrick, C. d. Kock, P. J. Smith, M. J. Adam and C. Orvig, *Organometallics*, 2012, **31**, 5748-5759.

160. N. Chavain, E. Davioud-Charvet, X. Trivelli, L. Mbeki, M. Rottmann, R. Brun and C. Biot, *Bioorg. Med. Chem.*, 2009, **17**, 8048-8059.

161. A. Singh, J. Gut, P. J. Rosenthal and V. Kumar, *Eur. J. Med. Chem.*, 2017, **125**, 269-277.

162. C. Biot, B. Pradines, M.-H. Sergeant, J. Gut, P. J. Rosenthal and K. Chibale, *Bioorg. Med. Chem. Lett.*, 2007, **17**, 6434-6438.

163. F. Bellot, F. Cosledan, L. Vendier, J. Brocard, B. Meunier and A. Robert, *J. Med. Chem.*, 2010, **53**, 4103-4109.

164. P. Chellan, V. M. Avery, S. Duffy, J. A. Triccas, G. Nagalingam, C. Tam, L. W. Cheng, J. Liu, K. M. Land and G. J. Clarkson, *Chem-Eur. J.*, 2018, **24**, 10078-10090.

165. A. Singh, A. Viljoen, L. Kremer and V. Kumar, *ChemistrySelect*, 2018, **3**, 8511-8513.

Chapter 2:

Synthesis and characterisation of 2-phenyl, 2-ferrocenyl and 2-pyridyl aminoquinoline-benzimidazole hybrids

2.1 Introduction

As mentioned in Chapter 1, molecular hybridisation has become an increasingly popular strategy in drug design and discovery.[1] The design of such hybrids has become a more rational process, where careful consideration is given to the possible intracellular targets and modes of action of the pharmacophore building blocks.[2, 3] Once the pharmacophore building blocks and appropriate binding sites have been chosen, the nature of the intermolecular linker becomes the next important consideration. Based on how the hybrid drug is designed to act, a linker with the desired properties is used. A linker capable of intracellular cleavage (cleavable linker) allows the hybrid to dissociate into individual active components and act independently.[2, 3] Alternatively, a linker which is resistant to metabolic cleavage (non-cleavable linker) would allow the hybrid to remain intact and act as one intracellularly.[2, 3] The latter may be desirable in cases where the aim is to overcome drug resistance and an overall synergistic effect is required.

Based on the past success of antimalarial drugs such as chloroquine (CQ) and amodiaquine, 4-aminoquinolines have featured prominently in antimalarial hybrid literature. Some examples of 4-aminoquinoline hybrids in the literature include combinations with triazines,[4] pyrimidines,[5] triazoles,[6] and most notably trioxanes.[7, 8] CQ and other 4-aminoquinolines act against the pathogenic erythrocytic stage of the *Plasmodium* life cycle.[9-11] CQ interferes with the parasite haem degradation pathway by inhibiting haemozoin formation in the acidic digestive vacuole, and thereby, kills the parasite.[9-11] Resistant *Plasmodium falciparum* mutants have developed a CQ resistance transporter (*Pf*CRT), which transports CQ out of the digestive vacuole, resulting in lower accumulation and decreased activity.[12] The design of hybrid compounds to overcome such mechanisms of resistance is of paramount importance in drug discovery.

Burgess *et al*. reported on the synthesis, *in vitro* antiplasmodium activity and *in vivo* antimalarial efficacy of a CQ-like hybrid designed to reverse or overcome resistance in resistant *P. falciparum* strains.[13] The hybrid structure, shown in Figure 2.1 (**I**), encompasses a chloroquine analogue covalently linked to an analogue of imipramine,[13] a reversal agent (RA) which is hypothesised to inhibit *Pf*CRT-associated CQ expulsion from the digestive vacuole.[14] In the *in vitro* screening, the hybrid maintained comparable low nanomolar IC_{50} values in both D6 (CQS) and Dd2 (CQR) strains, unlike the CQ control, suggesting a possible reversal of susceptibility to digestive vacuole export by *Pf*CRT.[13]

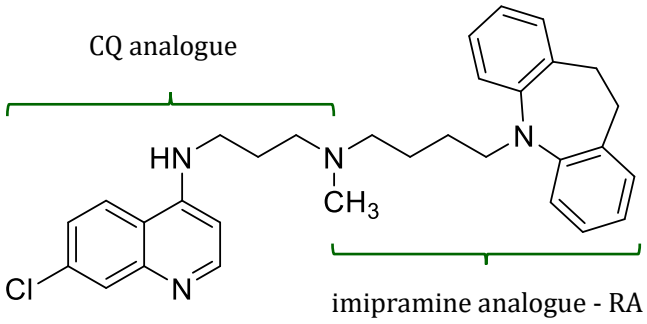

I

Figure 2.1 Chloroquine-imipramine hybrid (**I**).[13]

On the other hand, the benzimidazole scaffold represents another important class of heterocyclic pharmacophores. There are a number of benzimidazole-based drugs across the different pharmacological areas such as anti-tumour, antimicrobial, antiviral and antihistaminic to name a few.[15] The search for new benzimidazole-based agents for infectious diseases such as malaria and TB is ongoing, as reflected in the literature.[15-17] With regards to malaria, potential modes of action of benzimidazole derivatives have been elucidated. These include β-haematin (synthetic haemozoin) inhibition,[18, 19] as well as inhibition of parasitic dihydroorotate dehydrogenase (DHODH).[20]

Work by Chong *et al*. brought to light the antimalarial properties of benzimidazole-based antihistamine drug astemizole.[21] Following on from this, Musonda *et al.* reported on the synthesis and potent *in vitro* antiplasmodium activity and *in vivo* antimalarial activity of chloroquine-astemizole hybrids, shown in Figure 2.2.[22] In the K1 (CQR) strain of *P. falciparum*, hybrids **III**, **IV** and **V** were 3- to 10-fold more active *in vitro* than CQ, with IC_{50} values in the range 0.023 – 0.064 μM.[22] In addition, these hybrids displayed favourable cytotoxicity and *in vivo* antimalarial profiles.[22]

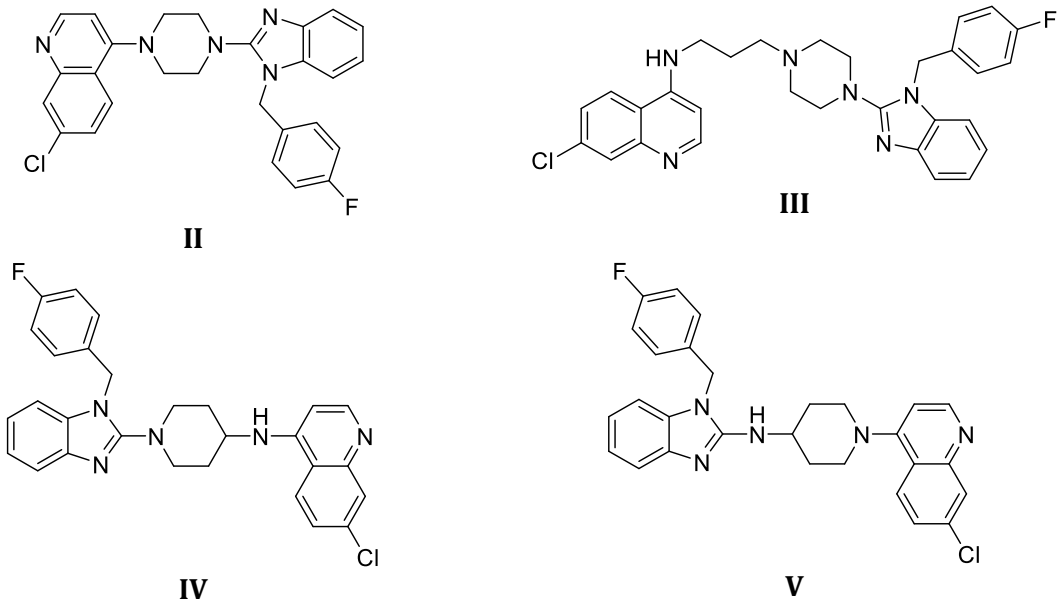

Figure 2.2 Chloroquine-astemizole hybrids.[22]

As seen for the chloroquine-imipramine hybrid, these chloroquine-astemizole hybrids demonstrate the potential to overcome or circumvent *P. falciparum* resistance using the hybrid approach. Based on these promising reports, this chapter focusses on the synthesis and characterisation of organic and organometallic aminoquinoline-benzimidazole hybrids with a non-cleavable propyl chain linker.

2.2 Results and Discussion

2.2.1 Synthesis and characterisation of nitro-containing and 1,2-diamine aminoquinoline precursors

Synthesis

The aminoquinoline precursor, *N*^{1}-(7-chloroquinolin-4-yl)-propane-1,3-diamine (**1**), was prepared using a modified literature method.[23] The nitro-containing precursors **2a** – **2e** and 1,2-diamine precursors **3a** – **3e** were prepared as illustrated in Scheme 2.1. Compound **1** was reacted with various nitrobenzene halide derivatives in *N*,*N*-dimethylformamide (DMF) to afford the five nitro-containing aminoquinoline precursors (**2a** – **2e**), *via* nucleophilic aromatic substitution reactions. Compounds **2a** – **2e** were isolated as bright yellow and orange powders in moderate yields (43 – 57%), displaying partial solubility in polar organic solvents. The nitro group in compounds **2a** – **2e** was

reduced by reaction with a zinc powder reducing agent, in the presence of ammonium chloride in anhydrous methanol. These reactions were performed under nitrogen atmosphere and the desired compounds (**3a** – **3e**) were isolated as either brown, beige, pink or purple powders, in high yields (76 – 98%). Compounds **3a – 3e** display solubility in alcoholic solvents, as well as enhanced solubility in polar organic solvents such as dichloromethane, ethyl acetate and chloroform, compared to their nitro-containing precursors.

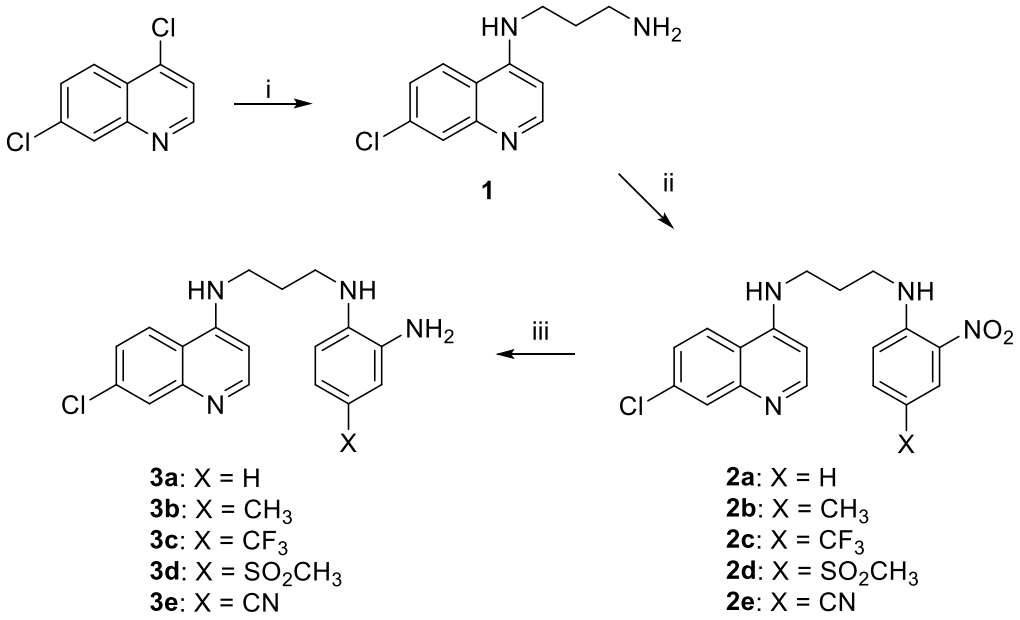

Scheme 2.1 Synthesis of aminoquinoline-containing precursors **1**, **2a** – **2e** and **3a** – **3e**. **Reagents and conditions** (i) 1,3-diaminopropane / 140 °C / 17 h; (ii) nitrobenzene derivative / DMF / 25 °C / 24 h; (iii) Zn / NH_4Cl / MeOH / rt / 24 h.

Motivation for the choice of X group

In this study, the substituent (X) at the 5-position of the benzimidazole moiety was varied with different groups chosen from the Craig Plot, which is often used in rational drug design. The Craig Plot categorises substituents based on their differing hydrophobicity (π) and electron-withdrawing/donating nature (σ). Specific substituents (CH_3, CF_3, SO_2CH_3 and CN) were chosen in order to probe the effect of the varying hydrophobic and electron-withdrawing/donating properties on the biological activity.

Reaction mechanisms

The nucleophilic aromatic substitution reaction proceeds *via* the proposed mechanism shown in Figure 2.3. The lone pair of electrons on the primary amine of N^1-(7-chloroquinolin-4-yl)-propane-1,3-diamine (**1**) acts as the nucleophile, attacking the electrophilic aromatic halide-bonded carbon atom, in a nucleophilic addition (A_N) step. This results in the delocalisation of electrons in the phenyl ring and through the nitro group. The nitro group of 1-fluoro-2-nitrobenzene is an activator toward nucleophilic substitution. Delocalisation of the negative charge into the phenyl ring results in elimination (E) of fluoride. Subsequent proton transfer generates a hydrogen halide (HF) and the desired product, N^1-(7-chloroquinolin-4-yl)-N^3-(2-nitrophenyl)-propane-1,3-diamine (**2a**).

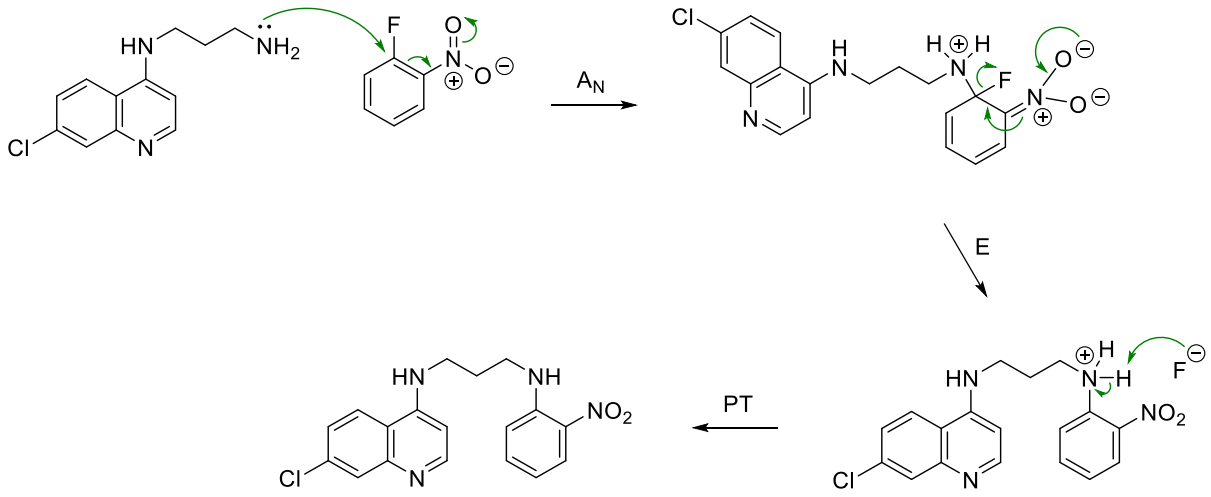

Figure 2.3 Nucleophilic aromatic substitution reaction mechanism in the formation of compound **2a**.

The reduction of a nitro group to an amine using zinc and ammonium chloride is proposed to occur by a succession of one-electron transfer steps, where zinc is the electron donor. Ammonium chloride in methanol provides mildly acidic conditions. The reaction proceeds *via* an *N*-phenyl hydroxylamine intermediate (R-NHOH), which is further reduced to afford the desired primary amine (R-NH) product.

Characterisation

Compounds **2a** – **2e** and **3a** – **3e** were fully characterised using ^{1}H and $^{13}C\{^{1}H\}$ nuclear magnetic resonance (NMR) spectroscopy, infrared (IR) spectroscopy and electron impact mass spectrometry (EI-MS). All characterisation attests to the successful synthesis of the desired products.

NMR spectroscopy

The ^{1}H NMR spectrum of compound **2a**, shown in Figure 2.4, displays aromatic proton signals at 8.39, 8.25, 7.79, 7.45 and 6.49 ppm for the five protons of the quinoline moiety. The four protons of the disubstituted phenyl ring are observed as four signals at 8.06, 7.50, 7.08 and 6.68 ppm, respectively. The amine proton adjacent to the phenyl moiety gives rise to a triplet at 8.20 ppm, and the amine proton adjacent to the quinoline moiety gives rise to a triplet at 7.35 ppm. The presence of the additional signals for the aromatic and amine protons confirms successful aromatic substitution.

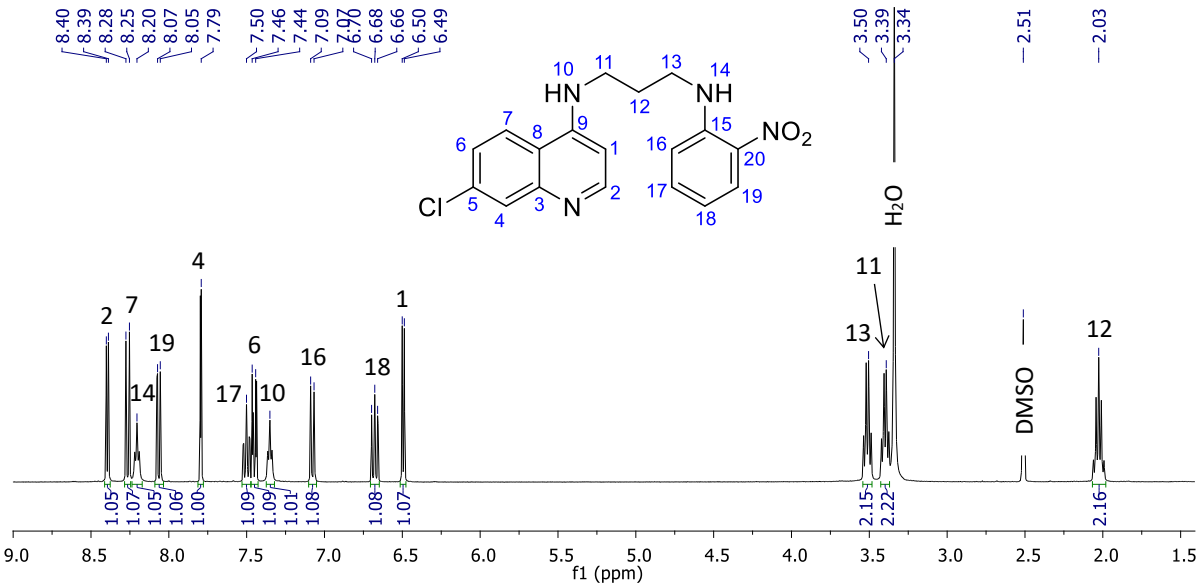

Figure 2.4 The ^{1}H NMR spectrum of compound **2a** in DMSO-d_6.

Additionally, the *N*-substituted methylene (CH_2) protons are observed as quartets at 3.51 and 3.40 ppm, respectively, both CH_2 groups coupling to their adjacent NH groups. The two more shielded methylene protons are displayed as a multiplet at 2.03 ppm. All assignments are shown in Figure 2.4.

The ^{1}H NMR spectra of compounds **2b – 2e** display peaks corresponding to the protons of the quinoline moiety and propyl spacer at similar chemical shifts, with similar multiplicities and coupling constants to that of compound **2a**. However, there is one fewer aromatic proton and, depending on the electronic nature of the phenyl ring substituent (X), the chemical shifts of the phenyl proton signals differ (shifting upfield or downfield) compared to that of compound **2a**. The stacked ^{1}H NMR spectra of compounds **2b** and **2d** are shown in Figure 2.5 as an example of this trend. The methylsulfonyl (SO_2CH_3) and trifluoromethyl (CF_3) groups of compounds **2d** and **2c** are electron-withdrawing, while the methyl (CH_3) of compound **2b** is inductively electron-donating in nature. As denoted by the asterisk in Figure 2.5, the triplet signal for the phenyl amine proton shifts significantly downfield in the spectrum of compound **2d** (8.70 ppm), and shifts slightly upfield in compound **2b** (8.12 ppm), compared to that of compound **2a** (8.21 ppm).

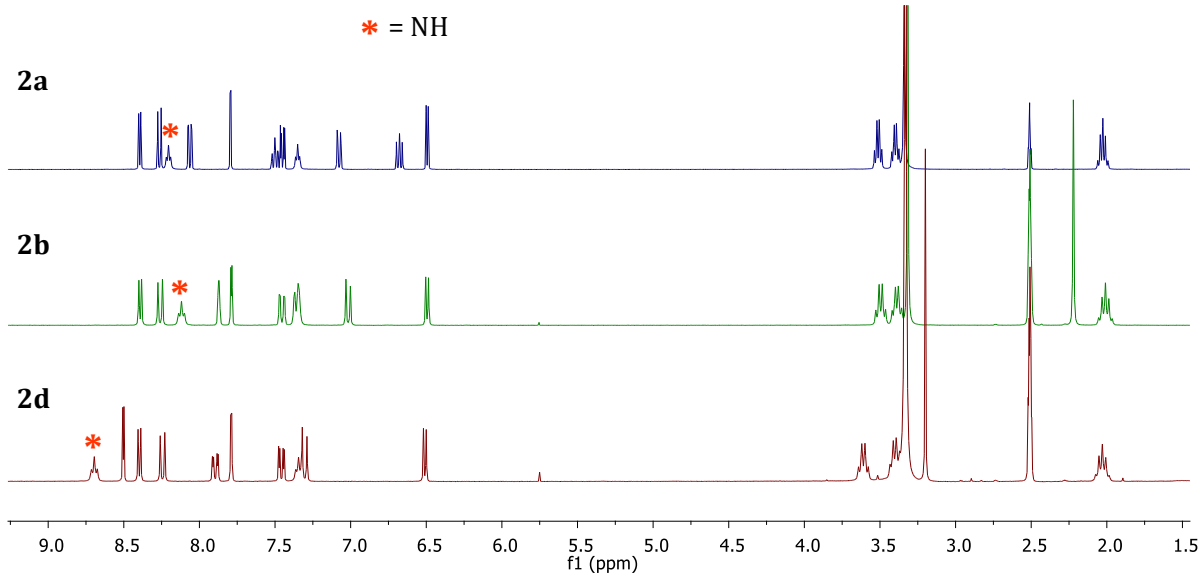

Figure 2.5. Stacked ^{1}H NMR spectra of compounds **2a**, **2b** and **2d**.

The ^{13}C{^{1}H} NMR spectra of compounds **2a – 2e** display all expected carbon atom signals. The aromatic carbon atoms of the quinoline and phenyl moieties give rise to fifteen signals in the characteristic region between 152 and 99 ppm. The signals assigned to the nitro-substituted carbon atoms appear relatively downfield between 144 and 148 ppm. The signals corresponding to the three methylene carbon atoms are observed between 41 and 27 ppm. Additionally, the spectra of compounds **2b** and **2d** display a signal at 19.9 and 44.2 ppm, corresponding to the methyl carbon atom for their methyl and

methylsulfonyl groups, respectively. The trifluoromethyl carbon atom and CF_3-substituted aromatic carbon atom of compound **2c** give rise to signals between 130 and 110 ppm, appearing as multiplets as a result of ^{13}C-^{19}F coupling.

The ^1H NMR spectrum of compound **3a** is shown in Figure 2.6. The two protons of the new amine group give rise to a broad singlet at 4.49 ppm, giving evidence of reduction of the nitro group in compound **2a**. The protons of the secondary amine adjacent to the phenyl group appears at 4.44 ppm, overlapping with the new primary amine signal. The five signals corresponding to the aromatic quinoline protons are retained at similar chemical shifts to that seen in the spectrum of nitro-containing precursor **2a**. However, the electron-donating effect of the amine (NH_2) group, which replaces the electron-withdrawing nitro (NO_2) group, has an overall shielding effect on the protons of the phenyl moiety, resulting in the coalescence of these signals between 6.57 and 6.39 ppm. These signals are more upfield compared to compound **2a**. This provides further evidence of amine formation. Once again, the two groups of methylene protons adjacent to the amine groups give rise to quartets at 3.41 and 3.18 ppm, respectively, and the more shielded methylene CH_2 signal appears at 2.00 ppm.

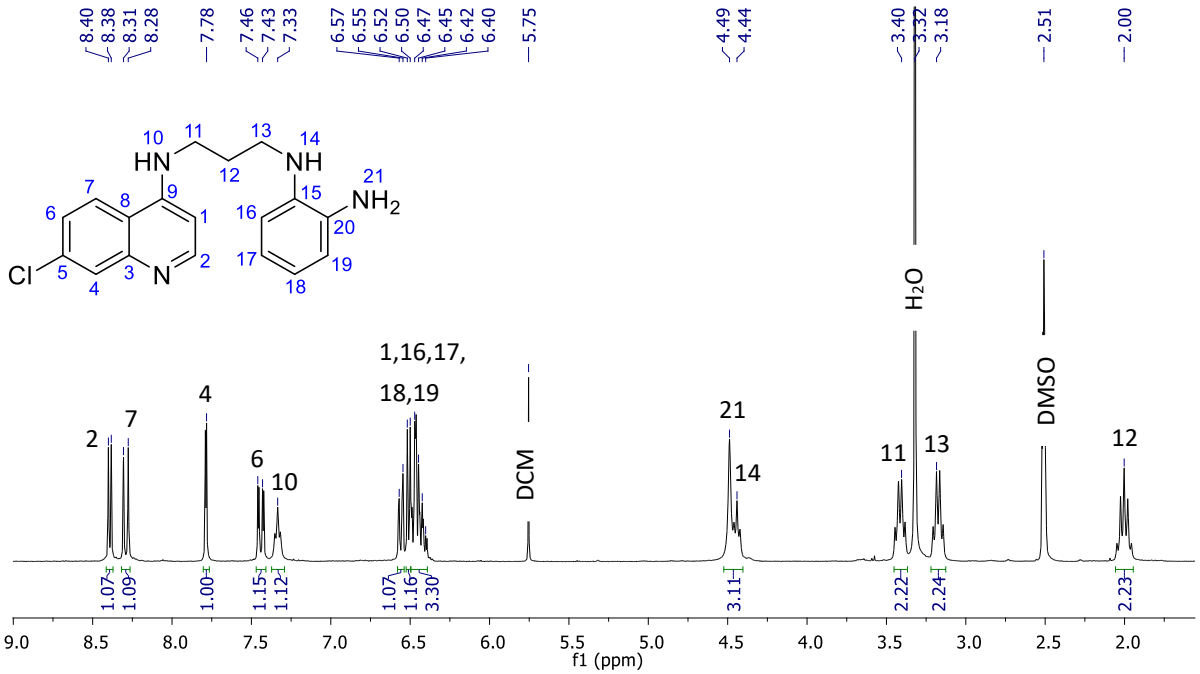

Figure 2.6 The ^1H NMR spectrum of compound **3a** in DMSO-d_6.

The ^1H NMR spectra of compounds **3b – 3e** retain the proton signals of the quinoline moiety and propyl spacer with similar chemical shifts, multiplicities and coupling

constants to that of their respective precursors. The electronic nature of the phenyl ring substituent (X) has shielding and deshielding effects on the phenyl aromatic and amine protons (NH and NH_2) only. The stacked NMR spectra of compounds **3a**, **3b** and **3d**, displayed in Figure 2.7, show these effects. Compared to compound **3a**, the methyl group of compound **3b** has a shielding effect, shifting the aromatic, NH and NH_2 proton signals slightly upfield. The trifluoromethyl group of compound **3c** has an overall deshielding effect, shifting the aromatic, NH an NH_2 proton signals significantly downfield.

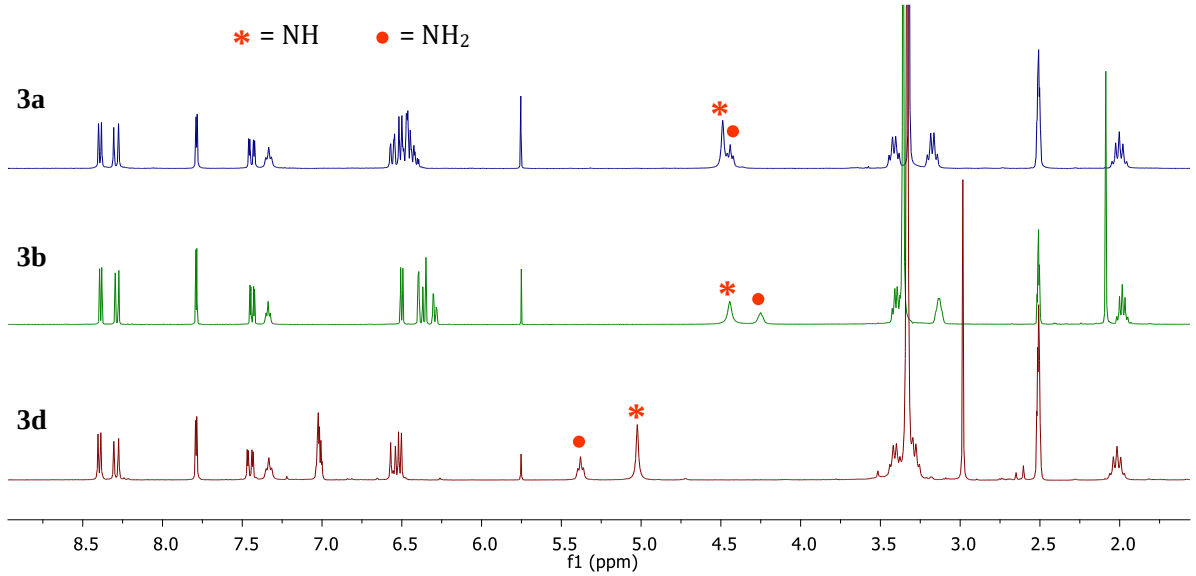

Figure 2.7 Stacked ^{1}H NMR spectra of compounds **3a**, **3b** and **3d**.

The $^{13}C\{^{1}H\}$ NMR spectra of compounds **3a** – **3e** display all expected peaks. The carbon atoms of the quinoline moiety and propyl spacer give rise to signals at similar chemical shifts to that seen in the spectra of the nitro-containing precursors. However, the signals corresponding to the carbon atoms of the phenyl group show a significant upfield shift due to the electron-donating nature of the new primary amine group.

Infrared spectroscopy

The solid-state infrared analysis of compounds **2a** – **2e** and **3a** – **3e** was carried out using Fourier Transform Infrared (FT-IR) spectroscopy, utilising Attenuated Total Reflectance (ATR). The IR spectra of compounds **2a** – **2e** display several significant absorption bands which further confirm their structures. Two amine ν(N-H) absorption bands are observed around 3300 cm^{-1}, as well as two bands corresponding to the ν(N-O) absorption around 1500 cm^{-1} and 1300 cm^{-1}, respectively. The imine ν(C=N) of the quinoline moiety is seen

between 1609 and 1621 cm^{-1}. These spectra also display an alkenyl ν(C=C) stretch between 1560 and 1580 cm^{-1}, for the aromatic rings of compounds **2a – 2e**. Additionally, the IR spectrum of compound **2c** displays a ν(C-F) absorption band corresponding to the trifluoromethyl moiety at 1324 cm^{-1}, compound **2d** displays ν(S=O) bands of the sulfonyl moiety at 1368 and 1136 cm^{-1}, and the spectrum of compound **2e** has a characteristic nitrile (C≡N) absorption band at 2222 cm^{-1}. These characteristic absorption bands for the X substituents are retained in the spectra of compounds **3c – 3e**. The IR spectra of compounds **3a – 3e** display four characteristic stretches. As expected, two ν(N-H) bands are present around 3400 and 3300 cm^{-1}, and the alkenyl ν(C=C) band appears at 1580 cm^{-1}. The quinoline ν(C=N) absorption band has shifted to a slightly lower wavenumber (1607 – 1611 cm^{-1}) compared to that in the respective precursors.

Mass spectrometry

The masses of the aminoquinoline precursors were determined using EI-MS. The mass spectra of compounds **2a – 2e** and **3a – 3c** reveal peaks corresponding to the molecular ions $[M]^+$, while the spectra of compounds **3d** and **3e** display peaks for the protonated molecular ion $[M+H]^+$. These results further confirm the structures of the desired compounds. The experimental and calculated *m*/*z* values are summarised in Table 2.1.

Table 2.1 Experimentally determined *m*/*z* values and their corresponding calculated values for compounds **2a – 2e** and **3a – 3e**.

Compound	Found *m*/*z*	Calculated *m*/*z*
2a	355.95 $[M]^+$	356.10
2b	370.04 $[M]^+$	370.12
2c	423.99 $[M]^+$	424.09
2d	433.97 $[M]^+$	434.08
2e	381.02 $[M]^+$	381.10
3a	326.10 $[M]^+$	326.13
3b	340.15 $[M]^+$	340.15
3c	394.11 $[M]^+$	394.12
3d	405.12 $[M+H]^+$	405.11
3e	352.14 $[M+H]^+$	352.14

2.2.2 Synthesis and characterisation of 2-phenyl, 2-ferrocenyl and 2-pyridyl aminoquinoline-benzimidazole hybrids

Synthesis

The final step in the synthetic route for the preparation of the aminoquinoline-benzimidazole hybrid targets, was the cyclo-condensation reaction of the 1,2-diamine precursors with various aldehydes. Compounds **3a** – **3e** were reacted with either benzaldehyde, ferrocenecarboxaldehyde or 2-pyridinecarboxaldehyde in the presence of a catalytic amount of trifluoroacetic acid (TFA) and anhydrous magnesium sulphate in ethanol. These reactions afforded 2-phenylbenzimidazoles **4a** – **4e**, 2-ferrocenylbenzimidazoles **5a** – **5e** and 2-pyridylbenzimidazoles **6a** – **6c** as shown in Scheme 2.2.

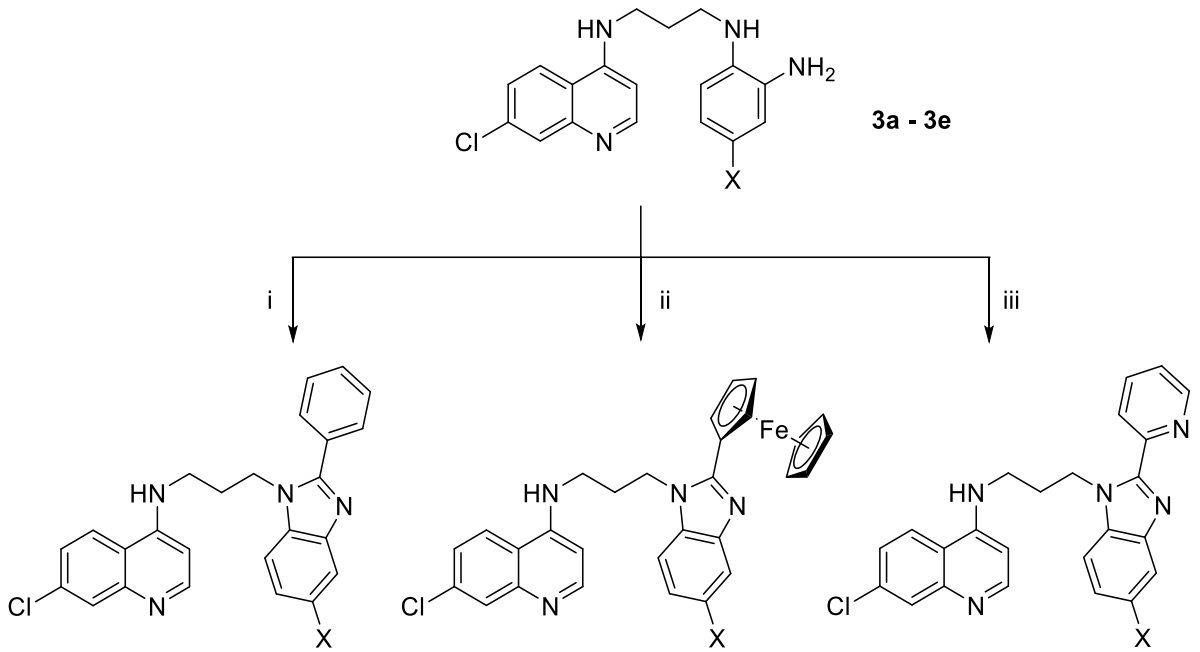

Scheme 2.2 Synthesis of 2-phenyl, 2-ferrocenyl and 2-pyridyl aminoquinoline-benzimidazole hybrids. **Reagents and conditions** (i) benzaldehyde / TFA / $MgSO_4$/ EtOH / 80 °C / 24 h; (ii) ferrocenecarboxaldehyde / TFA / $MgSO_4$ / EtOH / 80 °C / 48 h; (iii) 2-pyridinecarboxaldehyde / TFA / $MgSO_4$ / EtOH / 80 °C / 24 h.

Compounds **4a** – **4e** were isolated as either white, beige or pale-yellow powders in moderate to good yields (61 – 81%), while compounds **5a** – **5e** were isolated as orange powders in moderate yields (44 – 64%) and compounds **6a** – **6c** were isolated as yellow or beige powders in moderate yields (59 – 64%). All of the 2-substituted benzimidazole hybrids are soluble in polar organic solvents such as dichloromethane and ethanol, and insoluble in non-polar organic solvents.

Reaction mechanism

The cyclo-condensation reaction mechanism for the formation of benzimidazoles from 1,2-diamines and aldehydes under acidic conditions is not well described in the literature. Two recent articles proposed a mechanism for the formation of benzimidazoles from *o*-phenylenediamine and aldehydes under acidic conditions (*p*-toluenesulfonic acid or ammonium acetate).[24, 25] Based on these reports, the proposed cyclo-condensation reaction mechanism for the formation of these aminoquinoline-benzimidazole hybrids is depicted in Figure 2.8.

The presence of a catalytic amount of TFA activates the carbonyl group towards electrophilic attack. The lone pair of electrons on the secondary amine acts as the nucleophile, attacking the carbonyl carbon atom. This is followed by proton transfer and dehydration to form a reactive iminium ion intermediate. The primary amine nucleophile then attacks the benzylic carbon atom (δ+) and subsequent proton transfer results in the formation of a dihydrobenzimidazole derivative. The final step in the proposed mechanism involves the oxidation of this derivative to afford the desired benzimidazole **4a**. As oxidation is required to form the double bond, the reaction must proceed under oxidative conditions. Literature has reported on the use of air or oxidising agents such as copper(II) acetate, sodium metabisulfite, mercuric acetate and lead tetraacetate for this purpose.[17, 26] In this study, oxidation was brought about by air.

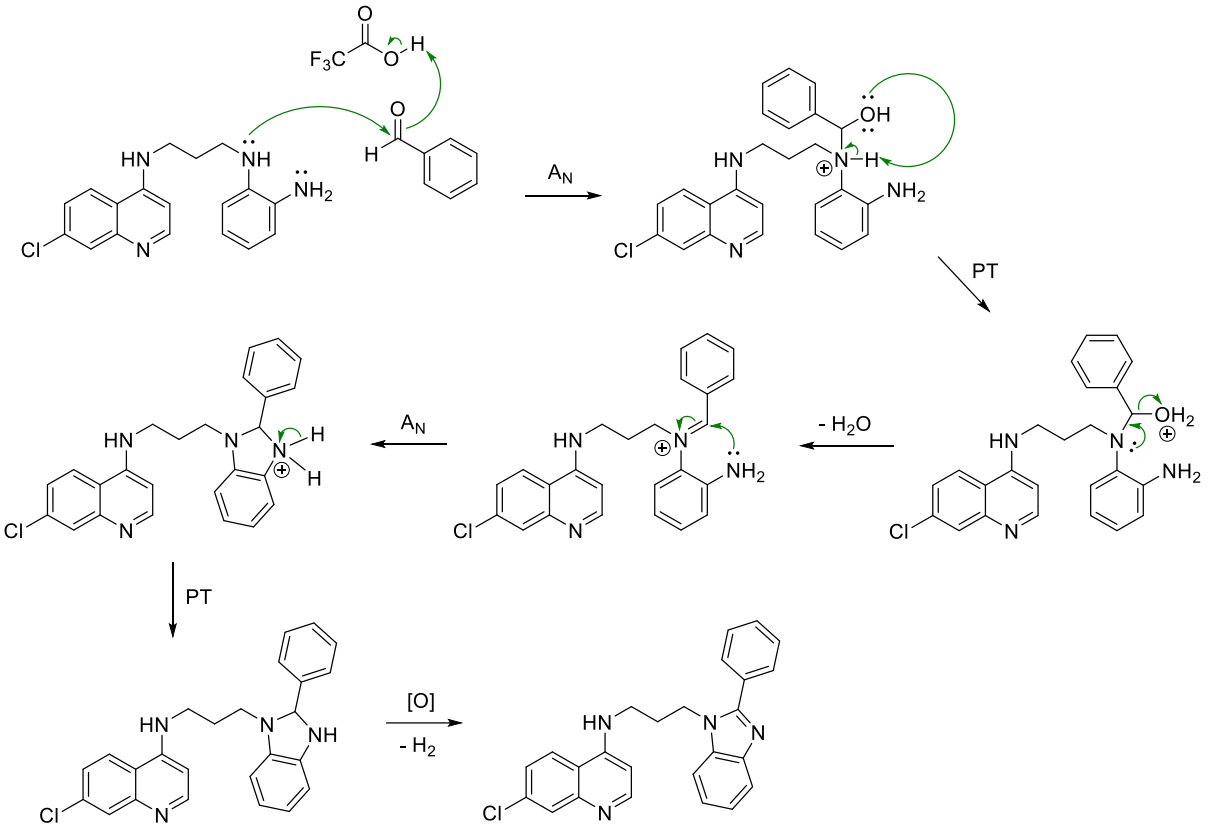

Figure 2.8 Proposed cyclo-condensation reaction mechanism in the formation of compound **4a**.

The proposed mechanism shown in Figure 2.8 depicts the secondary amine as the initial nucleophile, on the basis that it is the stronger nucleophile of the two amines. In general, in the absence of special circumstances, nucleophilicity follows the same trend as basicity, which would imply that the more substituted amine is more basic and thus more nucleophilic. Alternatively, the primary amine could initiate the nucleophilic attack on the electrophilic carbon atom, forming an alternate reactive iminium intermediate (under acidic conditions). The secondary amine would then execute the second nucleophilic attack on this intermediate, which, followed by air oxidation would afford the same desired product **4a**.

Characterisation

The organic and organometallic aminoquinoline-benzimidazole hybrids discussed here were fully characterised by NMR and IR spectroscopy, and high-resolution electrospray ionisation mass spectrometry (ESI-MS). The ^{1}H and $^{13}C\{^{1}H\}$ NMR assignments were made with the aid of 2D NMR experiments such as correlation spectroscopy (COSY) and heteronuclear single-quantum correlation spectroscopy (HSQC).

NMR spectroscopy

The ^{1}H NMR spectrum of compound **4a**, shown in Figure 2.9, displays distinct signals at 8.35, 8.14, 7.80, 7.44 and 6.31 ppm, corresponding to the five quinoline protons. The remaining aromatic protons of the benzimidazole and 2-phenyl moiety, as well as the secondary amine proton, are observed as two overlapping multiplet signals between 7.72 and 7.20 ppm.

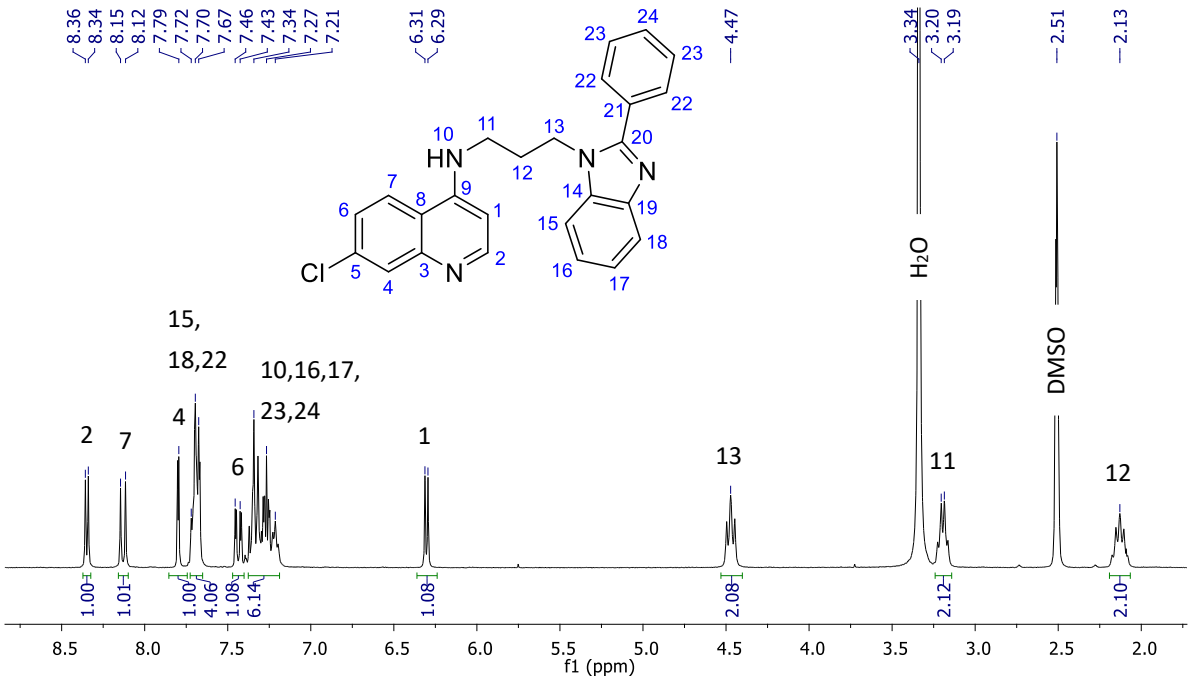

Figure 2.9 The ^{1}H NMR spectrum of compound **4a** in DMSO-d_6.

The signals in the region 8.50 – 6.00 ppm collectively integrate for fourteen aromatic protons, confirming incorporation of the 2-phenyl moiety, compared to the precursor **3a** (nine aromatic protons), and that the correct structure has been formed. No other amine proton signals are present in the spectrum, giving further evidence of cyclisation. The signal for the methylene protons adjacent to the newly formed benzimidazole moiety shows a significant downfield shift compared to that of compound **3a**, appearing as a triplet at 4.47 ppm. This provides further evidence of cyclisation, as this shift results from the electron-withdrawing inductive effect of the benzimidazole moiety. Furthermore, the remaining two groups of methylene protons give rise to a quartet (3.20 ppm) and pentet (2.13 ppm), respectively.

As seen in the ^{1}H NMR spectrum of compound **4a** (Figure 2.9), the aromatic protons of compounds **5a** – **5e** give rise to a series of distinct signals and overlapping multiplets in the region between 8.45 and 6.62 ppm. The ^{1}H NMR spectrum of compound **5a** is shown in Figure 2.10. Evidence of cyclisation with the ferrocenyl moiety is seen in the presence of a singlet (3.99 ppm) corresponding to the protons of the unsubstituted cyclopentadienyl (Cp) ring, as well as two triplets (4.75 and 4.14 ppm) for the four protons of the substituted Cp ring.

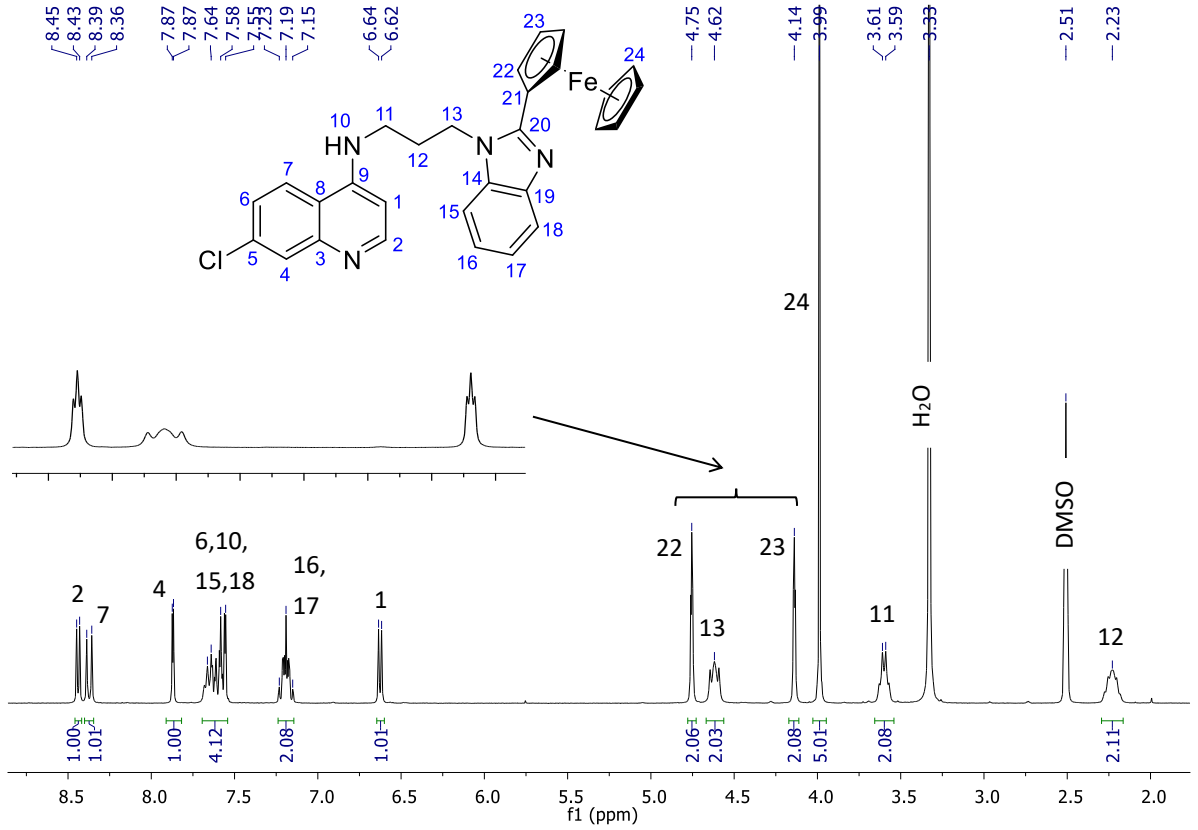

Figure 2.10 The ^{1}H NMR spectrum of compound **5a** in DMSO-d_6.

Further evidence of cyclisation can be seen in the downfield shift of the triplet corresponding to the methylene protons adjacent to the new benzimidazole moiety, which now appears at 4.62 ppm. The remaining methylene protons are observed as a quartet and pentet at 3.60 and 2.23 ppm, respectively.

The ^{1}H NMR spectrum of compound **6a** is displayed in Figure 2.11. Signals corresponding to the five quinoline protons are present at 8.34, 8.21, 7.79, 7.44 and 6.34 ppm. The four protons of the 2-substituted pyridyl ring give rise to peaks at 8.48, 8.27, 7.91 and 7.37 ppm, and provide evidence of successful cyclisation. The aromatic protons of the

benzimidazole moiety and the quinoline amine proton give rise to two overlapping multiplet signals between 7.75 and 7.25 ppm, integrating for five protons. Furthermore, signals for the protons of the propyl spacer are present at 4.99 (triplet), 3.29 (overlapping with the H_2O signal) and 2.23 ppm (pentet).

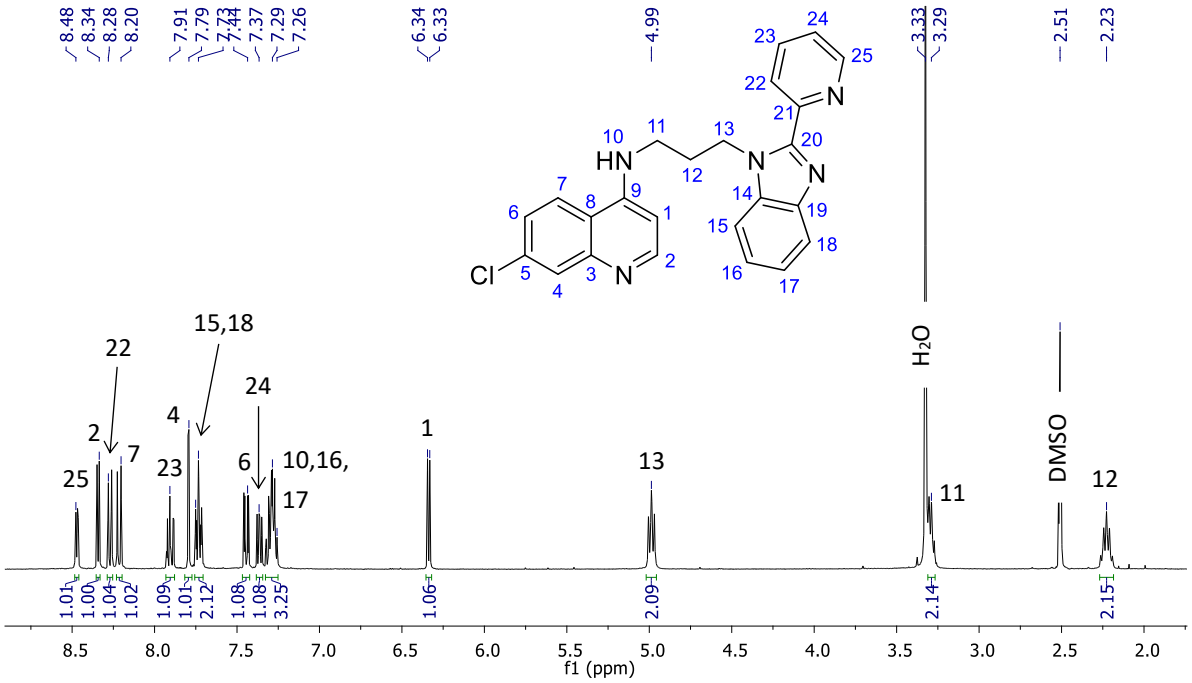

Figure 2.11 The ^{1}H NMR spectrum of compound **6a** in DMSO-d_6.

The ^{1}H NMR spectra of compounds **4b – 4e**, **5b – 5e** and **6b – 6c** shows some variation from that of compounds **4a**, **5a** and **6a**, respectively. The quinoline and amine protons show no significant shift, appearing at similar chemical shifts across all spectra. The aromatic protons of the newly formed benzimidazole ring shift depending the electronic effect of substituent at the 5-position. There is one less aromatic proton on the benzimidazole, and thus the signals in the aromatic region show less overlap and are more distinct, as depicted in Figure 2.12 for compounds **4b** and **4c**. The methyl group of compound **4b** has an inductively electron-donating effect, shifting the aromatic proton signals of the benzimidazole moiety upfield, to lower chemical shifts. The trifluoromethyl group of compound **4c** has an electron-withdrawing effect, resulting in the aromatic benzimidazole protons resonating more downfield, at higher chemical shifts. Additionally, a singlet for the methyl protons ($C\underline{H}_3$) of compounds **4b, 5b** and **6b** appears around 2.4 ppm, and the methyl protons ($SO_2C\underline{H}_3$) of compounds **4d** and **5d** resonate around 3.2 ppm.

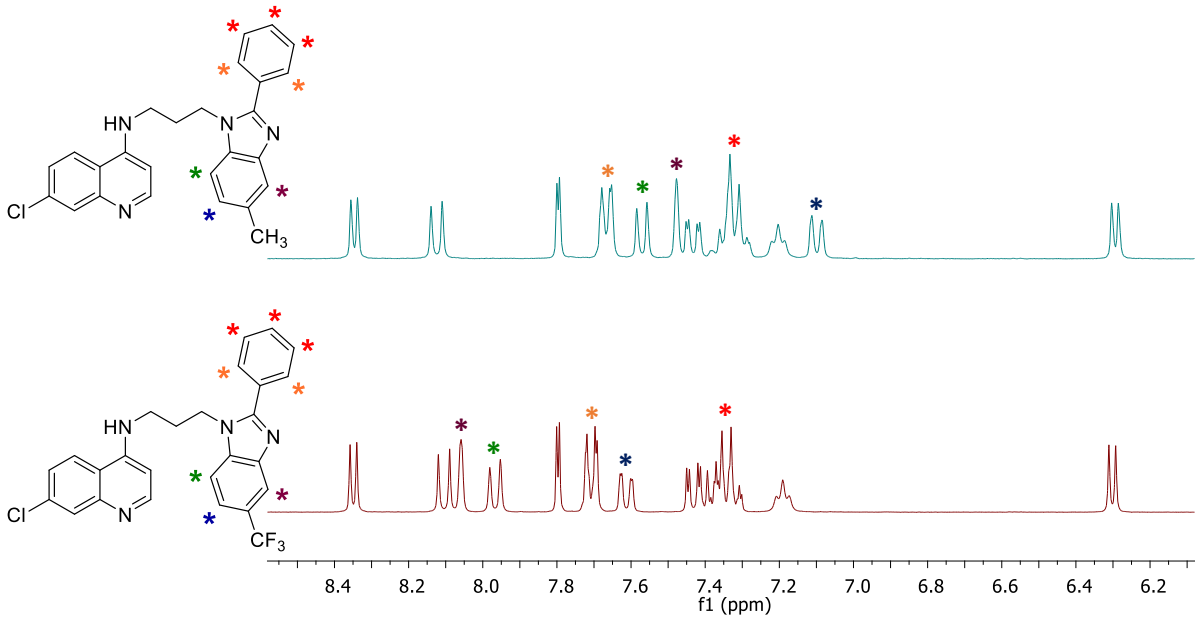

Figure 2.12 The aromatic region of the ^{1}H NMR spectra of compounds **4b** and **4c** in DMSO-d_6.

The ^{13}C{^{1}H} NMR spectra of compounds **4a – 4e**, **5a – 5e** and **6a – 6c** display all expected signals in the appropriate regions. All aromatic carbon atoms resonate between 156 and 99 ppm, while the methylene carbons give rise to three signals between 44 – 28 ppm. With the formation of the 2-substituted organic and organometallic benzimidazole moiety, new peaks are introduced into the spectra compared to the 1,2-diamine precursors. In addition to the new imine carbon, the spectra of compounds **4a – 4e** and **6a – 6c** gain seven and six additional carbons, respectively. The 2-ferrocenyl hybrids gain an imine carbon as well as ten Cp carbons. In the spectra of compounds **5a – 5e**, these ferrocenyl carbons resonate as four distinct signals between 74.3 and 69.0 ppm; one signal for the quaternary Cp carbon, two signals for the four carbons of the substituted Cp ring, and one intense signal for the five carbons of the unsubstituted Cp ring.

Infrared spectroscopy

The IR spectra of compounds **4a – 4e**, **5a – 5e** and **6a – 6c** differ slightly from that of their 1,2-diamine precursors, possessing the same characteristic absorption bands at slightly different wavenumbers. There is only one amine ν(N-H) absorption band around 3200 cm^{-1} for the lone quinoline amine moiety, compared to two bands (around 3400 and 3300 cm^{-1}) for the corresponding precursors. The alkenyl ν(C=C) stretch is retained and appears between 1570 and 1580 cm^{-1}. In addition, the ν(C=N) band, which corresponds to the overlapping bands of the quinoline and benzimidazole imine bonds, is observed

between 1609 and 1613 cm^{-1}. Compounds **6a** – **6c** give rise to an additional ν(C=N) absorption band for the pyridyl moiety at the 2-position of the benzimidazole. This band appears in the region 1590 – 1592 cm^{-1}, slightly overlapping with the ν(C=C) band. The ν(C=N) bands of compounds **4b**, **5b** and **6b** are shown in Figure 2.13. Furthermore, there are several diagnostic absorption bands present in the spectra. The trifluoromethyl ν(C-F) absorption band of compounds **4c**, **5c** and **6c** appears around 1330 cm^{-1}, the two sulfonyl ν(S=O) bands of compounds **4d** and **5d** are observed around 1367 cm^{-1} and in the region 1130 – 1170 cm^{-1}, while compounds **4e** and **5e** have nitrile a ν(C≡N) band between 2214 and 2222 cm^{-1}.

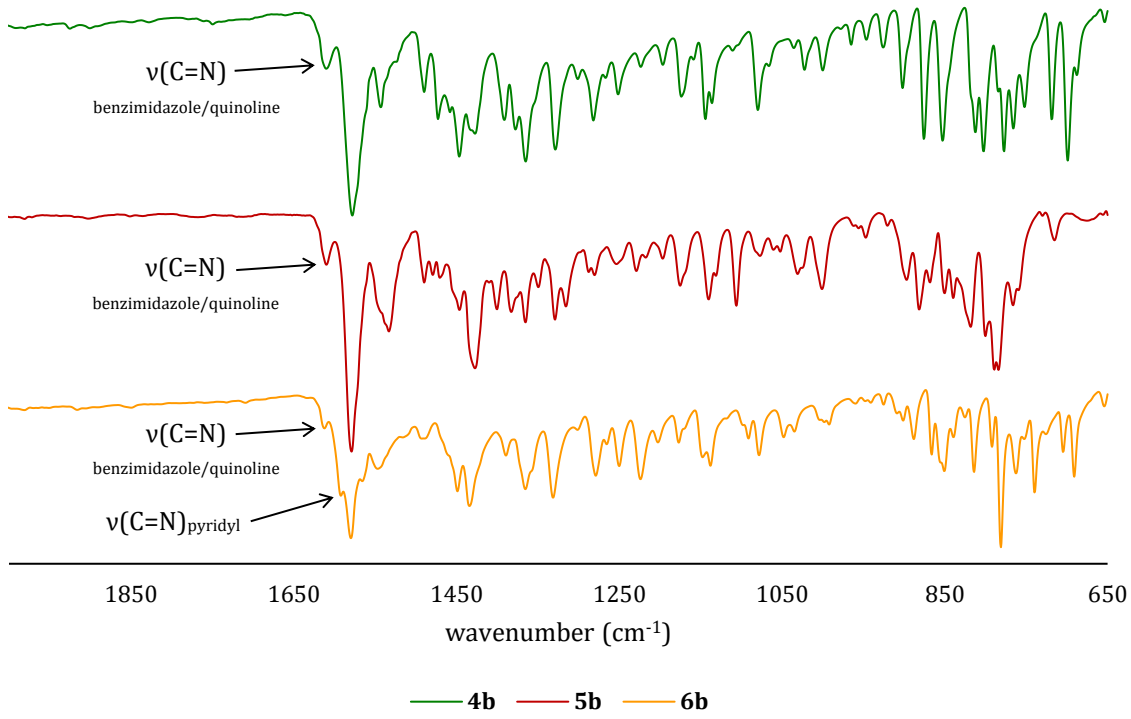

Figure 2.13 Stacked IR spectra of compounds **4b**, **5b** and **6b**.

Mass spectrometry

The masses of the 2-substituted aminoquinoline-benzimidazole hybrids (**4a** – **4e**, **5a** – **5e** and **6a** – **6c**) were determined using high-resolution ESI-MS. Analysed in the positive mode, the mass spectra of the synthesised organic and organometallic hybrids all display similar fragmentation patterns. The experimentally determined *m*/*z* values and their corresponding calculated values are listed in Table 2.2.

Table 2.2 Experimentally determined *m*/*z* values and their corresponding calculated values for compounds **4a** – **4e**, **5a** – **5e** and **6a** – **6c**.

Compound	Base peak (100% abundant)	
	Found *m*/*z*	Calculated *m*/*z*
4a	413.1534 $[M+H]^+$	413.1528
4b	214.0882 $[M+2H]^{2+}$	427.1684
4c	481.1410 $[M+H]^+$	481.1401
4d	246.0693 $[M+2H]^{2+}$	246.0688
4e	219.5773 $[M+2H]^{2+}$	219.5776
5a	521.1207 $[M+H]^+$	521.1190
5b	268.0718 $[M+2H]^{2+}$	268.0710
5c	295.0572 $[M+2H]^{2+}$	295.0568
5d	599.0969 $[M+H]^+$	599.0965
5e	273.5657 $[M+2H]^{2+}$	273.5608
6a	414.1485 $[M+H]^+$	414.1480
6b	428.1644 $[M+H]^+$	428.1637
6c	482.1353 $[M+H]^+$	482.1354

In the spectra of compounds **4a**, **4c**, **5a**, **5d**, **6a**, **6b** and **6c**, the $[M+H]^+$ fragment is observed as the 100% abundant base peak. For the remaining compounds **4b**, **4d**, **4e**, **5b**, **5c** and **5e**, base peaks corresponding to the $[M+2H]^{2+}$ fragment are observed in the mass spectra. For the compounds with the $[M+2H]^{2+}$ fragment as the base peak, the next most abundant peak in each spectrum corresponds to the $[M+H]^+$ fragment.

Molecular structures

Crystals of compounds **4b** and **5c**, suitable for single-crystal X-ray diffraction, were obtained and analysed. Crystals of compound **4b** were obtained by crystallisation in DMSO-d_6, forming colourless block crystals in a monoclinic crystal system with the $P2_1/c$ space group. Crystals of compound **5c** were obtained by slow evaporation in dichloromethane, forming red block crystals in a triclinic crystal system with the $P\bar{1}$ space group. The molecular structures of compounds **4b** and **5c** are shown in Figure 2.14 and Figure 2.15, respectively.

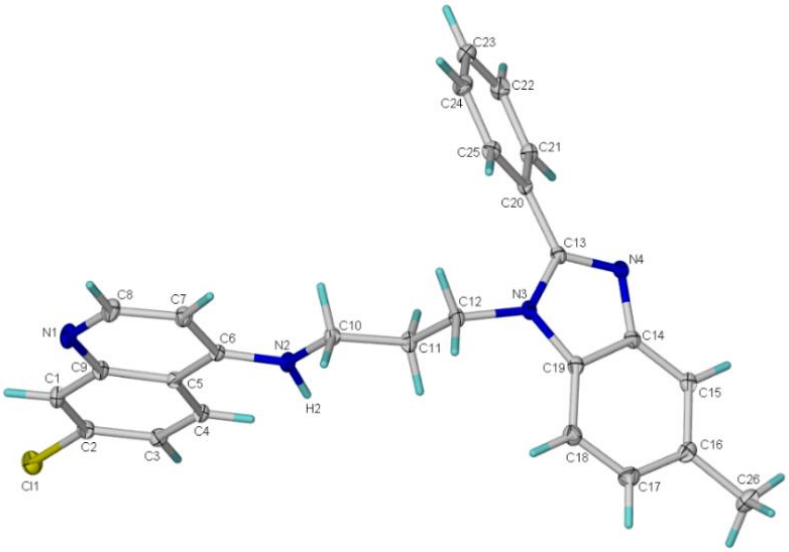

Figure 2.14 Molecular structure of compound **4b** at 40% probability ellipsoids (CCDC 1907165).

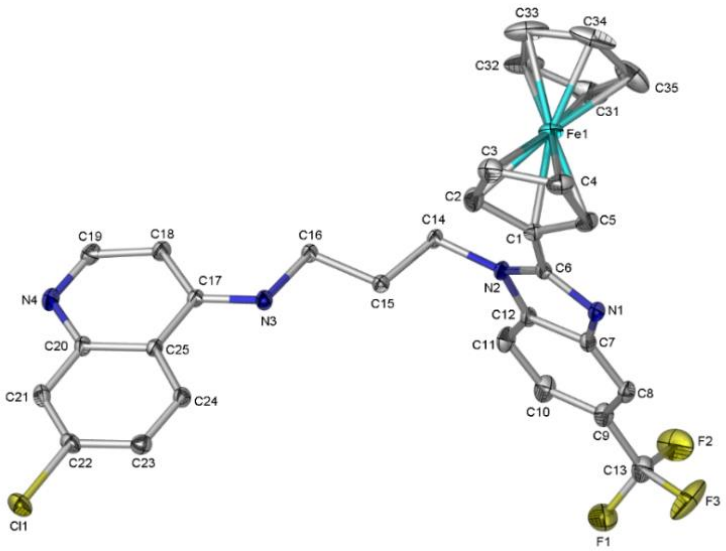

Figure 2.15 Molecular structure of compound **5c** at 40% probability ellipsoids (CCDC 1907167).

Selected bond lengths and angles are reported in Table 2.3 and crystallographic data in Table 2.4. The C(benzimidazole)-C(phenyl/ferrocenyl) bonds of **4b** and **5c** are similar in length, as well as the C(benzimidazole)-C(CH_3/CF_3) bonds. The C-F bonds of compound **5c** vary in length (1.330, 1.314 and 1.341 Å), in the range corresponding with lengths expected for this strong polar covalent bond. It is worth noting that in both **4b** and **5c**, the benzimidazole and its 2-substituted ring (phenyl for **4b** and substituted Cp for **5c**) are not co-planar. The torsion angle between the two ring systems is 45.2° in compound **4b** and a significantly lower value of 17.5° in compound **5c**.

Table 2.3 Selected bond lengths and torsion angles of compounds **4b** and **5c**.

	4b	**5c**
Bond lengths (Å)		
C(13) – C(20)	1.471(2)	–
C(1) – C(6)	–	1.456(3)
C(16) – C(26)	1.508(3)	–
C(9) – C(13)	–	1.498(4)
C(13) – F(1)	–	1.330(3)
C(13) – F(2)	–	1.341(3)
C(13) – F(3)	–	1.314(4)
Torsion angles (°)		
N(3) – C(13) – C(20) – C(25)	45.2(2)	–
C(2) – C(1) – C(6) – N(2)	–	17.5(4)

Table 2.4 Crystallographic data for compounds **4b** and **5c**.

	4b	**5c**
Chemical formula	$C_{26}H_{23}ClN_4$	$C_{30}H_{24}ClF_3FeN_4$
Formula weight	426.93	588.83
Crystal system	Monoclinic	Triclinic
Space group	$P2_1/c$	$P\bar{1}$
Crystal size (mm)	0.09 x 0.14 x 0.26	0.10 x 0.22 x 0.27
a, b, c (Å)	9.9226(7), 20.3115(15), 11.1094(8)	11.3141(14), 11.3620(14), 12.7390(15)
α, β, γ (°)	90, 102.539(2), 90	65.375(2), 82.417(3), 68.426(2)
V/ Å^3	2185.6(3)	1384.0(3)
Z	4	2
T/K	173	173
D_c/g.cm^{-3}	1.298	1.413
μ/mm^{-1}	0.196	0.688
Scan range/°	2.0 < θ < 27.2	1.8 < θ < 28.4
Unique reflections	4838	6923
Reflections used [I>2σ(I)]	3637	5461
R_{int}	0.067	0.050
R indices (all data)	R 0.0381, wR2 0.0952, S 1.03	R 0.0438, wR2 0.1168, S 1.05
Goodness-of-fit	1.03	1.05
Max, Min Δρ/e Å	-0.29, 0.22	-0.75, 0.60

2.3 Summary

Five new nitro-containing aminoquinoline precursors (**2a** – **2e**) were synthesised *via* nucleophilic aromatic substitution (S_NAr) reactions with various nitrobenzene halide derivatives. Compounds **2a** – **2e** were isolated as yellow or orange powders in moderate yields, displaying limited solubility in polar organic solvents. The nitro groups of compounds **2a** – **2e** were subsequently reduced using zinc and ammonium chloride, to afford 1,2-diamine aminoquinoline precursors **3a** – **3e**. These brown, white, purple and pink powders were isolated in high yields (> 85%), displaying enhanced solubility in polar organic solvents. The aminoquinoline precursors were characterised using various spectroscopic and analytical techniques, such as ^{1}H and $^{13}C\{^{1}H\}$ NMR spectroscopy, IR spectroscopy and electron impact mass spectrometry (EI-MS).

The 1,2-diamines were reacted with benzaldehyde or ferrocenecarboxaldehyde in a cyclo-condensation reaction to yield organic 2-phenylbenzimidazoles **4a** – **4e** or organometallic 2-ferrocenylbenzimidazoles **5a** – **5e**. Based on preliminary pharmacological results, selected aminoquinoline-benzimidazole hybrid scaffolds were altered to incorporate a pyridyl moiety. Compounds **3a** – **3c** were cyclo-condensed with 2-pyridinecarboxaldehyde to afford 2-pyridylbenzimidazoles **6a** – **6c**. These cyclo-condensation reactions produced moderate yields. Crystals of compounds **4b** and **5c** were grown and their molecular structures determined using single-crystal X-ray diffraction. The compounds were fully characterised using ^{1}H, $^{13}C\{^{1}H\}$, COSY and HSQC NMR spectroscopy, IR spectroscopy and electrospray ionisation mass spectrometry (ESI-MS). The purity of the aminoquinoline-benzimidazole hybrids was determined by HPLC and all confirmed to be greater than 97%.

2.4 References

1. J. Walsh and A. Bell, *Curr. Pharm. Des.*, 2009, **15**, 2970-2985.
2. R. Morphy, C. Kay and Z. Rankovic, *Drug Discov. Today*, 2004, **9**, 641-651.
3. R. Morphy and Z. Rankovic, *J. Med. Chem.*, 2005, **48**, 6523-6543.
4. S. Manohar, S. I. Khan and D. S. Rawat, *Chem. Biol. Drug Des.*, 2013, **81**, 625-630.
5. K. Singh, H. Kaur, K. Chibale and J. Balzarini, *Eur. J. Med. Chem.*, 2013, **66**, 314-323.
6. S. Manohar, S. I. Khan and D. S. Rawat, *Chem. Biol. Drug. Des.*, 2011, **78**, 124-136.
7. F. Coslédan, L. Fraisse, A. Pellet, F. Guillou, B. Mordmüller, P. G. Kremsner, A. Moreno, D. Mazier, J.-P. Maffrand and B. Meunier, *P. Natl. Acad. Sci. USA*, 2008, **105**, 17579-17584.
8. N. C. Araujo, V. Barton, M. Jones, P. A. Stocks, S. A. Ward, J. Davies, P. G. Bray, A. E. Shone, M. L. Cristiano and P. M. O'Neill, *Bioorg. Med. Chem. Lett.*, 2009, **19**, 2038-2043.
9. M. Foley and L. Tilley, *Pharmacol. Ther.*, 1998, **79**, 55-87.
10. C. D. Fitch, *Life Sci.*, 2004, **74**, 1957-1972.
11. H. Ginsburg, S. Ward and P. Bray, *Parasitol. Today*, 1999, **15**, 357-360.
12. A. Ecker, A. M. Lehane, J. Clain and D. A. Fidock, *Trends Parasitol.*, 2012, **28**, 504-514.
13. S. J. Burgess, A. Selzer, J. X. Kelly, M. J. Smilkstein, M. K. Riscoe and D. H. Peyton, *J. Med. Chem.*, 2006, **49**, 5623-5625.
14. A. J. Bitonti, A. Sjoerdsma, P. P. McCann, D. E. Kyle, A. Oduola, R. N. Rossan, W. K. Milhous and D. E. Davidson, *Science*, 1988, **242**, 1301-1303.
15. Y. Bansal and O. Silakari, *Bioorg. Med. Chem.*, 2012, **20**, 6208-6236.
16. N. Singh, A. Pandurangan, K. Rana, P. Anand, A. Ahamad and A. K. Tiwari, *Int. Curr. Pharm. J.*, 2012, **1**, 119-127.
17. R. S. Keri, A. Hiremathad, S. Budagumpi and B. M. Nagaraja, *Chem. Biol. Drug. Des.*, 2015, **86**, 19-65.
18. R. Deprez-Poulain and P. Melnyk, *Comb. Chem. High T. Scr.*, 2005, **8**, 39-48.
19. J. Camacho, A. Barazarte, N. Gamboa, J. Rodrigues, R. Rojas, A. Vaisberg, R. Gilman and J. Charris, *Bioorg. Med. Chem.*, 2011, **19**, 2023-2029.

20. R. T. Skerlj, C. M. Bastos, M. L. Booker, M. L. Kramer, R. H. Barker Jr, C. A. Celatka, T. J. O'Shea, B. Munoz, A. B. Sidhu and J. F. Cortese, *ACS Med. Chem. Lett.*, 2011, **2**, 708-713.
21. C. R. Chong, X. Chen, L. Shi, J. O. Liu and D. J. Sullivan Jr, *Nat. Chem. Biol.*, 2006, **2**, 415.
22. C. C. Musonda, G. A. Whitlock, M. J. Witty, R. Brun and M. Kaiser, *Bioorg. Med. Chem. Lett.*, 2009, **19**, 481-484.
23. C. C. Musonda, S. Little, V. Yardley and K. Chibale, *Bioorg. Med. Chem. Lett.*, 2007, **17**, 4733-4736.
24. H. Xiangming, M. Huiqiang and W. Yulu, *Arkivoc*, 2007, **13**, 150-154.
25. H. Sharghi, O. Asemani and R. Khalifeh, *Synthetic Commun.*, 2008, **38**, 1128-1136.
26. S. I. Alaqeel, *J. Saudi Chem. Soc.*, 2017, **21**, 229-237.

Chapter 3:

Pharmacological evaluation and mechanistic studies of 2-phenyl, 2-ferrocenyl and 2-pyridyl aminoquinoline-benzimidazole hybrids

3.1 Introduction

In the continued search for antimicrobial agents, the determination of *in vitro* drug efficacy represents a crucial preliminary step in the discovery process. For the various infectious diseases, *in vitro* screening protocols and detection methods have evolved over the years. With regards to *Plasmodium falciparum*, *in vitro* assays take advantage of the fact that asexual parasites can be cultured *in vitro* in human erythrocytes, to which multiple sensitive and resistant strains have been adapted. The cultured parasites are then dosed with different concentrations of the test compound and control drugs, such as chloroquine. Numerous assay protocols have been described, including assessment of ^{3}H-hypoxanthine uptake inhibition[1] and the microscopic analysis of Giemsa-stained parasites.[2, 3] Flow cytometry[2, 3] and fluorescence-based[4] approaches have also been described in recent literature.

Another assay protocol involves the determination of *Plasmodium* lactate dehydrogenase (pLDH) activity,[5] which was used to evaluate the compounds herein. This enzyme assay is based on the ability of lactate dehydrogenase (LDH) to catalyse the conversion of lactate to pyruvate, using 3-acetyl pyridine adenine dinucleotide (APAD) as a co-enzyme.[5, 6] APAD is reduced to 3-acetyl pyridine adenine dinucleotide reduced (APADH) in the process and its formation forms the basis of this assay. Human LDH catalyses this glycolytic reaction at a very slow rate, while pLDH rapidly catalyses the conversion.[5] Levels of parasitemia correlate well with pLDH activity, which is assessed colorimetrically, as illustrated in Figure 3.1. Parasite viability is detected using the Malstat™ method, which involves the addition of a tetrazolium dye.[6, 7] The APADH

formed reduces the tetrazolium dye (yellow) to formazan (blue) in the presence of phenazine ethosulfate.

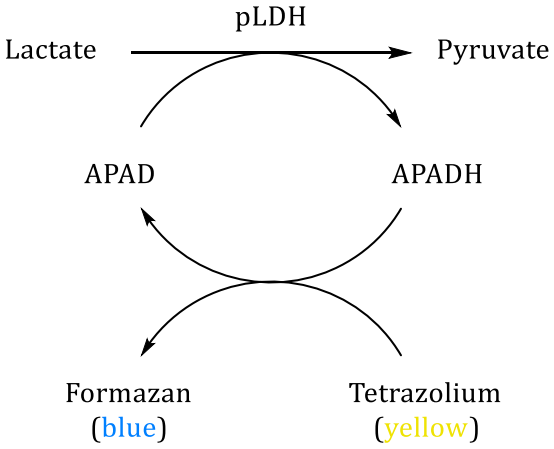

Figure 3.1 Principle of pLDH assay and Malstat™ method, used to determine parasite viability.

Cytotoxicity studies are often undertaken to determine the effect of test compounds on tumorigenic and non-tumorigenic cell lines. These screenings also aid in evaluating selectivity toward various microbes or cells. A common assay protocol assessing cytotoxicity is the 3-(4,5-dimethylthiazol-2-yl)-2,5-diphenyltetrazolium bromide (MTT) assay, which is also a colorimetric tetrazolium-based method.[8-10] In terms of *Mycobacterium tuberculosis*, there are a number of methods for determination of antibacterial susceptibility of test compounds.[11] Dilution methods allow the determination of minimum inhibitory concentrations (MICs), while disk diffusion methods generate results as zone diameter measurements.[11]

3.2 Pharmacological evaluation of aminoquinoline-benzimidazole hybrids

The pharmacological properties of the 2-phenyl, 2-ferrocenyl and 2-pyridyl aminoquinoline-benzimidazole hybrids (Figure 3.2), described in Chapter 2, were investigated. The hybrid compounds were screened *in vitro* against the NF54 chloroquine-sensitive (CQS) and K1 multidrug-resistant (MDR) strain of *Plasmodium falciparum* and their cytotoxicity was determined against the Chinese Hamster Ovarian (CHO) non-tumorigenic cell-line. Selected active and non-cytotoxic phenyl and ferrocenyl hybrids were evaluated for their *in vivo* efficacy in a *Plasmodium berghei* mouse model. Mechanistic studies to investigate the potential cell-free β-haematin inhibition activity,

cellular haemozoin inhibition activity and reactive oxygen species (ROS) generating ability, were performed on selected compounds. Furthermore, all hybrid compounds were evaluated for their *in vitro* antimycobacterial activity against the H37Rv strain of *Mycobacterium tuberculosis*.

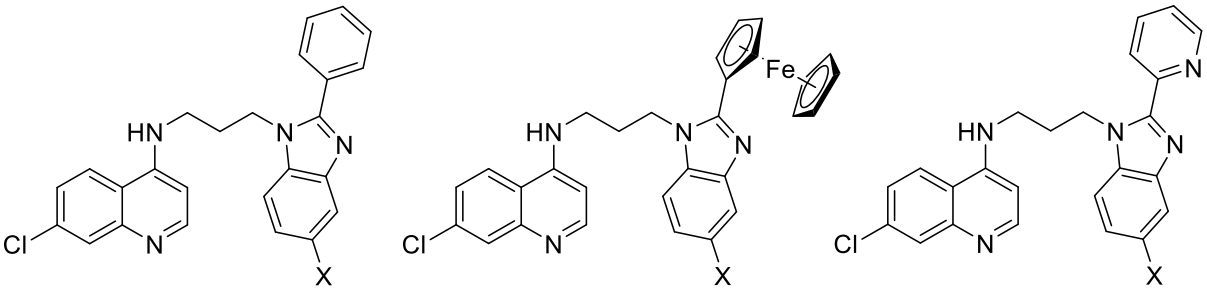

4a: X = H
4b: X = CH_3
4c: X = CF_3
4d: X = SO_2CH_3
4e: X = CN

5a: X = H
5b: X = CH_3
5c: X = CF_3
5d: X = SO_2CH_3
5e: X = CN

6a: X = H
6b: X = CH_3
6c: X = CF_3

Figure 3.2 Pharmacologically-screened aminoquinoline-benzimidazole hybrids (**4a – 4e**, **5a – 5e** and **6a – 6c**).

3.2.1 Predicting lipophilicity

The logP values of these hybrid compounds were estimated in order to gain insight into the relationship between their lipophilicity and pharmacological activity. The partition coefficient, logP, is the most commonly used measure of lipophilicity. The calculated logP (clogP) values of the organic hybrid compounds (**4a – 4e** and **6a – 6c**) were estimated using MarvinSketch V17.3.13.0, while that for the ferrocenyl hybrids (**5a – 5e**) required an alternative method. A method combining calculated values from MarvinSketch, the fragmental approach proposed by Mannhold and Rekker[12] and the ferrocenyl adaptation developed by Ahmedi and Lanez,[13-15] was employed.

The fragmental method, described by Rekker *et al*., makes use of theoretical constants for molecular substructures derived from experimental logP values of simple organic compounds.[12] The method takes into account differing chemical characteristics such as hydrogen bonding, electronegative centres and resonance, by the incorporation of correction values.[12] Lanez *et al*. adapted this method for the calculation of logP values of ferrocenyl compounds.[14] In this adapted method, the theoretical logP value of

ferrocene (Fc) is equal to the experimental value of 2.66.[14, 16] The logP contribution of a ferrocenyl group (Fc–H) is obtained by subtracting the fragmental constant of a hydrogen atom from that of Fc, to afford a value of 2.456.[14] In our modified approach, the latter value (Fc–H = 2.456), as well as the calculated values for corresponding phenyl derivatives from MarvinSketch, were combined to calculate the logP values of the ferrocenyl compounds. Twenty reference compounds (Figure 3.3), with known experimental logP values, were used to validate this method.

The following equation was used to calculate logP values for the ferrocenyl derivatives:

$$\mathbf{logP(_{Fc\ derivative}) = logP(_{benzene\ derivative}) - f(_{C6H5}) + f(_{Fc\text{-}H})}$$

where: clogP($_{benzene\ derivative}$) calculated using MarvinSketch,

f($_{C6H5}$) obtained from fragmental approach,[12]

f($_{Fc\text{-}H}$) obtained from Lanez *et al.*[14]

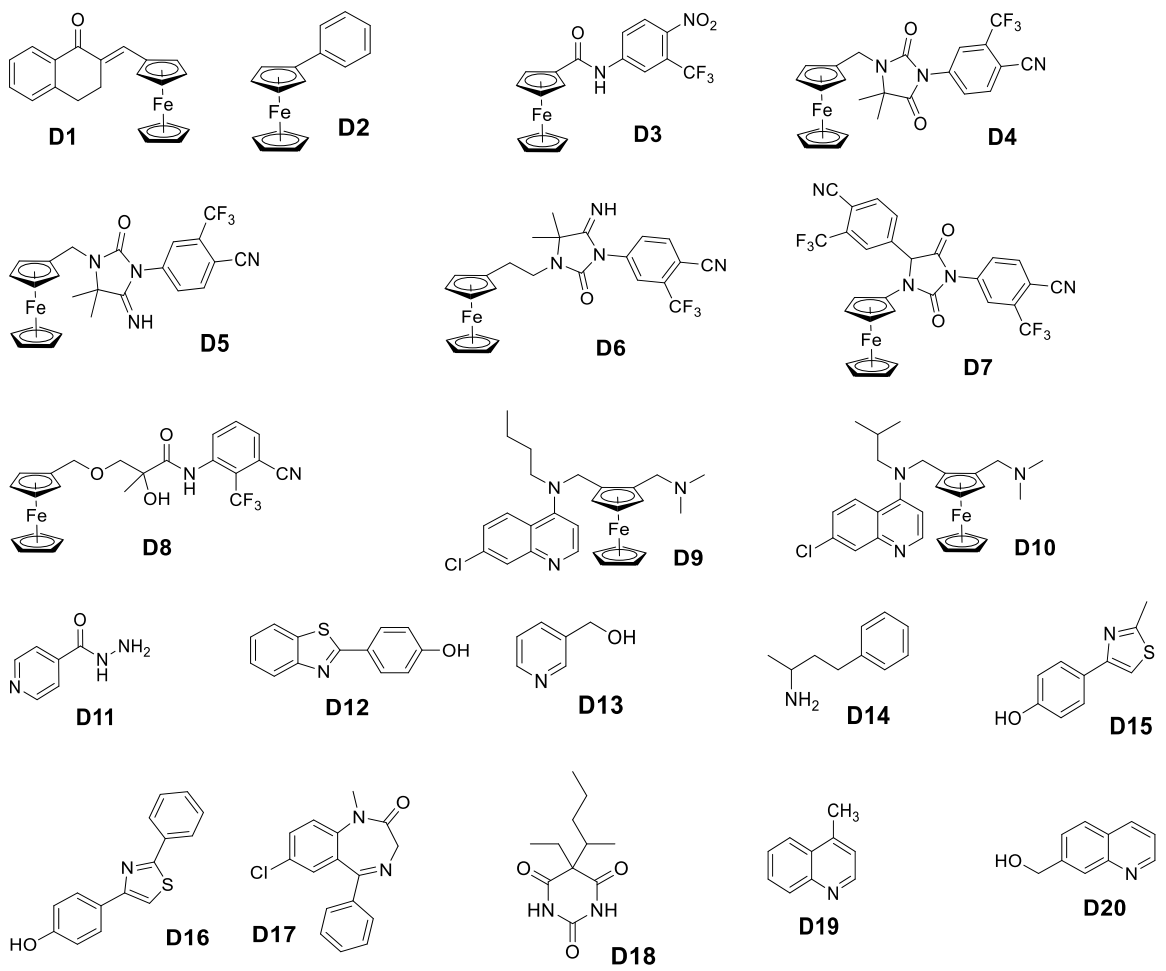

Figure 3.3 Reference ferrocenyl and organic derivatives (**D1**-**D20**) used to validate the method.

Representative calculation

A representative calculation of the logP value of the ferrocenyl compound **D1** is shown below. The calculated logP (clogP) value of the benzene derivative was determined using MarvinSketch v17.3.13. The logP value of the ferrocenyl derivative was calculated using the equation described previously.

$$\log P_{(\text{Fc derivative})} = \log P_{(\text{benzene derivative})} - f_{(C_6H_5)} + f_{(\text{Fc-H})}$$

$$= 4.336 - [6\times C + 5\times H] + 2.456$$

$$= 4.336 - [6(0.110) + 5(0.204)] + 2.456$$

$$= 5.112$$

Table 3.1 Experimental and estimated logP values for compounds **D1** – **D20**.

Compound	Experimental logP	Estimated logP
D1	5.27[17]	5.11
D2	4.59[13]	4.40
D3	4.42[18]	4.66
D4	5.23[14]	4.89
D5	4.68[19]	4.90
D6	5.04[14]	5.19
D7	6.47[15]	6.49
D8	4.63[18]	4.23
D9	6.70[15]	6.61
D10	6.60[15]	6.53
D11	-0.70[20]	-0.69
D12	3.86[21]	3.84
D13	-0.02[20]	-0.012
D14	2.12[22]	2.25
D15	2.82[21]	3.08
D16	4.65[21]	4.39
D17	2.68[20]	2.49
D18	2.10[20]	1.89
D19	2.61[23]	2.64
D20	1.29[23]	1.36

Theoretical clogP values were determined for ferrocenyl compounds **D1** – **D10**, using the aforementioned calculation, while the clogP values of compounds **D11** – **D20** were determined directly in MarvinSketch. The experimental values, taken from the literature, and estimated values are listed in Table 3.1. The data was plotted (Figure 3.4) and a regression analysis (Microsoft Excel) was used to determine the correlation between estimated and experimental values. The scatter plot resulted in a linear line of best fit, with a gradient close to 1 (m = 1.0105), an intercept approximately equal to zero (c = 0.0007) and R^2 of 0.9918, indicating a good correlation between the two sets of values. In addition, the regression analysis revealed a *p*-value (3.08×10^{-20}) smaller than 0.05, indicating no significant difference.

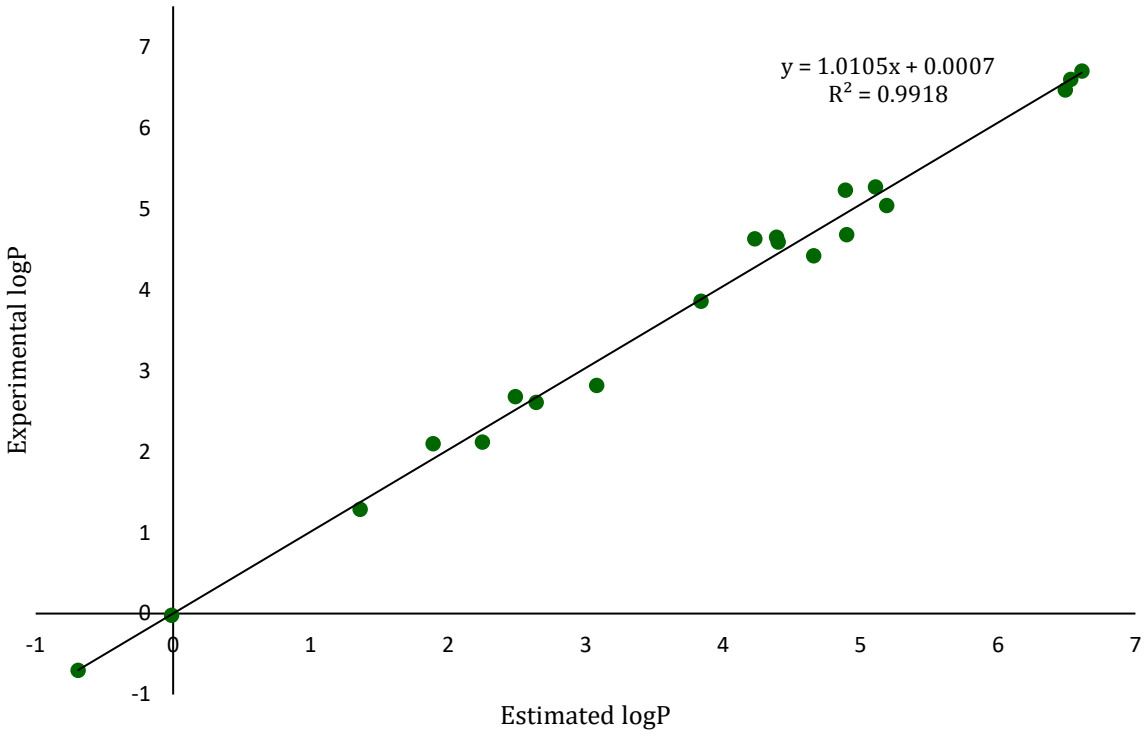

Figure 3.4 Linear relationship between experimental and estimated logP values.

Predicting the logP values of the aminoquinoline-benzimidazole hybrids

The calculated logP values of the ferrocenyl aminoquinoline-benzimidazole hybrids (**5a** – **5e**) were determined using this modified method. The clogP values of all of the hybrid compounds are listed in Table 3.2.

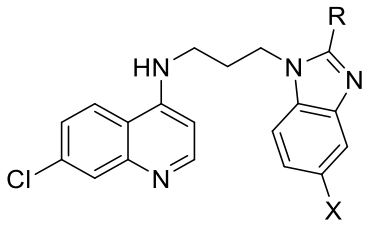

Table 3.2 Estimated logP values of compounds **4a** – **4e**, **5a** – **5e** and **6a** – **6c**.

Compound	R	X	logP
4a	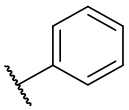	H	5.60
4b		CH_3	6.12
4c		CF_3	6.48
4d		SO_2CH_3	4.44
4e		CN	5.46
5a	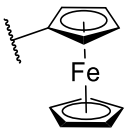	H	6.38
5b		CH_3	6.90
5c		CF_3	7.26
5d		SO_2CH_3	5.22
5e		CN	6.24
6a	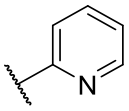	H	4.77
6b		CH_3	5.29
6c		CF_3	5.65

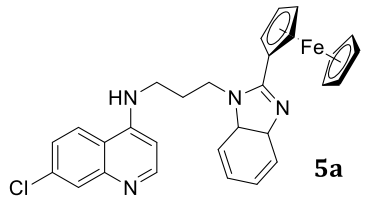

5a

Sample calculation:

$$\log P(_{\text{Fc derivative}}) = \log P(_{\text{compound 4a}}) - f(_{C6H5}) + f(_{Fc\text{-}H})$$

$$= 5.604 - [6(0.110) + 5(0.204)] + 2.456$$

$$= 6.38$$

3.2.2 *In vitro* antiplasmodium activity and cytotoxicity

The 2-phenyl, 2-ferrocenyl and 2-pyridyl aminoquinoline-benzimidazole hybrids (**4a – 4e**, **5a – 5e** and **6a – 6c**) were evaluated for their *in vitro* antiplasmodium activity using the *Plasmodium* lactate dehydrogenase (pLDH) assay.[5] All compounds were screened against the CQS NF54 and MDR K1 strains of *Plasmodium falciparum*. Chloroquine (CQ) and artesunate (AS) were used as positive control drugs. The IC_{50} values and resistance indices (RI) are listed in Table 3.3.

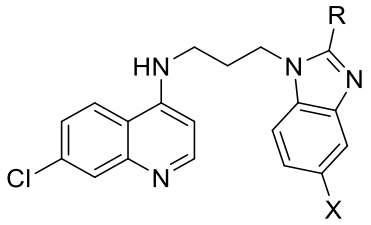

Table 3.3 *In vitro* antiplasmodium data and resistance indices of compounds **4a – 4e**, **5a – 5e**, **6a – 6c**, CQ and AS.

Compound	R	X	IC_{50} (μM) ± SE		RI[a]
			NF54	K1	
4a	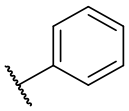	H	5.553 ± 0.063	0.201 ± 0.003	0.036
4b		CH_3	0.784 ± 0.016	0.457 ± 0.095	0.583
4c		CF_3	0.431 ± 0.012	0.151 ± 0.004	0.350
4d		SO_2CH_3	0.559 ± 0.011	1.832 ± 0.080	3.280
4e		CN	0.975 ± 0.017	0.179 ± 0.004	0.183
5a	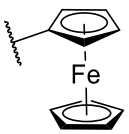	H	2.882 ± 0.048	0.339 ± 0.011	0.118
5b		CH_3	0.329 ± 0.005	0.283 ± 0.004	0.860
5c		CF_3	1.223 ± 0.100	0.658 ± 0.039	0.538
5d		SO_2CH_3	0.848 ± 0.007	0.579 ± 0.008	0.683
5e		CN	0.909 ± 0.019	0.565 ± 0.008	0.622
6a	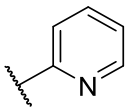	H	1.089 ± 0.168	> 20	-
6b		CH_3	4.984 ± 0.613	ND[b]	-
6c		CF_3	0.410 ± 0.028	> 20	-
CQ	-	-	0.0102 ± 0.0023	0.205 ± 0.007	20.098
AS	-	-	0.0098 ± 0.0011	ND[b]	-

[a]RI = IC_{50}(K1) / IC_{50}(NF54);

[b]ND = not determined

All of the phenyl-, ferrocenyl- and pyridyl-derived hybrids display good antiplasmodium activity, with most IC_{50} values in the sub-micromolar range. The IC_{50} values obtained in the CQS NF54 strain are graphically represented in Figure 3.5. In all cases except one, incorporation of the X substituent at the 5-position of the benzimidazole moiety significantly enhanced the antiplasmodium activity. This derivatisation resulted in mostly sub-micromolar IC_{50} values across the phenyl, ferrocenyl and pyridyl series, compared to the unsubstituted analogues (X = H). An exception in this case is the methyl-substituted pyridyl hybrid **6b** (IC_{50} = 4.984 μM), which is approximately 5-fold less active than the unsubstituted analogue **6a** (IC_{50} = 1.089 μM). The decreased activity of this analogue may be related limited solubility in the assay media observed at the test concentration.

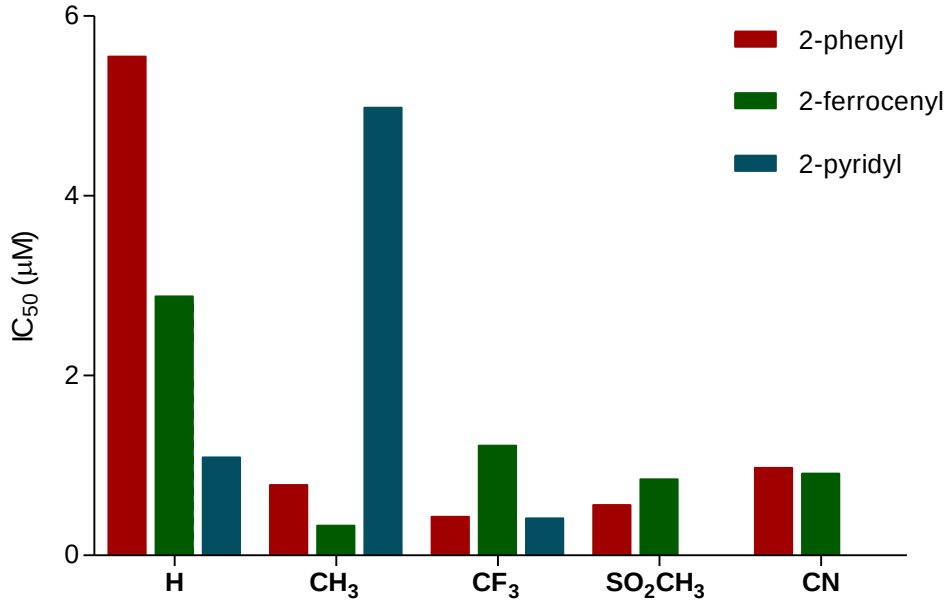

Figure 3.5 IC_{50} values of compounds **4a** – **4e**, **5a** – **5e** and **6a** – **6c** against the CQS NF54 strain of *P. falciparum*.

Comparing the organic phenyl hybrids and their corresponding organometallic ferrocenyl analogues in the NF54 strain reveals contrasting trends. Some of the ferrocenyl hybrids (**5a** and **5b**) displayed enhanced activity over their organic analogues (**4a** and **4b**). In addition, the phenyl hybrids **4c** and **4d** are more active than their ferrocenyl analogues **5c** and **5d**. With regards to ferrocenyl derivatisation, literature reports comparable *in vitro* CQS strain activity of organic drug chloroquine, and its ferrocenyl analogue ferroquine.[24] Furthermore, the activity of these hybrids does not

compare to that of the control drugs, CQ and AS, displaying at least 30-fold lower IC_{50} values.

As a result of their mostly sub-micromolar IC_{50} values, selected hybrids were evaluated against the MDR K1 strain of *P. falciparum*, and the IC_{50} values of compounds **4a** – **4e** and **5a** – **5e** are graphically represented in Figure 3.6. The pyridyl hybrids **6a** and **6c** were inactive at the highest concentration tested. In contrast to their activity in the CQS NF54 strain, the phenyl hybrids **4a** (0.201 μM), **4c** (0.151 μM) and **4e** (0.179 μM) gave rise to IC_{50} values comparable or lower than that of CQ (0.205 μM) in the MDR K1 strain. In general, most of the phenyl and ferrocenyl hybrids (**4a** – **4c**, **4e** and **5a** – **5e**) were more active in the resistant strain. The methylsulfonyl-substituted phenyl hybrid **4d** provides an exception, with greater than 3-fold lower activity in the resistant strain compared to the sensitive strain. Resistance indices (RI), defined as the quotient of IC_{50}(K1) and IC_{50}(NF54), were calculated. RI values equal to or less than one are favourable, and indicate that the compound is equally or more active in the resistant strain compared to the sensitive strain. Most hybrids had RI values less than 1, significantly lower than that of CQ (RI = 20), suggesting that they may not be susceptible to cross-resistance, and have potential greater applicability against resistant strains of *P. falciparum*.

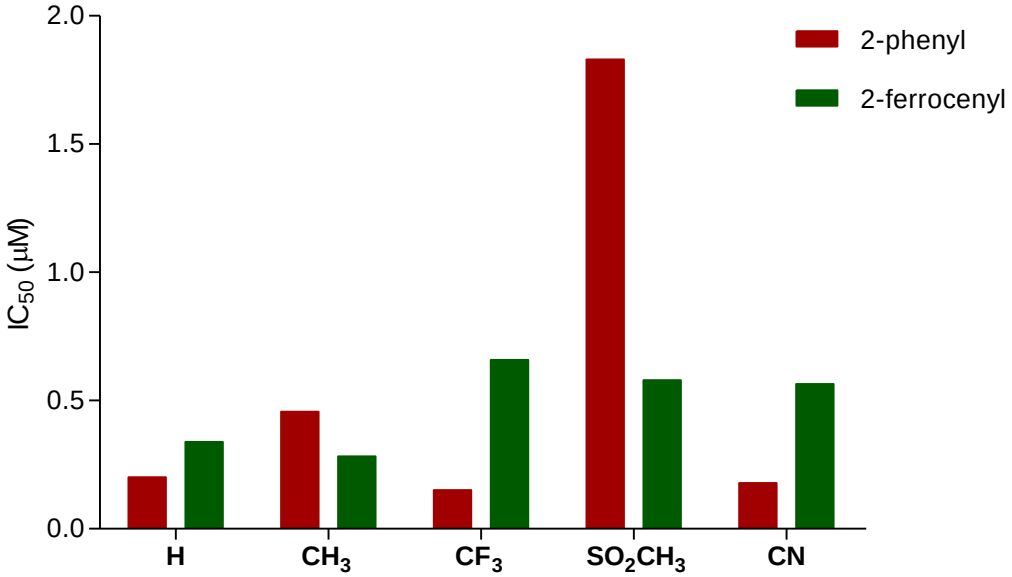

Figure 3.6 IC_{50} values of compounds **4a** – **4e** and **5a** – **5e** against the MDR K1 strain of *P. falciparum*.

In some cases, introduction of the organometallic ferrocenyl moiety resulted in enhanced antiplasmodium activity in the K1 strain, however, this trend is not consistent, as seen in the NF54 strain. The ferrocenyl hybrids **5b** and **5d** displayed enhanced activity compared to their organic phenyl analogues **4b** and **4d**. The phenyl hybrids **4a**, **4c** and **4e** proved more active than their ferrocenyl analogues **5a**, **5c** and **5e**. This is contrary to what was expected as there is a precedent for enhanced activity of ferrocenyl analogues in resistant strains. Literature reports 20-fold greater *in vitro* activity of ferroquine compared to chloroquine in CQR strains.[24]

The most active compound in the chloroquine-sensitive strain was the ferrocenyl-derived **5b** (0.329 μM), while in the resistant strain the phenyl-derived **4c** (0.151 μM) was most active. The most active analogues across the phenyl-, ferrocenyl and pyridyl series overall are compounds **4c** (CF_3), **5b** (CH_3) and **6c** (CF_3). Interestingly, all three of the most active analogues have a more hydrophobic substituent at the 5-position of the benzimidazole, suggesting a correlation between hydrophobicity and antiplasmodium activity. Although these analogues have relatively high logP values (Table 3.2) of 6.48 (**4c**), 6.90 (**5b**) and 5.65 (**6c**), there was no correlation between lipophilicity and antiplasmodium activity. It may also be interesting to note that compound **4d** (1.832 μM), which was comparatively less active in the resistant K1 strain, has the lowest logP value of 4.44.

Evaluation of individual components

These hybrid agents were prepared and pharmacologically evaluated on the basis that combination of the two pharmacophores would potentially result in enhanced activity compared to their parent compounds. Therefore, it is a worthwhile study to compare the pharmacological activity of the individual components of the hybrid with that of the hybrid itself. The structures of the individual components, the aminoquinoline **B1** and benzimidazole **B2**, are shown in Figure 3.7. A propyl chain was incorporated into the structures of both components in order to represent the propyl linker which is present in the hybrid structure.

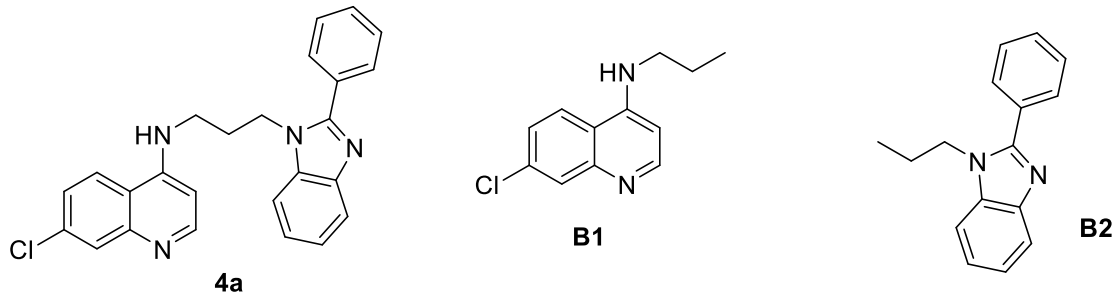

Figure 3.7 Structures of hybrid **4a** and components **B1** and **B2**.

Both components, **B1** and **B2**, were screened against the CQS NF54 and MDR K1 strains of *P. falciparum*, and their activity compared to the corresponding unsubstituted phenyl hybrid **4a** (Figure 3.7). The IC_{50} values obtained are represented graphically in Figure 3.8. In the NF54 strain, the aminoquinoline compound **B1** gave rise to a sub-micromolar IC_{50} value of 0.640 μM, displaying almost 9-fold greater activity than the hybrid **4a** (5.553 μM). The benzimidazole compound **B2** was inactive at the maximum concentration tested. It may be speculated that in the NF54 strain, the activity of the hybrid **4a** may be solely attributed to the presence of the aminoquinoline moiety, while the benzimidazole moiety has no effect, or in fact decreases the activity.

When evaluated in the K1 strain, hybrid **4a** displays superior activity compared to both components **B1** and **B2**, with an IC_{50} value of 0.201 μM. As mentioned earlier, the hybrid **4a** is more active in the resistant strain (RI = 0.036). The aminoquinoline **B1** does not maintain its potent activity in the resistant strain, displaying an almost 2-fold lower IC_{50} value of 1.13 μM (RI = 1.77). Once again, the benzimidazole **B2** was inactive. These results may suggest that it is the combination of the two pharmacophores, to form the hybrid compound **4a**, that gives rise to enhanced activity in the resistant strain, rather than the influence of the individual components. This may imply unique mechanisms of action, attributed to the hybrid structure, that allows it to overcome resistance mechanisms of the parasite.

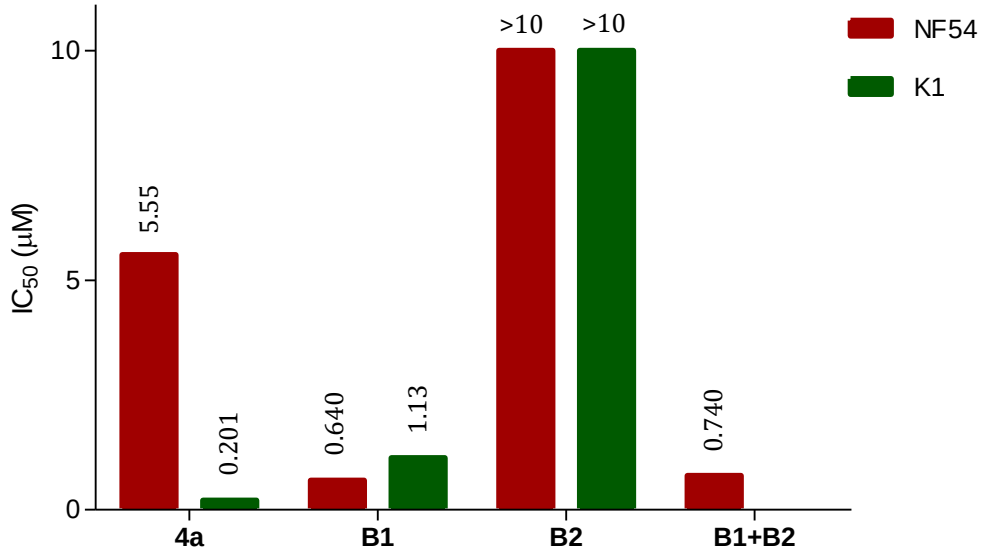

Figure 3.8 Antiplasmodium activity of hybrid **4a**, components **B1** and **B2**, and equimolar physical mixture **B1+B2**.

In addition, an equimolar physical mixture of the components (**B1+B2**) was also screened against the NF54 strain. The mixture **B1+B2** gave rise to an IC_{50} value of 0.740 μM, displaying comparable activity to the aminoquinoline **B1** alone. This may indicate that the activity of the physical mixture is attributed to the aminoquinoline **B1** alone, with little to no contribution from the benzimidazole **B2**. Furthermore, the equimolar mixture **B1+B2** proved significantly more active than the hybrid **4a** in the sensitive NF54 strain, suggesting that administration of the physical mixture of components is more effective in this case.

Isobologram analysis

An isobologram analysis was utilised in order to further explore and visualise the interaction between the two components, **B1** and **B2**, when tested *in vitro*. An isobologram analysis is a type of drug combination study, introduced by Loewe and Muischnek,[25] in which the combined effects or interactions of two or more drugs are analysed. A general example of an isobologram is shown in Figure 3.9,[26] depicting the different interactions that are possible for compound combinations. In a two-compound isobologram graph, the X and Y axes represent the dose axes of each compound and the points represent combinations of the two compounds. If the compounds have no

interaction, the points will form a straight line and the relationship is additive. When the combination is more effective than the individual compounds, the points lie below (to the left of) the zero interaction (additive) line and the relationship is synergistic. On the other hand, when the combination is less effective than the individual compounds, the points lie above (to the right of) the additive line and the relationship is antagonistic.[26]

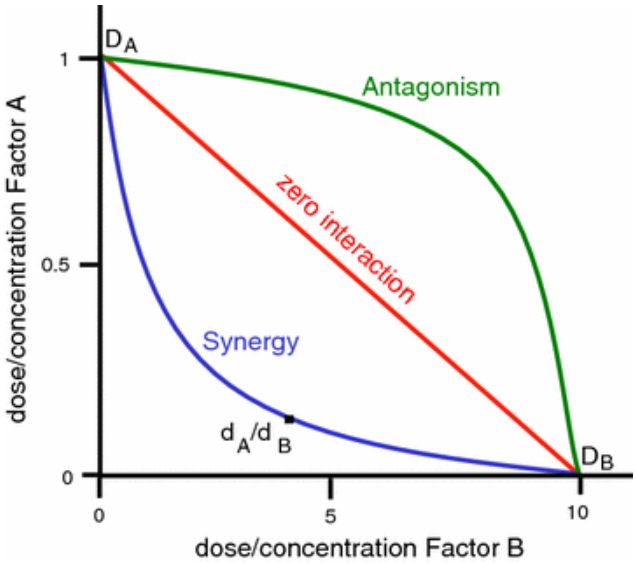

Figure 3.9 Typical isobologram depicting component relationships.[26]

The individual components (**B1** and **B2**) were tested in fixed ratios against the CQS NF54 strain of *P. falciparum*, following a modified isobologram method described by Fivelman *et al*.[27] The IC_{50} values of compounds **B1** and **B2** in the fixed ratio mixtures were determined and using their individual IC_{50} values (Figure 3.8), the fractional IC_{50} (FIC_{50}) values of compounds **B1** and **B2** were calculated (Table 3.4).

Table 3.4 Compound **B1** and **B2** ratios and fractional IC_{50} values.

Mixture	**B1** ratio	**B2** ratio	**B1** FIC_{50}[a]	**B2** FIC_{50}[a]
1	5	0	1	0
2	4	1	0.85	0.08
3	3	2	0.82	0.21
4	2	3	0.90	0.50
5	1	4	0.65	0.92
6	0	5	0	1
7	1	1	1.12	0.32

[a]FIC_{50} = IC_{50} of compound in mixture / IC_{50} of compound only

These FIC_{50} values were plotted to construct the isobologram shown in Figure 3.10. As seen in the isobologram, the relationship between compounds **B1** and **B2** is antagonistic for mixtures 4, 5 and 7. Mixtures 2 and 3 display additive relationships between compounds **B1** and **B2**. Antagonism is seen for the mixtures with equal or greater proportions of compound **B2**. Additivity is indicated for the mixtures with greater proportions of compound **B1**. These trends indicate that aminoquinoline **B1** confers the antiplasmodium activity, while benzimidazole **B2** exerts an antagonistic effect, decreasing the activity. This result confirms what was seen in the evaluation of the individual components and equimolar physical mixture, discussed earlier.

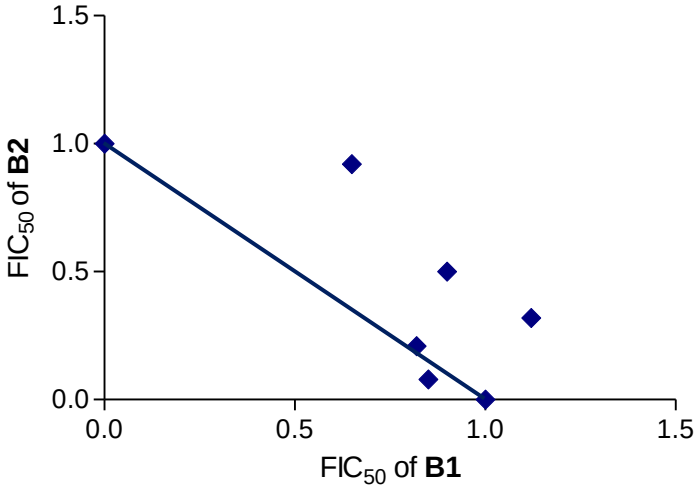

Figure 3.10 Isobologram of components **B1** and **B2**.

Cytotoxicity

The 2-phenyl and 2-ferrocenyl hybrids (**4a** – **4e** and **5a** – **5e**) were also screened for their cytotoxicity against the non-tumorigenic Chinese hamster ovarian (CHO) cell line, using the 3-(4,5-dimethylthiazol-2-yl)-2,5-diphenyltetrazolium bromide (MTT) assay.[8, 9] Emetine was used as the positive control drug. The cytotoxicity of the 2-pyridyl hybrids (**6a** – **6c**) was not evaluated as a result of their comparatively lower NF54 activity, which was not maintained in the resistant K1 strain. Compounds **4a** and **4c** – **4e** display low toxicity against the CHO cells, with moderate micromolar IC_{50} values in the range 16.2 – 42.0 μM, at least 1000-fold less active than the positive control, emetine (0.0162 μM). Compounds **4b** and **5a** – **5e** were non-cytotoxic (IC_{50} > 50 μM) at

the highest concentration tested. The selectivity indices (SI), shown in Table 3.5, were greater than 7 and 22 for the sensitive (SI_1) and resistant (SI_2) parasite strains, respectively. These values (> 1) indicate that these aminoquinoline-benzimidazole hybrids are selective towards the *Plasmodium* parasites, and suggests that their activity may attributed to mechanisms other than general cytotoxicity.

Table 3.5 Cytotoxicity data and selectivity indices of compounds **4a** – **4e**, **5a** – **5e** and emetine.

Compound	CHO IC_{50} (µM)	SI_1[a]	SI_2[b]
4a	42.01	7.57	209
4b	> 50	-	-
4c	16.16	37.5	107
4d	40.93	73.2	22.4
4e	38.87	39.9	217
5a	> 50	-	-
5b	> 50	-	-
5c	> 50	-	-
5d	> 50	-	-
5e	> 50	-	-
Emetine	0.0162	-	-

[a]$SI_1 = IC_{50}(CHO) / IC_{50}(NF54)$;

[b]$SI_2 = IC_{50}(CHO) / IC_{50}(K1)$

3.2.3 *In vivo* antimalarial activity

Based on their favourable *in vitro* activity and low cytotoxicity, the most active phenyl and ferrocenyl aminoquinoline-benzimidazole hybrids (**4c** and **5b**) were evaluated for their *in vivo* antimalarial efficacy in *Plasmodium berghei*-infected mice. Murine (rodent) *Plasmodium* species provide a practical model for the study of mammalian *Plasmodium* species. With regards to structure, physiology and life cycle, rodent plasmodia are analogous to mammalian malaria parasites.[28] Mice infected with the CQS *P. berghei* ANKA strain, were dosed orally at 4 × 50 mg/kg and the reduction in parasitemia relative to the control determined. Results of the *in vivo* screening are summarised in Table 3.6. None of the three dosed mice were cured at this concentration and thus lower concentrations were not administered. Dosing with the ferrocenyl hybrid **5b** resulted in significantly

enhanced inhibition of parasitemia (92%), compared to the phenyl hybrid **4c** (58%). Despite this vast difference in parasite inhibition, mice administered with either compound had the same mean survival time of seven days. This may suggest that compound **4c** has some immune-modulating properties, allowing the mice to survive for an extended period of time. Conversely, it may also suggest that the pharmacokinetic profile of compound **5b** is not optimal, with solubility-limited absorption a likely contributing factor, decreasing the survival time of the mice.

Table 3.6 *In vivo* data for compounds **4c** and **5b**.

Compound	R	X	oral dose (mg/kg)	% reduction in parasitemia (MSD)[a]	cured/infected
4c	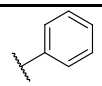	CF_3	4 × 50	58 (7)	0/3
5b	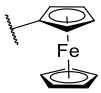	CH_3	4 × 50	92 (7)	0/3

[a]MSD = mean survival days

3.2.4 Mechanistic studies

3.2.4.1 β-haematin inhibition

Chloroquine and other quinoline-containing antimalarials are known to target the parasite-induced host haemoglobin degradation pathway by preventing the parasite from converting toxic haem to the non-toxic malaria pigment, haemozoin.[29-31] This results in the build-up of toxic haem, which damages the parasite.[29-31] In order to elucidate whether these aminoquinoline-benzimidazole hybrids inhibit haemozoin formation as a potential contributing mechanism, the most active 2-phenyl-, 2-ferrocenyl and 2-pyridyl-derived hybrids (**4c**, **5b** and **6c**) were evaluated for their ability to inhibit β-haematin (synthetic haemozoin) formation. The inhibition properties of these hybrid compounds were investigated using the Nonidet P-40 (NP-40) detergent-mediated assay, developed by Sandlin *et al*.[32] The β-haematin inhibition activity was quantified using the colorimetric pyridine ferrihaemochrome method developed by Egan *et al*.[33]

The log-based dose-response curves for compounds **4c**, **5b** and **6c** obtained from the NP-40 detergent-mediated assay, are shown in Figure 3.11, with CQ as the positive control. The IC_{50} values are reported in Table 3.7. The phenyl and ferrocenyl hybrids (**4c** and **5b**) are potent β-haematin inhibitors, both displaying IC_{50} values of 16 μM, at least four times more active than CQ (74 μM). The pyridyl hybrid **6c** was significantly less potent in comparison to the phenyl and ferrocenyl analogues, with a higher IC_{50} value of 54 μM, however, still lower than that of CQ. These results suggest that this series of hybrids may act by inhibition of haemozoin formation. However, this result is obtained in a cell-free assay and requires validation in the *P. falciparum* parasite.

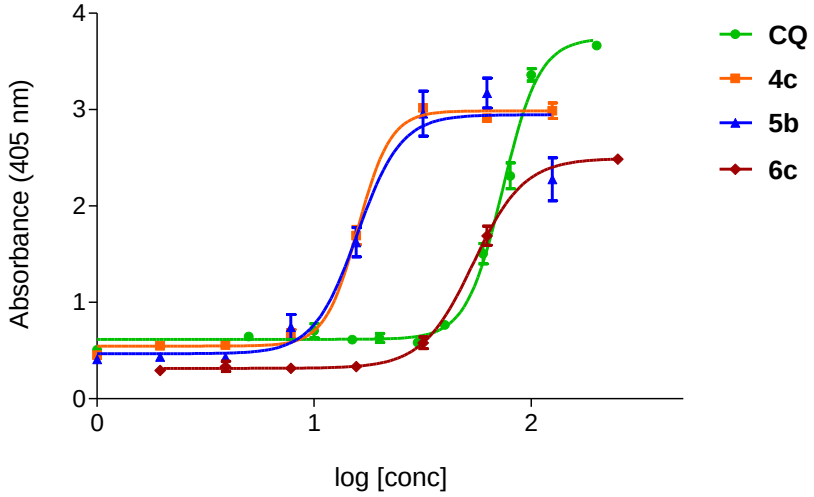

Figure 3.11 Dose-response curves of compounds **4c**, **5c**, **6c** and chloroquine (CQ).

Table 3.7 β-Haematin inhibition IC_{50} values of compounds **4c**, **5b**, **6c** and **CQ**.

Compound	IC_{50} (μM) [95% confidence interval]
4c	15.90 [15.31 to 16.51]
5b	15.80 [13.68 to 18.25]
6c	54.08 [51.22 to 57.09]
CQ	73.98 [71.14 to 76.94]

In addition, no direct correlation can be drawn between the β-haematin inhibition activity and the *in vitro* NF54/K1 strain antiplasmodium activity of these compounds, reported in Section 3.2.2. There is, however, a correlation between the β-haematin inhibition IC_{50} (βHIA_{IC50}) values and the lipophilicity of compounds **4c**, **5b** and **6c**. Compounds **4c** and **5b**, which have higher logP values of 6.48 and 6.90, respectively, display lower IC_{50}

values. Compound **6c**, which has a lower logP value of 5.65, displays a higher IC_{50} value. This suggests a positive correlation between lipophilicity and β-haematin inhibition activity, where greater lipophilicity of a compound results in enhanced activity.

3.2.4.2 Cellular haem fractionation

The β-haematin inhibition assay is routinely used to identify potential haemozoin inhibitors. Egan *et al*. translated this concept into malaria parasites cultured *in vitro*, to determine in-cell haemozoin inhibition ability.[34] The cellular haem fractionation assay directly quantifies the different haem species present in CQS *P. falciparum* parasites.[34] Originally applied to CQ, the method was modified and applied to different antimalarials.[35] True inhibitors of haemozoin formation gave rise to a dose-dependent increase in the amount of free haem and a corresponding decrease in the amount of haemozoin.[34, 35] In order to validate that these hybrid compounds are true haemozoin inhibitors, based on their β-haematin inhibition activity (Section 3.2.4.1), compound **5b** (βHIA_{IC50} = 15.8 μM) was subjected to a cellular haem fractionation assay. Parasites of the CQS NF54 strain were treated with increasing concentrations of compound **5b** and the amount of free haem, haemozoin and haemoglobin were determined. The graphs shown in Figure 3.12, depict the effect of compound **5b** on the amounts of the three species.

Following treatment with compound **5b**, there is a dose-dependent increase in the amount of free haem (Figure 3.12 – **I**), and a corresponding decrease in the amount of haemozoin (Figure 3.12 – **II**). The free haem referred to here is ferriprotoporphyrin IX (Fe(III)PPIX or haematin).[33, 35] The increase in Fe(III)PPIX and decrease in haemozoin indicates that compound **5b** inhibits the biocrystallisation process required to form haemozoin. Thus, this confirms that compound **5b** is a true inhibitor of haemozoin formation. Furthermore, there is also a dose-dependent increase in the amount of haemoglobin present in the parasite (Figure 3.12 – **III**). This is in agreement with previous studies, which have shown the presence of undigested haemoglobin in CQ-treated *P. falciparum* parasites.[36, 37] Literature has also suggested a causal link between the increase in free haem and the increase in haemoglobin, with the former occurring first.[34] Therefore, we speculate that upon treatment with compound **5b**, the accumulation of free haem results in the accumulation of undigested haemoglobin.

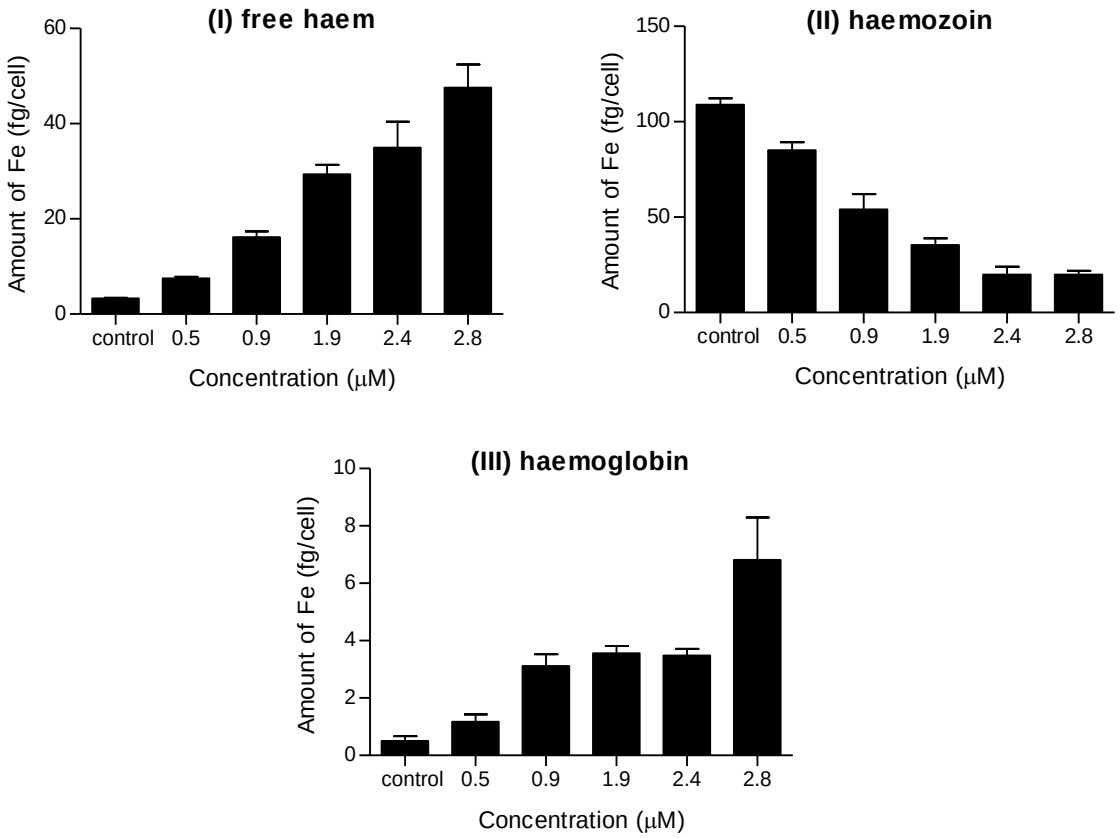

Figure 3.12 Amount of iron (Fe) present as (**I**) free haem, (**II**) haemozoin and (**III**) haemoglobin at varying concentrations of the compound **5b**.

3.2.4.3 Reactive oxygen species (ROS)

Hybrid chemotherapeutic agents are proposed to have dual or multiple modes of action, thus further mechanistic studies were pursued. The presence of a ferrocenyl moiety in compounds **5a** – **5e**, brings a potential additional mechanism of antiplasmodium action into consideration. Ferroquine, the ferrocenyl analogue of the antimalarial drug, chloroquine, is proposed to have a multifaceted mode of action, including the ability to generate reactive oxygen species (ROS).[38-41] This is ascribed to the ability of the redox-active iron (Fe) centre to cycle between Fe^{2+} and Fe^{3+} (ferrocene to ferrocenium), *via* a Fenton-like process (Equation 1 and 2), generating ROS and ultimately causing parasite damage.[38-41] Thus, a preliminary DNA cleavage study was undertaken in order to investigate whether the 2-ferrocenyl hybrids are able to generate ROS. Compound-DNA interaction assays were performed using the most active 2-ferrocenyl hybrid (**5b**). These experiments work on the principle that radicals are generated by reaction of the

compound of interest with hydrogen peroxide (H_2O_2) and ascorbic acid (AA). Cleavage of one or both strands of circular plasmid DNA (pUC57), which is used as the reporter molecule, is the result, and indicates the formation, of ROS. Results of the dose-dependent DNA-cleavage of pUC57 is measured by agarose gel electrophoresis, as depicted in Figure 3.13.

Equation 1 $Fe^{2+} + H_2O_2 \rightarrow Fe^{3+} + HO^{\cdot} + OH^-$

Equation 2 $Fe^{3+} + H_2O_2 \rightarrow Fe^{2+} + HOO^{\cdot} + H^+$

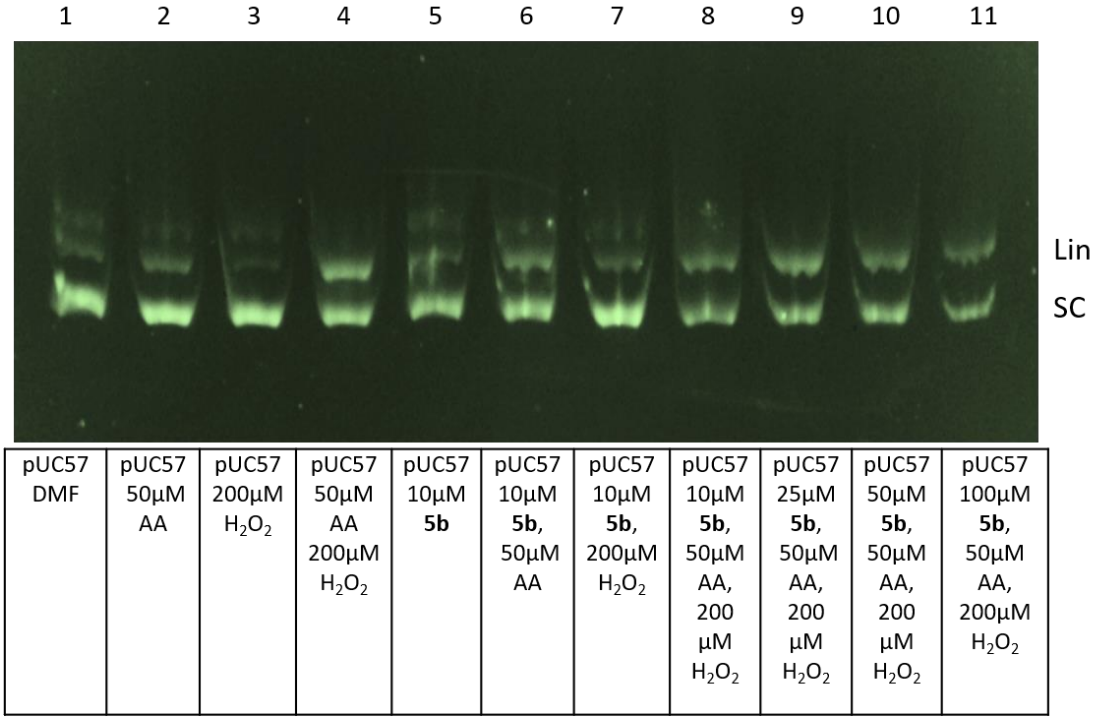

Figure 3.13 Agarose gel electrophoresis displaying DNA cleavage. Lin = linear DNA, SC = super-coiled DNA.

The gel displayed a slight increase in the amount of linear DNA on the addition of the compound **5b**. The small degree of DNA cleavage may be due to decreased solubility of compound **5b** in the mixtures over a period of time, as there was evidence of precipitation in wells at the 50 and 100 μM concentrations (lanes 10 and 11). Comparing lane 6 versus lane 7, it should be noted that a mixture of compound **5b** and ascorbic acid (lane 6) produced more linear (Lin) DNA than a mixture of compound **5b** and H_2O_2 (lane 7). This indicates that H_2O_2 was not completely necessary for DNA cleavage, while ascorbic acid was required. Overall, there remains a greater amount of super-coiled (SC) DNA than the

amount of linear DNA formed, suggesting that ROS generation is not appreciable. This assay thus suggests that the generation of ROS, *via* a Fenton-like process, is not a valid mechanism of activity for the 2-ferrocenyl hybrid compounds.

3.2.5 *In vitro* antimycobacterial activity

Within the context of repurposing and repositioning known drugs and scaffolds,[42] the 2-phenyl, 2-ferrocenyl and 2-pyridyl aminoquinoline-benzimidazole hybrid compounds were also screened for their *in vitro* antimycobacterial activity against the H37Rv strain of *Mycobacterium tuberculosis*. The minimum inhibitory concentration (MIC) values were determined using the broth micro dilution method.[11] Rifampicin was used as a positive control, and the 7-day MIC_{90} values are summarised in Table 3.8.

Table 3.8 Antimycobacterial activity of compounds **4a – 4e**, **5a – 5e**, **6a – 6c** and rifampicin.

Compound	Visual MIC_{90} (µM) [media: 7H9 GLU ADC]	Alamar blue assay: Calculated MIC_{90} (µM) [media: 7H9 GLU ADC]	Visual MIC_{90} (µM) [media: 7H9 GLU CAS]	Alamar blue assay: Calculated MIC_{90} (µM) [media: 7H9 GLU CAS]
4a	125	38.8	62.5	50.6
4b	125	>62.5	31.2	32.7
4c	62.5	89.1	15.6	15.8
4d	>125	>62.5	125	>125
4e	>125	>62.5	62.5	>125
5a	62.5	60.1	31.2	31.3
5b	31.2	29.7	15.6	28.7
5c	62.5	64.2	15.6	10.8
5d	>125	>125	125	>125
5e	>125	>125	31.2	>62.5
6a	-	>125	-	>125
6b	-	>125	-	>125
6c	-	>125	-	>125
Rifampicin	0.018	0.0156	0.018	0.0217

Compounds were screened in two different growth media, glucose-based Middlebrook 7H9-ADC (albumin-dextrose complex) and 7H9-CAS (casitone). Selected hybrids were moderately active against *M. tuberculosis*, generally exhibiting better activity in the 7H9-CAS medium. The calculated MIC_{90} values determined in 7H9-CAS media are graphically depicted in Figure 3.14. The pyridyl hybrids **6a** – **6c** were all inactive at the concentration tested. Compounds **4a** – **4c** and **5a** – **5c** showed moderate antimycobacterial activity (10.8 – 50.6 μM), while compounds **4d** – **4e** and **5d** – **5e** were inactive at the tested concentration. Considering only the phenyl and ferrocenyl hybrids, the more active hybrids (**4b** – **4c** and **5b** – **5c**) have the more hydrophobic X substituents (CH_3 or CF_3), while the inactive hybrids (**4d** – **4e** and **5d** – **5e**) have the less hydrophobic X substituents (SO_2CH_3 or CN). This suggests a link between hydrophobicity of the hybrid and its antimycobacterial activity.

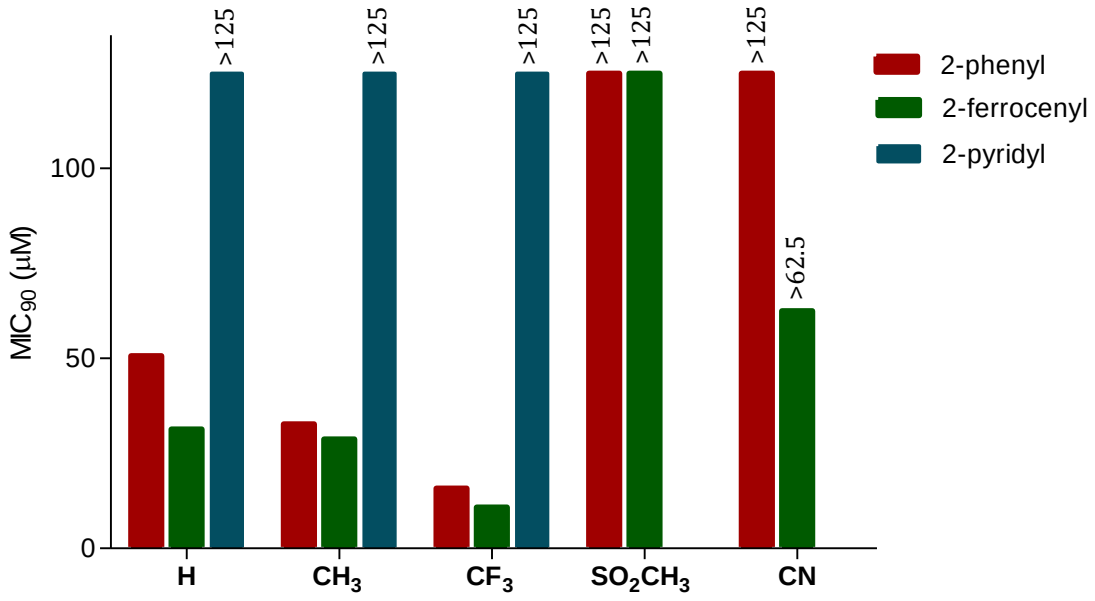

Figure 3.14 MIC_{90} values of compounds **4a** – **4e**, **5a** – **5e** and **6a** – **6c** against the H37Rv strain of *M. tuberculosis*.

It is noteworthy that there is a correlation between the MIC_{90} values of compounds **4a** – **4c** and **5a** – **5c**, and their lipophilicity, determined using logP values (Table 3.2). The graphs in Figure 3.15 depict the relationship between the logP and MIC_{90} values for the active hybrids. As the logP value of the compound increases, its MIC_{90} value decreases, indicating that antimycobacterial activity increases with increasing lipophilicity. This finding is supported, as recent literature has reported a positive correlation between

antimycobacterial activity and lipophilicity.[43, 44] Some studies have also indicated that selected lipophilic drugs had favourable activity against dormant and replicating *M. tuberculosis* compared to selected hydrophilic drugs.[45] The inactivity of the pyridyl hybrids **6a – 6c** against the H37Rv strain may be the result of their relatively lower lipophilicity (logP), compared to their corresponding phenyl and ferrocenyl analogues.

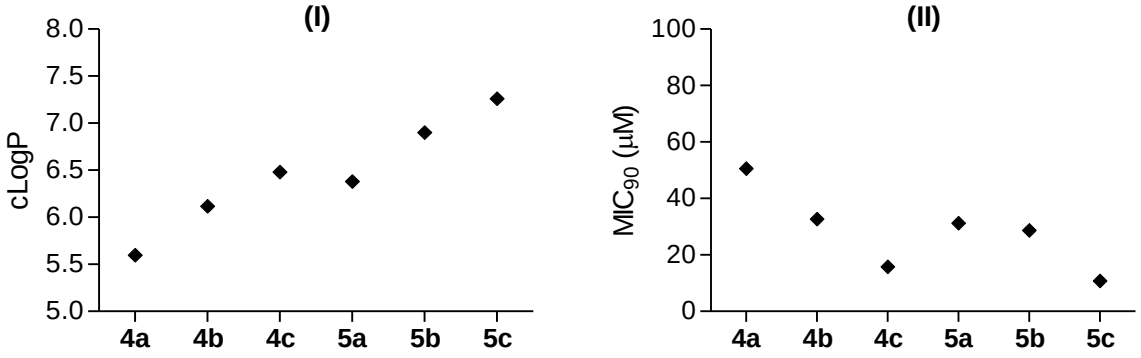

Figure 3.15 (**I**) Increase in clogP values; (**II**) Decrease in MIC_{90} values.

Furthermore, for the active hybrids (**4a – 4c** and **5a – 5c**), introduction of the organometallic ferrocenyl moiety (**5a – 5c**) resulted in an overall enhancement in the activity compared to the corresponding phenyl-derived analogues (**4a – 4c**). This trend, once again, may be related to lipophilicity. The ferrocenyl moiety contributes greater lipophilicity to the hybrid than the phenyl moiety, leading to overall higher logP values and resulting in lower MIC_{90} values (enhanced activity). These aminoquinoline-benzimidazole hybrids were, however, significantly less active than the positive control, the clinically-available drug rifampicin (0.0217 μM).

Evaluation of individual components

In a similar way to the individual component antiplasmodium study, the antimycobacterial activity of the aminoquinoline **B1** and the benzimidazole **B2** was evaluated and compared to that of the corresponding unsubstituted phenyl hybrid **4a**. The components, **B1** and **B2**, were screened against the H37Rv strain of *M. tuberculosis*. The MIC_{90} values obtained are represented graphically in Figure 3.16.

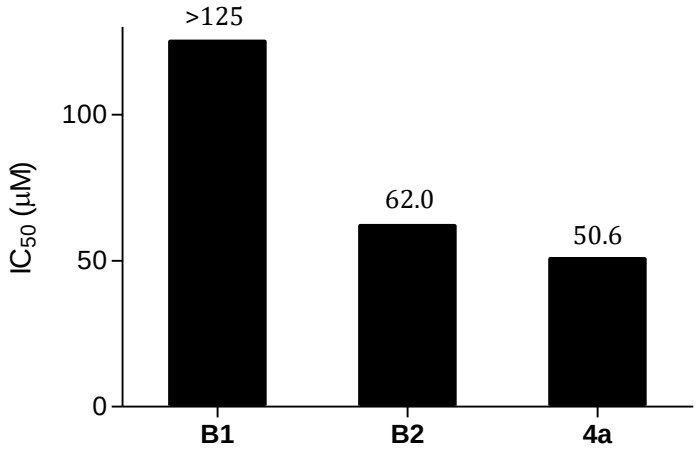

Figure 3.16 MIC_{90} values of hybrid **4a** and components **B1** and **B2**, against the H37Rv strain of *M. tuberculosis*.

Interestingly, the results of the antimycobacterial screening are contrary to the results observed in the antiplasmodium assay. The aminoquinoline **B1** was inactive at the tested concentration (MIC_{90} > 125 μM), while the benzimidazole **B2** had moderate micromolar activity (MIC_{90} = 62.0 μM). This vast difference in activity indicates that with regard to antimycobacterial activity, the benzimidazole moiety confers greater activity than the aminoquinoline moiety, and may suggest a greater contribution towards activity in the hybrid. However, hybrid **4a** outperformed both components **B1** and **B2**, with a lower MIC_{90} value of 50.6 μM. This suggests that the enhanced activity is the result of the combination of the two pharmacophores, rather than it being attributed to the influence of the individual moieties.

3.3 Summary

The 2-phenyl, 2-ferrocenyl and 2-pyridyl aminoquinoline-benzimidazole hybrids (**4a** – **4e**, **5a** – **5e** and **6a** – **6c**) were evaluated *in vitro* as potential antiparasitic agents against the chloroquine-sensitive NF54 strain and multidrug-resistant K1 strain of *Plasmodium falciparum*. In the sensitive strain, all compounds displayed good activity in the low micromolar and sub-micromolar range. In the resistant strain, the phenyl and ferrocenyl hybrids (**4a** – **4e** and **5a** – **5e**) were potent, with mostly sub-micromolar IC_{50} values and resistance indices less than one (RI < 1). The pyridyl hybrids (**6a** and **6c**) were inactive against K1 parasites at the test concentration. Compounds **4c** (phenyl-CF_3), **5b** (ferrocenyl-CH_3) and **6c** (pyridyl-CF_3) were the most active hybrids across the three series.

The *in vitro* antiplasmodium activity of the individual aminoquinoline and benzimidazole components (**B1** and **B2**) and an equimolar physical mixture (**B1+B2**) was also evaluated. The aminoquinoline **B1** displayed potent sub-micromolar activity against the CQS NF54 strain, while the benzimidazole **B2** was inactive. Against MDR K1 parasites, compound **B1** displayed decreased activity, while compound **B2** remained inactive. The hybrid **4a** was more active than either component in the resistant K1 strain. In the NF54 strain, the mixture **B1+B2** was significantly more potent than hybrid **4a**. An isobologram analysis of compounds **B1** and **B2** revealed an additive relationship between **B1** and **B2** at higher concentrations of **B1** and lower concentrations of **B2**. Conversely, an antagonistic relationship was observed at higher concentrations of **B2** and lower concentrations of **B1**.

Selected compounds were screened for their *in vitro* cytotoxicity against the Chinese hamster ovarian cell line (CHO) cell line. Some of the hybrids (**4a** and **4c** – **4e**) displayed low cytotoxicity, while others (**4b** and **5a** – **5e**) were inactive against the non-tumorigenic cell line at the concentration tested. All of the tested hybrids showed selectivity towards *Plasmodium* parasites, compared to the CHO cells.

The most active phenyl and ferrocenyl hybrids (**4c** and **5b**) were screened for their *in vivo* efficacy in mice infected with *Plasmodium berghei*. Dosed at a concentration of 4 × 50 mg/kg, the ferrocenyl hybrid **5b** was a significantly more potent inhibitor of

parasitemia than the phenyl hybrid **4c**. Despite this, the mean survival time of mice dosed with either compound was the same (7 days).

Mechanistic studies were performed on selected hybrids in order to elucidate possible contributing mechanisms of antiplasmodium action. The most active compounds (**4c**, **5b** and **6c**) were evaluated for their ability to inhibit β-haematin formation. Compounds **4c**, **5b** and **6c** were found to be moderate or potent inhibitors, with IC_{50} values lower than that of CQ. Compound **5b** was subjected to a cellular haem fractionation assay to validate the β-haematin inhibition assay result in the parasite. Treatment of NF54 parasites resulted in a dose-dependent increase in free haem, decrease in haemozoin, and increase in haemoglobin, confirming compound **5b** as a true haemozoin inhibitor. A preliminary DNA cleavage assay was performed to assess the reactive oxygen species (ROS) generating ability of compound **5b**. DNA cleavage to form linear DNA was not sufficient, indicating that ROS generation by compound **5b** was not appreciable.

All of the hybrid compounds were also evaluated as antimycobacterial agents against *Mycobacterium tuberculosis* H37Rv. The compounds with the less hydrophobic methylsulfonyl and nitrile substituents (**4d** – **4e** and **5d** – **5e**), as well as the 2-pyridyl hybrids (**6a** – **6c**) were inactive at the highest concentration tested. The inactive compounds are less lipophilic, displaying lower logP values. The more lipophilic compounds (**4a – 4c** and **5a – 5c**), with the more hydrophobic methyl and trifluoromethyl substituents, displayed moderate to good antimycobacterial activity. For these active compounds, the 2-ferrocenyl hybrids consistently displayed enhanced activity compared to their 2-phenyl analogues. Furthermore, the individual components (**B1** and **B2**) were also screened for their antimycobacterial activity. The benzimidazole **B2** was moderately active against the H37Rv strain and the aminoquinoline **B1** was inactive, while the hybrid **4a** was more active than either individual component.

3.4 References

1. R. E. Desjardins, C. Canfield, J. Haynes and J. Chulay, *Antimicrob. Agents Ch.*, 1979, **16**, 710-718.
2. D. A. Fidock, P. J. Rosenthal, S. L. Croft, R. Brun and S. Nwaka, *Nat. Rev. Drug Discov.*, 2004, **3**, 509.
3. B. S. Kalra, S. Chawla, P. Gupta and N. Valecha, *Indian J. Pharmacol.*, 2006, **38**, 5.
4. J. D. Johnson, R. A. Dennull, L. Gerena, M. Lopez-Sanchez, N. E. Roncal and N. C. Waters, *Antimicrob. Agents Ch.*, 2007, **51**, 1926-1933.
5. M. Makler, J. Ries, J. Williams, J. Bancroft, R. Piper, B. Gibbins and D. Hinrichs, *The Am. J. Trop. Med. Hyg.*, 1993, **48**, 739-741.
6. M. T. Makler and D. J. Hinrichs, *Am. J. Trop. Med.Hyg.*, 1993, **48**, 205-210.
7. R. Piper, J. Lebras, L. Wentworth, A. Hunt-Cooke, S. Houze, P. Chiodini and M. Makler, *Am. J. Trop. Med. Hyg.*, 1999, **60**, 109-118.
8. T. Mosmann, *J. Immunol. Methods*, 1983, **65**, 55-63.
9. J. Carmichael, W. G. DeGraff, A. F. Gazdar, J. D. Minna and J. B. Mitchell, *Cancer research*, 1987, **47**, 936-942.
10. P. Skehan, R. Storeng, D. Scudiero, A. Monks, J. McMahon, D. Vistica, J. T. Warren, H. Bokesch, S. Kenney and M. R. Boyd, *J. Natl. Cancer I.*, 1990, **82**, 1107-1112.
11. J. Jorgensen and J. Turnidge, in *Manual of Clinical Microbiology, Eleventh Edition*, American Society of Microbiology, 2015, 1253-1273.
12. R. Mannhold and R. F. Rekker, *Perspect. Drug Discov.* 2000, **18**, 1-18.
13. R. Ahmedi and T. Lanez. *Int. J. Pharm. Pharm. Sci.*, 2009, **1**, 182–189.
14. R. Ahmedi and T. Lanez, *Asian J. Chem.*, 2010, **22**, 299.
15. R. Ahmedi and T. Lanez, *J. Fundam. Appl. Sci.*, 2011, **3**, 183-193.
16. A. J. Leo and C. Hansch, *Perspect. Drug Discov.*, 1999, **17**, 1-25.
17. P. Perjési, K. Takács-Novák, Z. Rozmer, P. Sohár, R. Bozak and T. Allen, *Open Chem.*, 2012, **10**, 1500-1505.
18. O. Payen, S. Top, A. Vessières, E. Brulé, A. Lauzier, M.-A. Plamont, M. J. McGlinchey, H. Müller-Bunz and G. Jaouen, *J. Organomet. Chem.*, 2011, **696**, 1049-1056.
19. O. Payen, S. Top, A. Vessières, E. Brulé, M.-A. Plamont, M. J. McGlinchey, H. Müller-Bunz and G. Jaouen, *J. Med. Chem.*, 2008, **51**, 1791-1799.
20. A. Pyka, M. Babuska and M. Zachariasz, *Acta Pol Pharm*, 2006, **63**, 159-167.

21. B. Sadek, M. M. Al-Tabakha and K. M. S. Fahelelbom, *Molecules*, 2011, **16**, 9386-9396.
22. M. B. Kril and H. L. Fung, *J. Pharm. Sci.*, 1990, **79**, 440-443.
23. A. K. Debnath, R. L. L. de Compadre and C. Hansch, *Mutat. Res.*, 1992, **280**, 55-65.
24. C. Biot, G. Glorian, L. A. Maciejewski, J. S. Brocard, O. Domarle, G. Blampain, P. Millet, A. J. Georges, H. Abessolo and D. Dive, *J. Med. Chem.*, 1997, **40**, 3715-3718.
25. S. T. Loewe and H. Muischnek, *N-S Arch. Pharmacol.*, 1926, **114**, 313-326.
26. R. Dunne, *Coral reefs*, 2010, **29**, 145-152.
27. Q. L. Fivelman, I. S. Adagu and D. C. Warhurst, *Antimicrob. Agents Ch.*, 2004, **48**, 4097-4102.
28. R. Carter and C. L. Diggs, in *Parasitic protozoa*, 1977, **3**, 359-465.
29. M. Foley and L. Tilley, *Pharmacol. Therapeut.*, 1998, **79**, 55-87.
30. T. J. Egan and K. K. Ncokazi, *J. Inorg. Biochem.*, 2005, **99**, 1532-1539.
31. K. Kaur, M. Jain, R. P. Reddy and R. Jain, *Eur. J. Med. Chem.*, 2010, **45**, 3245-3264.
32. R. D. Sandlin, M. D. Carter, P. J. Lee, J. M. Auschwitz, S. E. Leed, J. D. Johnson and D. W. Wright, *Antimicrob. Agents Ch.*, 2011, **55**, 3363-3369.
33. K. K. Ncokazi and T. J. Egan, *Anal. Biochem.*, 2005, **338**, 306-319.
34. J. M. Combrinck, T. E. Mabotha, K. K. Ncokazi, M. A. Ambele, D. Taylor, P. J. Smith, H. C. Hoppe and T. J. Egan, *ACS Chem. Biol.*, 2012, **8**, 133-137.
35. J. M. Combrinck, K. Y. Fong, L. Gibhard, P. J. Smith, D. W. Wright and T. J. Egan, *Malaria J.*, 2015, **14**, 253.
36. M. Krugliak, J. Zhang and H. Ginsburg, *Mol. Biochem. Parasit.*, 2002, **119**, 249-256.
37. L. Roberts, T. J. Egan, K. A. Joiner and H. C. Hoppe, *Antimicrob. Agents Ch.*, 2008, **52**, 1840-1842.
38. N. Chavain, H. Vezin, D. Dive, N. Touati, J.-F. Paul, E. Buisine and C. Biot, *Mol. Pharm.*, 2008, **5**, 710-716.
39. F. Dubar, J. Khalife, J. Brocard, D. Dive and C. Biot, *Molecules*, 2008, **13**, 2900-2907.
40. F. Dubar, T. J. Egan, B. Pradines, D. Kuter, K. K. Ncokazi, D. Forge, J.-F. Paul, C. Pierrot, H. Kalamou and J. Khalife, *ACS Chem. Biol.*, 2011, **6**, 275-287.
41. P. F. Salas, C. Herrmann and C. Orvig, *Chem. Rev.*, 2013, **113**, 3450-3492.
42. M. A. Farha and E. D. Brown, *Nature Microbiol.*, 2019, **4**, 565-577.
43. R. C. Goldman, *Tuberculosis*, 2013, **93**, 569-588.

44. V. Makarov, B. Lechartier, M. Zhang, J. Neres, A. M. van der Sar, S. A. Raadsen, R. C. Hartkoorn, O. B. Ryabova, A. Vocat and L. A. Decosterd, *EMBO Mol. Med.*, 2014, **6**, 372-383.

45. G. Piccaro, G. Poce, M. Biava, F. Giannoni and L. Fattorini, *J. Antibiot.*, 2015, **68**, 711.

Chapter 4:

Synthesis and characterisation of neutral and cationic PGM-containing complexes of aminoquinoline-benzimidazole hybrids

4.1 Introduction

The previous use of arsenic-containing drugs in antibacterial (syphilis)[1] and antiparasitic (trypanosomiasis)[2] chemotherapy bodes well for the application of metal-based agents in the treatment of infectious diseases. On the other hand, the platinum-based anticancer drug cisplatin represents a landmark example of the use of Platinum Group Metals (PGMs) in chemotherapy.[3] As mentioned in Chapter 1 (Section 1.3.2), Sanchez-Delgado and co-workers reported some of the first organometallic PGM complexes in antiplasmodium studies, using rhodium and ruthenium metals.[4] These Rh- and Ru-chloroquine analogues presented promising results, particularly against resistant strains of the parasite[4] and this work was extended to the use of various other metals and scaffolds.[5]

More recently, strategies to incorporate organometallic PGM moieties into potential antimicrobial agents have extended to multidentate modes of coordination. Smith and co-workers have reported on the antiplasmodium activity of numerous complexes, incorporating various ligands and all six PGMs (Ru, Rh, Pd, Os, Ir and Pt).[6] Cyclometalated ruthenium(II), iridium(III) and rhodium(III)-benzimidazole complexes displaying good activity against sensitive and resistant strains of *P. falciparum* were recently reported.[7] The trifluoromethyl-substituted Ru(II) and Ir(III) analogues (Figure 4.1, **I** and **II**) proved more potent in the resistant K1 strain, displaying the lowest resistance indices (RIs) in the series (0.34 and 0.74, respectively).[7] In another study, the antiplasmodium activity of Rh(III) and Ir(III) aminoquinoline-based complexes, with *N^N* and *N^O*-coordination modes in the lateral side-chain, was presented.[8] Good sub-micromolar activity (IC_{50} < 1 μM) was observed for most complexes, with the Rh(III) *N^O* complexes

displaying superior activity. However, the Rh(III) *N^N* complex (**III**) was one of the only complexes in the series which maintained comparable activity against both the CQS NF54 and CQR Dd2 strains (RI ≈ 1), suggesting the absence of cross-resistance.[8]

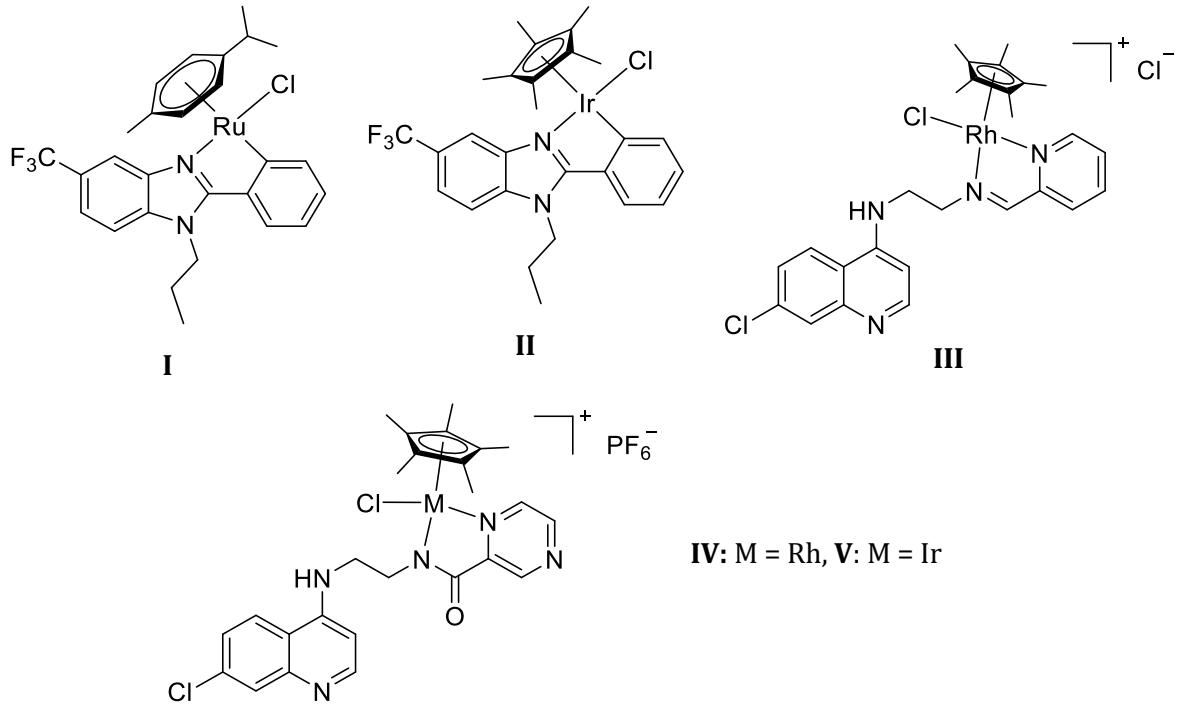

Figure 4.1 PGM-containing complexes active against *P. falciparum* and *M. tuberculosis*.

Examples of PGM-containing antimycobacterial agents in the literature are limited. Most relevant to this study, Ekengard *et al*. prepared cationic Rh(III) and Ir(III) complexes of pyrazinamide-aminoquinoline hybrids (Figure 4.1, **IV** and **V**), reporting on their antiplasmodium and antimycobacterial activity.[9] Against the CQS NF54 strain, the Rh(III) complex (**IV**) proved more active than the Ir(III) complex (**V**). In the antimycobacterial evaluation against the H37Rv strain, the two complexes showed comparable moderate micromolar activity (MIC_{99} = 20 μM), 16-fold greater than the corresponding ligand (MIC_{99} = 320 μM).[9]

With regards to metal-based hybrid agents, ferrocenyl derivatisation of organic-based hybrids has been explored, showing promising results in antiplasmodium screenings, as mentioned in Chapter 1 (Section 1.5.3). To our knowledge, reports on the preparation and antimicrobial application of half-sandwich PGM-containing hybrid compounds are limited. In this chapter, the synthesis and characterisation of iridium- and rhodium-containing aminoquinoline-benzimidazole hybrids is described.

4.2 Results and Discussion

Choice of ligands for subsequent complexation reactions

In the initial rational design of the aminoquinoline-benzimidazole hybrid ligands (Chapter 2), the substituent (X) at the 5-position of the benzimidazole scaffold was chosen from the Craig Plot in order to explore the effect of differing hydrophobic and electron- withdrawing/donating properties on the pharmacological activity. The ligands to be used in subsequent complexation reactions were chosen based on favourable antiplasmodium and antimycobacterial activity, as described in Chapter 3. On this basis, the hydrophobic methyl (**4b** and **6b**) and trifluoromethyl (**4c** and **6c**) analogues were accordingly selected to be taken further. The unsubstituted phenyl and pyridyl derivatives (**4a** and **6a**) were also included, in order to determine the effect of the electron-withdrawing or -donating 5-position substituent on the pharmacological properties relative to analogues lacking a substituent.

4.2.1 Synthesis and characterisation of neutral iridium(III) and rhodium(III) hybrid complexes

4.2.1.1 *C^N*-coordinated Ir(III) and Rh(III) pentamethylcyclopentadienyl (Cp*) complexes (7a – 7c and 8a – 8b)

Synthesis

Cyclometalated complexes were prepared by reacting selected phenyl aminoquinoline-benzimidazole hybrid ligands with various metal dimers, *via* C-H activation, as shown in Scheme 4.1. Compounds **4a** – **4c** were reacted with sodium acetate and pentamethylcyclopentadienyliridium(III) chloride dimer[10] in dichloromethane and ethanol at room temperature. This afforded the cyclometalated Ir(III) complexes (**7a** – **7c**) as dull yellow powders in moderate yields (52 – 63%). On the other hand, successful synthesis of the cyclometalated Rh(III) complexes required higher reaction temperatures, as reactions at room temperature afforded product mixtures with a low proportion of the desired product. Thus, compounds **4a** – **4b** were reacted with sodium acetate and pentamethylcyclopentadienylrhodium(III) chloride dimer[10] in dichloromethane and methanol at 65 °C. The desired cyclometalated Rh(III) complexes (**8a** – **8b**) were isolated as dull orange powders in low to moderate yields (36 – 47%).

The Ir(III) and Rh(III) complexes display good solubility in polar organic solvents, such as dichloromethane, chloroform and ethanol.

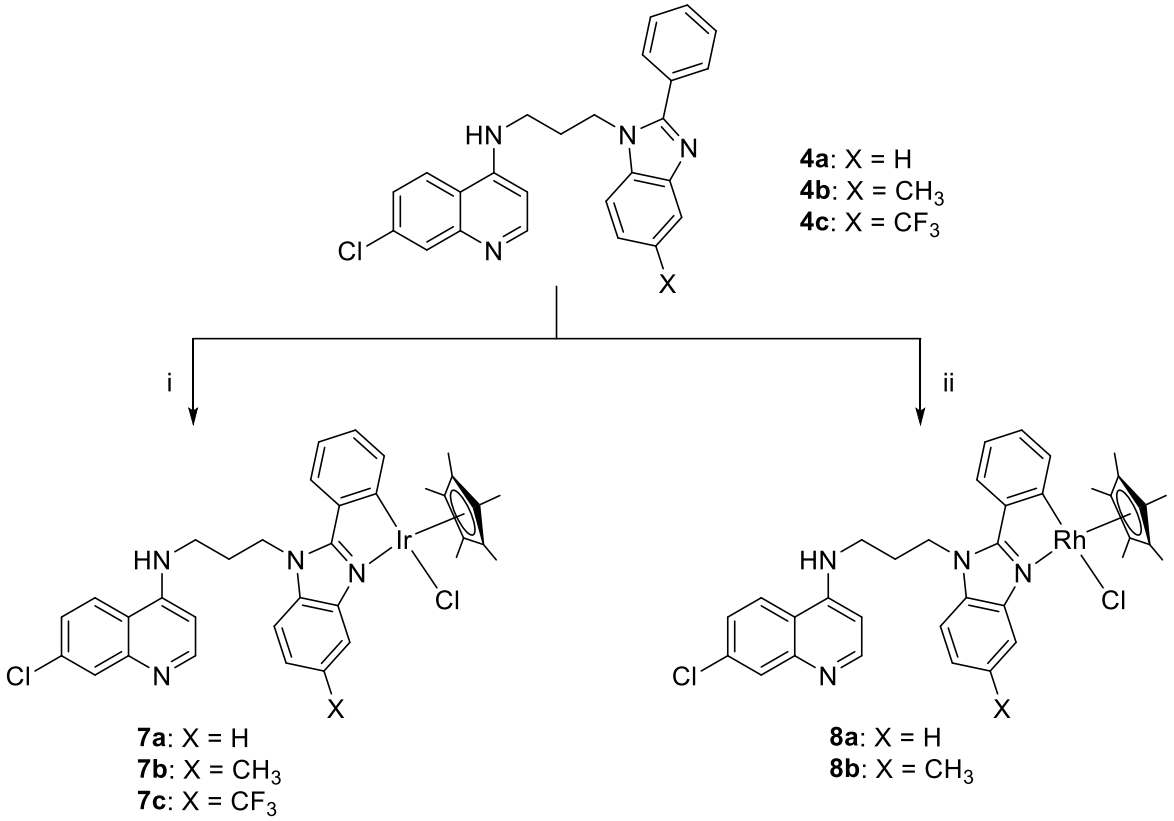

Scheme 4.1 Synthesis of cyclometalated Ir(III) and Rh(III) aminoquinoline-benzimidazole hybrid complexes. **Reagents and conditions** (i) $[Ir(Cp^*)Cl_2]_2$ / NaOAc / DCM:EtOH / 25 °C / 24 h; (ii) $[Rh(Cp^*)Cl_2]_2$ / NaOAc / DCM:MeOH / 65 °C / 96 h.

Reaction mechanism

The term *ortho*-metalation is used to describe metalations of phenyl-substituted ligands, such as the 2-phenyl hybrid ligands described in Chapter 2. The mechanism of cyclometalation *via* C-H activation has been widely studied and has been proposed for various Platinum Group Metal precursors including Pd(OAc),[11] $[(\eta^6\text{-arene})RuCl_2]_2$[12, 13] and $[(PMe_3)_3Ir(neopentyl)]$.[14] Most relevant to the study at hand, is the mechanism of the acetate-promoted cyclometalation of nitrogen donor ligands with half-sandwich Ir(III) and Rh(III) precursors. Mechanisms have been proposed by Davies and co-workers,[15, 16] as well as Jones and co-workers.[17, 18] The full mechanism is not fully understood and differs for various ligands, metal precursors and catalysts/bases. However, the respective groups of Davies and Jones have conducted experimental, theoretical and kinetic studies,

and have identified key steps and intermediates in the process.[15-18] Based on these studies, the proposed mechanism for the cyclometalation of the aminoquinoline-benzimidazole hybrids (**4a** – **4c**) is illustrated in Figure 4.2.

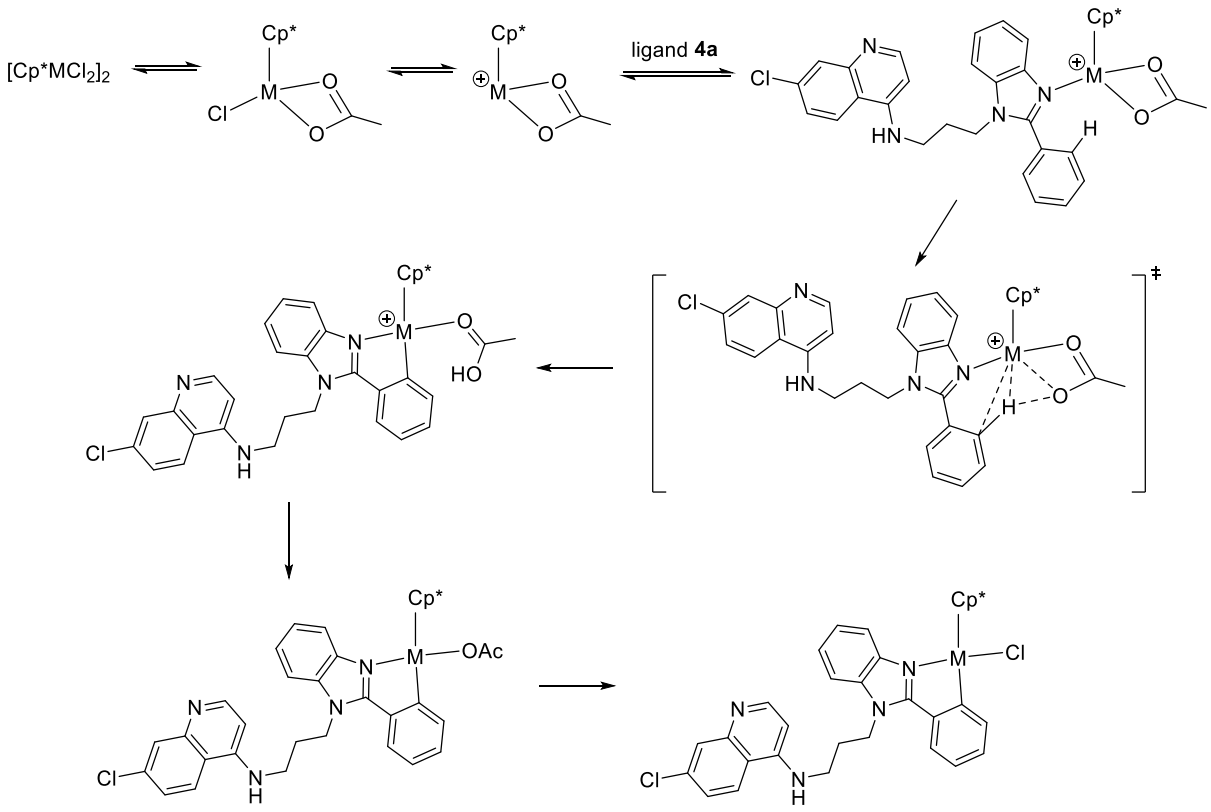

Figure 4.2 Proposed cyclometalation mechanism for the formation of complex **7a**.

It is widely accepted that the initial step is loss of a chloride anion and coordination of a bidentate acetate ligand, where it has a key role as an intramolecular base.[11] The remaining chloride anion then dissociates and the nitrogen-donor ligand coordinates to generate a positively charged iridium species, from which electrophilic C-H activation can occur.[15, 16] The mechanism then proceeds *via* a single, low-energy six-coordinate transition state, corresponding to displacement of an acetate oxygen atom by the incoming ortho C-H bond of the phenyl group (concerted metalation-deprotonation with assistance from the acetate group), leading to a C-H activated product.[16] This proposed transition state is similar to that calculated for acetate-assisted C-H activation of imines and amines using Ir(III), Rh(III) and Pd(II) precursors. The acetate-coordinated complex product is then formed, regenerating a neutral complex, followed by rapid conversion to the chloride product.

As mentioned previously, the cyclometalation reactions using $[Rh(Cp^*)Cl_2]_2$ proved challenging. Under the same mild reaction conditions as that for $[Ir(Cp^*)Cl_2]_2$, the reactions with $[Rh(Cp^*)Cl_2]_2$ were sluggish, only forming a small amount of the desired cyclometalated product. Using altered reaction conditions with elevated temperatures resulted in the formation of the desired product in low to moderate yields. There is literature precedent for the decreased reactivity of Rh(III) precursors toward C-H activation reactions compared to Ir(III) precursors. This trend has been noted for benzoate complexes,[19] as well as phenyl-imine and phenylpyridine complexes.[18] It is unclear whether or not this can be attributed to the differing electrophilicity of Ir(III) versus Rh(III). Furthermore, the electronic nature of the phenyl ring substituents also dictates the rate at which cyclometalation occurs. It has been shown that ligands with electron-donating substituents react faster than ligands with electron-withdrawing substituents, which is consistent with the proposed electrophilic mechanism of C-H activation.[17, 18] It should be noted that the trifluoromethyl-substituted Rh(III) complex could not be isolated with the desired purity. Reactions using various conditions resulted in very poor conversion to the desired product, and isolation of the pure complex separate from starting materials and side products was not achieved. This could be attributed to the decreased reactivity of the Rh(III) precursor as well as the presence of the electron-withdrawing CF_3 substituent, which decreases the reactivity of the *ortho*-position of the phenyl group.

Characterisation

The neutral cyclometalated iridium(III) and rhodium(III) complexes (**7a** – **7c** and **8a** – **8b**) were fully characterised using NMR (^{1}H, ^{13}C{^{1}H}, COSY and HSQC) and IR spectroscopy, and high-resolution ESI mass spectrometry.

NMR spectroscopy

The ^{1}H NMR spectra of compounds **7a** – **7c** and **8a** – **8b** all show similar trends. The spectrum of compound **7a**, recorded at 60 °C in DMSO-d_6, is shown in Figure 4.3. The protons of the quinoline moiety give rise to five characteristic signals at 8.40, 8.35, 7.80, 7.45 and 6.42 ppm, respectively. The protons of the benzimidazole moiety appear as a doublet (7.83 ppm) and a multiplet (7.57 – 7.49 ppm), which overlaps with the quinoline amine proton (H-10) signal. In addition, the two deshielded protons of the 2-phenyl

moiety (H-22/25, adjacent to the aromatic substitutions) give rise to an overlapping multiplet at 8.00 ppm. Two distinct diagnostic triplets (7.28 and 6.98 ppm, $^{3}J_{HH}$ = 7.5 Hz) are present for H-23 and H-24 of the 2-phenyl moiety, which are indicative of the 1,2-substitution of the phenyl ring. Signals in the aromatic region of the spectrum integrate for thirteen aromatic protons (fourteen aromatic protons in ligand **4a**), confirming the loss of one aromatic proton as a result of successful cyclometalation (*via* C-H activation) at an aromatic carbon.

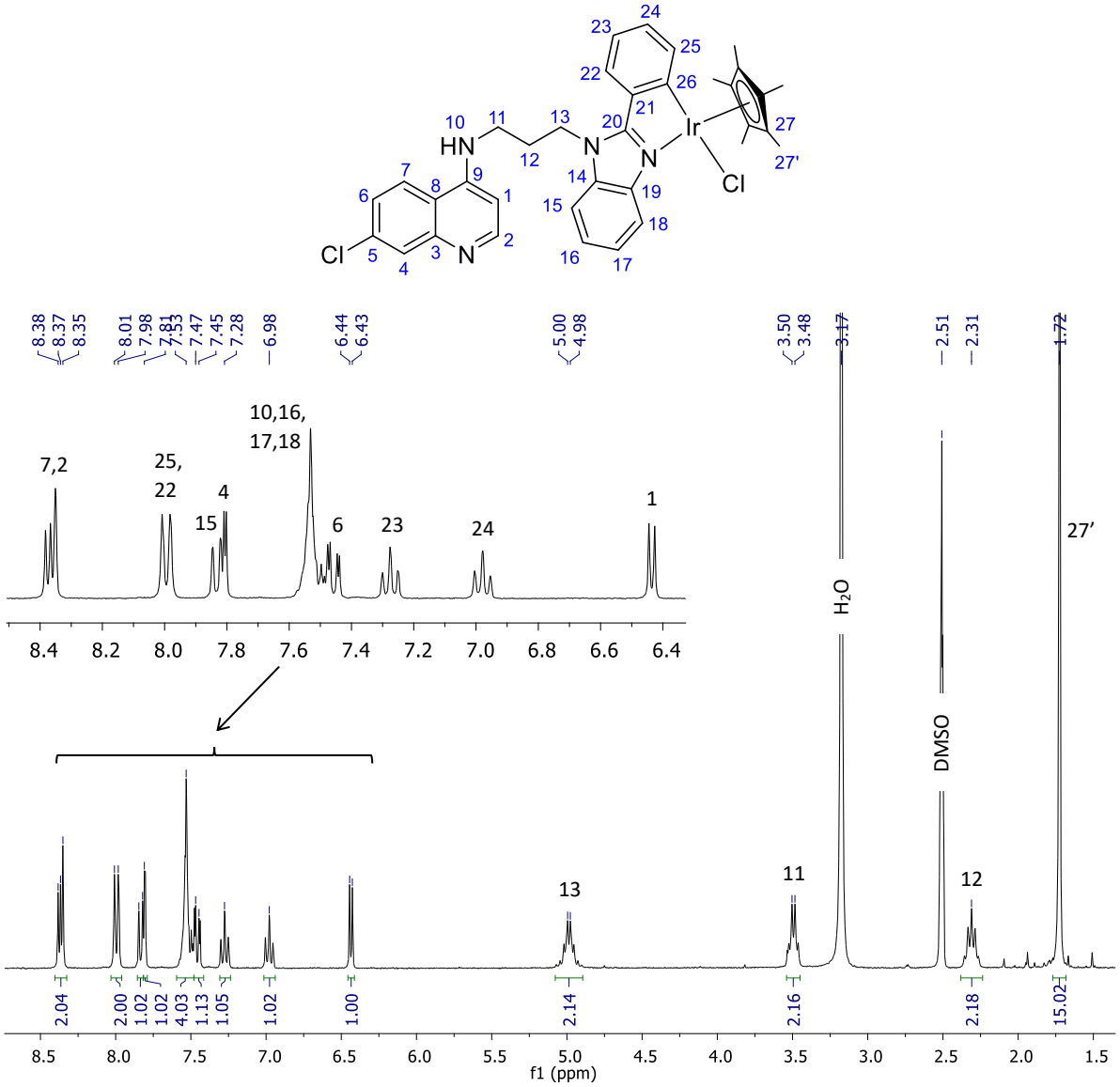

Figure 4.3 ^{1}H NMR spectrum of compound **7a** in DMSO-d_6 at 60 °C.

The methylene protons of the propyl linker appear as three signals at 4.99, 3.49 and 2.31 ppm respectively. The methylene protons (H-13) adjacent to the newly coordinated benzimidazole resonate as a multiplet (instead of a triplet) as a result of the chiral metal

centre, which renders these protons diasterotopic. The presence of an intense singlet at 1.72 ppm, corresponding to the fifteen protons of the pentamethylcyclopentadienyl (Cp*) ligand, provides further evidence of complexation.

The ^{1}H NMR spectrum of compound **8a** (M = Rh, X = H) is similar to that of compound **7a**, with signals appearing at similar chemical shifts, with similar multiplicities and coupling constants. However, the singlet corresponding to the Cp* protons is more shielded compared to that in compound **7a**, appearing at a slightly lower chemical shift (1.64 ppm), as a result of the Rh(III) metal centre being less electronegative than Ir(III). The same trend is seen in the spectra of compound **7b** and **8b**. The ^{1}H NMR spectra of compounds **7b**, **7c** and **8b** display signals for the quinoline moiety, phenyl ring and propyl linker at similar chemical shifts and with similar multiplicities and coupling constants to that of compounds **7a** and **8a**. The aromatic region displays signals integrating for twelve aromatic protons (thirteen in ligands **4b** and **4c**) as a result of the 5-position substitution (CH_3 and CF_3, respectively) on the benzimidazole moiety. The loss of an aromatic proton, compared to the respective ligands, confirms cyclometalation. The signals corresponding to the three protons of the benzimidazole moiety shift slightly upfield in the spectra of compounds **7b** and **8b**, and downfield for compound **7c**, as a result of the differing substituent electron-donating and -withdrawing effects, respectively. Additionally, the methyl groups of compounds **7b** and **8b** are observed as singlets at 2.57 and 2.55 ppm, respectively.

Conformational isomerism

Analysis of the ^{1}H NMR spectra of complexes **7a** – **7c** and **8a** – **8b** at room temperature revealed a doubling up of the amine, propyl, Cp* and selected aromatic proton signals, suggesting the presence of two structurally similar species in solution. The duplicate signals vary in intensity for the different complexes, having low intensity for compounds **7a** – **7b** and **8a** – **8b**, while appearing more intense for compound **7c** (approx. 3:2 intensity ratio). When recording the ^{1}H NMR spectra at an elevated temperature of 60 °C, these duplicate signals significantly decrease in intensity. The stacked ^{1}H NMR spectra of compound **7c** in DMSO-d_6 at room temperature and 60 °C is shown in Figure 4.4, with duplicate peaks marked.

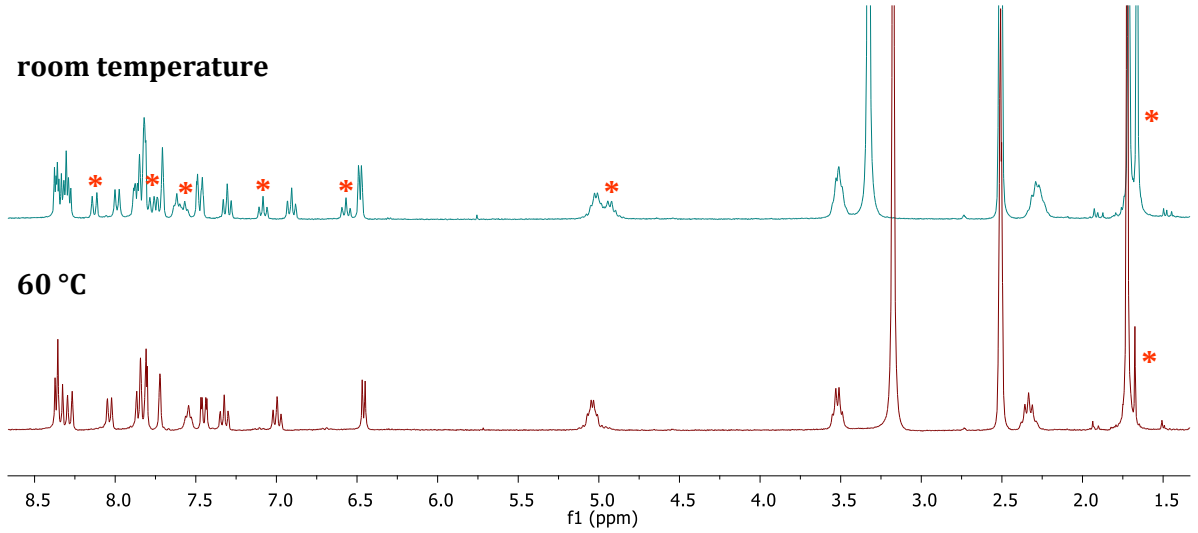

Figure 4.4 ^{1}H NMR spectra (DMSO-d_6) of compound **7c** at room temperature and 60 °C, depicting conformational isomerism.

This solution behaviour suggests the presence of stereoisomerism in the form of conformational isomers, in which isomers can interconvert by rotation about single bonds. It is speculated that two low energy conformers (rotamers) exist by rotation about the metal-Cp* bond. The energy required to overcome the rotational energy barrier in order to convert to a single lower energy, more stable conformer may be provided by the elevated temperature. In addition, a time-dependent NMR study revealed that conversion to a single set of signals, and thus one conformer, also occurs over extended periods of time in solution at room temperature.

The ^{13}C{^{1}H} NMR spectra of compounds **7a** – **7c** and **8a** – **8b** all display signals corresponding to the expected number of carbon atoms for the proposed structures. The presence of signals for the Cp* moiety confirms successful complexation. For the Ir(III) complexes **7a** – **7c**, the five methyl carbon atoms (C-27') of the Cp* moiety give rise to a single intense signal around 9.2 ppm, all experiencing the same chemical environment. Similarly, the five quaternary Cp* carbon atoms (C-27) resonate as one intense signal around 96.3 ppm. For the Rh(III) complexes **8a** and **8b**, the Cp* methyl carbon atoms give rise to a signal at 9.9 and 9.5 ppm, respectively. In contrast, the corresponding Cp* quaternary carbon atoms appear as two nearly overlapping signals at 101.9 and 102.5 ppm, respectively. The remaining aromatic carbon atoms of compounds **7a** – **7c** give rise to signals between 164.3 and 99.2 ppm, while that of compounds **8a** – **8b** appear

in the region 158.4 – 99.4 ppm. Across all spectra, the methylene carbons of the propyl linker give rise to three signals in the range 43.8 – 28.3 ppm. With regards to the 5-position substituents (X), a signal corresponding to the methyl carbon atoms of compounds **7b** and **8b** are observed around 21.9 and 21.6 ppm in either spectrum, respectively. Furthermore, the trifluoromethyl carbon atom (C-17') and CF_3-substituted aromatic carbon atom (C-17) of compound **7c** resonate as two multiplets in the region 130 – 121 ppm, with splitting resulting from ^{13}C–^{19}F coupling.

Infrared spectroscopy

The solid-state infrared spectra of compounds **7a** – **7c** and **8a** – **8b** were recorded using Attenuated Total Reflectance (ATR), and also provide evidence of metal coordination. The spectra of compounds **7a** – **7c** and **8a** – **8b** show similar absorption bands and trends. The IR spectra display a secondary amine ν(N-H) absorption band around 3200 cm^{-1}, as well as an aromatic ν(C=C) band around 1580 – 1584 cm^{-1}. In addition, the trifluoromethyl ν(C–F) stretch is observed at 1327 cm^{-1} in the IR spectrum of compound **7c**. The stacked spectra of ligand **4c** and corresponding cyclometalated iridium complex **7c** are shown in Figure 4.5.

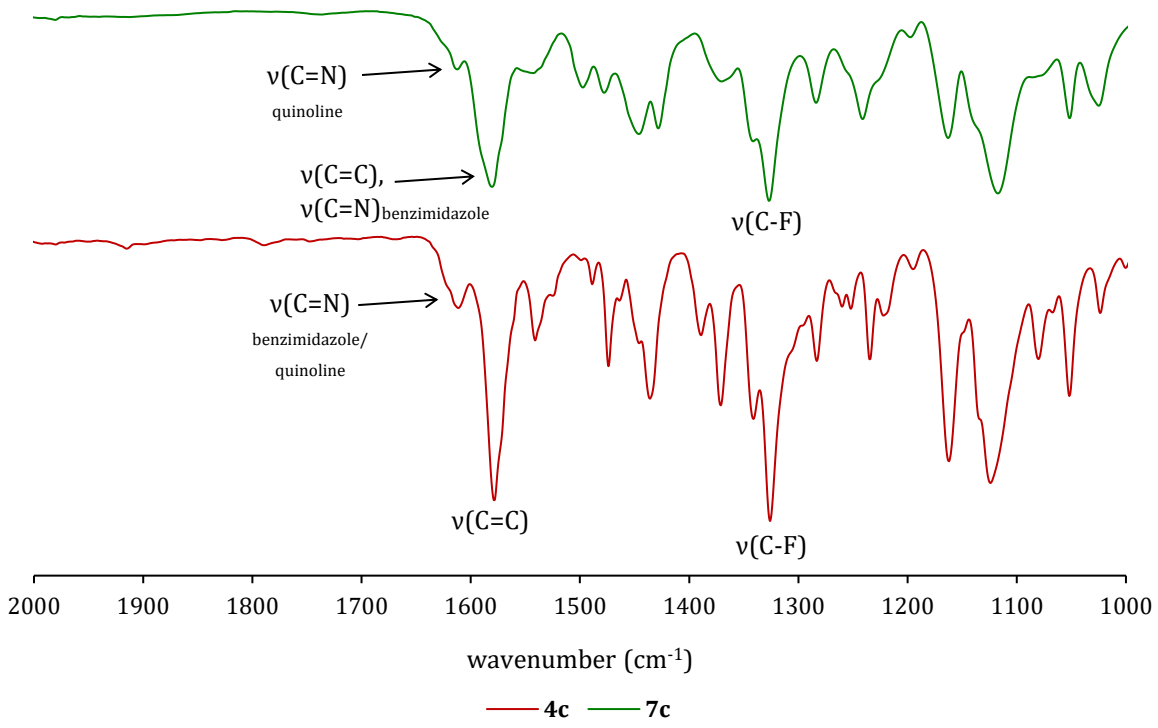

Figure 4.5 Stacked IR spectra of ligand **4c** and complex **7c**.

The region between 1620 and 1575 cm^{-1} in the spectra of the cyclometalated complexes differ from that of the respective ligands as a result of bidentate chelation. In ligands **4a** – **4c**, a ν(C=N) band around 1609 – 1611 cm^{-1} corresponds to both the quinoline and benzimidazole C=N bond. In complexes **7a** – **7c** and **8a** – **8b**, the ν(C=N) absorption band around 1609 – 1611 cm^{-1} has decreased in intensity and now only corresponds to the quinoline C=N bond. Upon coordination of the metal centre, the benzimidazole ν(C=N) absorption band shifts to a lower wavenumber, overlapping with the ν(C=C) band and resulting in a significantly broadened band around 1580 – 1584 cm^{-1}, which is seen in Figure 4.5. In some cases, the overlapping ν(C=N) and ν(C=C) band is so broad that the reduced intensity quinoline ν(C=N) band appears as only a shoulder.

The shift of the benzimidazole ν(C=N) absorption band to lower wavenumbers (1611 to 1584 cm^{-1}) is expected and results from a synergistic bonding interaction, which strengthens/shortens the metal-nitrogen bond and weakens/lengthens the C=N bond. The nitrogen of the imine bond is a sigma (σ)-donor and pi (π)-acceptor ligand. The metal–nitrogen bond involves σ-donation of electrons from nitrogen molecular orbitals to vacant orbitals of the metal, and π back-donation from filled metal d-orbitals to π*-orbitals of the nitrogen.[20] The weakening/lengthening of the C=N bond results in a lower infrared bond frequency compared to the ligand.

Mass spectrometry

The cyclometalated complexes were analysed by high-resolution ESI-MS to further confirm the proposed structures. The experimentally determined m/z values and corresponding calculated values are summarised in Table 4.1. All of the complexes show a similar fragmentation pattern. Compounds **7a** – **7c** and **8a** – **8b** have estimated theoretical exact molar masses of 774.1868, 788.2025, 842.1742, 684.1294 and 698.1450 g/mol, respectively.

Analysed in the positive mode, the 100% abundant base peak corresponding to the $[M\text{-}Cl+H]^{2+}$ fragment of each complex is observed at m/z 370.1120, 377.1207, 404.1064, 325.0846 and 332.0920 in the spectra of compounds **7a**, **7b**, **7c**, **8a** and **8b**, respectively. In addition, peaks corresponding to the $[M\text{-}Cl]^{+}$ fragment also appear in the spectra, with varying relative abundances (10 – 70%). Peaks at m/z 739.2164, 753.2330, 807.2064, 649.1589 and 663.1749 are observed, respectively.

Table 4.1 Experimentally determined m/z values and their corresponding calculated values for cyclometalated complexes **7a** – **7c** and **8a** – **8b**.

Compound	**Positive mode (base peak)**	
	Found m/z	**Calculated m/z**
7a	370.1120 $[M–Cl+H]^{2+}$	370.1129
7b	377.1207 $[M–Cl+H]^{2+}$	377.1207
7c	404.1064 $[M–Cl+H]^{2+}$	404.1066
8a	325.0846 $[M–Cl+H]^{2+}$	325.0842
8b	332.0920 $[M–Cl+H]^{2+}$	332.0920
	Negative mode	
	Found m/z	**Calculated m/z**
7a	773.1756 $[M–H]^{-}$	773.1795
7b	787.1949 $[M–H]^{-}$	787.1952
7c	841.1702 $[M–H]^{-}$	841.1669

Furthermore, analysed in the negative mode, the spectra of compounds **7a**, **7b** and **7c** reveal peaks corresponding to the $[M–H]^{-}$ fragments at m/z 773.1756, 787.1949 and 841.1702, respectively. No peaks were detected when compounds **8a** and **8b** were analysed in the negative mode. This mass spectral data further confirms the structures of the desired cyclometalated complexes.

4.2.1.2 *N*-coordinated Ir(III) and Rh(III) pentamethylcyclopentadienyl (Cp*) complexes (9a – 9c and 10a – 10c)

Synthesis

During the process of optimisation of the cyclometalation reactions (**7a** – **7c** and **8a** – **8b**), it was found that coordination selectively occurred at the quinoline nitrogen, in a monodentate mode, when using anhydrous methanol at room temperature. This monodentate coordination occurred preferentially, even in the presence of sodium acetate as a base, as shown in Scheme 4.2.

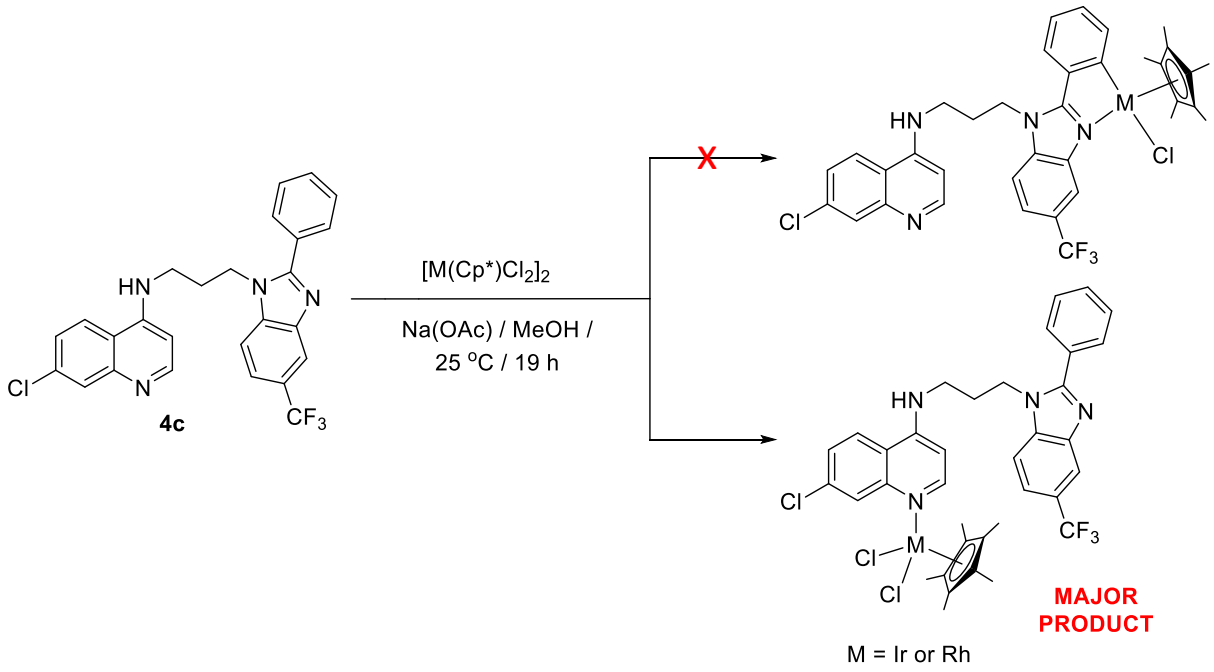

Scheme 4.2 Selective synthesis of quinoline *N*-coordinated Ir(III) and Rh(III) complexes in methanol at room temperature.

Consequently, the quinoline-coordinated Ir(III) and Rh(III) complexes (**9a** – **9c** and **10a** – **10c**) were synthesised by reaction of ligands **4a** – **4c** with the appropriate metal dimers ($[Ir(Cp^*)Cl_2]_2$ or $[Rh(Cp^*)Cl_2]_2$), in the absence of a base, as displayed in Scheme 4.3. The iridium complexes (**9a** – **9c**) were isolated as bright yellow powders in high yields (89 – 96%), while the rhodium complexes (**10a** – **10c**) were formed as bright orange powders in moderate to high yields (65 – 90%). All of the quinoline *N*-coordinated complexes had decreased solubility compared to their corresponding ligands, with limited solubility in polar organic solvents such as dichloromethane, chloroform and insolubility in methanol and ethanol.

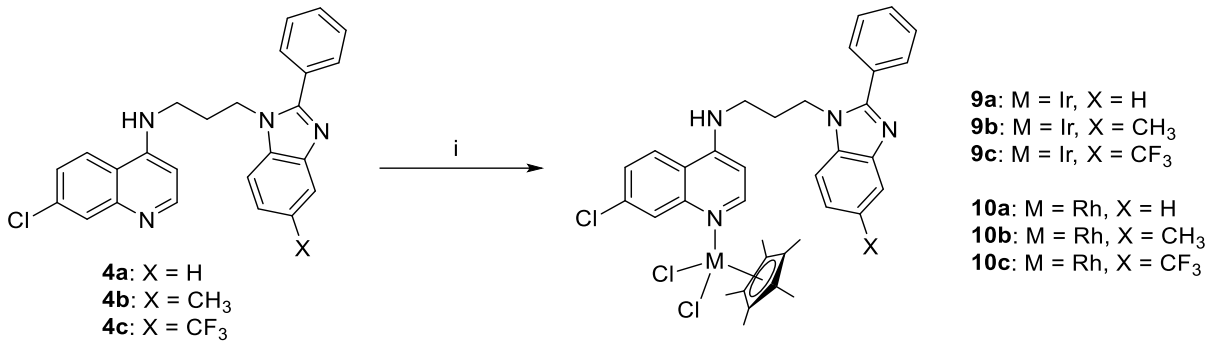

Scheme 4.3 Preparation of quinoline *N*-coordinated Ir(III) and Rh(III) complexes.
Reagents and conditions (i) $[M(Cp^*)Cl_2]_2$ / MeOH / 25 °C / 24 h.

Characterisation

The neutral quinoline *N*-coordinated iridium(III) and rhodium(III) complexes (**9a** – **9c** and **10a** – **10c**) were characterised using NMR (^{1}H and ^{13}C{^{1}H}) and IR spectroscopy and high-resolution ESI mass spectrometry.

NMR spectroscopy

The ^{1}H NMR spectra of complexes **9a** and **10a**, and the ligand **4a**, are displayed in Figure 4.6, for comparison. The spectra of the quinoline *N*-coordinated complexes **9a** and **10a** remain largely unchanged compared to the ligand **4a**, displaying a similar pattern of signals. This is expected as no covalent bonds have been affected, no protons have been displaced as seen for the cyclometalated complexes (**7a** – **7c** and **8a** – **8b**). However, the signals corresponding to the quinoline protons shift downfield compared to that of the ligand, suggesting coordination of the metal at the nitrogen atom of the quinoline moiety. The amine proton, which is *para* to the coordinated nitrogen atom, is also electronically affected as its corresponding triplet shifts significantly downfield, from 7.22 ppm (for ligand **4a**) to around 8.00 ppm. The presence of a singlet for the Cp* protons at 1.63 ppm further confirms that coordination has occurred. The ^{1}H NMR spectra of compounds **9b** – **9c** and **10b** – **10c** are similar to that of compounds **9a** and **10a**, however, only show a downfield shift in the amine proton signal. The protons of the methyl substituent of compounds **9b** and **10b** resonate at 2.44 ppm in their respective ^{1}H NMR spectra.

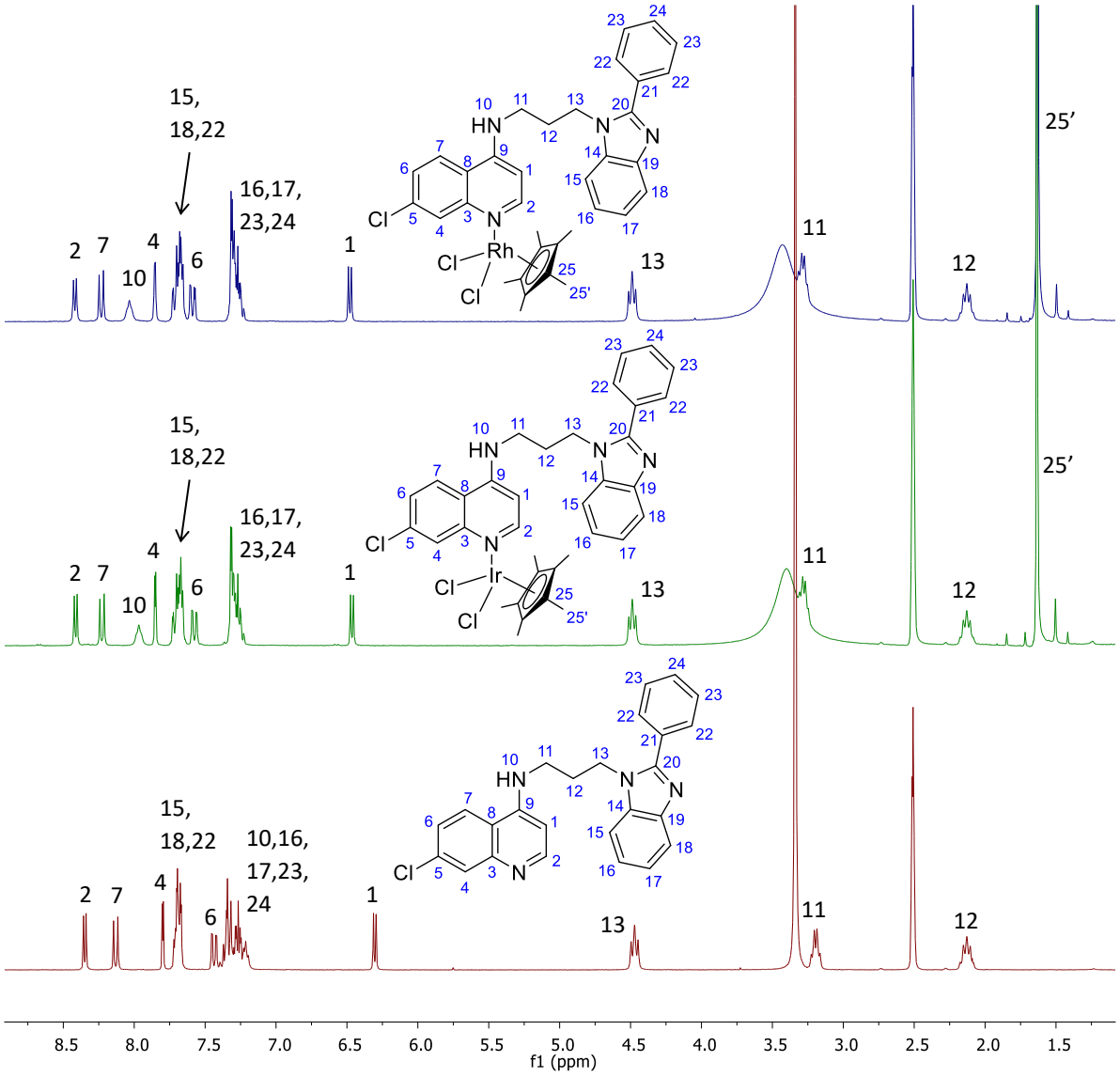

Figure 4.6 Stacked ^{1}H NMR spectra of compounds **4a**, **9a** and **10a** in DMSO-d_6.

In the $^{13}C\{^{1}H\}$ NMR spectra of compounds **9a – 9c** and **10a – 10c**, signals corresponding to the newly-introduced Cp* carbon atoms confirm successful coordination. In the spectra of the Ir(III) complexes **9a – 9c**, the five quaternary carbons atoms of the Cp* moiety give rise to an intense signal around 93.0 – 92.5 ppm. The Cp* quaternary carbon atoms of the Rh(III) complexes **10a – 10c** appear as two signals between 99.9 and 99.2 ppm. In all spectra, an intense signal in the range 9.4 – 8.6 ppm is observed for the Cp* methyl carbon atoms. The rest of the spectra remain largely unchanged compared to their respective ligands, with only slight shifts in signals in the aromatic region.

Infrared spectroscopy

Compounds **9a** – **9c** and **10a** – **10c** were analysed by solid-state IR spectroscopy using ATR and the absorption bands are summarised in Table 4.2. The effect of the monodentate coordination of the ligand can also be seen in the IR spectra. The ν(C=N) absorption band shifts to a slightly higher wavenumber compared to the respective ligands, appearing with a shoulder around 1611 to 1613 cm^{-1}. As this absorption band corresponds to the C=N bond of both the quinoline and benzimidazole entities, the slight shift in this broad band is likely due to the change in IR frequency of the $C=N_{quinoline}$ bond, while the $C=N_{benzimidazole}$ bond remains unchanged.

Interestingly, the aromatic ν(C=C) absorption band shifts to higher wavenumbers in the complexes. In the spectra of ligands **4a** – **4c**, the ν(C=C) absorption band is observed at 1578 cm^{-1}, while it appears at 1590 cm^{-1} for the Ir(III) complexes **9a** – **9c** and at 1588 cm^{-1} for the Rh(III) complexes **10a** – **10c**. This trend suggests that metal coordination *via* the quinoline nitrogen increases electron density in the quinoline ring, and thus increases the IR frequency of the aromatic C=C bonds. The trifluoromethyl substituent of compounds **9c** and **10c** give rise to a ν(C-F) absorption band at 1328 and 1327 cm^{-1}, respectively. Furthermore, the ν(N-H) stretching vibration is retained in all spectra, appearing around 3300 cm^{-1}.

Table 4.2 Infrared absorbances for compounds **9a** – **9c** and **10a** – **10c**.

Compound	ν (cm^{-1})			
	N–H	**C=N**	**C=C**	**C–F**
9a	3317	1613	1590	–
9b	3317	1611	1590	–
9c	3321	1613	1590	1328
10a	3313	1613	1588	–
10b	3306	1611	1588	–
10c	3310	1613	1588	1327

Mass spectrometry

The mass spectra of compounds **9a** – **9c** and **10a** – **10c** revealed complex fragmentation patterns when recorded in the positive mode. The exact molecular masses of compounds **9a** – **9c** and **10a** – **10c** were determined to be 810.1635, 824.1791, 878.1509, 720.1061, 734.1217 and 788.0934 g/mol, respectively. The identities of these complexes were confirmed by the presence of peaks at *m*/*z* 775.1938, 789.2087, 843.1803, 685.1360, 699.1505 and 753.1227, respectively, corresponding to $[M–Cl]^+$ fragments.

4.2.2 Synthesis and characterisation of cationic iridium(III) and rhodium(III) hybrid complexes

4.2.2.1 *N^N*-coordinated Ir(III) and Rh(III) pentamethylcyclopentadienyl (Cp*) complexes (11a – 11c and 12a – 12c)

Synthesis

Cationic *N^N*-coordinated Ir(III) and Rh(III) pentamethylcyclopentadienyl (Cp*) complexes were prepared *via* successive bridge-splitting and counter-ion exchange reactions, as shown in Scheme 4.4. In a one-pot synthesis, the 2-pyridyl aminoquinoline-benzimidazole ligands (**6a** – **6c**) were reacted with either the iridium dimer $[Ir(Cp^*)Cl_2]_2$ or rhodium dimer $[Rh(Cp^*)Cl_2]_2$ in dichloromethane and ethanol at room temperature. This was followed by counter-ion exchange using ammonium hexafluorophosphate in ethanol at 0 °C. These reactions afforded the desired cationic Ir(III) complexes (**11a** – **11c**) as yellow powders in moderate to good yields (53 – 71%), while the Rh(III) complexes (**12a** – **12c**) were isolated as orange powders in high yields (70 – 83%). These cationic Ir(III) and Rh(III) complexes display decreased solubility compared to the cyclometalated complexes (**7a** – **7c** and **8a** – **8b**). Complexes **11a** – **11c** and **12a** – **12c** are soluble in polar organic solvents such as acetone and methanol, and sparingly soluble in dichloromethane, chloroform and ethanol.

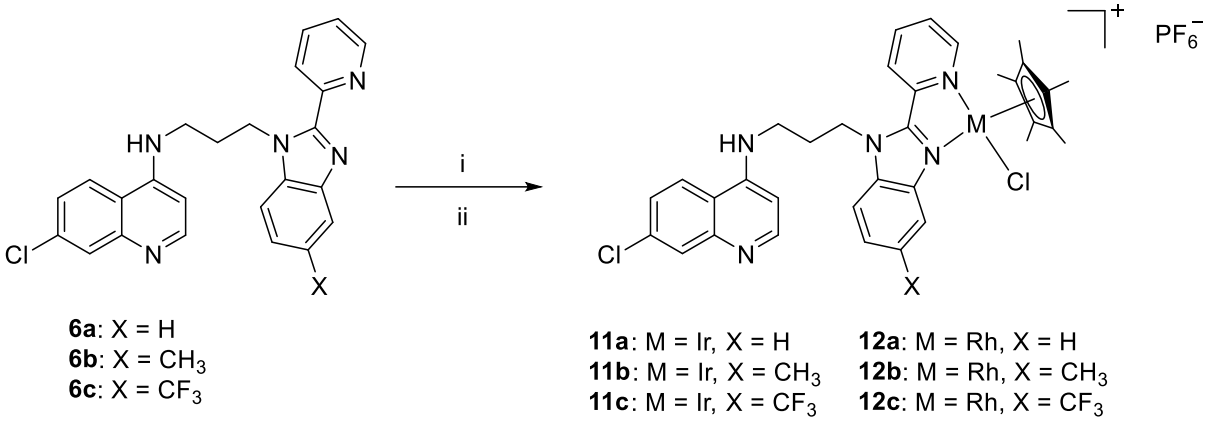

6a: X = H
6b: X = CH_3
6c: X = CF_3

11a: M = Ir, X = H
11b: M = Ir, X = CH_3
11c: M = Ir, X = CF_3

12a: M = Rh, X = H
12b: M = Rh, X = CH_3
12c: M = Rh, X = CF_3

Scheme 4.4 Preparation of cationic Ir(III)- and Rh(III)-Cp* complexes. **Reagents and conditions** (i) $[M(Cp^*)Cl_2]_2$ / DCM:EtOH / 25 °C /16 – 24 h; (ii) NH_4PF_6 / 0 °C / 2 h.

Characterisation

The cationic iridium(III) and rhodium(III)-Cp* complexes (**11a – 11c** and **12a – 12b**) were fully characterised using NMR (^1H, $^{13}C\{^1H\}$, $^{31}P\{1H\}$, COSY and HSQC) spectroscopy, IR spectroscopy, and high-resolution ESI mass spectrometry.

NMR spectroscopy

A general trend which is consistent across the ^1H NMR spectra of compounds **11a – 11c** and **12a – 12c**, is the overall downfield shift of all proton signals compared to their respective ligands (**6a – 6c**). This is expected as a result of the positive charge generated at the metal centre upon complexation, and thus provides evidence of successful chelation. The positively charged metal centre draws more electron density from the ligand, resulting in the deshielding effect seen in the NMR. The ^1H NMR spectrum of compound **11b** is displayed in Figure 4.7, and assignments are made as shown. Complexation is evidenced by the presence of a singlet (15H) at 1.69 ppm, corresponding to the protons of the Cp* moiety, which is introduced with the metal. The methylene protons of the propyl linker give rise to three signals at 5.05, 3.53 and 2.29 ppm, respectively. The multiplicity of the signals for the terminal methylene protons (H-13 and H-11) is indicative of a chiral metal centre, which brings about diastereotopicity in the propyl linker. In addition, the protons of the methyl substituent appear as a singlet at 2.57 ppm.

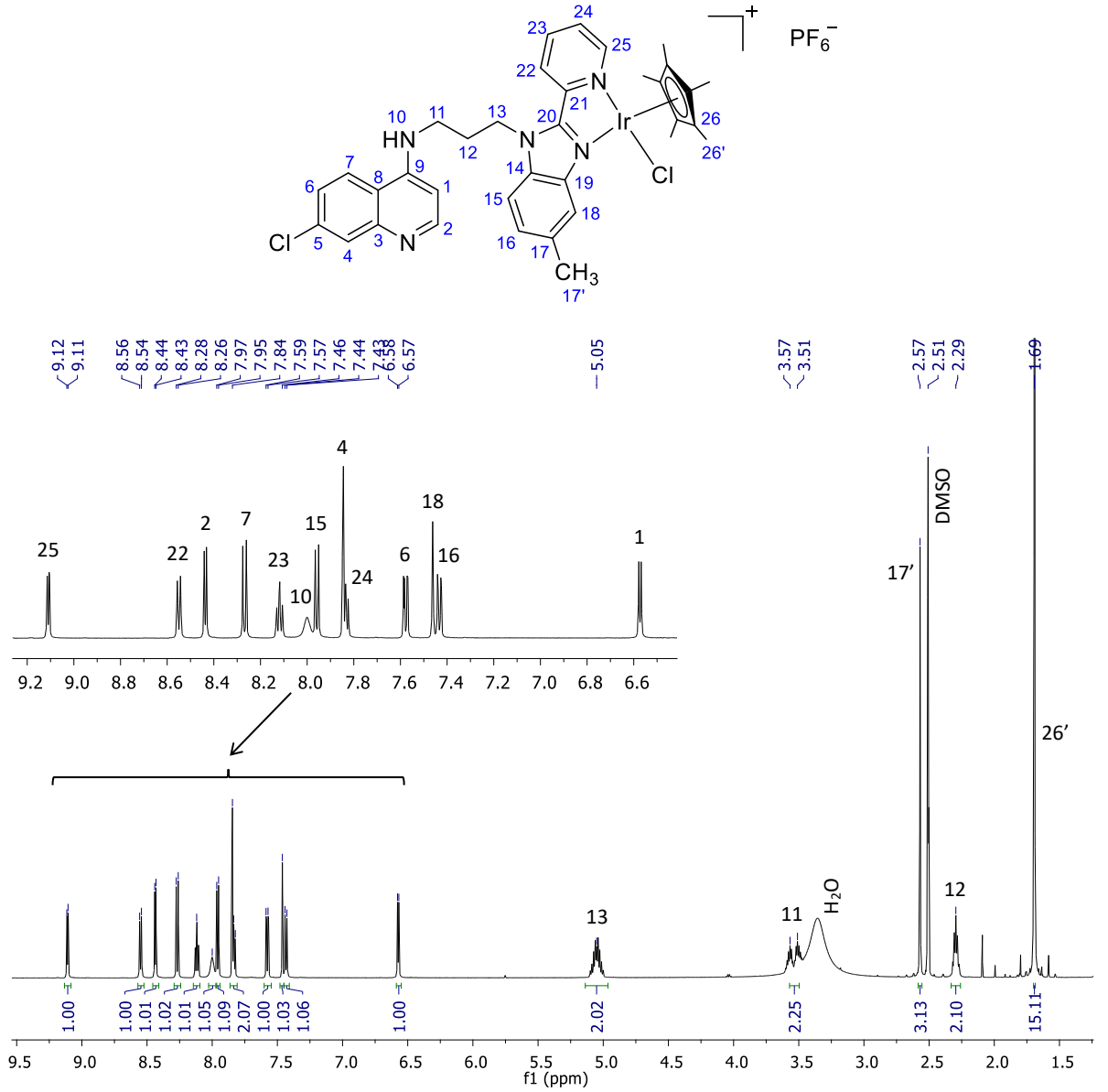

Figure 4.7 ^{1}H NMR spectrum of compound **11b** in DMSO-d_6.

The aromatic protons of the quinoline moiety give rise to five signals at 8.44, 8.27, 7.84, 7.58 and 6.57 ppm, respectively. The quinoline amine proton resonates as a broad signal at 8.00 ppm. There is minimal variation in the quinoline proton signals across the spectra of compounds **11a** – **11c** and **12a** – **12c**. The three aromatic protons of the benzimidazole moiety of compound **11b** resonate as a doublet (1H, 7.97 ppm) and an overlapping multiplet (2H, 7.46 – 7.42 ppm). In the spectra of compounds **11c** and **12c**, the electron-withdrawing nature of the trifluoromethyl substituent results in a shift of the benzimidazole proton signals downfield compared to compounds **11b** and **12b**. With the lack of a 5-position substituent, the spectra of compounds **11a** and **12a** give rise to three

signals integrating for four aromatic benzimidazole protons. The protons, H-25 and H-22, of the 1,2-substituted phenyl moiety resonate most downfield in the spectrum, at 9.11 (dd) and 8.55 ppm (d), respectively. The remaining aromatic protons, H-23 and H-24, are observed as a triplet at 8.12 and overlapping multiplet at 7.83 ppm, respectively.

The $^{13}C\{^{1}H\}$ NMR spectra of compounds **11a** – **11c** and **12a** – **12c** all display signals corresponding to the expected number of carbon atoms for the proposed structures. Complexation is confirmed by the presence of signals for the Cp* moiety. In the spectra of the Ir(III) complexes **11a** – **11c**, the five Cp* quaternary carbon atoms (C-26) give rise to one intense signal between 89.3 and 89.1 ppm, all experiencing the same chemical environment. In a similar way, the five methyl carbon atoms (C-26') of the Cp* moiety resonate as one intense signal in the range 9.4 – 9.3 ppm. On the other hand, for the Rh(III) complexes **12a** – **12c**, the five Cp* quaternary carbon atoms resonate in two different environments, giving rise to two nearly overlapping signals in the region 97.3 – 97.0 ppm. The corresponding five methyl carbon atoms of the Cp* moiety appear as one intense signal between 9.6 and 9.5 ppm, in similar way to that of compounds **11a** – **11c**.

For compounds **11a** – **11c** and **12a** – **12c**, the three methylene carbon atoms give rise to three signals in the region 44.5 – 28.0 ppm. The remaining aromatic carbon atoms resonate in the range 154.5 – 99.2 ppm for all six compounds. A signal for the carbon of the CH_3 substituent of compounds **11b** and **12b** is observed at 21.6 ppm in both spectra. In addition, the CF_3 carbon atom and CF_3-substituted aromatic carbon atom of compounds **11c** and **12c** appear as two multiplets between 128 and 121 ppm. Furthermore, the $^{31}P\{^{1}H\}$ NMR spectra of compounds **11a** – **11c** and **12a** – **12c** were recorded in order to confirm the presence of the hexafluorophosphate counter-ion. In the spectra of all complexes, a septet signal corresponding to the phosphorous atom of the PF_6^- moiety is observed at -144 ppm.

Infrared spectroscopy

Infrared spectral analysis of compounds **11a** – **11c** and **12a** – **12c**, performed using ATR, was used to further confirm successful complexation and ion exchange. A representative section of the IR spectra of complex **12b** and the ligand **6b** is displayed in Figure 4.8. The secondary amine ν(N-H) stretching frequency remains present upon coordination and is observed between 3337 and 3333 cm^{-1}. The aromatic ν(C=C) absorption band is observed in the range 1582 – 1580 cm^{-1}.

Complexation is evident by the shift in the imine ν(C=N) absorption bands. Contrary to the trend seen in the IR spectra of the neutral cyclometalated complexes (**7a** – **7c** and **8a** – **8b**), the ν(C=N) bands for the cationic complexes (**11a** – **11c** and **12a** – **12c**) shift to higher wavenumbers compared to their respective ligands. In the complexes, the benzimidazole ν(C=N) absorption band shifts to a slightly higher wavenumber, resulting in the noticeable broadening of the overlapping ν(C=N) band (1609 – 1613 cm^{-1}) for the benzimidazole and quinoline moieties. In addition, the pyridyl ν(C=N) band shifts to a significantly higher wavenumber, appearing as a shoulder in the region 1633 – 1631 cm^{-1}, compared to 1592 – 1590 cm^{-1} in the ligand.

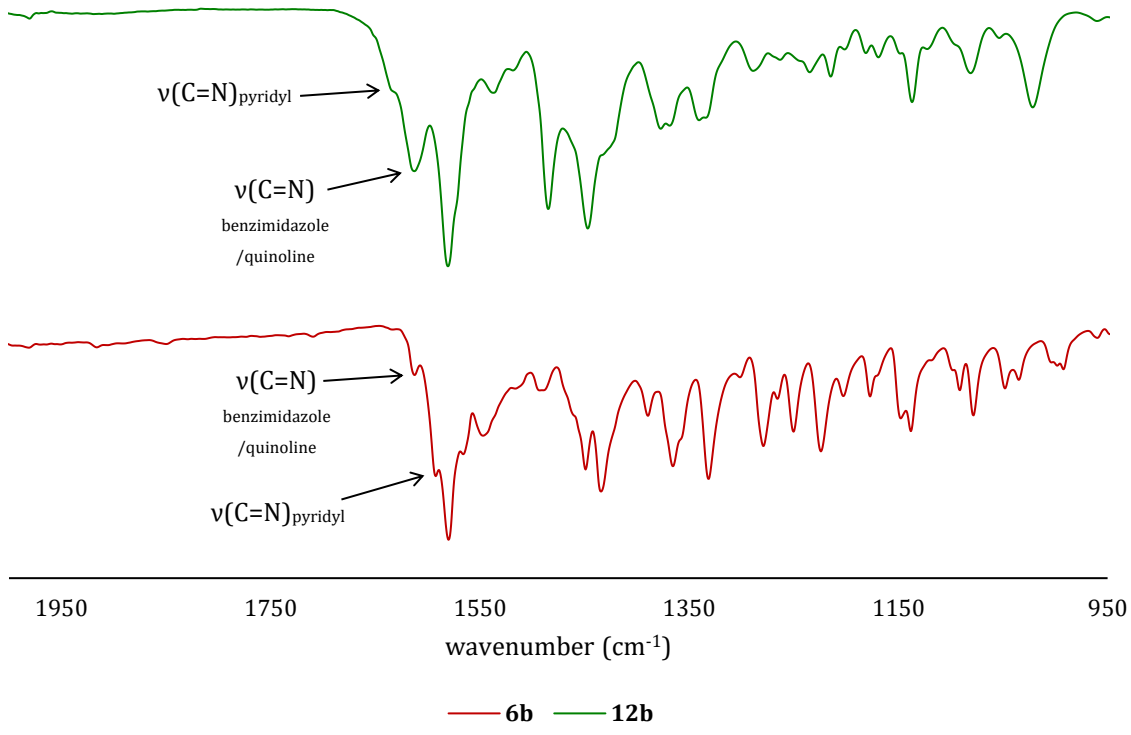

Figure 4.8 Section of the stacked IR spectra of ligand **6b** and complex **12b**.

These shifts in bond frequencies, are indicative of cationic complexes. Previous literature examples have shown the effect of the net charge of a complex on π-backbonding.[21, 22] The positive charge on the metal results in decreased electron density in the metal molecular orbitals and thus reduces the extent to which π-back-bonding can take place. Less back-bonding affords weaker and lengthened metal–nitrogen bonds and consequently, strengthening and shortening of the C=N bonds. The extent of this effect on the pyridyl C=N bond is more significant than that on the benzimidazole C=N bond.

Mass spectrometry

The structures of cationic complexes **11a – 11c** and **12a – 12c** were confirmed by ESI mass spectrometry, where M refers to the complex cation without the hexafluorophosphate counter-ion. Analysed in the positive mode, base peaks corresponding to the protonated molecular ion $[M+H]^{2+}$ fragment are observed for compounds **11a – 11c**, at m/z 388.5986, 395.6066 and 422.5920, respectively. The spectra of compounds **12a** and **12b** display base peaks for the $[M–Cl]^{2+}$ fragments at m/z 325.5818 and 332.5899, respectively. On the other, in the mass spectrum of compound **12c**, the base peak at m/z 240.0528 corresponds to the $[M–Cl+H]^{3+}$ fragment. The experimentally determined base peak values in the positive mode, as well as the calculated values are summarised in Table 4.3. In all cases, the two values are in agreement, confirming the complex structures. Presence of the hexafluorophosphate counter-ion was confirmed by mass spectral analysis in the negative mode. In the mass spectra of all complexes, a base peak corresponding to the $[PF_6]^-$ fragment is observed around m/z 144.9640, corroborating what was seen in the $^{31}P\{^1H\}$ NMR spectra.

Table 4.3 Experimentally determined base peak m/z values and corresponding calculated values for complexes **11a – 11c** and **12a – 12c**.

Compound	Base peak (100% abundant)	
	Found m/z	**Calculated m/z**
11a	388.5986 $[M+H]^{2+}$	388.5986
11b	395.6066 $[M+H]^{2+}$	395.6064
11c	422.5920 $[M+H]^{2+}$	422.5923
12a	325.5818 $[M–Cl]^{2+}$	325.5818
12b	332.5899 $[M–Cl]^{2+}$	332.5896
12c	240.0528 $[M–Cl+H]^{3+}$	240.0529

Molecular structure

Suitable crystals of compound **11b** were obtained and the molecular structure was confirmed by single-crystal X-ray diffraction. Crystals were grown by slow diffusion of hexane into a solution of compound **11b** in acetone, forming red block crystals in a monoclinic crystal system with the $P2_1/n$ space group. The molecular structure of compound **11b** is shown in Figure 4.9. There are two molecules of compound **11b** and three and a half molecules of acetone in the asymmetric unit.

The molecular structure shown in Figure 4.9 confirms the desired structure of compound **11b**, with the 2-pyridylbenzimidazole ligand coordinating in the bidentate-chelating mode, through the benzimidazole- and pyridyl-nitrogen atoms. In addition, preparation of the *N^N*-chelated Ir(III) complex results in a cationic species, which is confirmed by the presence of the hexafluorophosphate counter-ion in the molecular structure. The complex adopts a pseudo-tetrahedral geometry around the iridium metal centre, as seen in Figure 4.9. This three-dimensional shape, described as a 'piano-stool' geometry, is commonly adopted by half-sandwich complexes.

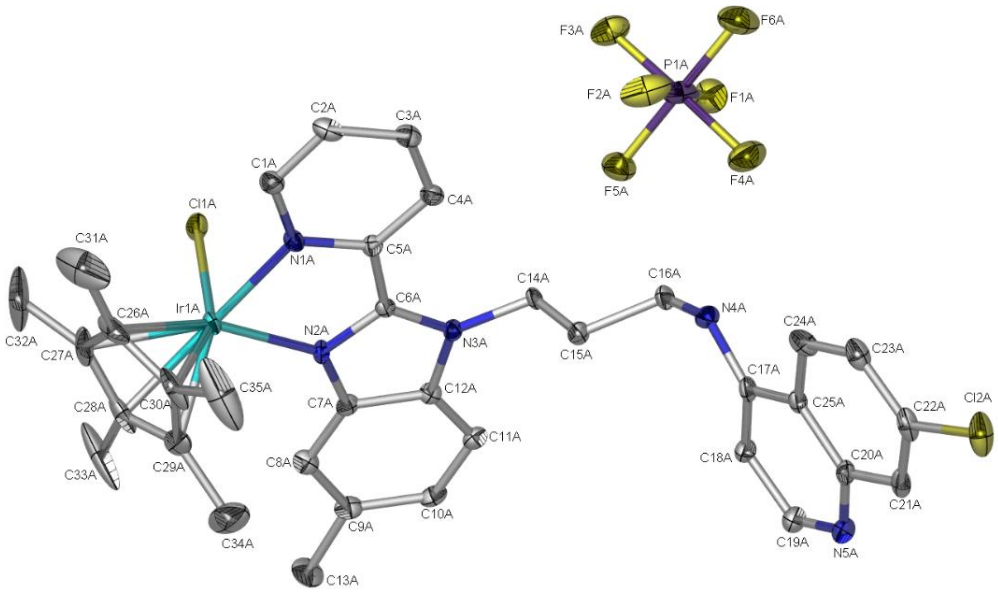

Figure 4.9 Molecular structure of compound **11b**, with ellipsoidal models drawn at the 40% probability level.

Selected bond lengths and angles are listed in Table 4.4 and crystallographic data in Table 4.5, respectively. The Ir–Cp* bond distances range between 1.339 and 1.467 Å. The Cl–Ir–N_1 and Cl–Ir–N_2 bond angles are comparable, at the near orthogonal 86.06 and 85.88°, respectively, while the N–Ir–N bond angle is 75.72°, significantly smaller than the former. These bond angles are in agreement with structurally similar *N^N*-coordinated Ir(III),[23] Rh(III)[23, 24] and Ru(II)[23-25] complexes in the literature. The Ir–Cl and Ir–N_{pyr} bond lengths are comparable, with distances of 1.594 and 1.587 Å, respectively. The Ir–N_{imine} bond length is shorter, measuring at 1.349 Å. Although the geometry and bond angles about the metal centre correlate well with analogous complexes in the literature, the metal-ligand bond lengths in the molecular structure of complex **11b** are shorter than corresponding bond lengths reported. Analogous M–$N_{imine/pyr}$ lengths are approximately 2.1 Å, while M–Cl lengths are approximately 2.4 Å in the literature.[23, 25]

Table 4.4 Selected bond lengths and angles of compound **11b**

	11b
Bond lengths (Å)	
Ir(1A) – Cl(1A)	1.594(4)
Ir(1A) – N(1A)	1.587(4)
Ir(1A) – N(2A)	1.349(6)
Ir(1A) – C(26A)	1.357(6)
Ir(1A) – C(27A)	1.392(6)
Ir(1A) – C(28A)	1.339(5)
Ir(1A) – C(29A)	1.398(6)
Ir(1A) – C(30A)	1.467(5)
Bond angles (°)	
Cl(1A) – Ir(1A) – N(1A)	86.06(12)
Cl(1A) – Ir(1A) – N(2A)	85.88(12)
N(1A) – Ir(1A) – N(2A)	75.72(14)

Table 4.5 Crystallographic data for compound **11b**

	11b
Chemical formula	$C_{35}H_{37}Cl_2IrN_5F_6P$
Formula weight	935.80
Crystal system	Monoclinic
Space group	$P2_1/n$
Crystal size (mm)	0.10 × 0.14 × 0.15
a, b, c (Å)	14.8624(11), 23.0137(18), 26.002(2)
α, β, γ (°)	90, 102.009(2), 90
V/ Å^3	8699.1(12)
Z	2
T/K	100
D_c/g.cm^{-3}	1.584
μ/mm^{-1}	3.294
Scan range/°	1.2 < θ < 27.5
Unique reflections	19922
Reflections used [I > 2σ(I)]	14511
R_{int}	0.097
R indices (all data)	R 0.0400, wR2 0.0929, S 1.01
Goodness-of-fit	1.01
Max, Min Δρ/e Å	-1.22, 1.94

4.2.2.2 *N^N*-coordinated Rh(III) 2-phenylpyridyl (ppy) complexes (13a – 13c)

Synthesis

Cationic *N^N*-coordinated Rh(III) 2-phenylpyridyl (ppy) complexes were prepared *via* successive bridge-splitting and counter-ion exchange reactions as depicted in Scheme 4.5. In a one-pot synthesis similar to that for complexes **11a** – **11c** and **12a** – **12c**, the pyridyl aminoquinoline-benzimidazole ligands (**6a** – **6c**) were reacted with dichlorotetrakis(2-(2-pyridinyl)phenyl)dirhodium(III)[26] in dichloromethane and methanol at 65 °C. This was followed by subsequent anion exchange of the chloride ion using ammonium hexafluorophosphate in dichloromethane and ethanol at room temperature. The desired cationic Rh(III) complexes (**13a** – **13c**) were isolated as either

dark orange crystals, pale-yellow or beige powders in moderate to high yields (71 – 89%). These complexes are soluble in a range of organic solvents such as dichloromethane, methanol and acetone, and are sparingly soluble in ethanol and ethyl acetate.

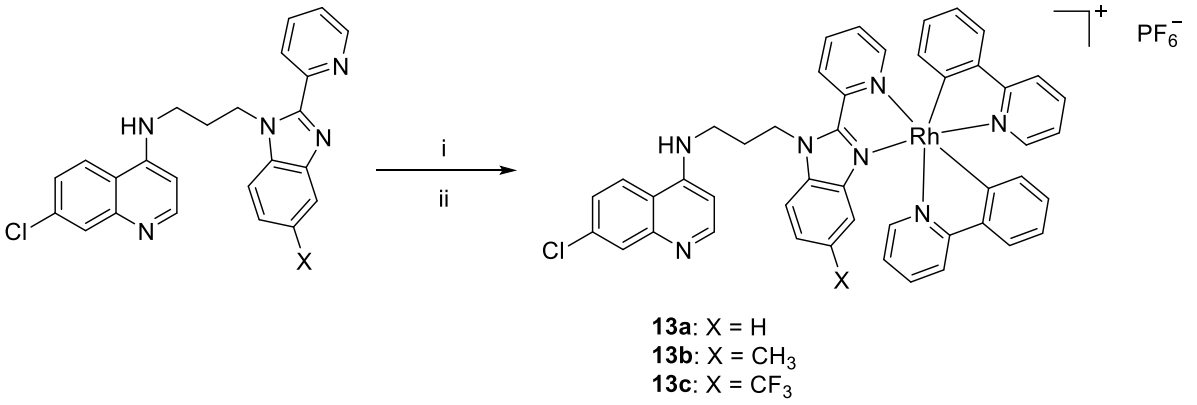

Scheme 4.5 Preparation of cationic Rh(III)-ppy complexes. **Reagents and conditions** (i) $[Rh(ppy)_2Cl]_2$ / DCM:MeOH / 65 °C / 24 h; (ii) NH_4PF_6 / 25 °C / 2 h.

Characterisation

The structures of the cationic rhodium-ppy complexes (**13a** – **13c**) were confirmed using NMR (^1H, $^{13}C\{^1H\}$, $^{31}P\{^1H\}$, COSY and HSQC) and IR spectroscopy, and high-resolution ESI mass spectrometry.

NMR spectroscopy

As seen for the previous cationic complexes (**11a** – **11c** and **12a** – **12c**, Section 4.2.2.1), in the spectra of complexes **13a** – **13c**, most signals shift downfield compared to their respective ligands. This deshielding effect results from the presence of the electron-deficient rhodium centre, which draws electron density from the ligands, and thus provides evidence of successful coordination. The ^1H NMR spectra of compounds **13a** – **13c** all display similar trends, with slight chemical shift differences in the aromatic proton signals based on the electron-withdrawing or -donating effect of the 5-position substituent (H, CH_3 or CF_3). The ^1H NMR spectrum of compound **13b** is shown in Figure 4.10, depicting the proton assignments.

The methylene protons of the propyl linker give rise to three multiplets at 5.00, 3.64 and 2.38 ppm, respectively. The increased multiplicity/splitting of the signals for H-13, H-12

and H-11 (Figure 4.10, zoomed in with the water signal suppressed) suggests diasterotopicity of these methylene protons. This effect is the result of the chirality of the coordinated metal centre, and thus confirms successful complexation of the bidentate ligand. The amine proton gives rise to a broad signal at 9.04 ppm, most downfield in the spectrum.

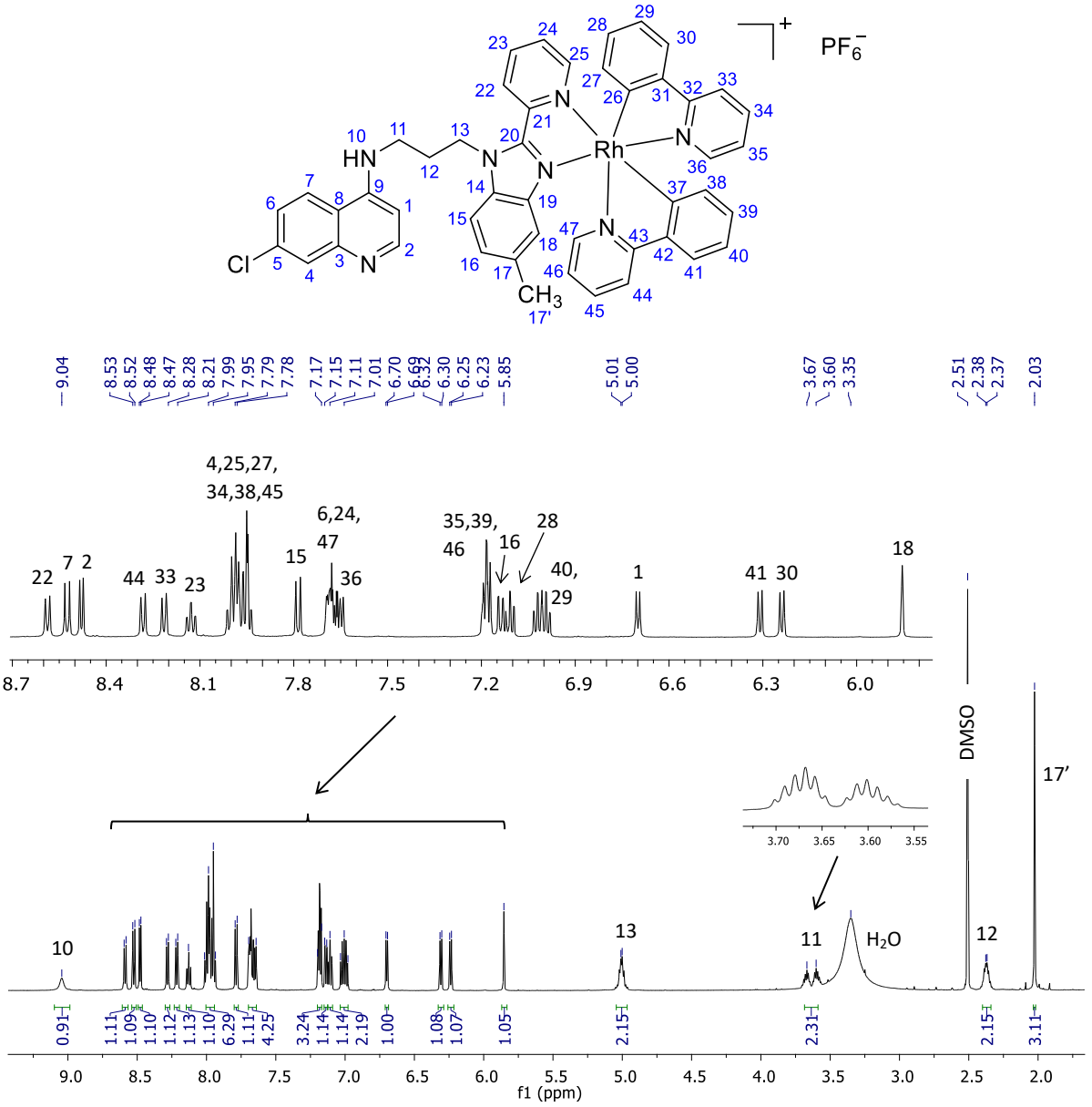

Figure 4.10 ^{1}H NMR spectrum of complex **13b** in DMSO-d_6.

Signals between 8.6 and 5.8 ppm integrate for twenty-eight aromatic protons collectively, for the quinoline, benzimidazole and phenyl moieties, as well as the two 2-phenylpyridine ligands. There is great overlap of signals in this region and proton assignments were made with the aid of 2D correlation spectroscopy (COSY). The protons of the two identical

2-phenylpyridyl ligands do not experience identical chemical environments, with each proton resonating individually in the spectrum. Corresponding proton pairs resonate close together with similar multiplicities and coupling constants. In Figure 4.10, proton pairs H-41/H-30 and H-44/H-33 provide an excellent example of this trend. Contrary to the trend of signals shifting downfield compared to that in the ligand, aromatic proton H-18 (4-position of the benzimidazole, adjacent to the methyl substituent) shifts significantly upfield upon complexation, from 7.52 ppm in ligand **6b** to 5.85 ppm in compound **13b**. Similarly, in the spectrum of compound **13c**, the aromatic proton at the 4-position of the benzimidazole shifts upfield, from 8.11 ppm in ligand **6c** to 6.44 ppm in compound **13c**. In addition, the protons of the methyl substituent of compound **13b** are observed as a singlet at 2.03 ppm, shifted upfield compared to that of the ligand (2.44 ppm).

In the $^{31}P\{^{1}H\}$ NMR spectra of compounds **13a** – **13c**, a septet is observed around -144 ppm, corresponding to the phosphorous atom of the hexafluorophosphate counter-ion. Furthermore, the $^{13}C\{^{1}H\}$ NMR spectra of compounds **13a** – **13c** were also recorded. Compared to the spectra of the respective ligands, the additional signals in the aromatic region attest to the incorporation of the two 2-phenylpyridyl ligands, confirming successful complexation. For all complexes, the forty-three aromatic carbon atoms, as well as the trifluoromethyl carbon atom of compound **13c**, resonate between 168.9 and 99.0 ppm. The methyl carbon atom of compound **13b** gives rise to a signal at 21.5 ppm. In addition, the methylene carbon atoms of the propyl linker give rise to three signals around 43.8, 40.5 and 28.3 ppm, respectively.

Infrared spectroscopy

Infrared spectral analysis of compounds **13a** – **13c** were carried out using ATR. The shifts of some absorption bands compared to the ligands, and the appearance of new bands confirms the desired structures. The absorption bands for compounds **13a** – **13c** are summarised in Table 4.6. The secondary amine ν(N-H) and aromatic ν(C=C) stretching frequencies are retained in the spectra at 3345 and 1580 – 1581 cm^{-1}, respectively. The newly-introduced 2-phenylpyridyl moieties gives rise to a sharp ν(C=N) absorption band in the region 1604 – 1606 cm^{-1}, confirming successful complexation.

Coordination of the metal is also evidenced in the shifts of the ν(C=N) absorption bands corresponding to the pyridyl and benzimidazole moieties. As mentioned for complexes **11a – 11c** and **12a – 12c** (Section 4.2.3.1, Figure 4.8), the cationic nature of the rhodium metal centre of complexes **13a – 13c** results in decreased back-donation and consequently weakened rhodium-ligand bonds and strengthened C=N bonds. The shorter C=N bond in the complex compared to the ligand is evident by the shift of the ν(C=N) bands to higher wavenumbers in the IR spectra. The pyridyl ν(C=N) band shifts from 1590 – 1592 cm^{-1} in the ligands to 1629 cm^{-1} in the complexes, while the benzimidazole ν(C=N) band only shifts slightly from 1609 – 1613 cm^{-1} in the ligands to 1615 cm^{-1} in the complexes, appearing as a shoulder. The quinoline ν(C=N) band is also retained in the spectra, overlapping with the benzimidazole and ppy ν(C=N) bands, resulting in the absorption band broadening.

Table 4.6 Infrared absorbances for compounds **13a – 13c**.

Compound	ν (cm^{-1})				
	N-H	**C=N_{pyr} (sh)[a,b]**	**C=$N_{benz/quin}$ (sh)[b,c]**	**C=N_{ppy}[d]**	**C=C**
13a	3345	1629	1615	1604	1581
13b	3345	1629	1615	1604	1580
13c	3345	1629	1615	1606	1581

[a]pyr = pyridyl, [b]sh = shoulder, [c]benz/quin = benzimidazole/quinoline, [d]ppy = 2-phenylpyridyl

Mass spectrometry

The correct structures of complexes **13a – 13c**, and the presence of the hexafluorophosphate counter-ion was confirmed using ESI mass spectrometry, where M refers to the complex cation excluding the PF_6^- counter-ion. The exact molecular masses of the cationic complexes **13a – 13c**, without the hexafluorophosphate ion, are 824.1776, 838.1932 and 892.1650 $g.mol^{-1}$, respectively. Peaks corresponding to the molecular ion $[M]^+$ fragments are observed at m/z 824.1747, 838.1908 and 892.1625 in the mass spectra, respectively. The mass spectra also reveal interesting fragmentation patterns for these complexes, with the aminoquinoline-benzimidazole ligands (**6a – 6c**) cleaving from the metal under the applied analysis conditions. Peaks corresponding to the $[Rh(ppy)_2]^+$ fragment (m/z 411.0366) and the protonated ligand $[L+H]^+$ fragment are observed in the

spectra of complexes **13a – 13c**. The mass spectrum (positive mode) of complex **13b** is displayed in Figure 4.11, showing the fragments observed.

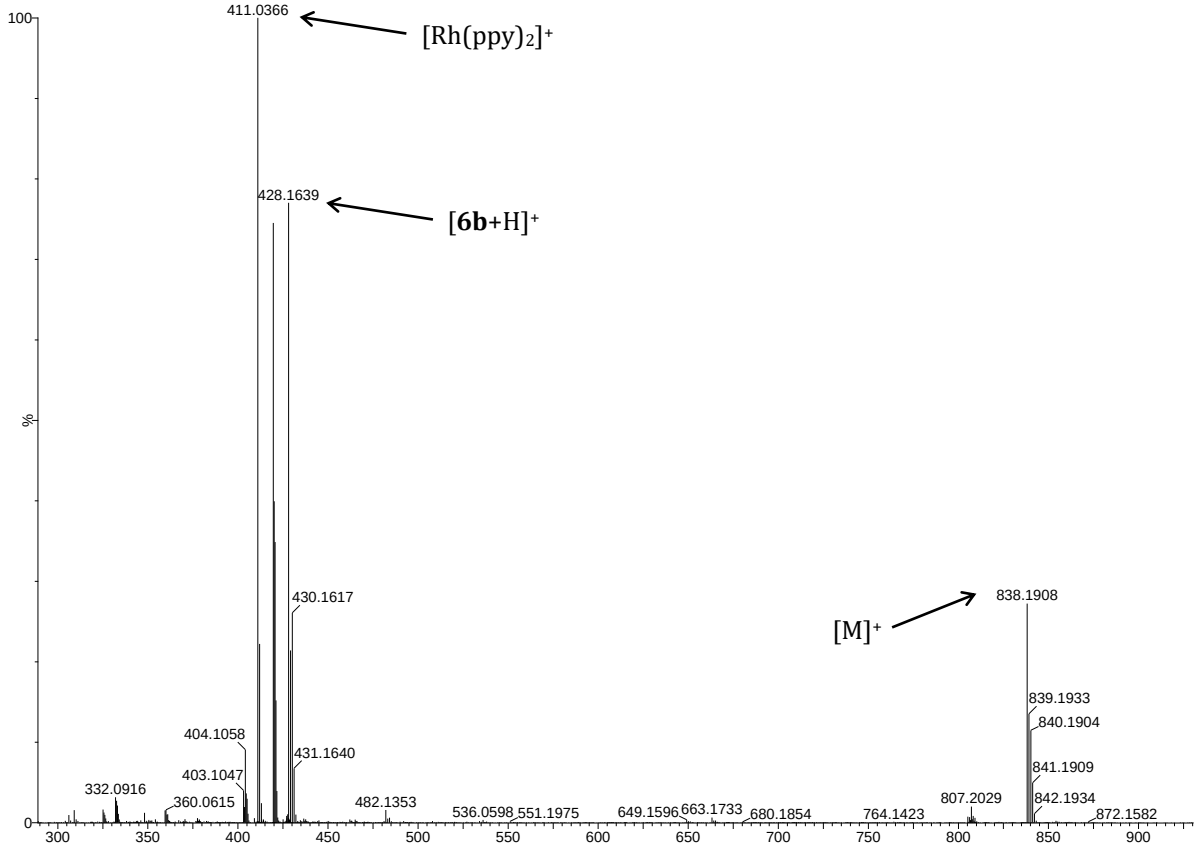

Figure 4.11 Mass spectrum (positive mode) of compound **13b**.

In addition, analysis of compounds **13a – 13c** in the negative mode confirmed the presence of the hexafluorophosphate anion. In the mass spectra of all three complexes, a base peak corresponding to the $[PF_6]^-$ fragment is observed around m/z 144, further confirming what was seen in the $^{31}P\{^1H\}$ NMR spectra.

4.3 Summary

Based on their superior antiplasmodium and antimycobacterial activities, as well as favourable resistance indices and low cytotoxicity, 2-phenyl hybrid ligands **4a** – **4c** and 2-pyridyl hybrid ligands **6a** – **6c** were selected for complexation with various Platinum Group Metal dimers. Cyclometalated (*C*^*N*-coordinated) iridium(III)- and rhodium(III) complexes **7a** – **7c** and **8a** – **8b** were prepared *via* C-H activation reactions. Two equivalents of ligands **4a** – **4c** were reacted with one equivalent of the iridium dimer $[Ir(Cp^*)(Cl)_2]_2$ or rhodium dimer $[Rh(Cp^*)(Cl)_2]$ in the presence of sodium acetate. Successful synthesis of complexes **7a** – **7c** required only mild conditions, proceeding at room temperature, while complexes **8a** – **8b** required elevated temperatures for successful synthesis. The decreased reactivity of the Rh(III) is in line with the proposed electrophilic mechanism of C-H activation during cyclometalation. In addition, quinoline *N*-coordinated iridium(III) and rhodium(III) complexes **9a** – **9c** and **10a** – **10c** complexes were synthesised, as a result of their selective formation under certain reaction conditions. These eleven new neutral complexes were fully characterised using ^1H and $^{13}C\{^1H\}$ NMR spectroscopy, IR spectroscopy and high-resolution ESI mass spectrometry. The ^1H NMR spectra of compounds **7a** – **7c** and **8a** – **8b** each revealed the presence of two conformational isomers, which convert to the proposed more stable of the two isomers upon heating of the NMR sample or extended periods of time in solution.

Furthermore, two sets of cationic *N*^*N*-coordinated complexes were also prepared. Two equivalents of ligands **6a** – **6c** were reacted with one of either the iridium dimer $[Ir(Cp^*)(Cl)_2]_2$ or rhodium dimer $[Rh(Cp^*)(Cl)_2]_2$, *via* bridge-splitting reactions to afford the cationic complexes as chloride salts, which were not isolated. This was followed by counter-ion exchange with ammonium hexafluorophosphate to yield the desired cationic Ir(III)- and Rh(III)-Cp* complexes (**11a** – **11c** and **12a** – **12c**) as hexafluorophosphate salts. In a similar way, cationic Rh(III)-ppy complexes **13a** – **13c** were synthesised by reaction of ligands **6a** – **6c** with a rhodium dimer $[Rh(ppy)_2Cl]_2$, *via* bridge-splitting reactions, followed by counter-ion exchange with ammonium hexafluorophosphate. The initial bridge-splitting step to form complexes **11a** – **11c** and **12a** – **12c** were performed at room temperature, while that for complexes **13a** – **13c** required elevated temperatures due to limited solubility of the $[Rh(ppy)_2Cl]_2$ dimer. These nine new

cationic complexes were fully characterised using NMR (^{1}H, $^{13}C\{^{1}H\}$, $^{31}P\{^{1}H\}$, COSY and HSQC) and IR spectroscopy, and high-resolution ESI mass spectrometry.

4.4 References

1. K. Williams, *J. Roy. Soc. Med.*, 2009, **102**, 343-348.
2. S. Gibaud and G. Jaouen, in *Medicinal Organometallic Chemistry*, Springer, 2010, pp. 1-20.
3. B. Rosenberg and L. Vancamp, *Nature*, 1969, **222**, 385-386.
4. R. A. Sánchez-Delgado, M. Navarro, H. Pérez and J. A. Urbina, *J. Med. Chem.*, 1996, **39**, 1095-1099.
5. P. F. Salas, C. Herrmann and C. Orvig, *Chem. Rev.*, 2013, **113**, 3450-3492.
6. N. Baartzes, T. Stringer and G. S. Smith, in *Advances in Bioorganometallic Chemistry*, Elsevier, 2019, pp. 193-213.
7. L. Rylands, A. Welsh, K. Maepa, T. Stringer, D. Taylor, K. Chibale and G. S. Smith, *Eur. J. Med. Chem.*, 2019, **161**, 11-21.
8. E. Ekengard, K. Kumar, T. Fogeron, C. de Kock, P. J. Smith, M. Haukka, M. Monari and E. Nordlander, *Dalton Trans.*, 2016, **45**, 3905-3917.
9. E. Ekengard, I. Bergare, J. Hansson, I. Doverbratt, M. Monari, B. Gordhan, B. Kana, C. d. Kock, P. J. Smith and E. Nordlander, *J. Mex. Chem. Soc.*, 2017, **61**, 158-166.
10. C. White, A. Yates, P. Maitlis and D. Heinekey, *Inorg. Syn.*, 1992, 228-234.
11. D. L. Davies, S. M. Donald and S. A. Macgregor, *J. Am. Chem. Soc.*, 2005, **127**, 13754-13755.
12. S. Attar, J. H. Nelson, J. Fischer, A. de Cian, J.-P. Sutter and M. Pfeffer, *Organometallics*, 1995, **14**, 4559-4569.
13. S. Fernandez, M. Pfeffer, V. Ritleng and C. Sirlin, *Organometallics*, 1999, **18**, 2390-2394.
14. T. G. P. Harper, P. J. Desrosiers and T. C. Flood, *Organometallics*, 1990, **9**, 2523-2528.
15. D. L. Davies, O. Al-Duaij, J. Fawcett, M. Giardiello, S. T. Hilton and D. R. Russell, *Dalton Trans.*, 2003, 4132-4138.

16. D. L. Davies, S. M. Donald, O. Al-Duaij, S. A. Macgregor and M. Pölleth, *J. Am. Chem. Soc.*, 2006, **128**, 4210-4211.
17. L. Li, W. W. Brennessel and W. D. Jones, *Organometallics*, 2009, **28**, 3492-3500.
18. A. P. Walsh and W. D. Jones, *Organometallics*, 2015, **34**, 3400-3407.
19. J. M. Kisenyi, G. J. Sunley, J. A. Cabeza, A. J. Smith, H. Adams, N. J. Salt and P. M. Maitlis, *J. Chem. Soc. Dalton*, 1987, 2459-2466.
20. C. Housecroft and A. Sharpe, in *Inorganic Chemistry*, Pearson, 2008, pp 806-814.
21. R. E. Shepherd, Y. Chen and C. R. Johnson, *Inorg. Chim. Acta*, 1998, **267**, 11-18.
22. M. C. MacInnis, J. C. DeMott, E. M. Zolnhofer, J. Zhou, K. Meyer, R. P. Hughes and O. V. Ozerov, *Chem*, 2016, **1**, 902-920.
23. A. R. Burgoyne, B. C. Makhubela, M. Meyer and G. S. Smith, *Eur. J. Inorg. Chem.*, 2015, **2015**, 1433-1444.
24. G. Gupta, B. Therrien and K. M. Rao, *J. Organomet. Chem.*, 2010, **695**, 753-759.
25. P. Govender, A. K. Renfrew, C. M. Clavel, P. J. Dyson, B. Therrien and G. S. Smith, *Dalton Trans.*, 2011, **40**, 1158-1167.
26. M. S. Lowry, W. R. Hudson, R. A. Pascal and S. Bernhard, *J. Am. Chem. Soc.*, 2004, **126**, 14129-14135.

Chapter 5:

Pharmacological evaluation of PGM-containing aminoquinoline-benzimidazole hybrid complexes

5.1 Introduction

A special consideration in the process of drug development is the mechanism of action, the way in which the 'drug' will exert its pharmacological effect. Metal-based compounds have demonstrated a number of different modes of action in various diseases, including DNA interaction,[1] enzyme inhibition,[2] generation of reactive oxygen species (ROS)[3] and induction of apoptosis.[4] Some compounds are known to target the survival mechanisms of the microbe of interest. The latter is of particular importance with regards to tackling *Plasmodium falciparum* parasites. The haem degradation pathway is a prominent target in the parasite life cycle, in which drugs are aimed at inhibiting haemozoin formation.

The detergent-mediated Nonidet P-40 (NP-40) β-haematin inhibition assay, developed by Sandlin *et al*.,[5] is a high throughput screen used to identify potential inhibitors of haemozoin formation, and was used to evaluate the compounds herein. The neutral NP-40 detergent provides a lipophilic environment, mimicking lipids in the parasite digestive vacuole, which mediates the formation of β-haematin (synthetic haemozoin).[5] The pyridine ferrohaemochrome method, developed by Egan *et al*.,[6] is often used to measure the inhibition activity. In this quantification method, pyridine forms a complex with haematin (β-haematin precursor) only, in mixtures of both haematin and β-haematin. Its absorbance correlates with, and is a measure of, the β-haematin inhibition activity of a compound.[6]

In addition to the aforementioned mechanisms of action, metal-based compounds provide novel ways to overcome or evade resistance, by taking advantage of their catalytic properties. In contrast to stoichiometric reactions, intracellular catalysis by catalytic metallodrugs may only require low dosages to be administered in order for transformations to take place.[7, 8] This may reduce toxicity, unwanted side-reactions and

undesirable side-effects. Transfer hydrogenation is a versatile reduction process, which has demonstrated applicability in aqueous media, using sodium formate as the hydride source.[9] This bodes well for its application in biological media/systems using biomolecules.

With regards to transformations of biomolecules, transfer hydrogenation reactions involving the NAD^+/NADH couple, utilising metal-based catalysts, have been explored.[10, 11] The coenzymes, NAD^+ and NADH, take part in redox reactions essential to the metabolism of living organisms, and thus their interconversion may represent an important target intracellularly. Sadler and co-workers have previously reported on the NAD^+/NADH transfer hydrogenation activity of ruthenium-containing complexes in cancer cells, using sodium formate as a hydride source.[8, 12]

Most relevant to the study at hand, Stringer *et al*. investigated the transfer hydrogenation of NAD^+ by iridium- and rhodium-containing complexes, in the context of *Plasmodium* parasites.[13] The transfer hydrogenation activity of half-sandwich Ir(III) and Rh(III) complexes, in the presence of sodium formate, was demonstrated in a cell-free environment.[13] The principle of the cell-free assay is depicted in Figure 5.1, and is modified from the *Plasmodium* lactate dehydrogenase (pLDH) assay. In this case, NADH reduces the tetrazolium dye to formazan, which is quantified using absorption spectroscopy and serves as a measure of activity. Furthermore, an investigation of the K1 strain parasite viability suggested that co-administration of the Ir(III) complex and sodium formate lead to transfer hydrogenation in the parasite.[13]

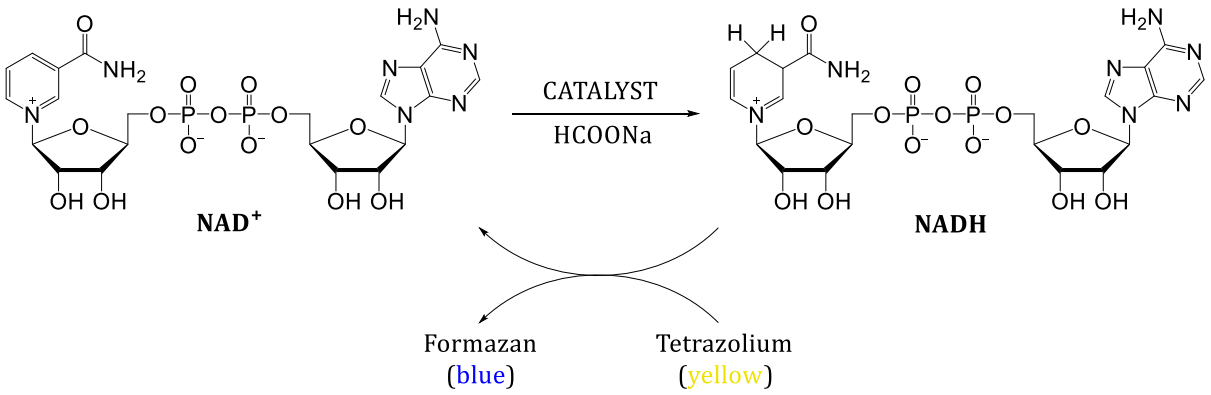

Figure 5.1 Principle of cell-free transfer hydrogenation assay.

5.2 Pharmacological evaluation of Ir(III) and Rh(III) aminoquinoline-benzimidazole hybrid complexes

The pharmacological activities of the neutral and cationic Ir(III) and Rh(III) complexes (**7** – **8** and **11** – **13**, Figure 5.2), described in Chapter 4, were evaluated. The complexes were screened *in vitro* against the chloroquine-sensitive NF54 and multidrug-resistant K1 strains of *Plasmodium falciparum*. Their cytotoxicity was determined against the non-tumorigenic Chinese hamster ovarian (CHO) cell-line. Mechanistic studies were performed on selected complexes, probing their β-haematin inhibition activity and their ability to catalyse transfer hydrogenation reactions. In addition, the *in vitro* antimycobacterial activity of all complexes was determined against the H37Rv strain of *Mycobacterium tuberculosis*.

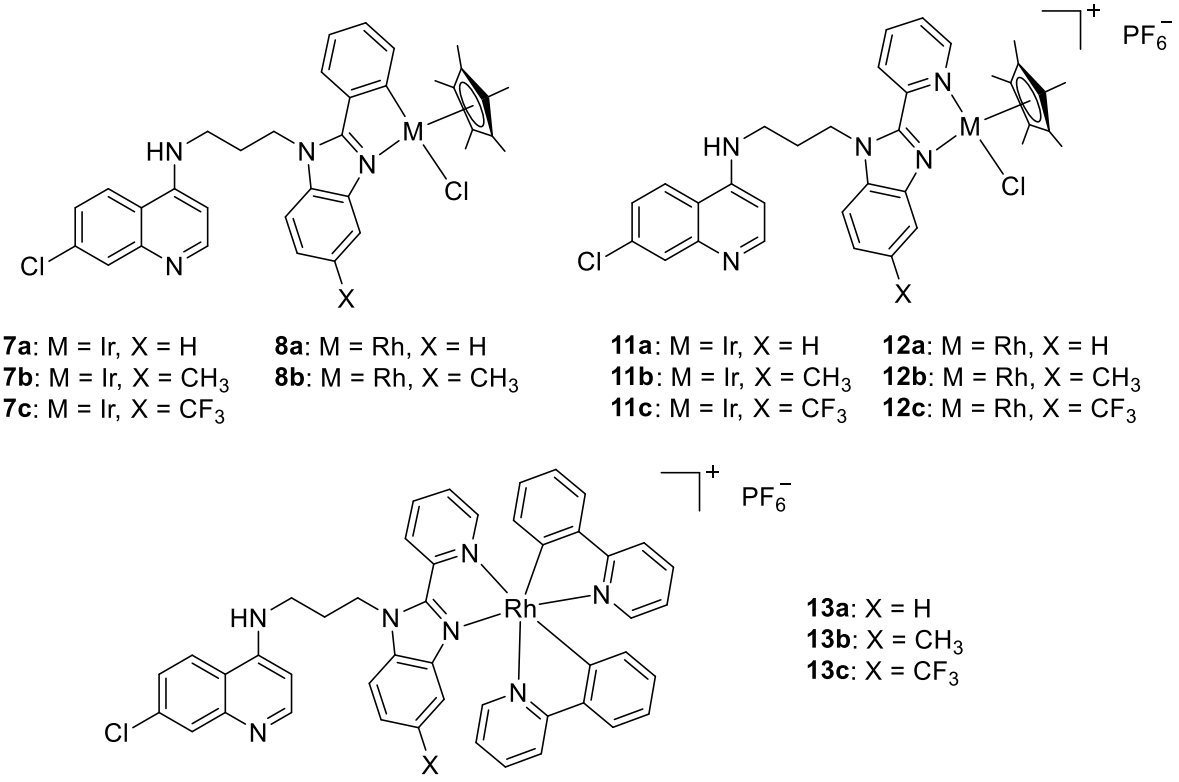

Figure 5.2 Pharmacologically screened PGM-containing aminoquinoline-benzimidazole hybrid complexes (**7** – **8** and **11** – **13**).

The neutral quinoline *N*-coordinated Ir(III) and Rh(III) complexes (**9** – **10**) were not evaluated for their biological activity as a result of their instability in dimethyl sulfoxide (DMSO), the solvent used to prepare stock solutions for biological screenings. DMSO-based stock solutions are required for the *in vitro* antiplasmodium, cytotoxicity and

antimycobacterial assays, as well as the β-haematin inhibition mechanistic study. Gasser *et al*. investigated the DMSO-mediated ligand dissociation of a range of *N*-heterocyclic-[Ru(η^6-arene)Cl$_2$] complexes.[14] It was observed, visually and by ^{1}H NMR spectroscopy, that the *N*-coordinated complex readily undergoes a ligand exchange reaction in DMSO.[14] The ^{1}H NMR spectrum of the proposed complex in DMSO-*d*$_6$, displays signals corresponding to a physical mixture of the *N*-heterocyclic ligand and the [Ru(η^6-arene)(DMSO)Cl$_2$] complex.[14] This ligand exchange was revealed to have implications on the outcomes of the biological evaluation.[14]

The stability of these quinoline *N*-coordinated complexes (**9a – 9c** and **10a – 10c**) in DMSO-*d*$_6$ was monitored by ^{1}H NMR spectroscopy. The stacked ^{1}H NMR spectra of compounds **9b**, **4b** and [Ir(Cl$_2$)(Cp*)]$_2$ in DMSO-*d*$_6$ are depicted in Figure 5.3. The spectrum of the proposed complex shows signals corresponding to the protons of the aminoquinoline-benzimidazole and Cp* ligand, with no differences in chemical shifts compared to the starting materials. This trend is consistent for all of the Ir(III) and Rh(III) quinoline *N*-coordinated complexes.

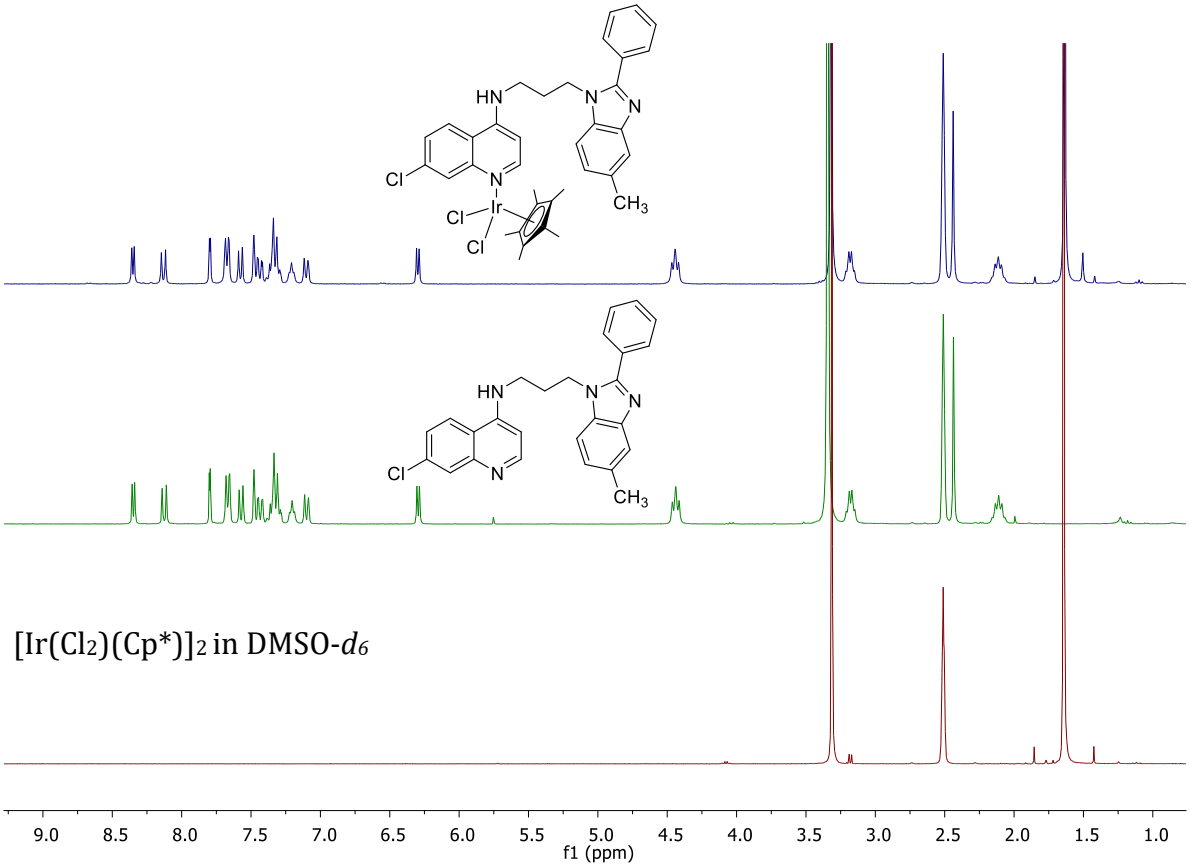

Figure 5.3 Stacked ^{1}H NMR spectra of complex **9b**, ligand **4b** and [Ir(Cl$_2$)(Cp*)]$_2$ in DMSO-*d*$_6$.

The proposed ligand exchange reaction which takes place in solution is shown in Scheme 5.1. We speculate that this ligand dissociation and exchange occurs at varying rates for the different analogues (M = Ir or Rh and X = H, CH_3 or CF_3). The spectra of compounds **9a** – **9c** and **10a** – **10c** initially display downfield shifts in selected proton signals, consistent with metal-coordination, which after some time shift upfield as a result of DMSO-mediated ligand dissociation. Further evidence of metal-ligand bond dissociation was provided using single crystal X-ray diffraction. Crystals grown from a DMSO-d_6 solution of complex **9b** were determined to be that of ligand **4b** alone, with no metal coordination.

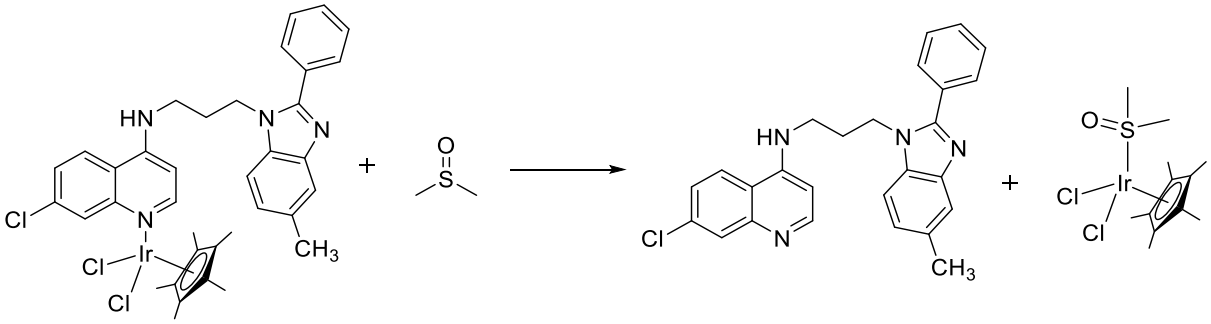

Scheme 5.1 The proposed ligand exchange reaction taking place in solution.

5.2.1 *In vitro* antiplasmodium activity and cytotoxicity

The *C*^*N*-coordinated (**7** – **8**) and *N*^*N*-coordinated (**11** – **13**) Ir(III) and Rh(III) complexes were evaluated for their *in vitro* antiplasmodium activity using the *Plasmodium* lactate dehydrogenase (pLDH) assay,[15] described in Chapter 3 (Section 3.1). All complexes were screened against the CQS NF54 strain of *P. falciparum* and selected complexes, which were sufficiently active in this strain (IC_{50} ≤ 2 μM), were screened against the MDR K1 strain. Chloroquine (CQ) was used as the control drug in the screening. The IC_{50} values and resistance indices (RI) are summarised in Table 5.1. In general, most of the PGM-containing aminoquinoline-benzimidazole hybrid complexes display good antiplasmodium activity, with IC_{50} values in the low micromolar and sub-micromolar range.

Table 5.1 *In vitro* antiplasmodium data for compounds **7** – **8**, **11** – **13** and CQ.

Compound	M	X	IC_{50} (μM) ± SE		RI[a]
			NF54	K1	
7a	Ir	H	2.007 ± 0.075	2.844 ± 0.030	1.417
7b	Ir	CH_3	1.676 ± 0.171	2.181 ± 0.025	1.301
7c	Ir	CF_3	0.488 ± 0.062	0.688 ± 0.032	1.410
8a	Rh	H	1.073 ± 0.028	2.217 ± 0.167	2.066
8b	Rh	CH_3	1.327 ± 0.255	1.810 ± 0.176	1.364
11a	Ir	H	> 10	ND[b]	–
11b	Ir	CH_3	> 10	ND[b]	–
11c	Ir	CF_3	1.454 ± 0.043	> 10	–
12a	Rh	H	2.001 ± 0.148	> 10	–
12b	Rh	CH_3	1.867 ± 0.562	> 10	–
12c	Rh	CF_3	0.194 ± 0.066	> 10	–
13a	Rh	H	0.326 ± 0.002	0.844 ± 0.144	2.589
13b	Rh	CH_3	0.313 ± 0.005	0.228 ± 0.003	0.728
13c	Rh	CF_3	0.404 ± 0.010	1.302 ± 0.494	3.223
CQ	–	–	0.0160 ± 0.0005	0.164 ± 0.018	10.250

[a]RI = IC_{50}(K1) / IC_{50}(NF54);

[b]ND = not determined

The IC_{50} values obtained against the CQS NF54 strain are graphically depicted in Figure 5.4. With regards to the neutral cyclometalated complexes, the unsubstituted Rh(III) complex **8a** (1.073 μM) is more active than the corresponding Ir(III) complex **7a** (2.007 μM), while the methyl-substituted complexes **8b** and **7b** have comparable activity (1.327 and 1.676 μM). Interestingly, the activity of the Ir(III) complexes appears to increase with increasing hydrophobicity of the 5-position benzimidazole substituent (X). The unsubstituted and methyl-substituted compounds **7a** and **7b** are 3- to 4-fold less active than the trifluoromethyl-substituted analogue **7c**. Compound **7c** is the most active of the neutral compounds in the CQS NF54 strain, with the lowest IC_{50} value of 0.488 μM. This may suggest a correlation between antiplasmodium activity and hydrophobicity, as well as the closely-related property of lipophilicity. However, this trend is not observed for the Rh(III) complexes.

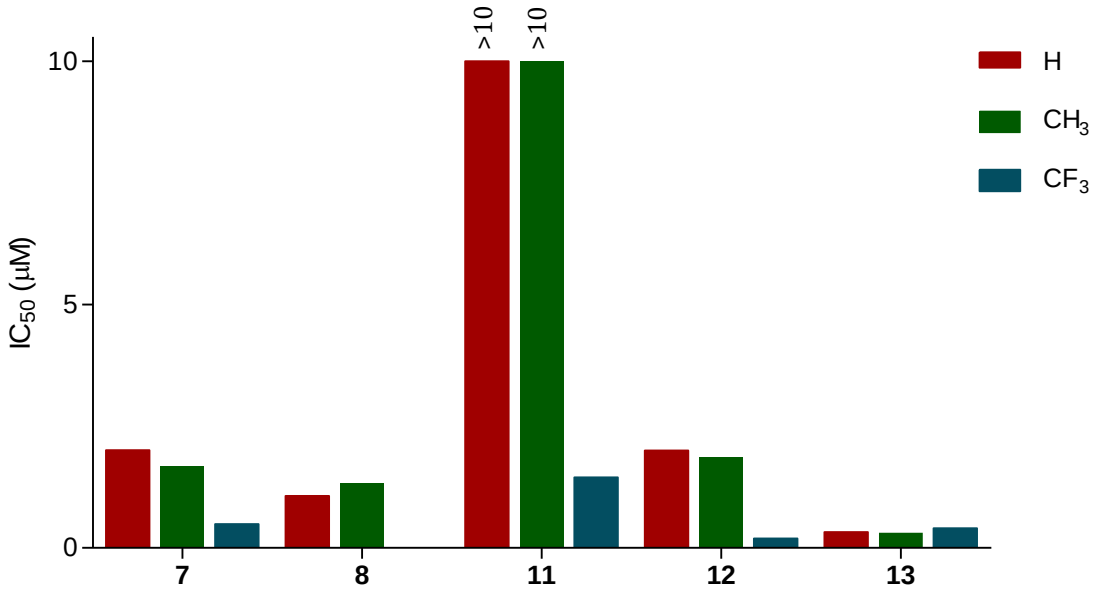

Figure 5.4 IC_{50} values of compounds **7** – **8** and **11** – **13** against the CQS NF54 strain of *P. falciparum*.

For the cationic pentamethylcyclopentadienyl (Cp*) series, the unsubstituted and methyl-substituted Ir(III) complexes **11a** and **11b** were inactive (IC_{50} > 10 μM) against the NF54 strain at the tested concentration. The trifluoromethyl-substituted compound **11c**, however, displays good activity in the low micromolar range. The Rh(III) complexes **12a** – **12c** display significantly enhanced activity compared to their corresponding Ir(III) complexes **11a** – **11c**. In addition, the analogues with the more hydrophobic trifluoromethyl group (**11c** and **12c**) are the most active of the Ir(III) and Rh(III) complexes, giving rise to IC_{50} values of 1.454 and 0.194 μM, respectively. Comparing the activity of the neutral and cationic M-Cp* series, the neutral Ir(III) and Rh(III) complexes (**7** – **8**) generally outperformed their corresponding cationic complexes (**11** – **12**).

The potent sub-micromolar activity of the cationic Rh(III) phenylpyridyl (ppy) complexes (**13a** – **13c**) reiterates the favourable antiplasmodium properties attributed to the rhodium metal centre. Compounds **13a**, **13b** and **13c** have comparable activity against the NF54 strain, displaying IC_{50} values of 0.326, 0.313 and 0.404 μM, respectively. The general superior activity of these Rh(III)-ppy complexes, compared to the M-Cp* complexes, may be related to the planarity of the ppy ligands. A cationic platinum complex of 1,10-phenanthroline, reported by Egan *et al.*, demonstrated a strong interaction with ferriprotoporphyrin IX (haemozoin precursor), as well as β-haematin

inhibition ability.[16] The strong interaction with ferriprotoporphyrin IX was attributed in part to the presence of an extended planar phenanthroline ring system with delocalized electrons.[16] Considering haemozoin inhibition as a possible mechanism of action for these hybrid complexes, the planar ppy ligand system of complexes **13a** – **13c** may have greater interaction with ferriprotoporphyrin IX, which may have implications on their potential haemozoin inhibition ability.

Selected hybrid complexes were evaluated in the MDR K1 strain of *P. falciparum*. The cationic Ir(III)-Cp* complexes, **11a** and **11b**, were not screened as a result of their inactivity in the CQS NF54 strain. In addition, the remaining cationic M-Cp* complexes (**11c** and **12a** – **12c**) were inactive against K1 parasites (IC_{50} > 10 μM) at the tested concentration. With the exception of the aforementioned compounds, all tested compounds displayed good antiplasmodium activity in the low to sub-micromolar range. The IC_{50} values obtained against the K1 strain are graphically represented in Figure 5.5.

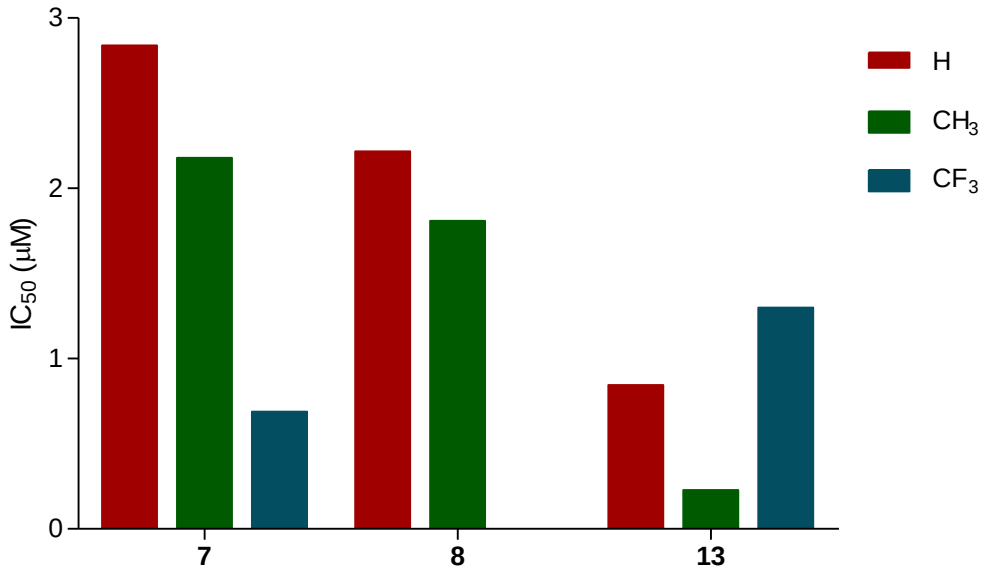

Figure 5.5 IC_{50} values of compounds **7** – **8** and **11** – **13** against the MDR K1 strain of *P. falciparum*.

In the resistant K1 strain, the neutral iridium and rhodium complexes are comparably active. The unsubstituted and methyl-substituted Ir(III) complexes (**7a** and **7b**) and their corresponding Rh(III) analogues (**8a** and **8b**) give rise to IC_{50} values in the range 2.844 – 1.810 μM. Once again, the activity of the analogue with the more hydrophobic X substituent is enhanced. The most active neutral complex against the K1 strain is the

trifluoromethyl-substituted Ir(III) complex **7c**, displaying an IC_{50} value of 0.688 μM. In contrast, the CF_3-substituted Rh(III)-ppy complex **13c** (1.302 μM) was the least active of its series. Cationic complexes **13a** and **13b** are the most active unsubstituted and methyl-substituted analogues overall, giving rise to sub-micromolar IC_{50} values of 0.844 and 0.228 μM, respectively.

When comparing the activity of the compounds in the CQS NF54 and MDR K1 strains, it can be seen that in general, most of the compounds have comparable or decreased activity in the resistant strain. Compounds **7a** – **7c**, **8a** – **8b**, **13a** and **13c** all display resistance indices in the range 1.3 – 3.2 (RI ≥ 1), significantly lower than that of CQ. The compounds with RI values close to one may be applicable in both sensitive and resistant strains of *P. falciparum*. Compound **13b** provides an exception in this regard, displaying enhanced activity in the resistant strain compared to the sensitive strain. The cationic Rh(III)-ppy complex **13b** has a RI value of 0.728 (RI < 1), suggesting that it is not susceptible to cross-resistance and indicating a potential to overcome parasite resistance.

With regards to the effect of organometallic derivatisation on the antiplasmodium activity, the activity of the PGM-containing complexes (**7** – **8** and **11** – **13**) was compared to that of the corresponding ligands (described in Chapter 3). Contrasting trends are revealed across the different series and *P. falciparum* strains. In the NF54 strain, the neutral unsubstituted Ir(III) and Rh(III) complexes, **7a** and **8a**, are almost 3- and 5-fold more potent than the ligand **4a** (5.553 μM). Cationic complexes **12b**, **12c**, **13a** and **13b** are more active than their respective ligands **6a** (1.089 μM), **6b** (4.984 μM) and **6c** (0.410 μM). Trifluoromethyl-substituted complexes **7c** and **13c** maintained comparable activity to their respective ligands **4c** (0.431 μM) and **6c**. Interestingly, in the K1 strain, the coordination of the $[Rh(ppy)_2]$ moiety to the inactive ligands, **6a** and **6c** (> 20 μM), resulted in potent sub-micromolar activity in complexes **13a** and **13c**. In all other cases, higher IC_{50} values were observed for the complexes compared to the ligands, as activity was not maintained upon coordination of the metal.

Cytotoxicity

The *C^N*-coordinated Ir(III) and Rh(III) complexes (**7a** – **7c** and **8a** – **8b**) and selected *N^N*-coordinated Rh(III) complexes (**13a** – **13c**) were screened against the non-tumorigenic CHO cell-line, to determine their cytotoxicity and to evaluate selectivity. The compounds were evaluated using the MTT assay[17, 18] and emetine was used as the control drug. The cytotoxicity of the *N^N*-coordinated Ir(III)-Cp* and Rh(III)-Cp* complexes (**11a** – **11c** and **12a** – **12c**) was not determined as a result of their inactivity in the NF54 strain (**11a** and **11b**) and the K1 strain (**11c** and **12a** – **12c**) of *P. falciparum*. In general, all tested compounds displayed low or no cytotoxicity against the non-tumorigenic cells. The IC_{50} values and selectivity indices (SI) of the screened compounds are reported in Table 5.2.

Table 5.2 Cytotoxicity data and selectivity indices for selected compounds (**7** – **8** and **13**) and the control, emetine.

Compound	CHO IC_{50} (μM)	SI_1[a]	SI_2[b]
7a	> 50	–	–
7b	> 50	–	–
7c	14.14	28.98	20.55
8a	133.30	124.23	60.13
8b	78.89	59.45	43.59
13a	91.52	280.74	108.44
13b	106.36	339.81	466.49
13c	60.63	150.07	46.57
Emetine	0.0181	-	-

[a]SI_1 = IC_{50}(CHO) / IC_{50}(NF54);

[b]SI_2 = IC_{50}(CHO) / IC_{50}(K1)

Compound **7c** displayed low toxicity towards the CHO cells, giving rise to a moderate micromolar IC_{50} value of 14.14 μM. Compounds **7a** – **7b**, **8a** – **8b** and **13a** – **13c** were non-cytotoxic at the highest concentration tested, with IC_{50} values greater than 50 μM. The selectivity indices (SI) were determined to gauge the selectivity of the tested compounds for the sensitive and resistant *Plasmodium* strains compared to the CHO cell-line. The SI values were calculated to be greater than 28 and 20 for the sensitive NF54 (SI_1) and resistant K1 (SI_2) strains, respectively. These values, which are significantly greater than

one, suggest that these Ir(III) and Rh(III)-containing hybrid complexes are selective toward parasite strains. In addition, it may also imply that the antiplasmodium properties of these complexes are the result of mechanisms other than general cytotoxicity.

5.2.2 Mechanistic studies

5.2.2.1 β-haematin inhibition

Selected active complexes from each series were evaluated for a potential mechanism of action which takes place in the *Plasmodium* digestive vacuole. The detergent-mediated NP-40 assay[5] and subsequent colorimetric pyridine ferrihaemochrome method[6] were used to assess the β-haematin (synthetic haemozoin) inhibition ability of the iridium and rhodium complexes of interest. Compounds **7a**, **7c**, **8a**, **8b**, **11c**, **12c** and **13b** were tested, and CQ was used as the positive control. The IC_{50} values obtained are listed in Table 5.3.

Table 5.3 β-haematin inhibition activity of compounds **7a**, **7c**, **8a**, **8b**, **11c**, **12c** and **13b**.

Compound	IC_{50} (μM) [95% confidence interval]
7a	13.88 [12.13 to 15.88]
7c	16.03 [14.43 to 17.81]
8a	31.05 [30.03 to 32.09]
8b	36.34 [33.63 to 39.28]
11c	5.46 [5.01 to 5.95]
12c	8.39 [7.83 to 8.99]
13b	11.68 [10.50 to 12.99]
CQ	73.98 [71.14 to 76.94]

In general, all of the tested compounds are potent inhibitors of β-haematin formation in the cell-free assay, at least 2-fold more active than CQ (74 μM). The IC_{50} values are graphically represented in Figure 5.6, displaying the trends observed. The X substituent appears to have no significant effect on the β-haematin inhibition activity. The unsubstituted and trifluoromethyl-substituted Ir(III) complexes (**7a** and **7c**) have comparable IC_{50} values, as do the unsubstituted and methyl-substituted Rh(III) complexes (**8a** and **8b**). The cationic *N^N*-coordinated complexes (**11** – **13**), outperformed the neutral *C^N*-coordinated complexes (**7** – **8**), giving rise to IC_{50} values

in the range 5.46 – 11.68 μM, compared to 13.88 – 36.34 μM for complexes **7** – **8**. The superior activity of the cationic compounds may be the result of their enhanced solubility in the assay medium over time, compared to the neutral compounds. This may allow greater interaction with the haematin species, thus leading to greater inhibition of β-haematin formation.

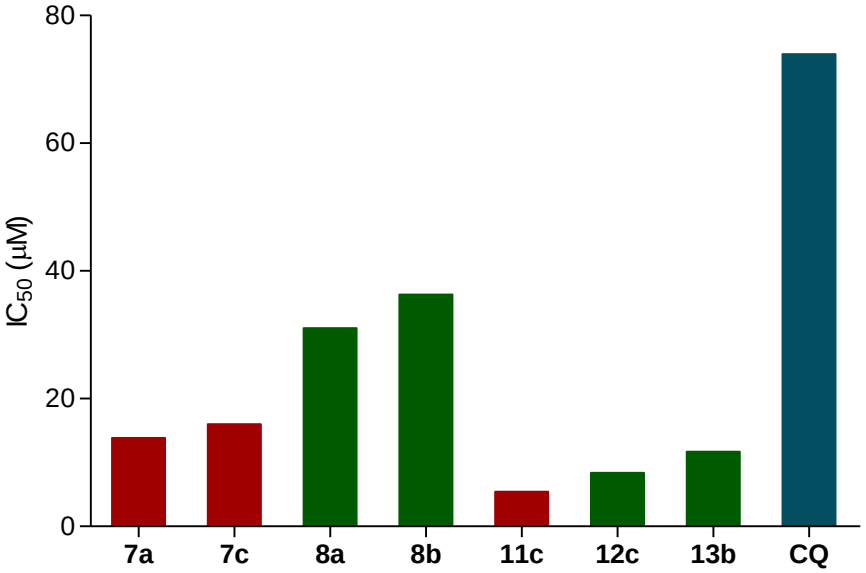

Figure 5.6 IC_{50} values compounds **7a**, **7c**, **8a**, **8b**, **11c**, **12c** and **13b** towards β-haematin inhibition.

In addition, the effect of the different metals on β-haematin inhibition activity is clearly seen in Figure 5.6. Across the neutral and cationic M-Cp* series, the Ir(III)-containing complexes display enhanced activity compared to the Rh(III)-containing analogues. For the neutral M-Cp* complexes, the Ir(III) complexes **7a** and **7c** (13.88 – 16.03 μM) have IC_{50} values approximately two-fold lower than the Rh(III) complexes **8a** and **8b** (31.05 – 36.34 μM). For the cationic M-Cp* complexes, Ir(III) complex **11c** (5.46 μM) displays an IC_{50} value about 1.5-fold lower than Rh(III) complex **12c** (8.39 μM). This difference in activity may be the result of differences in lipophilicity, as observed for the 2-phenyl, 2-ferrocenyl and 2-pyridyl aminoquinoline-benzimidazole hybrids in Chapter 3 (Section 3.2.4.1). Although logP values of these aminoquinoline-benzimidazole hybrid Ir(III) and Rh(III) complexes have not been determined, previous literature reports higher logP values (and thus greater lipophilicity) for a d^6 low-spin Ir(III) half-sandwich complex compared to the isostructural Rh(III) complex.[19] Furthermore, there is no discernable

correlation between β-haematin inhibition activity and the *in vitro* antiplasmodium activity (NF54/K1), reported in Section 5.2.1.

5.2.2.2 Transfer hydrogenation

As discussed in Section 5.1, the catalytic activities of metal-based compounds can be utilised to establish novel modes of antimicrobial action. Selected compounds (**7a** and **8a**) were evaluated for their ability to catalyse the transfer hydrogenation of β-nicotinamide adenine dinucleotide (NAD^+) to form β-nicotinamide adenine dinucleotide reduced (NADH) in the presence of sodium formate as the hydride source.

As a preliminary study, neutral cyclometalated complexes **7a** and **8a** were subjected to a qualitative screening of their ability to reduce NAD^+ to NADH using sodium formate, by means of ^1H NMR spectroscopic experiments. Compound **7a** or **8a**, sodium formate and NAD^+ were combined and the ^1H NMR spectra of the mixtures were recorded over a period of one hour. In order to mimic biological or assay conditions, the samples were maintained at a temperature of 310 K (37 °C). The ^1H NMR spectra, recorded five minutes after sample preparation, after thirty minutes and one hour for each compound (**7a** and **8a**), are shown in Figure 5.7.

The regioselective reduction of NAD^+ to form 1,4-NADH is confirmed by differences in the spectra. The conversion effected by each catalyst takes place at varying rates, as demonstrated by the appearance of 1,4-NADH at different times. For Ir(III) complex **7a**, a considerable amount of 1,4-NADH had already formed immediately after sample preparation, and complete conversion had taken place after thirty minutes. On the other hand, for Rh(III) complex **8a**, only trace amounts of 1,4-NADH was formed immediately after sample preparation. After thirty minutes, only trace amounts of NAD^+ remained, with complete conversion taking place by one hour.

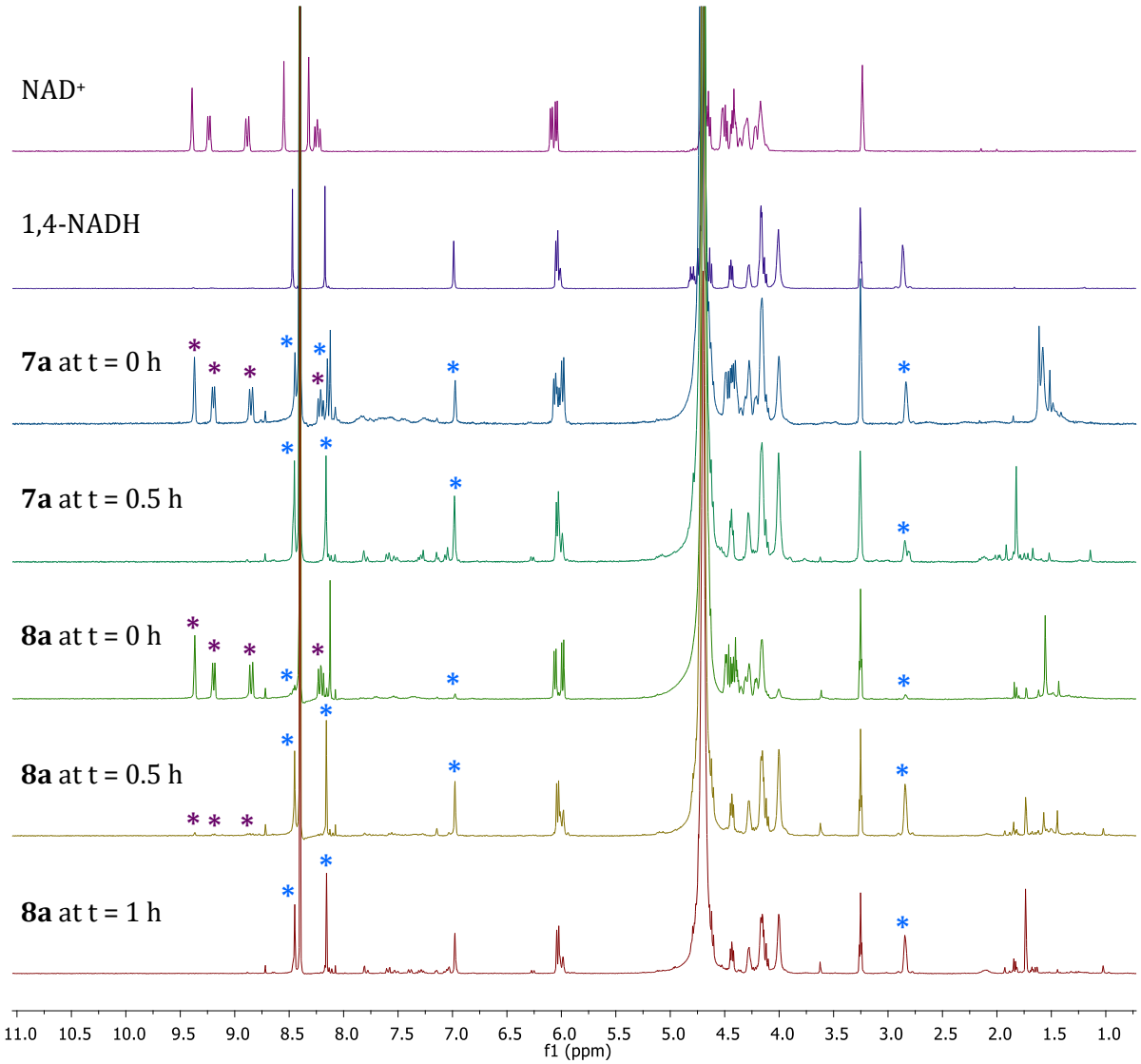

Figure 5.7 Stacked ^{1}H NMR spectra of a mixture of compound **7a** or **8a**, NAD^+ and sodium formate in D_2O/MeOD at 310K over time. * = signals for NAD^+ and * = signals for 1,4-NADH.

The transfer hydrogenation ability of the hybrid complexes in a cell-free environment was then monitored using a method described by Stringer *et al.*,[13] based on the pLDH assay (Chapter 3, Section 3.1).[15, 20] In the modified assay, the complex of interest catalyses the conversion of NAD^+ to NADH, using sodium formate as the hydrogen source. In an analogous way to APADH in the pLDH/Malstat™ assay,[20, 21] the NADH formed reduces the nitroblue tetrazolium (NBT) to formazan.[13] The conversion of the yellow NBT to blue formazan, quantified by absorption spectroscopy, serves as a measure of the transfer hydrogenation activity of the complex. Different concentrations of the complex (**7a** or **8a**) were incubated (37 °C, pH 7.4) with NAD^+ and sodium formate for six hours, allowing the complex to catalyse the reduction, followed by addition of NBT and further incubation.

The 96-well plate setup for complexes **7a** and **8a** is shown in Figure 5.8. Visually, the presence of the blue colour (formazan) in the wells is indicative of the conversion of NAD^+ to NADH. Based on the development of formazan, it seems as though complex **8a** has greater catalytic activity than complex **7a**, as formazan is present at lower concentrations of complex **8a**.

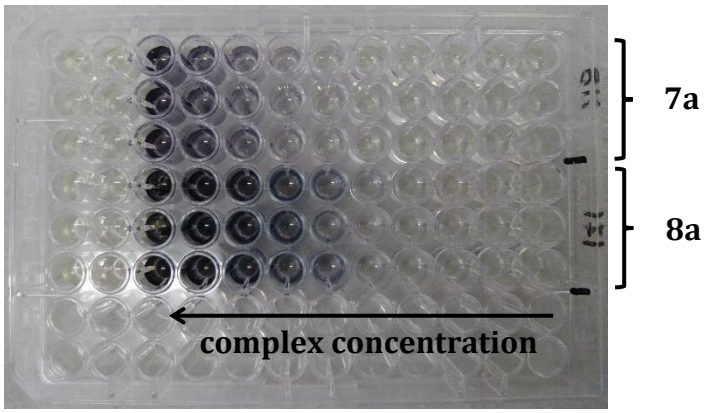

Figure 5.8 Plate layout of cell-free transfer hydrogenation experiment after 16-hour incubation.

The absorbance values, recorded at 600 nm, are proportional to the amount of the formazan present, and thus indicates transfer activity. The absorbance values of complexes **7a** and **8a** at the varying concentrations (2250 – 4 μM) are graphically depicted in Figure 5.9.

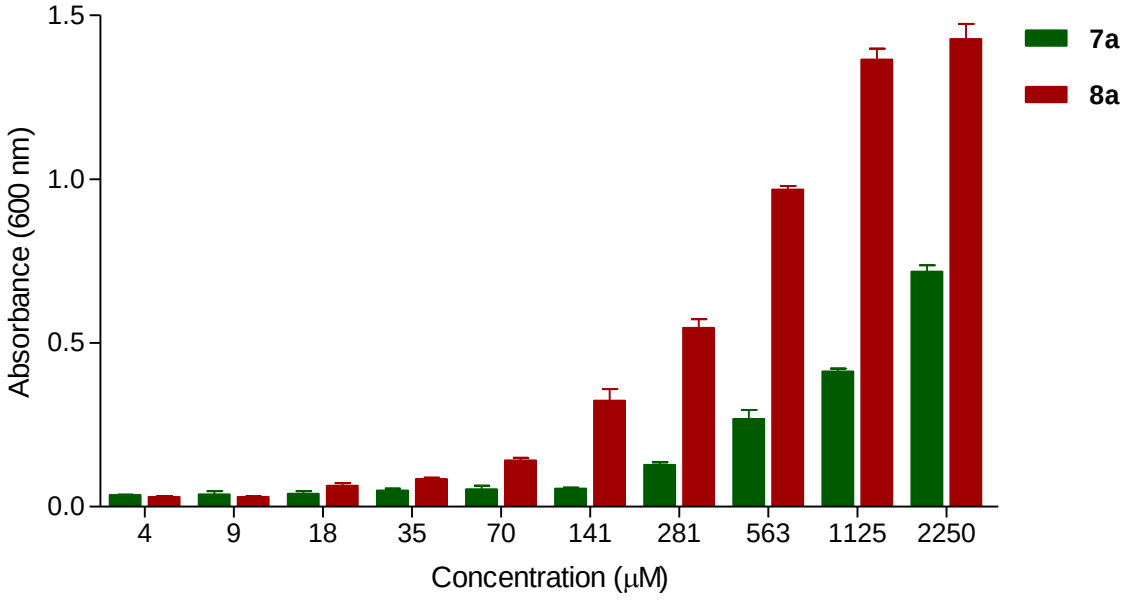

Figure 5.9 Absorbance values obtained in cell-free experiments for compounds **7a** and **8a**.

For both complexes **7a** and **8a**, there is a concentration-dependent increase in the amount of formazan formed. This indicates that, under the given conditions (37 °C and pH = 7.4), both complexes catalyse the transfer hydrogenation of NAD^+ to NADH in a concentration-dependent manner. The Rh(III) complex **8a** is significantly more active than the Ir(III) complex **7a**, consistently achieving greater conversion at every concentration. This is in agreement with the visual result (Figure 5.8). In contrast, in the study by Stringer *et al*., the Ir(III) complex was found to be slightly more active than the corresponding Rh(III) complex.[13]

The coenzyme NAD^+ provides a unique and important target within *Plasmodium* parasites. Previous studies have demonstrated elevated levels of NAD^+ during the asexual erythrocytic stage of the life cycle of various *Plasmodium* species.[22-26] NAD^+ is essential for the glycolytic pathway, and has been identified as an enzyme substrate in other cellular processes such as DNA repair[27] and calcium signalling.[28] In this way, the regulation of NAD^+ by a therapeutic agent may have significant implications for the parasite. With this in mind, the *in vitro* antiplasmodium activity of the Ir(III) complex **7a** was screened against the CQS NF54 strain of *P*. *falciparum*, in the presence of varying concentrations of sodium formate.

The percentage parasite viability for two concentrations of complex **7a** (2500 and 1250 ng/ml), co-administered with sodium formate (0, 5, 10 and 20 mM), is depicted in Figure 5.10. As expected, treatment with a greater concentration of complex **7a** results in lower parasite viability. In the absence of sodium formate (0 mM), 52 and 86% parasite viability were observed for 2500 and 1250 ng/ml of complex **7a**, respectively. For both concentrations of complex **7a**, there is a stepwise decrease in the parasite viability with increasing concentrations of sodium formate. Comparing 0 mM to 20 mM sodium formate at 2500 and 1250 ng/ml of complex **7a**, there is an 11% and 9% difference in parasite viability, respectively. These differences were found to be statistically insignificant using a two-tailed t-test at the 95% confidence interval. Therefore, the effect of co-administration of sodium formate with complex **7a** on parasite viability is not significant and may suggest that complex **7a** does not have significant transfer hydrogenation activity in the parasite.

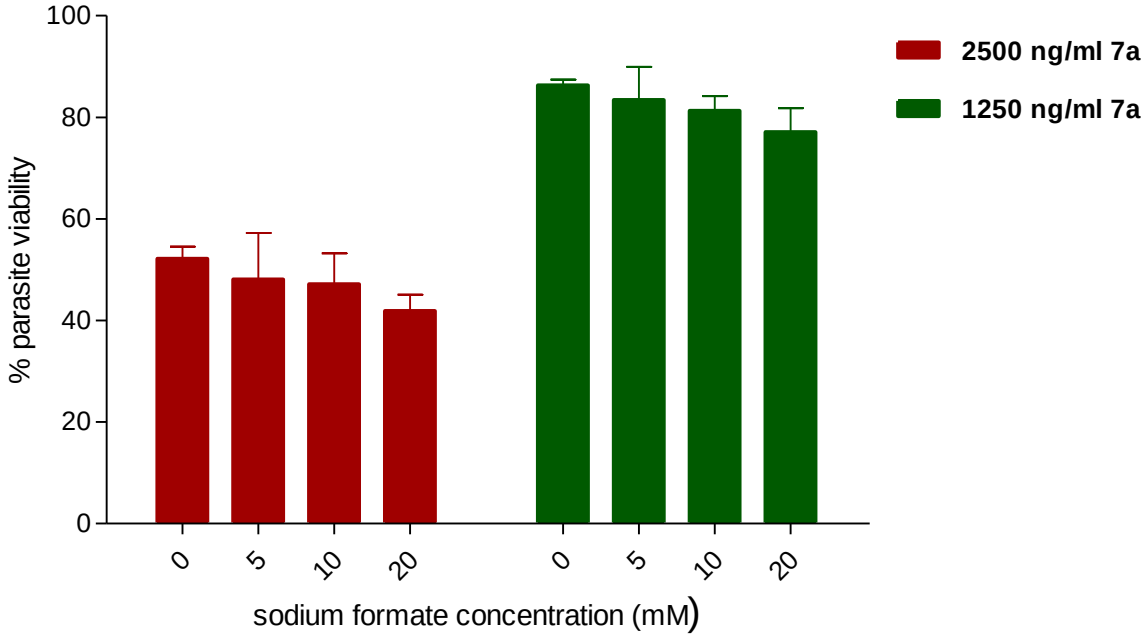

Figure 5.10 Parasite viability observed in the NF54 strain of *P. falciparum*, when complex **7a** (2500 and 1250 ng/ml) was incubated with sodium formate (0, 5, 10 and 20 mM).

5.2.3 *In vitro* antimycobacterial activity

To our knowledge, literature reports exploring the antimycobacterial properties of PGM-containing hybrid complexes are limited. An example of antimycobacterial iridium(III)- and rhodium(III)-containing hybrid complexes[29] was briefly discussed in Chapter 3 (Section 3.1). With this in mind, the *C*^*N*-coordinated and *N*^*N*-coordinated Ir(III) and Rh(III) complexes (**7** – **8** and **11** – **13**) were evaluated for their *in vitro* activity against the H37Rv strain of *M. tuberculosis*. Using the broth micro dilution method,[30] minimum inhibitory concentration (MIC) values were determined. The 7-day MIC_{90} values for the complexes as well as the control, rifampicin, are summarised in Table 5.4. The compounds were screened using two different growth media, the glucose-based Middlebrook 7H9-ADC (albumin-dextrose complex) and 7H9-CAS (casitone). Similar trends in activity were observed in both media, however, general higher activity (lower MIC_{90} values) was exhibited in the 7H9-CAS medium.

Table 5.4 Antimycobacterial activity of compounds **7** – **8** and **11** – **13**.

Compound	Day 7 MIC_{90} (μM) [media: 7H9 GLU CAS]	Day 7 MIC_{90} (μM) [media: 7H9 GLU ADC]
7a	0.488	4.244
7b	1.490	7.813
7c	1.100	3.652
8a	8.778	15.309
8b	8.183	15.800
11a	62.500	> 125
11b	39.218	> 125
11c	31.250	31.250
12a	31.250	62.500
12b	19.215	47.679
12c	17.994	31.250
13a	4.495	1.161
13b	4.233	0.889
13c	7.141	2.085
Rifampicin	0.026	0.002

The MIC_{90} values determined in the 7H9-CAS medium are graphically represented in Figure 5.11. Most of the compounds displayed moderate to good antimycobacterial activity in the range 0.488 – 62.5 μM. These PGM-containing aminoquinoline-benzimidazole hybrid complexes are significantly less active than the positive control, displaying MIC_{90} values at least twenty-fold higher than the antibiotic rifampicin (0.026 μM). With regards to the neutral complexes, the Ir(III) complexes **7a** – **7c** are significantly more active than the Rh(III) complexes **8a** – **8b**. Compounds **7a** – **7c** gave rise to MIC_{90} values between 0.488 and 1.490 μM, about 5-fold lower than that for compounds **8a** – **8b** (8.778 and 8.183 μM). For these cyclometalated complexes, there is no discernable trend with regards to the antimycobacterial activity and the substituent (X) at the 5-position of the benzimidazole.

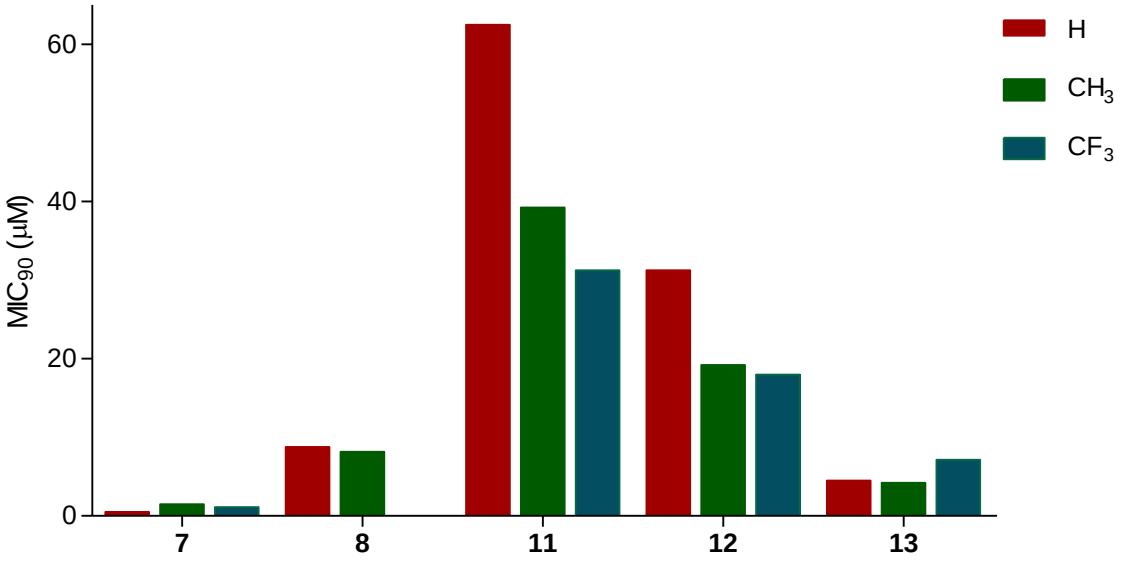

Figure 5.11 MIC_{90} values of compounds **7** – **8** and **11** – **13** against the H37Rv stain of *M. tuberculosis*.

Considering the cationic Ir(III)- and Rh(III)-Cp* complexes, **11** – **12**, an interesting trend is observed with regards to the 5-position substituent (X). For both the Ir(III) complexes (**11a** – **11c**) and the Rh(III) complexes (**12a** – **12c**), the antimycobacterial activity increases with incorporation of the hydrophobic substituents (CH_3 and CF_3). The unsubstituted Ir(III) and Rh(III) complexes (**11a** and **12a**) are the least active in the series, with MIC_{90} values of 62.5 and 31.25 μM, respectively. Substitution of the hydrophobic methyl group (**11b** and **12b**) enhances the activity, giving decreased MIC_{90} values of 39.219 and 19.215 μM, respectively. The analogues with the more hydrophobic trifluoromethyl group (**11c** and **12c**) have the lowest MIC_{90} values of 31.25 and 17.994 μM, respectively. This trend in activity suggests a correlation between hydrophobicity and the antimycobacterial activity.

The link between hydrophobicity and the antimycobacterial activity suggests a possible relationship between lipophilicity and the activity. A positive correlation was observed for the antimycobacterial activity of 2-phenyl and 2-ferrocenyl hybrid compounds, reported in Chapter 3. These findings are supported by recent studies, which have reported on the relationship between lipophilicity and antimycobacterial properties.[31-33] Contrary to what was observed for the neutral M-Cp* complexes, for the cationic M-Cp* complexes, the Ir(III) complexes **11a** – **11c** are consistently less active than their

corresponding Rh(III) analogues **12a** – **12c**. Each Rh(III) complex is almost 2-fold more active than its corresponding Ir(III) complex, as is evident in Figure 5.11. Considering the two M-Cp* series, the neutral complexes **7** – **8** significantly outperformed their corresponding cationic complexes **11** – **12**.

The cationic Rh(III)-ppy complexes, **13a** – **13c**, display good activity against *M. tuberculosis* H37Rv, with MIC_{90} values in the range 4.233 – 7.141 μM. The unsubstituted **13a** (4.495 μM) and methyl-substituted **13b** (4.233 μM) had comparable activity, while the trifluoromethyl-substituted **13c** (7.141 μM) was slightly less active. Comparing the two series of cationic compounds, the Rh(III)-ppy complexes are significantly more active than the Ir(III)- and Rh(III)-Cp* complexes. Once again, these differences in activity may be attributed to differences in hydrophobicity. Compounds **11** – **12** have a hydrophobic Cp* ligand, while compounds **13a** – **13c** each have two 2-phenylpyridyl ligands, which contributes greater hydrophobicity, and thus may confer greater antimycobacterial activity.

With regards to the strategy of organometallic derivatisation, the antimycobacterial activity of the PGM-containing complexes was compared to that of the respective ligands (described in Chapter 3). The graphs in Figure 5.12 show the comparison of the MIC_{90} values of the ligands (**4** and **6**) and the neutral (**7** – **8**) and cationic (**11** – **13**) complexes. In all cases, introduction of the Ir(III) and Rh(III) moieties resulted in enhanced antimycobacterial activity compared to the ligands. The 2-phenyl hybrid ligands (**4a** – **4c**) display moderate micromolar MIC_{90} values (15.8 – 50.6 μM) and coordination of the metal moiety results in low micromolar and even sub-micromolar MIC_{90} values for the neutral cyclometalated complexes (**7a** – **7c** and **8a** – **8b**). While the 2-pyridyl hybrid ligands (**6a** – **6c**) are inactive against *M. tuberculosis* (MIC_{90} > 125 μM), coordination of the metal gave rise to cationic complexes (**11a** – **11c**, **12a** – **12c** and **13a** – **13c**) which are active in the moderate and low micromolar range.

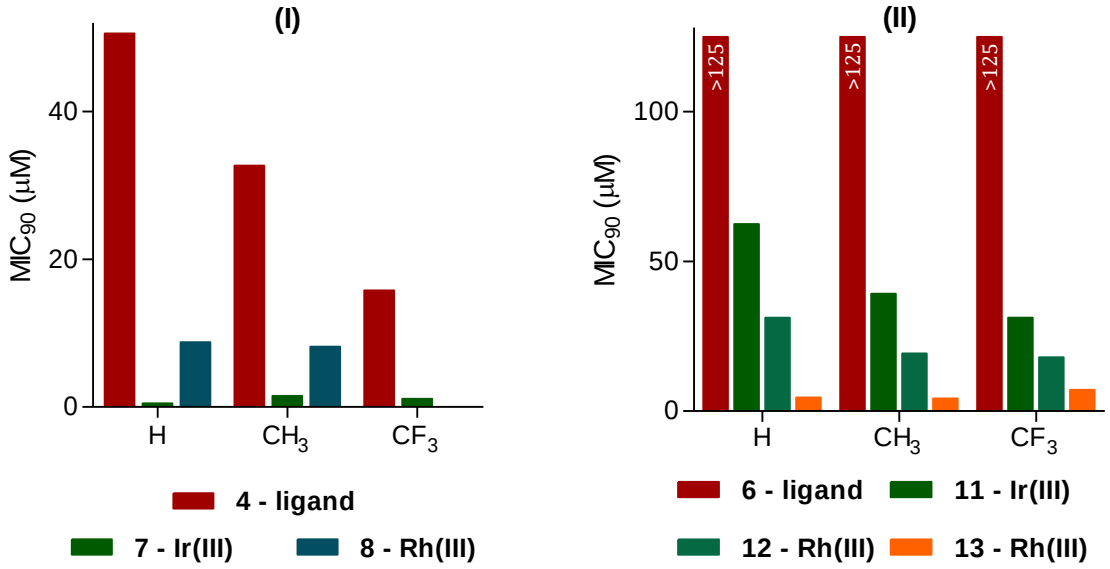

Figure 5.12 Comparison of (**I**) MIC_{90} values of the 2-phenyl hybrid ligands (**4**) and the neutral cyclometalated complexes (**7** and **8**); (**II**) MIC_{90} values of the 2-pyridyl hybrids (**6**) and the cationic complexes (**11** – **13**).

5.3 Summary

The neutral *C^N*-coordinated and cationic *N^N*-coordinated iridium and rhodium complexes (**7** – **8** and **11** – **13**) were screened for their potential antiparasitic properties against the CQS NF54 strain and MDR K1 strain of *Plasmodium falciparum*. In the NF54 strain, most compounds displayed good activity with IC_{50} values in the low to sub-micromolar range. However, within the cationic M-Cp* series, the unsubstituted and methyl-substituted Ir(III) analogues (**11a** and **11b**) were inactive at the concentration tested. When selected compounds were evaluated against the K1 strain, the neutral M-Cp* complexes and cationic Rh-ppy complexes were potent, once again displaying low to sub-micromolar IC_{50} values. In this case, the cationic M-Cp* complexes (**11c** and **12a** – **12c**) proved inactive at the test concentration. Most compounds had resistance indices equal to or above one (RI ≥ 1), indicating comparable or decreased activity in the resistant strain compared to the sensitive strain. The lower RI values (RI ≈ 1), suggest applicability of these complexes in both sensitive and resistant strains.

However, the methyl-substituted Rh(III)-ppy complex **13b** provides an exception, with a RI value of 0.728 (RI < 1), indicating enhanced activity in the resistant strain.

Selected active compounds were also screened against the non-tumorigenic Chinese hamster ovarian (CHO) cell line, in order to evaluate their cytotoxicity. The trifluoromethyl-substituted Ir(III)-Cp* complex **7c** displayed low cytotoxicity compared to the control (emetine), with a moderate micromolar IC_{50} value of 14.14 μM. All remaining compounds (**7a** – **7b**, **8a** – **8b** and **13a** – **13c**) were non-cytotoxic against the CHO cells, displaying IC_{50} values greater than 50 μM. All of the tested hybrid complexes showed selectivity toward the parasitic strains, compared to the CHO cell-line.

Selected compounds with favourable antiplasmodium and cytotoxic properties were subjected to further mechanistic studies. Active compounds from each series were screened for their β-haematin inhibition ability. In the cell-free assay, all of the evaluated compounds (**7a**, **7c**, **8a**, **8b**, **11c**, **12c** and **13b**) were determined to be good to potent inhibitors of β-haematin formation. All compounds displayed improved inhibitory effects (IC_{50} values) compared to the control, CQ. In addition, NMR spectroscopic and cell-free experiments were utilised in order to gain insight into the transfer hydrogenation ability of selected hybrid complexes (**7a** and **8a**). Both the Ir(III) complex **7a** and Rh(III) complex **8a** demonstrated the ability to catalyse the conversion of NAD^+ to NADH under biological or assay conditions. The co-administration of complex **7a** and sodium formate did not have a significant effect on NF54 parasite viability *in vitro*.

Furthermore, all of the hybrid complexes were also evaluated for activity against the H37Rv strain of *Mycobacterium tuberculosis*. Overall, all compounds displayed moderate to good antimycobacterial activity. The neutral M-Cp* complexes (**7a** – **7c** and **8a** – **8b**) and the cationic Rh(III)-ppy complexes (**13a** – **13c**) were most active, displaying low micromolar MIC_{90} values. Moderate micromolar MIC_{90} values were observed for the less active cationic M-Cp* complexes (**11a** – **11c** and **12a** – **12c**). The activity of the cationic M-Cp* complexes showed a positive correlation with the hydrophobicity of the 5-position substituent (X), suggesting a further link between antimycobacterial activity and lipophilicity.

5.4 References

1. L. J. Boerner and J. M. Zaleski, *Curr. Opin. Chem. Biol.*, 2005, **9**, 135-144.
2. K. J. Kilpin and P. J. Dyson, *Chem. Sci.*, 2013, **4**, 1410-1419.
3. M. Patra and G. Gasser, *Nat. Rev. Chem.*, 2017, **1**, 0066.
4. N. Cutillas, G. S. Yellol, C. de Haro, C. Vicente, V. Rodríguez and J. Ruiz, *Coordin. Chem. Rev.*, 2013, **257**, 2784-2797.
5. R. D. Sandlin, M. D. Carter, P. J. Lee, J. M. Auschwitz, S. E. Leed, J. D. Johnson and D. W. Wright, *Antimicrob. Agents Ch.*, 2011, **55**, 3363-3369.
6. K. K. Ncokazi and T. J. Egan, *Anal. Biochem.*, 2005, **338**, 306-319.
7. J. J. Soldevila-Barreda and N. Metzler-Nolte, *Chem. Rev.*, 2019, **119**, 829-869.
8. J. J. Soldevila-Barreda and P. J. Sadler, *Curr. Opin. Chem. Biol.*, 2015, **25**, 172-183.
9. X. Wu, X. Li, W. Hems, F. King and J. Xiao, *Org. Biomol. Chem.*, 2004, **2**, 1818-1821.
10. R. Ruppert, S. Herrmann and E. Steckhan, *J. Chem. Soc., Chem. Comm.*, 1988, 1150-1151.
11. J. J. Soldevila-Barreda, P. C. Bruijnincx, A. Habtemariam, G. J. Clarkson, R. J. Deeth and P. J. Sadler, *Organometallics*, 2012, **31**, 5958-5967.
12. J. J. Soldevila-Barreda, I. Romero-Canelón, A. Habtemariam and P. J. Sadler, *Nature Commun.*, 2015, **6**, 6582.
13. T. Stringer, D. R. Melis and G. S. Smith, *Dalton Trans.*, 2019, **48**, 13143-13148.
14. M. Patra, T. Joshi, V. Pierroz, K. Ingram, M. Kaiser, S. Ferrari, B. Spingler, J. Keiser and G. Gasser, *Chem. Eur. J.*, 2013, **19**, 14768-14772.
15. M. Makler, J. Ries, J. Williams, J. Bancroft, R. Piper, B. Gibbins and D. Hinrichs, *Am. J. Trop. Med. Hyg.*, 1993, **48**, 739-741.
16. T. J. Egan, K. R. Koch, P. L. Swan, C. Clarkson, D. A. Van Schalkwyk and P. J. Smith, *J. Med. Chem.*, 2004, **47**, 2926-2934.
17. T. Mosmann, *J. Immunol. Methods*, 1983, **65**, 55-63.
18. J. Carmichael, W. G. DeGraff, A. F. Gazdar, J. D. Minna and J. B. Mitchell, *Cancer Res.*, 1987, **47**, 936-942.
19. A. Gilewska, B. Barszcz, J. Masternak, K. Kazimierczuk, J. Sitkowski, J. Wietrzyk and E. Turlej, *J. Biol. Inorg. Chem.*, 2019, 1-16.
20. M. T. Makler and D. J. Hinrichs, *Am. J. Trop. Med. Hyg.*, 1993, **48**, 205-210.

21. R. Piper, J. Lebras, L. Wentworth, A. Hunt-Cooke, S. Houze, P. Chiodini and M. Makler, *Am. J. Trop. Med. Hyg.*, 1999, **60**, 109-118.
22. K. Nagarajan, *BBA - Gen. Subjects*, 1964, **93**, 176-179.
23. I. W. Sherman, *Am. J. Trop. Med. Hyg.*, 1966, **15**, 814-817.
24. C. R. Zerez, E. J. Roth, S. Schulman and K. R. Tanaka, *Blood*, 1990, **75**, 1705-1710.
25. K. L. Olszewski, J. M. Morrisey, D. Wilinski, J. M. Burns, A. B. Vaidya, J. D. Rabinowitz and M. Llinás, *Cell Host Microbe*, 2009, **5**, 191-199.
26. J. K. O'Hara, L. J. Kerwin, S. A. Cobbold, J. Tai, T. A. Bedell, P. J. Reider and M. Llinás, *PLoS One*, 2014, **9**, e94061.
27. M. Nakamura, A. Bhatnagar and J. Sadoshima, *Circ. Res.*, 2012, **111**, 604-610.
28. R. A. Billington, S. Bruzzone, A. De Flora, A. A. Genazzani, F. Koch-Nolte, M. Ziegler and E. Zocchi, *Mol. Med.*, 2006, **12**, 324-327.
29. E. Ekengard, I. Bergare, J. Hansson, I. Doverbratt, M. Monari, B. Gordhan, B. Kana, C. de Kock, P. J. Smith and E. Nordlander, *J. Mex. Chem. Soc.*, 2017, **61**, 158-166.
30. J. Jorgensen and J. Turnidge, in *Manual of Clinical Microbiology, Eleventh Edition*, American Society of Microbiology, 2015, pp. 1253-1273.
31. R. C. Goldman, *Tuberculosis*, 2013, **93**, 569-588.
32. V. Makarov, B. Lechartier, M. Zhang, J. Neres, A. M. van der Sar, S. A. Raadsen, R. C. Hartkoorn, O. B. Ryabova, A. Vocat and L. A. Decosterd, *EMBO Mol. Med.*, 2014, **6**, 372-383.
33. G. Piccaro, G. Poce, M. Biava, F. Giannoni and L. Fattorini, *J. Antibiot.*, 2015, **68**, 711.

Chapter 6:

Conclusions and Future Outlook

6.1 Conclusions

The overall aim of this project was to develop aminoquinoline-benzimidazole hybrid compounds and their organometallic complexes as antimicrobial agents. Initially, a series of 2-phenyl (**4a** – **4e**), 2-ferrocenyl (**5a** – **5e**) and 2-pyridyl (**6a** – **6e**) aminoquinoline-benzimidazole hybrids were synthesised through successive nucleophilic aromatic substitution, reduction and cyclo-condensation reactions. Subsequently, the most pharmacologically active 2-phenyl hybrid ligands were reacted with Platinum Group Metal dimers, $[Ir(Cp^*)Cl_2]_2$ and $[Rh(Cp^*)Cl_2]_2$. This afforded neutral *C^N*-coordinated M-Cp* complexes (**7a** – **7c** and **8a** – **8b**) *via* C-H activation reactions, as well as quinoline *N*-coordinated M-Cp* complexes (**9a** – **9c** and **10a** – **10c**). Furthermore, the 2-pyridyl hybrid ligands were reacted with $[Ir(Cp^*)Cl_2]_2$ and $[Rh(Cp^*)Cl_2]_2$, as well as $[Rh(ppy)_2Cl]_2$ to yield cationic *N^N*-coordinated M-Cp* (**11a** – **11c** and **12a** – **12c**) and Rh(III)-ppy (**13a** – **13c**) complexes, respectively. The proposed compound structures were confirmed through characterisation using ^1H and $^{13}C\{^1H\}$ NMR spectroscopy, IR spectroscopy and mass spectrometry.

The 2-phenyl, 2-ferrocenyl and 2-pyridyl hybrid compounds were evaluated for their *in vitro* activity against the chloroquine-sensitive (CQS) NF54 and multidrug-resistant (MDR) K1 strains of *Plasmodium falciparum*. The organic and ferrocenyl hybrids displayed good activity against the NF54 strain, with IC_{50} values in the low to sub-micromolar range (5.553 – 0.329 μM). In general, the phenyl and ferrocenyl hybrid compounds were more potent in the resistant K1 strain, with most mostly sub-micromolar IC_{50} values (0.658 – 0.151 μM). For most of the hybrids, the resistance indices were less than one (RI < 1), indicating the absence of cross-resistance with CQ, and suggesting greater applicability in resistant strains. In contrast, the methylsulfonyl-substituted phenyl hybrid (**4d**) and pyridyl hybrids (**6a** and **6c**) were comparatively less active in the K1 strain (RI > 1). These hybrids are among the least lipophilic in the series.

The effect of ferrocenyl derivatisation on the antiplasmodium activity was inconsistent across the two strains. In some cases, the ferrocenyl hybrids (**5a** – **5e**) were more active than the phenyl analogues (**4a** – **4e**), and in others not. The most active phenyl, ferrocenyl and pyridyl hybrids overall were compounds **4c** (CF_3), **5b** (CH_3) and **6c** (CF_3), respectively. These all contain hydrophobic substituents, suggesting a correlation between hydrophobicity and antiplasmodium activity. In general, the antiplasmodium activity of these hybrids can be summarised as seen below:

2-phenyl hybrids ≈ 2-ferrocenyl hybrids > 2-pyridyl hybrids

The individual aminoquinoline (**B1**) and benzimidazole (**B2**) components of the general hybrid structure were also screened in order to assess their efficacy compared to that of the hybrid. Most significantly, hybrid **4a** was more potent than either of the individual components in the resistant K1 strain. This result indicates that the combination of the two components allows the hybrid to overcome or evade resistance in K1 parasites, rather than the enhanced K1 activity being attributed to the influence of either component. Combination studies in the sensitive NF54 strain revealed that an equimolar physical mixture of components (**B1**+**B2**) was more active than hybrid **4a**, indicating that in this case, a 'combination therapy' was more efficacious than the corresponding 'hybrid therapy'. Furthermore, isobologram analysis of the individual components in the NF54 strain revealed additive and antagonistic relationships for the co-administration of components **B1** and **B2** in different relative concentrations. In combination, the aminoquinoline confers activity, while the benzimidazole has no enhancing effect or decreases activity, indicating that this combination is not ideal as a physical mixture against the NF54 strain. This conclusion does not hold for the aminoquinoline-benzimidazole hybrid in the resistant K1 strain.

The phenyl and ferrocenyl hybrids were evaluated for their cytotoxicity against the non-tumorigenic Chinese Hamster Ovarian (CHO) cell line. All of the hybrid compounds were non-cytotoxic and selectivity indices indicated selectivity toward the *P. falciparum* strains (SI > 1). Based on their favourable *in vitro* antiplasmodium activity and non-cytotoxicity, the most active 2-phenyl hybrid (**4c**) and 2-ferrocenyl hybrid (**5b**) were evaluated *in vivo* against *Plasmodium berghei* in mice. Oral administration (4 × 50 mg/kg) with ferrocenyl hybrid **5b** resulted in 92% reduction in parasitemia, while phenyl hybrid

4c resulted in 58% reduction. The organometallic hybrid was a significantly more potent inhibitor than the organic hybrid *in vivo*.

The most active phenyl, ferrocenyl and pyridyl hybrids (**4c**, **5b** and **6c**) were subjected to a β-haematin inhibition assay and were all found to be good to potent inhibitors of synthetic haemozoin formation under the cell-free assay conditions. The β-haematin inhibition activity correlated well with lipophilicity, where hybrids **4c** and **5b**, with higher logP values were significantly more active than hybrid **6c**, which has a lower logP value. To confirm this mechanism of action in the parasite, a cellular haem fractionation assay was performed using ferrocenyl hybrid **5b**, which confirmed that it is a bona fide haemozoin inhibitor in the parasite. In the interest of exploring a possible multifaceted mode of action of these hybrids, reactive oxygen species (ROS) generation of the ferrocenyl hybrids was investigated by means of a DNA-cleavage assay. However, hybrid **5b** displayed insignificant ROS-generating ability in this preliminary study.

In addition, all organic and ferrocenyl aminoquinoline-benzimidazole hybrids were screened for their *in vitro* activity against the H37Rv strain of *Mycobacterium tuberculosis*. The substituent at the 5-position of the benzimidazole played a pivotal role in tuning the antimycobacterial activity. Substitution with the less hydrophobic groups (SO_2CH_3 and CN) resulted in hybrids (**4d** – **4e** and **5d** – **5e**) which were inactive at the maximum tested concentration. On the other hand, substitution with the more hydrophobic groups (CH_3 and CF_3) gave hybrids (**4b** – **4c** and **5b** – **5c**) with moderate to good activity (32.7 – 10.8 μM). The 5-position substituent of the hybrid significantly affected logP values, revealing a positive correlation between lipophilicity and antimycobacterial activity. It is worth noting that the more lipophilic ferrocenyl hybrids were consistently more potent than their corresponding less lipophilic phenyl analogues, while the least lipophilic pyridyl hybrids were inactive (MIC_{90} > 125 μM).

2-ferrocenyl hybrids > 2-phenyl hybrids > 2-pyridyl hybrids

Furthermore, when evaluated against the H37Rv strain, the individual aminoquinoline (**B1**) and benzimidazole (**B2**) components, administered individually, proved less active than the corresponding hybrid (**4a**) against the H37Rv strain. The results of the

individual component studies and aforementioned combination studies reveal merit in the development of hybrid antimicrobial agents.

The *C^N*- and *N^N*-coordinated PGM hybrid complexes were also evaluated against the CQS NF54 and MDR K1 strains of *P*. *falciparum*. In the sensitive NF54 strain, the hybrid complexes generally displayed good activity in the low to sub-micromolar range (2.007 – 0.194 μM). When tested in the resistant K1 strain, the cationic M-Cp* complexes (**11c**, **12a** – **12c**) did not retain activity, proving inactive at the tested concentration. The remaining neutral M-Cp* and cationic Rh(III)-ppy complexes retained activity in the K1 strain, displaying comparable or slightly higher IC_{50} values (2.844 – 0.228 μM) compared to that in the NF54 strain. Resistance indices for these complexes were greater than or equal to one (RI = 1 – 3), significantly lower than that of CQ. The lower RI values bode well for their application against both sensitive and resistant strains. Overall, the cationic Rh(III)-ppy complexes were most potent across both strains, with complex **13b** being the most active and the only compound in the series demonstrating enhanced activity in the resistant K1 strain (RI < 1). Within this series of PGM-containing hybrids, the antiplasmodium activity can be summarised as follows:

cationic Rh(III)-ppy > neutral Ir(III)/Rh(III)-Cp* > cationic Ir(III)/Rh(III)-Cp*

When considering the effect of organometallic derivatisation on the antiplasmodium activity, contrasting trends were observed. However, the cationic Rh(III)-ppy complexes (**13a** – **13c**) consistently displayed enhanced activity compared to the ligands (**6a** – **6c**) across both strains of *P*. *falciparum*. Selected hybrid complexes were evaluated against non-tumorigenic CHO cells, displaying non-cytotoxicity overall. SI values indicate great selectivity toward *P*. *falciparum* and suggest that the antiplasmodium activity of these complexes may be attributed to mechanisms other than general cytotoxicity. Once again, β-haematin inhibition was explored as a possible mechanism of action. The selected PGM-containing hybrid complexes (**7a**, **7c**, **8a**, **8b**, **11c**, **12c** and **13b**) displayed potent inhibition of β-haematin formation, with the Ir(III)-Cp* complexes consistently outperforming the Rh(III)-Cp* complexes.

In a bid to explore a potentially novel mode of antiplasmodium action, the transfer hydrogenation catalytic ability of Ir(III) and Rh(III) *C^N*-coordinated hybrid complexes

(**7a** and **8a**) was investigated. The hybrid complexes were used to effect the reduction of NAD^+ to NADH, in the presence of sodium formate as the hydride source. In ^1H NMR experiments and under cell-free assay conditions, both complexes demonstrated the ability to catalyse the conversion. However, in the *in vitro* antiplasmodium assay, co-administration of Ir(III) complex **7a** with sodium formate did not have a significant effect on parasite viability (NF54). This suggests that the extent of transfer hydrogenation is not significant within the parasite.

Furthermore, the *C^N*- and *N^N*-coordinated PGM hybrid complexes (**7** – **8** and **11** – **13**) generally displayed moderate to good activity when screened against *M*. *tuberculosis* H37Rv. The neutral M-Cp* and cationic Rh(III)-ppy complexes displayed low micromolar MIC_{90} values (8.78 – 0.488 μM), significantly outperforming the cationic M-Cp* complexes (62.50 – 17.99 μM). Overall, the Ir(III) *C^N*-coordinated complexes were most potent, displaying MIC_{90} values in the low to sub-micromolar range (1.490 – 0.488 μM). It is interesting to note that with regards to antimycobacterial activity, the PGM-containing hybrid complexes were consistently more active than the corresponding ligands. In the case of complex **7a**, metal coordination resulted in a 100-fold increase in activity compared to ligand **4a**. It can thus be concluded that in this study, incorporation of PGMs into organic hybrid scaffolds results in significantly enhanced antimycobacterial activity.

PGM-containing hybrid complexes >>> organic hybrid ligands

6.2 Future outlook

The aminoquinoline-benzimidazole hybrids and their PGM-containing complexes studied herein display promising pharmacological properties. These results do, however, raise a few further questions and new ideas, which can be addressed through structural modifications of the hybrids, as well as further pharmacological and mechanistic studies.

An important question to be answered is with regards to what happens to the hybrid compound once it has been administered to a living organism. Pharmacokinetics refers to the study of how a drug is absorbed, distributed, metabolised and excreted (ADME). In our study of the *in vivo* efficacy of selected hybrid compounds in *P*. *berghei*-infected mice ferrocenyl hybrid **5b** displayed significantly enhanced inhibition compared to phenyl hybrid **4c**. An evaluation of the pharmacokinetics may help to understand why there is a vast difference in activity at the *in vivo* level, compared to similar activity *in vitro*. Furthermore, a study of all four properties may also aid in rationalizing why mice treated with either hybrid compound had the same mean survival time, despite the aforementioned more potent inhibition exhibited by hybrid **5b**.

Another question which arises, is whether or not these hybrids maintain the same mechanism of action in both sensitive and resistant strains of *P*. *falciparum*. The organic and organometallic hybrids displayed potent β-haematin inhibition activity and the ferrocenyl hybrid **5b** was confirmed to inhibit haemozoin formation in sensitive NF54 parasites. With this in mind, cellular haem fractionation experiments on these hybrids could be conducted using resistant K1 parasites, in order to confirm that the mechanism of action is maintained. Furthermore, hybrid agents are speculated to act *via* dual or multiple modes of action. Therefore, additional mechanistic studies could be undertaken to elucidate the possible additional modes of action which are coupled to haemozoin inhibition for these hybrids. The inhibition of enzymes, such as cysteine protease and dihydroorotate dehydrogenase, could be investigated in this regard.

Modifications, based on the outcomes of this study, can be made to the hybrid structure in order to enhance pharmacological properties. The preparation of an optimised ferrocenyl hybrid is proposed for enhanced antimalarial activity. It is clear from the potent activity of ferroquine, as well as the ferrocenyl hybrids in this study, that

incorporation of the ferrocenyl moiety often results in enhanced activity in resistant strains of *P. falciparum* (RI < 1). The improved activity of the ferrocenyl analogues may be the result of a number of factors including increased lipophilicity and redox accessibility. In some instances, highly lipophilic compounds may have decreased cellular uptake due to strong interactions with cell membranes. To counteract this effect, a water-soluble substituent can be incorporated at the 5-position of the benzimidazole, which may also improve the overall solubility of the hybrid. An additional secondary amine could also be incorporated into the linker, which may enhance accumulation in the digestive vacuole through pH trapping, thus leading to enhanced activity. The proposed structural modifications to the hybrid are depicted in Figure 6.1.

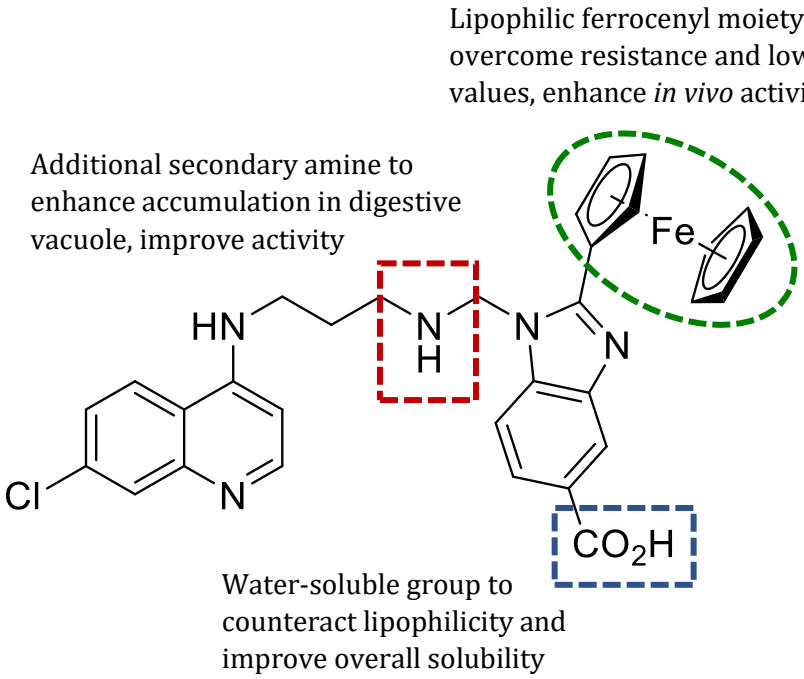

Figure 6.1 Structural modifications for a new potential antimalarial hybrid.

This study revealed the use of organometallic hybrid compounds against *M. tuberculosis* to be a promising endeavor. Incorporation of the ferrocenyl or PGM moieties significantly enhanced antimycobacterial activity compared to their corresponding organic analogues. The neutral Ir(III)-Cp* hybrid complexes (**7a** – **7c**) displayed low to sub-micromolar MIC_{90} values against the susceptible H37Rv strain. These hybrid complexes should be further evaluated against MDR-TB strains, in order to gauge whether or not they retain their potent activity. Furthermore, structural modifications can be made to the hybrids at

hand, to improve their antimycobacterial properties. We propose an organometallic hybrid incorporating the highly lipophilic ferrocenyl moiety as well as an Ir(III)-Cp* entity. This can be achieved through the cyclometalation of a ferrocenyl hybrid with an Ir(III)-Cp* moiety, to afford the neutral heterobimetallic complex shown in Figure 6.2. This modification would ideally combine the favourable effects of the two moieties, resulting in potentially further enhanced antimycobacterial activity.

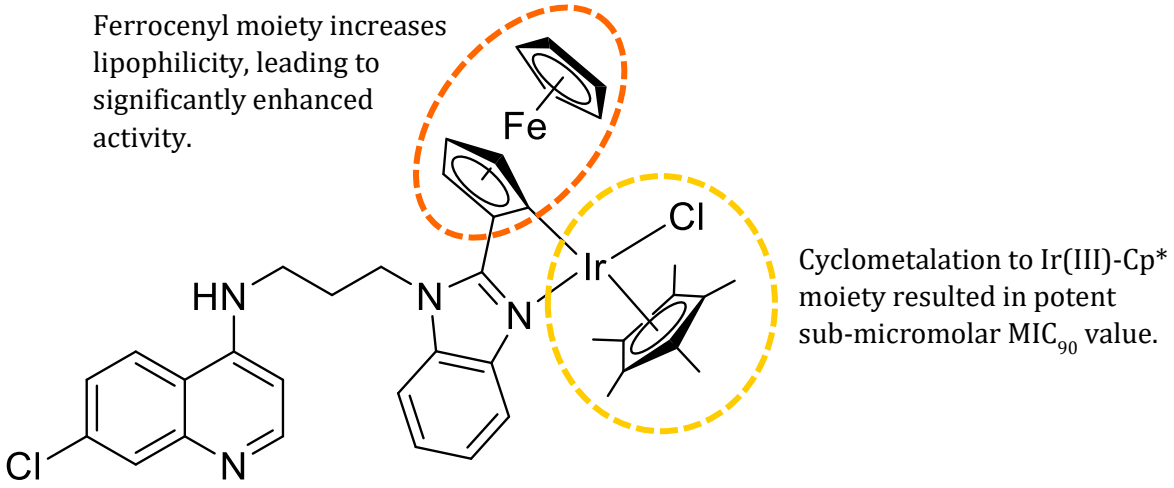

Figure 6.2 Structural modification for a new potential antimycobacterial hybrid.

Chapter 7:

Experimental

7.1 General remarks

All reagents and solvents were purchased from commercial sources (Sigma Aldrich, Combi-blocks, Kimix and Merck). The aminoquinoline precursor, *N*^{1}-(7-chloroquinolin-4-yl)-propane-1,3-diamine (**1**),[1] and the metal dimers, $[Ir(Cp^*)Cl_2]_2$,[2] $[Rh(Cp^*)Cl_2]_2$,[2] and $[Rh(ppy)_2Cl]_2$,[3] were prepared using modified literature methods.

Infrared (IR) absorptions were measured on a Perkin-Elmer Spectrum 100 FT-IR spectrometer using Attenuated Total Reflectance (ATR). Nuclear Magnetic Resonance (NMR) spectra were recorded on a Varian Mercury XR300 MHz (^{1}H at 300.08 MHz), a Bruker 400 Biospin GmbH (^{1}H at 400.22 MHz, ^{13}C{^{1}H} at 100.65 MHz, ^{31}P{^{1}H} at 161.80 MHz) or a Bruker 600 FT spectrometer (^{1}H at 600.10 MHz, ^{13}C{^{1}H} at 150.60 MHz) spectrometer at 30 °C. Chemical shifts are reported using tetramethylsilane (TMS) as the internal standard. Mass spectrometry determinations were carried out using Electron Impact (EI) on a JEOL GC Matell instrument or Electrospray Ionisation (ESI) on a Waters API Quattro Micro triple quadrupole mass spectrometer with data recorded using both the positive and negative modes. Melting points were determined using a Büchi Melting Point Apparatus B-540.

Purity was determined using an analytical Agilent HPLC 1260 equipped with an Agilent DAD 1260 UV/vis detector and a X Bridge C18 column (2.5 µM, 50 mm × 3 mm). The compounds were eluted using a mixture of solvent A (10 mM NH_4OAc/H_2O) and solvent B (10 mM NH_4OAc/MeOH) at a flow rate of 0.9 mL/min (**4a** – **4e** and **6a** – **6c**) or 0.5 mL/min (**5a** – **5e**). The gradient elution conditions for compounds **4a** – **4e** and **6a** – **6c** were as follows: 15% solvent B between 0 and 0.5 min, 15–100% solvent B between 0.5 and 1.2 min, 100% solvent B between 1.2 and 4.5 min. The gradient elution conditions for compounds **5a** – **5e** were as follows: 10% solvent B between 0 and 2 min, 10–90% solvent B between 2 and 8 min, 90% solvent B between 8 and 9 min. Purity was determined at 280 nm. All compounds were confirmed to have >97% purity.

Single-crystal X-ray diffraction data were collected on a Bruker KAPPA APEX II DUO diffractometer using graphite-monochromated Mo-Kα radiation (χ = 0.71073 Å). Data collection was carried out at 173(2) K for compounds **4b** and **5c**, and 100(2) K for compound **11b**. Temperature was controlled by an Oxford Cryostream cooling system (Oxford Cryostat). Cell refinement and data reduction were performed using the program SAINT.[4] The data were scaled, and absorption correction performed using SADABS.[5] The structures were solved by direct methods using SHELXS-97[5] and refined by full-matrix least-squares methods based on F^2 using SHELXL-2014[5] or SHELXL-2018[5] and using the graphics interface program X-Seed.[6, 7] The programs X-Seed and POV-Ray[8] were used to prepare molecular graphic images.

7.2 Aminoquinoline precursors

7.2.1 General method for synthesis of nitro-containing precursors (2a – 2e)

A nitrobenzene derivative (1.5 eq.) was added to a stirring solution of compound **1** (1 eq.) in anhydrous DMF (5 ml), and the reaction mixture was stirred at room temperature under N_2 for 24 hours. Thereafter, 1 M NaOH (50 ml) was added to basify the mixture, which was then extracted with DCM or EtOAc (3 × 50 ml). The organic fractions were collected and washed with brine (3 × 50 ml). The organic layer was collected, dried over anhydrous Na_2SO_4 and filtered by gravity. The solvent of the filtrate was removed to afford the crude product as a bright yellow or orange solid. The crude product was purified by column chromatography (silica gel) using DCM:MeOH (19:1). Subsequent trituration in diethyl ether afforded the desired product as a bright yellow or orange powder, which was collected by suction filtration.

*N^1-(7-chloroquinolin-4-yl)-N^3-(2-nitrophenyl)-propane-1,3-diamine (**2a**)*

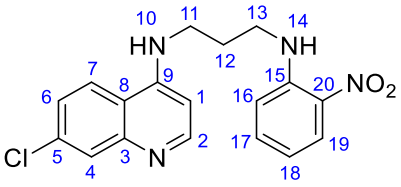

1-Fluoro-2-nitrobenzene (1.02 ml, 9.67 mmol), compound **1** (1.52 g, 6.45 mmol). Product: Yellow powder. Yield: 1.20 g, 52.2%. R_f(DCM:MeOH, 19:1): 0.25. **M.p.** 181.9 – 183.6 °C. **^{1}H NMR (400 MHz, DMSO-d_6):** δ (ppm) = 8.39 (d, $^3J_{HH}$ = 5.5 Hz, 1H, H-2), 8.25 (d, $^3J_{HH}$ = 9.1 Hz, 1H, H-7), 8.20 (t, $^3J_{HH}$ = 5.7 Hz, 1H, H-14), 8.06 (dd, $^3J_{HH}$ = 8.6, $^4J_{HH}$ = 1.6 Hz, 1H, H-19), 7.79 (d, $^3J_{HH}$ = 2.3

Hz, 1H, H-4), 7.50 (m, 1H, H-17), 7.45 (dd, $^{3}J_{HH}$ = 9.1, $^{4}J_{HH}$ = 2.3 Hz, 1H, H-6), 7.35 (t, $^{3}J_{HH}$ = 5.4 Hz, 1H, H-10), 7.08 (dd, $^{3}J_{HH}$ = 8.7, $^{4}J_{HH}$ = 0.9 Hz, 1H, H-16), 6.68 (m, 1H, H-18), 6.49 (d, $^{3}J_{HH}$ = 5.5 Hz, 1H, H-1), 3.51 (q, $^{3}J_{HH}$ = 6.6 Hz, 2H, H-13), 3.40 (q, $^{3}J_{HH}$ = 6.6 Hz, 2H, H-11), 2.03 (p, $^{3}J_{HH}$ = 6.8 Hz, 2H, H-12). **^{13}C{^{1}H} NMR (101 MHz, DMSO-*d*$_6$):** δ (ppm) = 152.4, 150.5, 149.6, 145.6, 137.0, 133.9, 131.6, 128.0, 126.8, 124.5 (2C), 118.0, 115.6, 114.9, 99.2, 40.5, 40.4, 27.5. **FT-IR (ATR, cm^{-1}):** ν = 3377 (N–H), 3306 (N–H), 1621 (C=N), 1568 (C=C), 1530 (N–O), 1360 (N–O). **EI-MS:** *m*/*z* 355.95 (91.0%, [M]$^{+}$), calculated 356.10.

*N^{1}-(7-chloroquinolin-4-yl)-N^{3}-(4-methyl-2-nitrophenyl)propane-1,3-diamine (**2b**)*

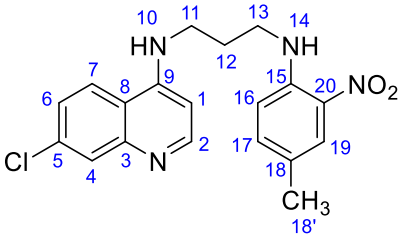

4-Fluoro-3-nitrotoluene (0.992 g, 6.40 mmol), compound **1** (1.00 g, 4.24 mmol). Product: Orange powder. Yield: 0.688 g, 43.7%. R$_f$(DCM:MeOH, 19:1): 0.23. **M.p.** 198.1 – 199.9 °C. **^{1}H NMR (400 MHz, DMSO-*d*$_6$):** δ (ppm) = 8.39 (d, $^{3}J_{HH}$ = 5.5 Hz, 1H, H-2), 8.26 (d, $^{3}J_{HH}$ = 9.0 Hz, 1H, H-7), 8.12 (t, $^{3}J_{HH}$ = 5.7 Hz, 1H, H-14), 7.87 (m, 1H, H-19), 7.79 (d, $^{4}J_{HH}$ = 2.3 Hz, 1H, H-4), 7.45 (dd, $^{3}J_{HH}$ = 9.0, 2.3 Hz, 1H, H-6), 7.38 – 7.32 (overlapping m, 2H, H-10/17), 7.01 (d, $^{3}J_{HH}$ = 9.0 Hz, 1H, H-16), 6.49 (d, $^{3}J_{HH}$ = 5.5 Hz, 1H, H-1), 3.49 (q, $^{3}J_{HH}$ = 6.6 Hz, 2H, H-13), 3.39 (q, $^{3}J_{HH}$ = 6.6 Hz, 3H, H-11), 2.22 (s, 3H, H-18'), 2.01 (p, $^{3}J_{HH}$ = 6.8 Hz, 2H, H-12). **^{13}C{^{1}H} NMR (101 MHz, DMSO-*d*$_6$):** δ (ppm) = 152.4, 150.5, 149.6, 144.0, 138.5, 133.9, 131.1, 128.0, 125.7, 124.7, 124.5 (2C), 118.0, 115.0, 99.2, 40.5, 40.4, 27.6, 19.9. **FT-IR (ATR, cm^{-1}):** ν = 3417 (N–H), 3361 (N–H), 1609 (C=N), 1570 (C=C), 1520 (N–O), 1350 (N–O). **EI-MS:** *m*/*z* 370.04 (100%, [M]$^{+}$), calculated 370.12.

*N^{1}-(7-chloroquinolin-4-yl)-N^{3}-(2-nitro-4-(trifluoromethyl)phenyl)propane-1,3-diamine (**2c**)*

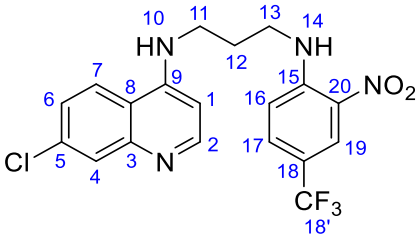

4-Chloro-3-nitrobenzotrifluoride (01.43 ml, 9.58 mmol), compound **1** (1.51 g, 6.41 mmol). Product: Yellow powder. Yield: 1.54 g, 56.6%. R$_f$(DCM:MeOH, 19:1): 0.21. **M.p.** 210.4 – 212.8 °C. **^{1}H NMR (400 MHz, DMSO-*d*$_6$):** δ (ppm) = 8.56 (t, $^{3}J_{HH}$ = 5.8 Hz, 1H, H-14), 8.39 (d, $^{3}J_{HH}$ = 5.5 Hz, 1H, H-2), 8.30 (dd, $^{3}J_{HH}$ = 2.3, $^{4}J_{HH}$ = 0.9 Hz, 1H, H-19), 8.24 (d, $^{3}J_{HH}$ = 9.1 Hz, 1H, H-7), 7.79 (d, $^{4}J_{HH}$ = 2.3 Hz, 1H, H-4), 7.75 (dd, $^{3}J_{HH}$ = 9.2, $^{4}J_{HH}$ = 2.3 Hz, 1H, H-17), 7.45 (dd, $^{3}J_{HH}$ = 9.0, $^{4}J_{HH}$ = 2.3 Hz, 1H, H-6), 7.34 (t, $^{3}J_{HH}$ = 5.4 Hz, 1H, H-10), 7.28 (d, $^{3}J_{HH}$ =

9.2 Hz, 1H, H-16), 6.50 (d, $^3J_{HH}$ = 5.5 Hz, 1H, H-1), 3.58 (q, $^3J_{HH}$ = 6.6 Hz, 2H, H-13), 3.40 (q, $^3J_{HH}$ = 6.6 Hz, 2H, H-11), 2.02 (p, $^3J_{HH}$ = 6.7 Hz, 2H, H-12). **^{13}C{^{1}H} NMR (101 MHz, DMSO-*d*$_6$):** δ (ppm) = 152.4, 150.5, 149.6, 147.2, 133.9, 132.3, 130.7, 128.0, 124.6, 124.5 (2C), 123.0 118.0, 116.4, 115.5, 99.2, 40.8, 40.3, 27.3. **FT-IR (ATR, cm^{-1}):** ν = 3361 (N–H), 3218 (N–H), 1609 (C=N), 1568 (C=C), 1536 (N–O), 1366 (N–O), 1324 (C–F). **EI-MS:** *m*/*z* 423.99 (94%, [M]$^+$), calculated 424.09.

*N^1-(7-chloroquinolin-4-yl)-N^3-(4-(methylsulfonyl)-2-nitrophenyl)propane-1,3-diamine (**2d**)*

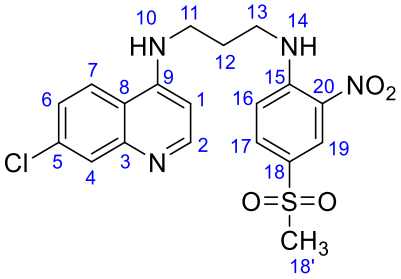

1-Fluoro-4-methanesulfonyl-2-nitrobenzene (0.848 g, 3.87 mmol), compound **1** (0.625 g, 2.65 mmol). Product: Yellow powder. Yield: 0.516 g, 46.0%. R$_f$(DCM:MeOH, 19:1): 0.17. **M.p.** 202.0 – 204.4 °C. **^{1}H NMR (400 MHz, DMSO-*d*$_6$):** δ (ppm) = 8.69 (t, $^3J_{HH}$ = 5.9 Hz, 1H, H-14), 8.50 (d, $^4J_{HH}$ = 2.3 Hz, 1H, H-19), 8.40 (d, $^3J_{HH}$ = 5.4 Hz, 1H, H-2), 8.24 (d, $^3J_{HH}$ = 9.1 Hz, 1H, H-7), 7.89 (dd, $^3J_{HH}$ = 9.1, $^4J_{HH}$ = 2.2 Hz, 1H, H-17), 7.79 (d, $^4J_{HH}$ = 2.2 Hz, 1H, H-4), 7.46 (dd, $^3J_{HH}$ = 9.0, $^4J_{HH}$ = 2.3 Hz, 1H, H-6), 7.34 (t, $^3J_{HH}$ = 5.4 Hz, 1H, H-10), 7.30 (d, $^3J_{HH}$ = 9.3 Hz, 1H, H-16), 6.51 (d, $^3J_{HH}$ = 5.5 Hz, 1H, H-1), 3.61 (q, $^3J_{HH}$ = 6.5 Hz, 2H, H-13), 3.39 (q, $^3J_{HH}$ = 6.5 Hz, 2H, H-11), 3.20 (s, 3H, H-18') 2.03 (p, $^3J_{HH}$ = 6.7 Hz, 2H, H-12). **^{13}C{^{1}H} NMR (101 MHz, DMSO-*d*$_6$):** δ (ppm) = 152.4, 150.5, 149.5, 147.8, 133.9 (2C), 130.5, 128.0, 127.5, 126.7, 124.5 (2C), 118.0, 116.1, 99.2, 44.3, 40.9, 40.3, 27.2. **FT-IR (ATR, cm^{-1}):** ν = 3381 (N–H), 3218 (N–H), 1617 (C=N), 1570 (C=C), 1520 (N–O), 1368 (S=O), 1350(N–O), 1136 (S=O). **EI-MS:** *m*/*z* 433.97 (38.5%, [M]$^+$), calculated 434.08.

*4-((3-((7-chloroquinolin-4-yl)amino)propyl)amino)-3-nitrobenzonitrile (**2e**)*

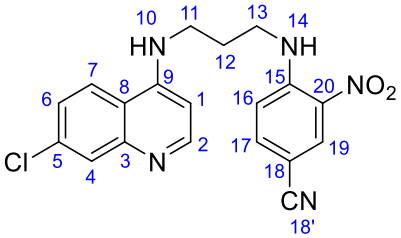

4-Chloro-3-nitrobenzonitrile (0.587 g, 3.22 mmol), compound **1** (0.513 g, 2.18 mmol). Product: Yellow powder. Yield: 0.415 g, 51.8%. R$_f$(DCM:MeOH, 19:1): 0.19. **M.p.** 205.7 – 207.9 °C. **^{1}H NMR (400 MHz, DMSO-*d*$_6$):** δ (ppm) = 8.66 (t, $^3J_{HH}$ = 5.8 Hz, 1H, H-14), 8.50 (d, $^4J_{HH}$ = 2.0 Hz, 1H, H-19), 8.39 (d, $^3J_{HH}$ = 5.5 Hz, 1H, H-2), 8.23 (d, $^3J_{HH}$ = 9.1 Hz, 1H, H-7), 7.80 – 7.77 (overlapping m, 2H, H-4/17), 7.45 (dd, $^3J_{HH}$ = 9.1, $^4J_{HH}$ = 2.3 Hz, 1H, H-6), 7.33 (t, $^3J_{HH}$ = 5.4 Hz, 1H, H-10), 7.23 (d, $^3J_{HH}$ = 9.2 Hz, 1H, H-16), 6.50 (d, $^3J_{HH}$ = 5.5 Hz, 1H,

H-1), 3.58 (q, $^{3}J_{HH}$ = 6.6 Hz, 2H, H-13), 3.39 (q, $^{3}J_{HH}$ = 6.6 Hz, 2H, H-11), 2.01 (p, $^{3}J_{HH}$ = 6.7 Hz, 2H, H-12). **^{13}C{^{1}H} NMR (101 MHz, DMSO-*d*$_6$):** δ (ppm) = 152.4, 150.4, 149.5, 147.3, 138.1, 133.9, 132.4, 131.3, 128.0, 124.5 (2C), 118.7, 118.0, 116.2, 99.2, 96.8, 40.8, 40.3, 27.2. **FT-IR (ATR, cm^{-1}):** ν = 3369 (N–H), 3306 (N–H), 2222 (C≡N), 1621 (C=N), 1578 (C=C), 1522 (N–O), 1367 (N–O). **EI-MS:** *m*/*z* 381.02 (74.4%, [M]$^{+}$), calculated 381.10.

7.2.2 General method for synthesis of 1,2-diamine precursors (3a – 3e)

Ammonium chloride (10 eq.) was added to a stirring mixture of the appropriate nitro-containing aminoquinoline precursor (**2a** – **2e**) (1 eq.) in anhydrous methanol (100 ml) and the yellow mixture was stirred under N_2 for 15 min. Zinc powder (20 eq.) was then added, and the resulting grey mixture was stirred vigorously at room temperature under N_2 for 24 hours. Thereafter, 1 M NaOH (20 ml) was added to basify the mixture, which was then filtered through Celite®. The MeOH was removed under reduced pressure, and the aqueous mixture extracted using DCM (3 × 50 ml). The organic fractions were collected and washed with brine (2 × 50 ml), followed by water (1 × 50 ml). The organic layer was collected, dried over anhydrous Na_2SO_4 and filtered by gravity. The solvent of the filtrate was removed to afford the desired product as a brown, beige, pink or purple powder.

*N^{1}-(3-((7-chloroquinolin-4-yl)amino)propyl)benzene-1,2-diamine (**3a**)*

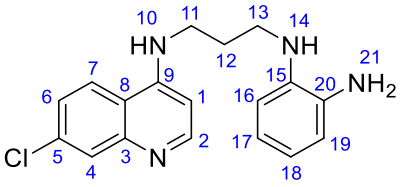

Ammonium chloride (0.757 g, 14.2 mmol), compound **2a** (0.503 g, 1.41 mmol), zinc powder (1.87 g, 28.6 mmol). Product: Brown powder. Yield: 0.440 g, 95.5%. **M.p.** 169.1 – 170.8 °C. **^{1}H NMR (400 MHz, DMSO-*d*$_6$):** δ (ppm) = 8.40 (d, $^{3}J_{HH}$ = 5.4 Hz, 1H, H-2), 8.30 (d, $^{3}J_{HH}$ = 9.0 Hz, 1H, H-7), 7.80 (d, $^{4}J_{HH}$ = 2.2 Hz, 1H, H-4), 7.44 (dd, $^{3}J_{HH}$ = 9.0, $^{4}J_{HH}$ = 2.3 Hz, 1H, H-6), 7.33 (t, $^{3}J_{HH}$ = 5.3 Hz, 1H, H-10), 6.57-6.40 (m, 5H, H-1/16/17/18/19), 4.49 (m, 2H, H-21), 4.44 (m, 1H, H-14), 3.42 (q, $^{3}J_{HH}$ = 6.8 Hz, 2H, H-11), 3.18 (q, $^{3}J_{HH}$ = 6.8 Hz, 2H, H-13), 2.01 (p, $^{3}J_{HH}$ = 6.8 Hz, 2H, H-12). **^{13}C{^{1}H} NMR (101 MHz, DMSO-*d*$_6$):** δ (ppm) = 152.4, 150.6, 149.6, 136.4, 135.8, 133.8, 128.0, 124.6, 124.5, 118.1, 118.0, 117.4, 114.6, 110.5, 99.2, 41.7, 41.1, 28.0. **FT-IR (ATR,**

cm^{-1}): ν = 3413 (N–H), 3349 (N–H), 1611 (C=N), 1580 (C=C). **EI-MS:** *m/z* 326.10 (94.4%, [M]$^+$), calculated 326.13.

*N^1-(3-((7-chloroquinolin-4-yl)amino)propyl)-4-methylbenzene-1,2-diamine (**3b**)*

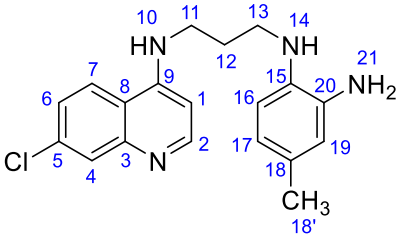

Ammonium chloride (0.953 g, 17.8 mmol), compound **2b** (0.655 g, 1.75 mmol), zinc powder (2.29 g, 35.0 mmol). Product: Purple powder. Yield: 0.589 g, 97.8%. **M.p.** 134.7 – 138.7 °C. **^{1}H NMR (400 MHz, DMSO-*d*$_6$):** δ (ppm) = 8.39 (d, $^3J_{HH}$ = 5.4 Hz, 1H, H-2), 8.29 (d, $^3J_{HH}$ = 9.0 Hz, 1H, H-7), 7.79 (d, $^4J_{HH}$ = 2.3 Hz, 1H, H-4), 7.44 (dd, $^3J_{HH}$ = 9.0, $^4J_{HH}$ = 2.3 Hz, 1H, H-6), 7.34 (t, $^3J_{HH}$ = 5.2 Hz, 1H, H-10), 6.50 (d, $^3J_{HH}$ = 5.5 Hz, 1H, H-1), 6.40 (d, $^4J_{HH}$ = 1.7 Hz, 1H, H-19), 6.36 (d, $^3J_{HH}$ = 7.9 Hz, 1H, H-16), 6.29 (dd, $^3J_{HH}$ = 7.9, $^4J_{HH}$ = 1.7 Hz, 1H, H-17), 4.44 (br s, 2H, H-21), 4.25 (m, 1H, H-14), 3.40 (q, $^3J_{HH}$ = 6.8 Hz, 2H, H-11), 3.13 (q, $^3J_{HH}$ = 6.8 Hz, 2H, H-13), 2.09 (s, 3H, H-18'), 1.98 (p, $^3J_{HH}$ = 6.8 Hz, 2H, H-12). **^{13}C{^{1}H} NMR (101 MHz, DMSO-*d*$_6$):** δ (ppm) = 152.4, 150.6, 149.6, 136.0, 134.1, 133.8, 128.0, 125.9, 124.6, 124.5, 118.3, 118.0, 115.6, 110.9, 99.2, 42.1, 41.1, 28.0, 20.9. **FT-IR (ATR, cm^{-1}):** ν = 3349 (br, N–H), 1607 (C=N), 1578 (C=C). **EI-MS:** *m/z* 340.15 (62.5%, [M]$^+$), calculated 340.15.

*N^1-(3-((7-chloroquinolin-4-yl)amino)propyl)-4-(trifluoromethyl)benzene-1,2-diamine (**3c**)*

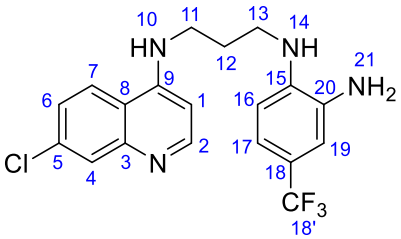

Ammonium chloride (0.953 g, 17.8 mmol), compound **2c** (0.755 g, 1.78 mmol), zinc powder (2.42 g, 37.0 mmol). Product: Purple powder. Yield: 0.674 g, 96.1%. **M.p.** 174.9 – 176.0 °C. **^{1}H NMR (400 MHz, DMSO-*d*$_6$):** δ (ppm) = 8.39 (d, $^3J_{HH}$ = 5.4 Hz, 1H, H-2), 8.29 (d, $^3J_{HH}$ = 9.1 Hz, 1H, H-7), 7.79 (d, $^4J_{HH}$ = 2.3 Hz, 1H, H-4), 7.45 (dd, $^3J_{HH}$ = 9.0, $^4J_{HH}$ = 2.3 Hz, 1H, H-6), 7.33 (t, $^3J_{HH}$ = 5.3 Hz, 1H, H-10), 6.82 (d, $^4J_{HH}$ = 2.1 Hz, 1H, H-19), 6.79 (dd, $^3J_{HH}$ = 8.7 Hz, $^4J_{HH}$ = 2.1 Hz 1H, H-17), 6.53-6.50 (overlapping m, 2H, H-1/16), 5.10 (t, $^3J_{HH}$ = 5.3 Hz, 1H, H-14), 4.94 (s, 2H, H-21), 3.41 (q, $^3J_{HH}$ = 6.8 Hz, 2H, H-11), 3.25 (q, $^3J_{HH}$ = 6.8 Hz, 2H, H-13), 2.01 (p, $^3J_{HH}$ = 6.8 Hz, 2H, H-12). **^{13}C{^{1}H NMR (101 MHz, DMSO-*d*$_6$):** δ (ppm) = 152.4, 150.6, 149.6, 139.3, 135.6, 133.9, 128.0, 127.4, 124.6, 124.5, 118.0, 116.7, 115.0, 109.8, 108.7, 99.2, 41.3, 40.9, 27.6. **FT-IR (ATR, cm^{-1}):** ν = 3377 (br, N–H), 1611 (C=N), 1581 (C=C), 1328 (C–F). **EI-MS:** *m/z* 394.11 (56.6%, [M]$^+$), calculated 394.12.

*N^1-(3-((7-chloroquinolin-4-yl)amino)propyl)-4-(methylsulfonyl)benzene-1,2-diamine (**3d**)*

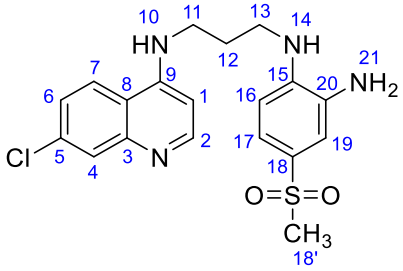

Ammonium chloride (0.242 g, 4.52 mmol), compound **2d** (0.192 g, 0.454 mmol), zinc powder (0.592 g, 9.05 mmol). Product: Brown powder. Yield: 0.148 g, 80.5%. **M.p.** 227.2 – 229.5 °C. **^{1}H NMR (400 MHz, DMSO-d_6):** δ (ppm) = 8.40 (d, $^3J_{HH}$ = 5.5 Hz, 1H, H-2), 8.29 (d, $^3J_{HH}$ = 9.1 Hz, 1H, H-7), 7.79 (d, $^4J_{HH}$ = 2.3 Hz, 1H, H-4), 7.45 (dd, $^3J_{HH}$ = 9.1, $^4J_{HH}$ = 2.3 Hz, 1H, H-6), 7.34 (t, $^3J_{HH}$ = 5.2 Hz, 1H, H-10), 7.02 (overlapping m, 2H, H-17/19), 6.56 (d, $^3J_{HH}$ = 8.9 Hz, 1H, H-16), 6.51 (d, $^3J_{HH}$ = 5.5 Hz, 1H, H-1), 5.38 (t, $^3J_{HH}$ = 5.3 Hz, 1H, H-14), 5.03 (br s, 2H, H-21), 3.41 (q, $^3J_{HH}$ = 6.8 Hz, 2H, H-11), 3.29 (q, $^3J_{HH}$ = 6.8 Hz, 2H, H-13), 2.99 (s, 3H, H-18'), 2.02 (p, $^3J_{HH}$ = 6.8 Hz, 2H, H-12). **^{13}C{^{1}H} NMR (101 MHz, DMSO-d_6):** δ (ppm) = 152.4, 150.6, 149.6, 140.5, 135.4, 133.9, 128.0, 127.5, 124.6, 124.5, 118.0 (2C), 111.4, 108.3, 99.3, 45.1, 41.2, 40.8, 27.6. **FT-IR (ATR, cm^{-1}):** ν = 3401 (N–H), 3345 (N–H), 1611 (C=N), 1580 (C=C), 1370 (S=O), 1124 (S=O). **EI-MS:** *m/z* 405.12 (100%, $[M+H]^+$), calculated 405.11.

*3-Amino-4-((3-((7-chloroquinolin-4-yl)amino)propyl)amino)benzonitrile (**3e**)*

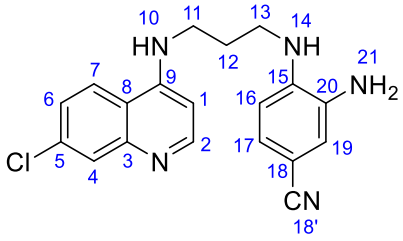

Ammonium chloride (0.592 g, 11.1 mmol), compound **2e** (0.406 g, 1.10 mmol), zinc powder (1.45 g, 22.2 mmol). Product: Pink powder. Yield: 0.294 g, 75.7%. **M.p.** 250.1 – 253.4 °C. **^{1}H NMR (400 MHz, DMSO-d_6):** δ (ppm) = 8.38 (d, $^3J_{HH}$ = 5.4 Hz, 1H, H-2), 8.27 (d, $^3J_{HH}$ = 9.1 Hz, 1H, H-7), 7.77 (d, $^4J_{HH}$ = 2.3 Hz, 1H, H-4), 7.43 (dd, $^3J_{HH}$ = 9.1, $^4J_{HH}$ = 2.3 Hz, 1H, ArH), 7.29 (t, $^3J_{HH}$ = 5.1 Hz, 1H, H-10), 6.89 (dd, $^3J_{HH}$ = 8.2, $^4J_{HH}$ = 2.0 Hz, 1H, H-17), 6.78 (d, $^4J_{HH}$ = 2.0 Hz, 1H, H-19), 6.49-6.47 (overlapping m, 2H, H-1/16), 5.42 (t, $^3J_{HH}$ = 5.1 Hz, 2H, H-14), 4.97 (s, 2H, H-21), 3.38 (q, $^3J_{HH}$ = 6.8 Hz, 2H, H-11), 3.26 (m, 2H, H-13), 1.99 (p, $^3J_{HH}$ = 6.8 Hz, 2H, H-12). **^{13}C{^{1}H} NMR (101 MHz, DMSO-d_6)** δ 152.4, 150.6, 149.6, 140.5, 135.7, 133.8, 128.0, 124.6, 124.5, 123.3, 121.5, 118.0, 115.4, 109.2, 99.3, 97.1, 41.0, 40.8, 27.6. **FT-IR (ATR, cm^{-1}):** ν = 3417 (N–H), 3393 (N–H), 2202 (C≡N), 1609 (C=N), 1580 (C=C). **EI-MS:** *m/z* 352.14 (100%, $[M+H]^+$), calculated 352.14.

7.3 Aminoquinoline-benzimidazole hybrids

7.3.1 General method for synthesis of 2-phenyl hybrids (4a – 4e)

A 1,2-diamine aminoquinoline precursor (**3a** – **3e**) (1 eq.), benzaldehyde (1.5 eq.) and TFA (0.1 eq.) were dissolved in ethanol (25 ml). Anhydrous $MgSO_4$ (5 eq.) was added and the brown reaction mixture was refluxed for 24 hours. Thereafter, the resulting brown mixture was filtered by gravity and the solvent of the filtrate was removed to give a brown residue. To this crude residue, 1 M NaOH (50 ml) was added and the mixture was extracted using DCM (3 × 50 ml). The organic fractions were collected and washed with brine (2 × 50 ml), followed by water (1 × 30 ml). The organic layer was collected, dried over anhydrous Na_2SO_4 and filtered by gravity. The solvent of the filtrate was removed to afford the crude product as a dark orange residue. The crude product was purified by column chromatography (silica gel) using EtOAc (100%). Subsequent precipitation from DCM/pet. ether (40 – 60 °C) afforded the desired product as a white, pale-yellow or beige powder, which was collected by suction filtration and dried *in vacuo*.

*7-Chloro-N-(3-(2-phenyl-1H-benzo[d]imidazole-1-yl)propyl)quinolin-4-amine (**4a**)*

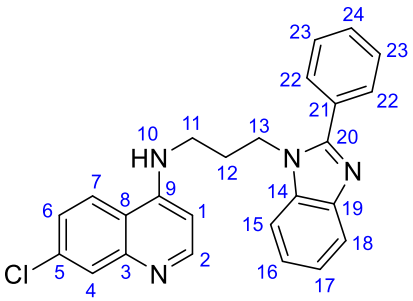

Compound **3a** (0.502 g, 1.54 mmol), benzaldehyde (0.235 ml, 2.31 mmol), TFA (11.7 µl, 0.153 mmol) and anhydrous $MgSO_4$ (0.927 g, 7.70 mmol). Product: Pale-yellow powder. Yield: 0.407 g, 64.2%. R_f(EtOAc, 100%): 0.15. **M.p.** 180.9 – 182.5 °C. **^{1}H NMR (300 MHz, DMSO-*d*$_6$):** δ (ppm) = 8.35 (d, $^3J_{HH}$ = 5.5 Hz, 1H, H-2), 8.13 (d, $^3J_{HH}$ = 9.1, 1H, H-7), 7.80 (d, $^4J_{HH}$ = 2.2 Hz, 1H, H-4), 7.75 – 7.61 (m, 4H, H-15/18/22), 7.44 (dd, $^3J_{HH}$ = 9.1, $^4J_{HH}$ = 2.2 Hz, 1H, H-6), 7.40 – 7.24 (m, 5H, H-16/17/23/24), 7.21 (t, $^3J_{HH}$ = 4.8 Hz, 1H, H-10) 6.30 (d, $^3J_{HH}$ = 5.5 Hz, 1H, H-1), 4.47 (t, $^3J_{HH}$ = 7.4 Hz, 2H, H-13), 3.19 (m, 2H, H-11), 2.13 (m, 2H, H-12).**^{13}C{^{1}H} NMR (101 MHz, DMSO-*d*$_6$):** δ 153.4, 152.3, 150.3, 149.5, 143.1, 136.1, 133.9, 130.8, 129.9, 129.4 (2C), 129.0 (2C), 127.9, 124.5 (2C), 122.9, 122.5, 119.7, 118.0, 111.3, 99.1, 42.5, 39.8, 28.4. **FT-IR (ATR, cm^{-1}):** ν = 3433 (N–H), 1611 (C=N$_{benz/quin}$), 1578 (C=C). **ESI-MS:** *m*/*z* 413.1534 (100%, $[M+H]^+$), calculated 413.1528. **HPLC** purity >99% (t_R = 2.30 min).

*7-Chloro-N-(3-(5-(methyl)-2-phenyl-1H-benzo[d]imidazol-1-yl)propyl)quinolin-4-amine (**4b**)*

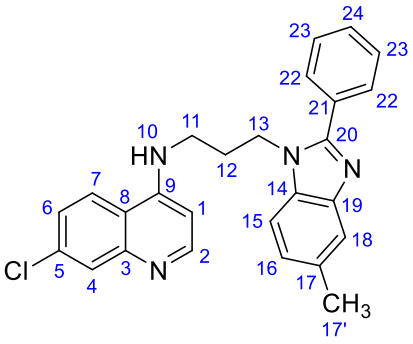

Compound **3b** (0.405 g, 1.19 mmol), benzaldehyde (0.181 ml, 1.78 mmol), TFA (8.98 µl, 0.119 mmol) and anhydrous $MgSO_4$ (0.716 g, 5.95 mmol). Product: Pale-yellow powder. Yield: 0.307 g, 60.5%. R_f(EtOAc, 100%): 0.14. **M.p.** 248.2 – 250.2 °C. **^{1}H NMR (300 MHz, DMSO-*d*$_6$):** δ (ppm) = 8.35 (d, $^3J_{HH}$ = 5.4 Hz, 1H, H-2), 8.13 (d, $^3J_{HH}$ = 9.1 Hz, 1H, H-7), 7.80 (d, $^4J_{HH}$ = 2.2 Hz, 1H, H-4), 7.71 – 7.63 (m, 2H, H-22), 7.57 (d, $^3J_{HH}$ = 8.3 Hz, 1H, H-15), 7.48 (m, 1H, H-18), 7.43 (dd, $^3J_{HH}$ = 9.1, $^4J_{HH}$ = 2.2 Hz, 1H, H-6), 7.39 – 7.26 (overlapping m, 3H, H-23/24), 7.21 (t, $^3J_{HH}$ = 5.2 Hz, 1H, H-10), 7.10 (d, $^3J_{HH}$ = 8.3 Hz, 1H, H-16), 6.29 (d, $^3J_{HH}$ = 5.4 Hz, 1H, H-1), 4.44 (t, $^3J_{HH}$ = 7.3 Hz, 1H, H-13), 3.18 (m, 2H, H-11), 2.43 (s, 3H, H-17') 2.11 (m, 2H, H-12). **^{13}C{^{1}H} NMR (101 MHz, DMSO-*d*$_6$):** δ 153.3, 152.3, 150.3, 149.5, 143.5, 134.3, 133.9, 131.5, 130.9, 129.8, 129.4 (2C), 128.9 (2C), 127.9, 124.5 (2C), 124.3, 119.4, 118.0, 110.9, 99.1, 42.5, 39.9, 28.4, 21.6. **FT-IR (ATR, cm^{-1}):** ν = 3250 (N–H), 1609 (C=N$_{benz/quin}$), 1578 (C=C). **ESI-MS:** *m/z* 214.0882 (100%, $[M+2H]^{2+}$), calculated 214.0878; *m/z* 427.1690 (30%, $[M+H]^+$), calculated 427.1684. **HPLC** purity >99% (t_R = 2.37 min).

*7-Chloro-N-(3-(5-(trifluoromethyl)-2-phenyl-1H-benzo[d]imidazol-1-yl)propyl)quinolin-4-amine (**4c**)*

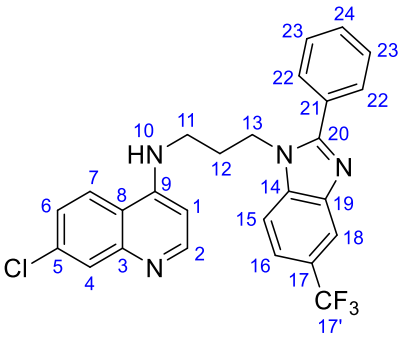

Compound **3c** (0.250 g, 0.633 mmol), benzaldehyde (0.0965 ml, 0.950 mmol), TFA (4.84 µl, 0.0633 mmol) and anhydrous $MgSO_4$ (0.381 g, 3.17 mmol). Product: White powder. Yield: 0.248 g, 81.4%. R_f(EtOAc, 100%): 0.26. **M.p.** 197.8 – 199.6 °C. **^{1}H NMR (300 MHz, DMSO-*d6*):** δ (ppm) = 8.35 (d, $^3J_{HH}$ = 5.4 Hz, 1H, H-2), 8.10 (d, $^3J_{HH}$ = 9.1 Hz, 1H, H-7), 8.06 (m, 1H, H-18) 7.97 (d, $^3J_{HH}$ = 8.6 Hz, 1H, H-15), 7.80 (d, $^4J_{HH}$ = 2.2 Hz, 1H, H-4), 7.74 – 7.67 (m, 2H, H-22), 7.61 (dd, $^3J_{HH}$ = 8.6, $^4J_{HH}$ = 1.1 Hz, 1H, H-16), 7.43 (dd, $^3J_{HH}$ = 9.1, $^4J_{HH}$ = 2.2 Hz, 1H, H-6), 7.40 – 7.28 (overlapping m, 3H, H-23/24), 7.19 (t, $^3J_{HH}$ = 5.1 Hz, 1H, H-10), 6.30 (d, $^3J_{HH}$ = 5.4 Hz, 1H, H-1), 4.54 (t, $^3J_{HH}$ = 7.4 Hz, 1H, H-13), 3.20 (m, 2H, H-11), 2.13 (m, 1H, H-12).

$^{13}C\{^{1}H\}$ NMR (101 MHz, DMSO-*d*$_6$): δ (ppm) = 155.8, 152.3, 150.3, 149.5, 142.5, 138.4, 133.9, 130.4, 130.1, 129.5 (2C), 129.1 (2C), 127.9, 126.8, 124.5 (2C), 123.3, 119.5, 118.0, 117.0, 112.5, 99.2, 42.9, 39.7, 28.2. **FT-IR (ATR, cm^{-1}):** ν = 3278 (N–H), 1611 (C=N$_{benz/quin}$), 1578 (C=C), 1326 (C–F). **ESI-MS:** *m*/*z* 481.1410 (100%, $[M+H]^+$), calculated 481.1401. **HPLC** purity 99% (t_R = 2.44 min).

*7-Chloro-N-(3-(5-(methylsulfonyl)-2-phenyl-1H-benzo[d]imidazol-1-yl)propyl)quinolin-4-amine (**4d**)*

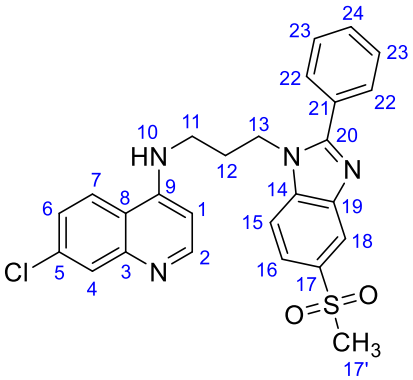

Compound **3d** (0.0600 g, 0.148 mmol), benzaldehyde (0.0226 g, 0.222 mmol), TFA (1.13 µl, 0.0148 mmol) and anhydrous $MgSO_4$ (0.0891 g, 0.740 mmol). Product: Beige powder. Yield: 0.0453 g, 62.3%. R_f(EtOAc, 100%): 0.06. **M.p.** 94.1 – 96.5 °C. **^{1}H NMR (300 MHz, DMSO-*d*$_6$):** δ (ppm) = 8.35 (d, $^{3}J_{HH}$ = 5.5 Hz, 1H, H-2), 8.24 (d, $^{4}J_{HH}$ = 1.6 Hz, 1H, H-18), 8.11 (d, $^{3}J_{HH}$ = 9.1 Hz, 1H, H-7), 8.00 (d, $^{3}J_{HH}$ = 8.6 Hz, 1H, H-15), 7.83 (dd, $^{3}J_{HH}$ = 8.6, $^{4}J_{HH}$ = 1.6 Hz, 1H, H-16), 7.80 (d, $^{4}J_{HH}$ = 2.2 Hz, 1H, H-4), 7.73 – 7.69 (m, 2H, H-22), 7.44 (dd, $^{3}J_{HH}$ = 9.1, $^{4}J_{HH}$ = 2.2 Hz, 1H, H-6), 7.42 – 7.30 (overlapping m, 3H, H-23/24), 7.20 (t, $^{3}J_{HH}$ = 5.3 Hz, 1H, H-10), 6.31 (d, $^{3}J_{HH}$ = 5.5 Hz, 1H, H-1), 4.55 (t, $^{3}J_{HH}$ = 7.3 Hz, 1H, H-13), 3.24 (s, 3H, H-17'), 3.20 (m, 2H, H-11), 2.13 (m, 2H, H-12). **$^{13}C\{^{1}H\}$ NMR (101 MHz, DMSO-*d*$_6$):** δ (ppm) = 156.3, 152.3, 150.3, 149.5, 142.4, 139.2, 135.2, 133.9, 130.5, 129.9, 129.5 (2C), 129.1 (2C), 127.9, 124.5 (2C), 121.4, 119.3, 118.0, 112.4, 99.2, 44.7, 42.9, 39.8, 28.2. **FT-IR (ATR, cm^{-1}):** ν = 3397 (N–H), 1609 (C=N$_{benz/quin}$), 1578 (C=C), 1368 (S=O), 1136 (S=O). **ESI-MS:** *m*/*z* 246.0693 (100%, $[M+2H]^{2+}$), calculated 246.0688; *m*/*z* 491.1313 (80%, $[M+H]^+$), calculated 491.1303. **HPLC** purity >99% (t_R = 2.20 min).

*1-(3-((7-Chloroquinolin-4-yl)amino)propyl)-2-phenyl-1H-benzo[d]imidazole-5-carbonitrile (**4e**)*

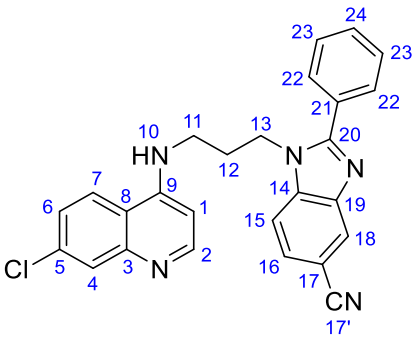

Compound **3e** (0.141 g, 0.401 mmol), benzaldehyde (0.0607 ml, 0.597 mmol), TFA (3.04 µl, 0.0397 mmol) and anhydrous $MgSO_4$ (0.244 g, 1.99 mmol). Product: Beige powder. Yield: 0.115 g, 65.5%. R_f(EtOAc, 100%): 0.12. **M.p.** 228.8 – 230.5 °C. **^{1}H NMR (300 MHz, DMSO-*d*$_6$):** δ (ppm) = 8.35 (d, $^3J_{HH}$ = 5.5 Hz, 1H, H-2), 8.25 (d, $^4J_{HH}$ = 1.0 Hz, 1H, H-18), 8.10 (d, $^3J_{HH}$ = 9.1 Hz, 1H, H-7), 7.97 (d, $^3J_{HH}$ = 8.4 Hz, 1H, H-15), 7.80 (d, $^4J_{HH}$ = 2.2 Hz, 1H, H-4), 7.72 – 7.69 (overlapping m, 3H, H-16/22), 7.44 (dd, $^3J_{HH}$ = 9.1, $^4J_{HH}$ = 2.2 Hz, 1H, H-6), 7.40 – 7.27 (overlapping m, 3H, H-23/24), 7.21 (t, $^3J_{HH}$ = 5.1 Hz, 1H, H-10), 6.30 (d, $^3J_{HH}$ = 5.5 Hz, 1H, H-1), 4.53 (t, $^3J_{HH}$ = 7.3 Hz, 2H, H-13), 3.19 (m, 2H, H-11), 2.11 (m, 2H, H-12). **^{13}C{^{1}H} NMR (101 MHz, DMSO-*d*$_6$):** δ (ppm) = 156.1, 152.3, 150.2, 149.5, 142.6, 139.1, 133.9, 130.5, 129.8, 129.5 (2C), 129.1 (2C), 128.0, 126.3, 124.6, 124.5 (2C), 120.3, 118.0, 113.0, 104.8, 99.2, 42.9, 39.7, 28.2. **FT-IR (ATR, cm^{-1}):** ν = 3175 (N–H), 1611 (C=N$_{benz/quin}$), 1580 (C=C), 2214 (C≡N). **ESI-MS:** *m/z* 219.5773 (100%, $[M+2H]^{2+}$), calculated 219.5776; *m/z* 438.1470 (90%, $[M+H]^+$), calculated 438.1480. **HPLC** purity >99% (t_R = 2.30 min).

7.3.2 General method for synthesis of 2-ferrocenyl hybrids (5a – 5e)

A 1,2-diamine aminoquinoline precursor (**3a** – **3e**) (1 eq.), ferrocenecarboxaldehyde (1.5 eq.) and TFA (0.1 eq.) were dissolved in EtOH (25 ml). Anhydrous $MgSO_4$ (5 eq.) was added and the dark red reaction mixture was refluxed for 48 hours. Thereafter, the resulting dark red mixture was filtered by gravity and the solvent of the filtrate was removed to give a red residue. To this crude residue, 1 M NaOH (50 ml) was added and the mixture was extracted using DCM (3 × 50 ml). The organic fractions were collected and washed with brine (2 × 50 ml), followed by water (1 × 30 ml). The organic layer was collected, dried over anhydrous Na_2SO_4 and filtered by gravity. The solvent of the filtrate was removed to afford the crude product as a red residue. The crude product was purified by column chromatography (silica gel) using EtOAc (100%). Compounds **5a** – **5e** were isolated as orange powders and dried *in vacuo*.

*7-Chloro-N-(3-(2-ferrocenyl-1H-benzo[d]imidazole-1-yl)propyl)quinolin-4-amine (**5a**)*

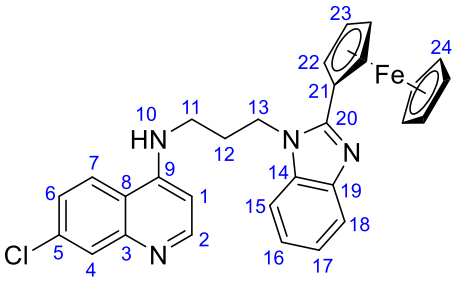

Compound **3a** (0.102 g, 0.312 mmol), ferrocenecarboxaldehyde (0.100 g, 0.467 mmol), TFA (2.50 µl, 0.0327 mmol) and anhydrous $MgSO_4$ (0.184 g, 1.53 mmol). Product: Orange powder. Yield: 0.0742 g, 45.6%. R_f(EtOAc, 100%): 0.26. **M.p.** 227.0 – 228.3 °C. **^{1}H NMR (300 MHz, DMSO-*d*$_6$):** δ (ppm) = 8.44 (d, $^3J_{HH}$ = 5.5 Hz, 1H, H-2), 8.37 (d, $^3J_{HH}$ = 9.1 Hz, 1H, H-7), 7.87 (d, $^4J_{HH}$ = 2.2 Hz, 1H, H-4), 7.69 – 7.57 (overlapping m, 3H, H-10/15/18), 7.56 (d, $^4J_{HH}$ = 2.2 Hz, 1H, H-6), 7.25 – 7.14 (overlapping m, 2H, H-16/17), 6.63 (d, $^3J_{HH}$ = 5.5 Hz, 1H, H-1), 4.75 (t, $^3J_{HH}$ = 1.8 Hz, 2H, H-22), 4.62 (m, 2H, H-13), 4.14 (t, $^3J_{HH}$ = 1.8 Hz, 2H, H-23), 3.99 (s, 5H, H-24), 3.60 (q, $^3J_{HH}$ = 5.7 Hz, 2H, H-11), 2.23 (m, 2H, H-12). **^{13}C{^{1}H} NMR (101 MHz, DMSO-*d*$_6$):** δ (ppm) = 152.5, 152.5, 150.4, 149.8, 143.2, 136.5, 134.0, 128.1, 124.7, 124.6, 122.1 (2C), 118.7, 118.1, 110.3, 99.5, 74.1, 70.1 (2C), 69.7 (5C), 69.1 (2C), 42.3, 39.5, 29.1. **FT-IR (ATR, cm^{-1}):** ν = 3437 (N–H), 1609 (C=N$_{benz/quin}$), 1574 (C=C). **ESI-MS:** *m/z* 521.1207 (100%, $[M+H]^+$), calculated 521.1190. **HPLC** purity >99% (t_R = 6.75 min).

*7-Chloro-N-(3-(5-(methyl)-2-ferrocenyl-1H-benzo[d]imidazol-1-yl)propyl)quinolin-4-amine (**5b**)*

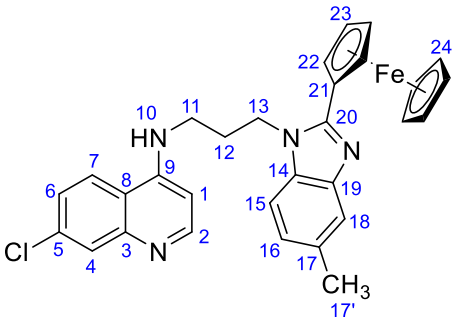

Compound **3b** (0.0813 g, 0.239 mmol), ferrocenecarboxaldehyde (0.0774 g, 0.362 mmol), TFA (2.30 µl, 0.0301 mmol) and anhydrous $MgSO_4$ (0.146 g, 1.21 mmol). Product: Orange powder. Yield: 0.0718 g, 56.3%. R_f(EtOAc, 100%): 0.29. **M.p.** 114.2 – 115.9 °C. **^{1}H NMR (400 MHz, DMSO-*d*$_6$):** δ (ppm) = 8.44 (d, $^3J_{HH}$ = 5.5 Hz, 1H, H-2), 8.37 (d, $^3J_{HH}$ = 9.1 Hz, 1H, H-7), 7.87 (d, $^4J_{HH}$ = 2.3 Hz, 1H, H-4), 7.65 (t, $^3J_{HH}$ = 5.5 Hz, 1H, H-10), 7.57 (dd, $^3J_{HH}$ = 9.1, $^4J_{HH}$ = 2.3 Hz, 1H, H-6), 7.49 (d, $^3J_{HH}$ = 8.3 Hz, 1H, H-15), 7.36 (m, 1H, H-18), 7.03 (dd, $^3J_{HH}$ = 8.3, $^4J_{HH}$ = 1.2 Hz, 1H, H-16), 6.62 (d, $^3J_{HH}$ = 5.5 Hz, 1H, H-1), 4.74 (t, $^3J_{HH}$ = 1.9 Hz, 2H, H-22), 4.58 (m, 2H, H-13), 4.13 (t, $^3J_{HH}$ = 1.9 Hz, 2H, H-23), 3.98 (s, 5H, H-24) 3.58 (q, $^3J_{HH}$ = 6.0 Hz, 2H, H-11), 2.41 (s, 3H, H-17'), 2.21 (m, 2H, H-12). **^{13}C{^{1}H} NMR (101 MHz, DMSO-*d*$_6$):** δ (ppm) = 152.5, 152.3, 150.4, 149.8, 143.6, 134.7,

134.0, 131.1, 128.1, 124.7, 124.6, 123.4, 118.5, 118.1, 109.8, 99.5, 74.3, 70.0 (2C), 69.7 (5C), 69.0 (2C), 42.3, 39.7, 29.1, 21.7. **FT-IR (ATR, cm^{-1}):** ν = 3254 (N–H), 1609 (C=N$_{benz/quin}$), 1580 (C=C). **ESI-MS:** *m/z* 268.0718 (100%, [M+2H]$^{2+}$), calculated 268.0710; *m/z* 535.1367 (23%, [M+H]$^{+}$), calculated 535.1346. **HPLC** purity 99% (t_R = 6.98 min).

*7-Chloro-N-(3-(5-(trifluoromethyl)-2-ferrocenyl-1H-benzo[d]imidazol-1-yl)propyl)quinolin-4-amine (**5c**)*

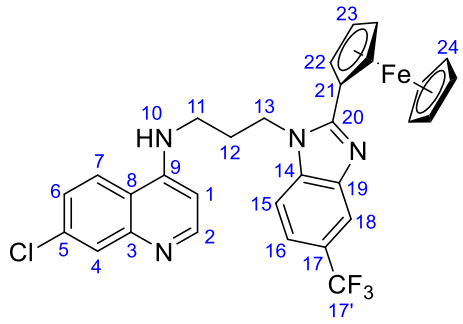

Compound **3c** (0.140 g, 0.355 mmol), ferrocenecarboxaldehyde (0.117 g, 0.547 mmol), TFA (3.43 µl, 0.0355 mmol) and anhydrous $MgSO_4$ (0.214 g, 1.78 mmol). Product: Orange powder. Yield: 0.107 g, 51.2%. R_f(EtOAc, 100%): 0.39. **M.p.** 184.2 – 185.7 °C. **^{1}H NMR (400 MHz, DMSO-*d*$_6$):** δ (ppm) = 8.44 (d, $^3J_{HH}$ = 5.3 Hz, 1H, H-2), 8.36 (d, $^3J_{HH}$ = 9.0 Hz, 1H, H-7), 7.92 (m, 1H, H-18), 7.90 – 7.85 (overlapping m, 2H, H-4/15), 7.67 (t, $^3J_{HH}$ = 5.2 Hz, 1H, H-10), 7.58 (dd, $^3J_{HH}$ = 9.0, $^4J_{HH}$ = 2.0 Hz, 1H, H-6), 7.54 (d, $^3J_{HH}$ = 8.7 Hz, 1H, H-16), 6.64 (d, $^3J_{HH}$ = 5.3 Hz, 1H, H-1), 4.79 (m, 2H, H-22), 4.67 (m, 2H, H-13), 4.16 (m, 2H, H-23), 4.00 (s, 5H, H-24), 3.61 (m, 2H, H-11), 2.24 (m, 2H, H-12). **^{13}C{^{1}H} NMR (101 MHz, DMSO-*d*$_6$):** δ (ppm) = 155.5, 152.5, 150.4, 149.8, 142.7, 138.9, 134.0, 128.1, 127.0, 124.7, 124.5, 123.0, 118.7, 118.1, 115.9, 111.3, 99.5, 73.0, 70.5 (2C), 69.9 (5C), 69.3 (2C), 42.7, 39.6, 29.0. **FT-IR (ATR, cm^{-1}):** ν = 3266 (N–H), 1611 (C=N$_{benz/quin}$), 1582 (C=C), 1328 (C–F). **ESI-MS:** *m/z* 295.0572 (100%, [M+2H]$^{2+}$), calculated 295.0568; *m/z* 589.1068 (32%, [M+H]$^{+}$), calculated 589.1064. **HPLC** purity >99% (t_R = 8.73 min).

*7-Chloro-N-(3-(5-(methylsulfonyl)-2-ferrocenyl-1H-benzo[d]imidazol-1-yl)propyl)quinolin-4-amine (**5d**)*

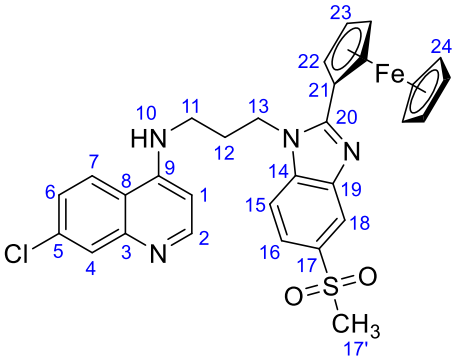

Compound **3d** (0.159 g, 0.393 mmol), ferrocenecarboxaldehyde (0.130 g, 0.607 mmol), TFA (3.01 µl, 0.0393 mmol) and anhydrous $MgSO_4$ (0.239 g, 1.99 mmol). Product: Orange powder. Yield: 0.128 g, 54.4%. R_f(EtOAc, 100%): 0.10. **M.p** 164.0 – 166.0 °C. **^{1}H NMR (300 MHz, DMSO-*d*$_6$):** δ (ppm) = 8.45 (d, $^3J_{HH}$ = 5.5 Hz, 1H, H-2), 8.37 (d, $^3J_{HH}$ = 9.0 Hz, 1H, H-7), 8.10 (d, $^4J_{HH}$ = 1.5 Hz, 1H, H-18), 7.92 (d, $^3J_{HH}$ = 8.5 Hz, 1H, H-15), 7.87 (d, $^4J_{HH}$ = 2.1 Hz, 1H, H-4), 7.76 (dd, $^3J_{HH}$ = 8.5, $^4J_{HH}$ = 1.5 Hz, 1H, H-16), 7.68 (t, $^3J_{HH}$ = 5.4 Hz, 1H, H-10), 7.58 (dd, $^3J_{HH}$ = 9.0, $^4J_{HH}$ = 2.1 Hz, 1H, H-6), 6.65 (d, $^3J_{HH}$ = 5.5 Hz, 1H, H-1), 4.80 (m, 2H, H-22), 4.68 (m, 2H, H-13), 4.18 (m, 2H, H-23), 4.00 (s, 5H, H-24), 3.62 (m, 2H, H-11), 3.22 (s, 3H, H-17'), 2.24 (m, 2H, H-12). **^{13}C{^{1}H} NMR (101 MHz, DMSO-*d*$_6$):** δ (ppm) = 156.5, 156.2, 152.5, 150.4, 142.6, 139.7, 134.9, 134.0, 128.2, 124.7 (2C), 124.6, 120.6, 118.0, 111.2, 99.6, 72.8, 70.6 (2C), 69.9 (5C), 69.4 (2C), 44.7, 42.8, 39.6, 29.0. **FT-IR (ATR, cm^{-1}):** ν = 3242 (N–H), 1609 (C=N$_{benz/quin}$), 1580 (C=C), 1366 (S=O), 1136 (S=O). **ESI-MS:** *m/z* 599.0969 (100%, $[M+H]^+$), calculated 599.0965. **HPLC** purity 97% (t_R = 7.55 min).

*1-(3-((7-Chloroquinolin-4-yl)amino)propyl)-2-ferrocenyl-1H-benzo[d]imidazole-5-carbonitrile (**5e**)*

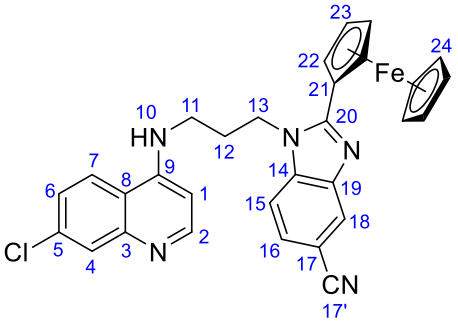

Compound **3e** (0.141 g, 0.398 mmol), ferrocenecarboxaldehyde (0.131 g, 0.614 mmol), TFA (3.04 µl, 0.0398 mmol) and anhydrous $MgSO_4$ (0.240 g, 1.99 mmol). Product: Orange powder. Yield: 0.0954 g, 43.9%. R_f(EtOAc, 100%): 0.21. **M.p.** 222.9 – 224.4 °C. **^{1}H NMR (300 MHz, DMSO-*d*$_6$):** δ (ppm) = 8.44 (d, $^3J_{HH}$ = 5.4 Hz, 1H, H-2), 8.37 (d, $^3J_{HH}$ = 9.1 Hz, 1H, H-7), 8.09 (m, 1H, H-18), 7.91 – 7.85 (overlapping m, 2H, H-4/15), 7.71 (t, $^3J_{HH}$ = 5.2 Hz, 1H, H-10), 7.66 – 7.56 (overlapping m, 2H, H-6/16), 6.64 (d, $^3J_{HH}$ = 5.4 Hz, 1H, H-1), 4.77 (m, 2H, H-22), 4.66 (m, 2H, H-13), 4.15 (m, 2H, H-23), 4.00

(s, 5H, H-24), 3.61 (m, 2H, H-11), 2.21 (m, 2H, H-12). **$^{13}C\{^{1}H\}$ NMR (101 MHz, DMSO-d_6):** δ (ppm) = 156.0, 152.5, 150.4, 149.8, 142.7, 139.6, 134.0, 128.1, 125.6, 124.7, 124.5, 123.2, 120.5, 118.1, 111.9, 104.3, 99.5, 72.7, 70.7 (2C), 69.9 (5C), 69.4 (2C), 42.7, 39.5, 29.0. **FT-IR (ATR, cm^{-1}):** ν = 3242 (N–H), 1609 (C=N$_{benz/quin}$), 1580 (C=C), 2222 (C≡N). **ESI-MS:** *m/z* 273.5657 (100%, $[M+2H]^{2+}$), calculated 273.5608; *m/z* 546.1166 (47%, $[M+H]^{+}$), calculated 546.1142. **HPLC** purity 97% (t_R = 8.02 min).

7.3.3 General method for synthesis of 2-pyridyl hybrids (6a – 6c)

Compound **3a**, **3b** or **3c** (1 eq.), 2-pyridinecarboxaldehyde (1.5 eq.) and TFA (0.1 eq.) were dissolved in ethanol (25 ml). Anhydrous $MgSO_4$ (5 eq.) was added and the brown reaction mixture was refluxed for 24 hours. Thereafter, the resulting brown mixture was filtered by gravity and the solvent of the filtrate was removed to give a brown residue. To this crude residue, 1 M NaOH (50 ml) was added and the mixture was extracted using DCM (3 x 50 ml). The organic fractions were combined and washed with brine (2 x 50 ml). the organic layer was collected, dried over anhydrous Na_2SO_4, filtered by gravity and the solvent of the filtrate was removed to afford a dull orange/brown solid. The crude product was purified by column chromatography (silica gel) using EtOAc (100%). Compounds **6a** – **6c** were isolated as pale-yellow or beige powders and dried *in vacuo*.

*7-chloro-N-(3-(2-(pyridin-2-yl)-1H-benzo[d]imidazol-1-yl)propyl)quinolin-4-amine (**6a**)*

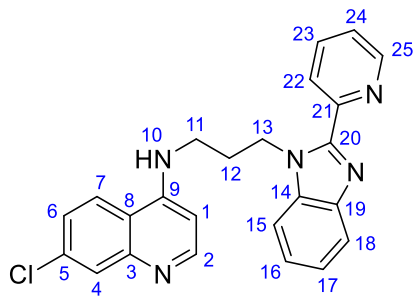

Compound **3a** (0.222 g, 0.680 mmol), 2-pyridinecarboxaldehyde (0.0971 ml, 1.02 mmol), TFA (0.00520 ml, 0.0680 mmol) and anhydrous $MgSO_4$ (0.409 g, 3.40 mmol). Product: Pale-yellow powder. Yield: 0.166 g, 59.1%. **M.p.** 201.9 – 203.0 °C. **^{1}H NMR (400 MHz, DMSO-d_6):** δ 8.47 (ddd, $^{3}J_{HH}$ = 4.8, $^{4}J_{HH}$ = 1.8, $^{5}J_{HH}$ = 0.9 Hz, 1H, H-25), 8.34 (d, $^{3}J_{HH}$ = 5.5 Hz, 1H, H-2), 8.27 (dt, $^{3}J_{HH}$ = 8.0, 1.2 Hz, 1H, H-22), 8.21 (d, $^{3}J_{HH}$ = 9.1 Hz, 1H, H-7), 7.90 (td, $^{3}J_{HH}$ = 7.8, $^{4}J_{HH}$ = 1.8 Hz, 1H, H-23), 7.79 (d, $^{4}J_{HH}$ = 2.3 Hz, 1H, H-4), 7.76 – 7.71 (overlapping m, 2H, H-15/18), 7.44 (dd, $^{3}J_{HH}$ = 9.1, $^{4}J_{HH}$ = 2.3 Hz, 1H, H-6), 7.36 (ddd, $^{3}J_{HH}$ = 7.6, $^{3}J_{HH}$ = 4.8, $^{4}J_{HH}$ = 1.2 Hz, 1H, H-24), 7.33 – 7.25 (overlapping m, 3H, H-10/16/17), 6.34 (d, $^{3}J_{HH}$ = 5.5 Hz, 1H, H-1), 4.99 (t, $^{3}J_{HH}$ = 7.3 Hz,

2H, H-13), 3.29 (m, 2H, H-11), 2.23 (m, 2H, H-12). **^{13}C{^{1}H} NMR (101 MHz, DMSO-*d*$_6$):** δ 152.3, 150.4 (2C), 149.9, 149.6, 149.1, 142.6, 137.7, 136.9, 133.8, 128.0, 124.8, 124.5 (3C), 123.6, 122.9, 120.1, 118.0, 111.3, 99.1, 43.3, 40.1, 29.0. **IR (ATR, cm^{-1}):** ν = 3194 (N–H), 1609 (C=N$_{benz/quin}$), 1592 (C=N$_{pyr}$), 1580 (C=C). **ESI-MS:** *m/z* 414.1485 (100%, [M+H]$^+$), calculated 414.1480. **HPLC** purity 99% (t_R = 2.62 min).

*7-chloro-N-(3-(5-methyl-2-(pyridin-2-yl)-1H-benzo[d]imidazol-1-yl)propyl)quinolin-4-amine (**6b**)*

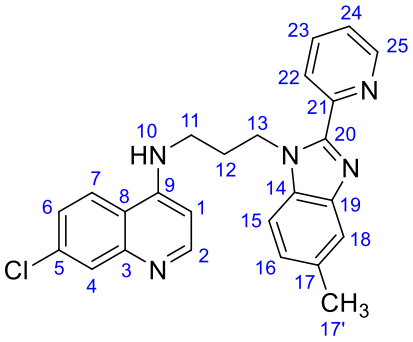

Compound **3b** (0.186 g, 0.545 mmol), 2-pyridinecarboxaldehyde (0.0777 ml, 0.817 mmol), TFA (0.00417 ml, 0.0545 mmol) and anhydrous $MgSO_4$ (0.331 g, 2.75 mmol). Product: Beige powder. Yield: 0.146 g, 62.4%. **M.p.** 216.0 – 217.5 °C. **^{1}H NMR (300 MHz, DMSO-*d*$_6$):** δ 8.46 (d, $^{3}J_{HH}$ = 4.8 Hz, $^{4}J_{HH}$ = 1.7 Hz, $^{5}J_{HH}$ = 0.9 Hz 1H, H-25), 8.34 (d, $^{3}J_{HH}$ = 5.5 Hz, 1H, H-2), 8.25 (dt, $^{3}J_{HH}$ = 8.0 Hz, $^{4}J_{HH}$ = 1.0 Hz, 1H, H-22), 8.21 (d, $^{3}J_{HH}$ = 9.1 Hz, 1H, H-7), 7.89 (td, $^{3}J_{HH}$ = 7.8, $^{4}J_{HH}$ = 1.8 Hz, 1H, H-23), 7.79 (d, $^{4}J_{HH}$ = 2.3 Hz, 1H, H-4), 7.60 (d, $^{3}J_{HH}$ = 8.3 Hz, 1H, H-15), 7.52 (m, 1H, H-18), 7.44 (dd, $^{3}J_{HH}$ = 9.1, $^{4}J_{HH}$ = 2.3 Hz, 1H, H-6), 7.35 (ddd, $^{3}J_{HH}$ = 7.6, $^{3}J_{HH}$ = 4.8, $^{4}J_{HH}$ = 1.2 Hz, 1H, H-24), 7.28 (t, $^{3}J_{HH}$ = 5.5 Hz, 1H, H-10), 7.13 (dd, $^{3}J_{HH}$ = 8.3, $^{4}J_{HH}$ = 1.2 Hz, 1H, H-16), 6.33 (d, $^{3}J_{HH}$ = 5.5 Hz, 1H, H-1), 4.95 (t, $^{3}J_{HH}$ = 7.1 Hz, 2H, H-13), 3.28 (m, 2H, H-11), 2.44 (s, 3H, H-17'), 2.20 (m, 2H, H-12). **^{13}C{^{1}H} NMR (101 MHz, DMSO-*d*$_6$):** δ 152.2, 150.4, 149.7, 149.4, 149.1, 142.9, 137.6, 135.0, 133.9, 132.0, 127.9, 125.2, 124.7, 124.5, 124.5 (2C), 124.4, 119.6, 118.0, 110.8, 99.1, 43.3, 40.1, 29.0, 21.6. **FT-IR (ATR, cm^{-1}):** ν = 3171 (N–H), 1611 (C=N$_{benz/quin}$), 1592 (C=N$_{pyr}$), 1580 (C=C). **ESI-MS:** *m/z* 428.1644 (100%, [M+H]$^+$), calculated 428.1637. **HPLC** purity >99% (t_R = 2.33 min).

*7-chloro-N-(3-(2-(pyridin-2-yl)-5-(trifluoromethyl)-1H-benzo[d]imidazol-1-yl)propyl)quinolin-4-amine (**6c**)*

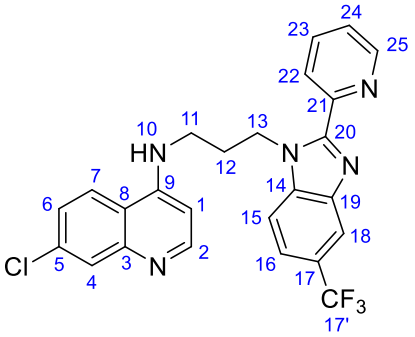

Compound **3c** (0.402 g, 1.02 mmol), 2-pyridinecarboxaldehyde (0.145 ml, 1.53 mmol), TFA (0.00781 ml, 0.102 mmol), anhydrous $MgSO_4$ (0.616 g, 5.12 mmol). Product: Beige powder. Yield: 0.298 g, 60.7%. **M.p.** 200.0 – 201.0 °C. **^{1}H NMR (400 MHz, DMSO-*d*$_6$):** δ 8.45 (ddd, $^3J_{HH}$ = 4.8, $^4J_{HH}$ = 1.6, $^5J_{HH}$ = 0.8 Hz, 1H, H-25), 8.31 (d, $^3J_{HH}$ = 5.5 Hz, 1H, H-2), 8.24 (dt, $^3J_{HH}$ = 8.0, $^4J_{HH}$ = 1.2 Hz, 1H, H-22), 8.15 (d, $^3J_{HH}$ = 9.1 Hz, 1H, H-7), 8.08 (m, 1H, H-18), 7.95 (d, $^3J_{HH}$ = 8.7 Hz, 1H, H-15), 7.91 (td, $^3J_{HH}$ = 7.8, $^4J_{HH}$ = 1.6 Hz, 1H, H-23), 7.77 (d, $^4J_{HH}$ = 2.3 Hz, 1H, H-4), 7.60 (dd, $^3J_{HH}$ = 8.7, $^4J_{HH}$ = 1.6 Hz, 1H, H-16), 7.41 (dd, $^3J_{HH}$ = 9.1, $^4J_{HH}$ = 2.3 Hz, 1H, H-6), 7.37 (ddd, $^3J_{HH}$ = 7.6, $^3J_{HH}$ = 4.8, $^4J_{HH}$ = 1.2 Hz, 1H, H-24), 7.25 (t, $^3J_{HH}$ = 5.2 Hz, 1H, H-10), 6.33 (d, $^3J_{HH}$ = 5.5 Hz, 1H, H-1), 5.01 (t, $^3J_{HH}$ = 7.2 Hz, 2H, H-13), 3.28 (m, 2H, H-11), 2.21 (m, 2H, H-12). **^{13}C{^{1}H} NMR (101 MHz, DMSO-*d*$_6$):** δ 152.2 (2C), 150.4, 149.7, 149.4, 149.2, 141.9, 139.1, 137.9, 133.9, 127.9, 126.8, 125.1 (2C), 124.5 (2C), 124.0, 120.1, 118.0, 117.4, 112.6, 99.1, 43.8, 40.1, 28.9. **FT-IR (ATR, cm^{-1}):** ν = 3179 (N–H), 1613 (C=N$_{benz/quin}$), 1590 (C=N$_{pyr}$), 1580 (C=C), 1330 (C–F). **ESI-MS:** *m/z* 482.1353 (100%, $[M+H]^+$), calculated 482.1354. **HPLC** purity 99% (t_R = 2.41 min).

7.4 Neutral iridium(III) and rhodium(III) hybrid complexes

7.4.1 General method for synthesis of C^N-coordinated Ir(III)-Cp complexes (7a – 7c)*

Sodium acetate (1.5 eq.) was added to a stirring solution of ligand **4a**, **4b** or **4c** (1 eq.) in dry DCM (10 ml) and EtOH (2 ml), and the yellow solution was stirred under N_2 for 1.5 hours. A solution of pentamethylcyclopentadienyliridium(III) chloride (0.5 eq.) in DCM (20 ml) was added dropwise over 30 minutes and the orange solution was stirred for a further 24 hours. The resulting cloudy orange reaction mixture was filtered through Celite® and the solvent of the filtrate was removed to afford an orange residue. This crude product was purified by column chromatography (aluminium oxide) using $CHCl_3$:MeOH

(97:3) for compounds **7a** or **7b**, and $CHCl_3$ (100%) for compound **7c**. Subsequent precipitation from DCM/pentane afforded the desired product as a dull yellow powder, which was collected by suction filtration and dried *in vacuo*.

Unsubstituted cyclometalated Ir(III)-Cp complex (**7a**)*

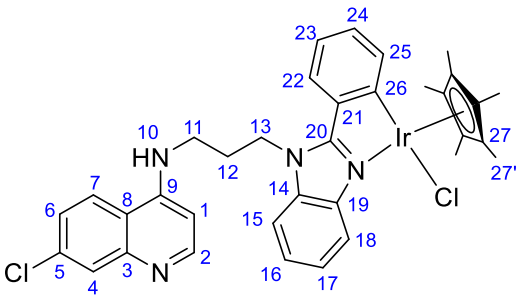

Sodium acetate (0.0182 g, 0.222 mmol), compound **4a** (0.0581 g, 0.141 mmol), $[Ir(Cp^*)Cl_2]_2$ (0.0560 g, 0.0703 mmol). Product: Dull yellow powder. Yield: 0.0687 g, 63.0%. **M.p.** 204.0 – 206.3 °C. **^{1}H NMR (300 MHz, DMSO-*d*$_6$):** δ 8.40 (d, $^3J_{HH}$ = 9.1 Hz, 1H, H-7), 8.35 (d, $^3J_{HH}$ = 5.4 Hz, 1H, H-2), 8.00 (m, 2H, H-22/25), 7.83 (d, $^3J_{HH}$ = 7.5 Hz, 1H, H-15), 7.80 (d, $^4J_{HH}$ = 2.2 Hz, 1H, H-4), 7.70 (t, $^3J_{HH}$ = 5.1 Hz, 1H, H-10), 7.59 – 7.47 (overlapping m, 3H, H-16/17/18), 7.45 (dd, $^3J_{HH}$ = 9.0, $^4J_{HH}$ = 2.2 Hz, 1H, H-6), 7.27 (t, $^3J_{HH}$ = 7.5 Hz, 1H, H-23), 6.98 (t, $^3J_{HH}$ = 7.5 Hz, 1H, H-24), 6.42 (d, $^3J_{HH}$ = 5.4 Hz, 1H, H-1), 4.99 (m, 2H, H-13), 3.49 (m, 2H, H-11), 2.31 (m, 2H, H-12), 1.72 (s, 15H, H-27'). **^{13}C{^{1}H} NMR (151 MHz, DMSO-*d*$_6$):** δ 161.7, 154.5, 152.3, 150.4, 149.6, 138.3, 137.5, 136.0, 134.3, 133.9, 131.5, 127.9, 126.4, 125.0, 124.9 (2C), 124.9, 124.6, 118.1, 116.0, 113.0, 99.1, 96.3 (5C), 43.2, 40.5, 28.3, 9.2 (5C). **FT-IR (ATR, cm^{-1}):** ν = 3254 (N–H), 1609 (C=N$_{quin}$), 1580 (C=C/C=N$_{benz}$). **ESI-MS:** *m/z* 370.1120 (100%, $[M–Cl+H]^{2+}$), calculated 370.1129; *m/z* 773.1756 (60%, $[M–H]^-$), calculated 773.1795.

Methyl-substituted cyclometalated Ir(III)-Cp complex (**7b**)*

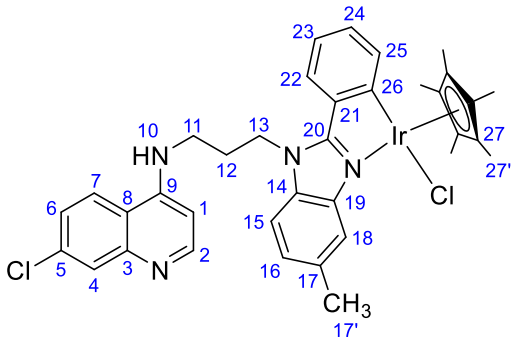

Sodium acetate (0.0182 g, 0.222 mmol), compound **4b** (0.0599 g, 0.140 mmol), $[Ir(Cp^*)Cl_2]_2$ (0.0559 g, 0.0702 mmol). Product: Dull yellow powder. Yield: 0.0689 g, 62.6%. **M.p.** 204.4 – 207.2 °C. **^{1}H NMR (400 MHz, DMSO-*d*$_6$):** δ 8.38-8.35 (overlapping m, 2H, H-2/7), 7.93 (d, $^3J_{HH}$ = 7.8 Hz, 1H, H-25), 7.89 (d, $^3J_{HH}$ = 8.5 Hz, 1H, H-15), 7.80 (m, 2H, H-4/22), 7.72 (t, $^3J_{HH}$ = 4.4 Hz, 1H, H-10), 7.47 (dd, $^3J_{HH}$ = 9.0, $^4J_{HH}$ = 2.2 Hz, 1H, H-6), 7.33 (d, $^3J_{HH}$ = 8.5 Hz, 1H, H-16), 7.27 – 7.23 (overlapping m, 2H, H-18/23), 6.90 (t, $^3J_{HH}$ = 7.3 Hz, 1H, H-24), 6.44 (d, $^3J_{HH}$ = 5.5 Hz, 1H,

H-1), 4.94 (m, 2H, H-13), 3.47 (m, 2H, H-11), 2.56 (s, 3H, H-17'), 2.25 (m, 2H, H-12), 1.72 (s, 15H, H-27'). **$^{13}C\{^{1}H\}$ NMR (101 MHz, DMSO-*d*$_6$):** δ 161.4, 154.2, 152.3, 150.4, 149.6, 138.6, 137.4, 134.7, 134.3, 134.2, 133.9, 131.4, 127.9, 126.3, 126.2, 124.9, 124.7, 124.6, 118.0, 115.4, 112.7, 99.1, 96.3 (5C), 43.1, 40.3, 28.4, 21.7, 9.2 (5C). **FT-IR (ATR, cm^{-1}):** ν = 3274 (N–H), 1611 (C=N$_{quin}$), 1584 (C=C/C=N$_{benz}$). **ESI-MS:** *m/z* 370.1207 (100%, $[M\text{-}Cl+H]^{2+}$), calculated 377.1207; *m/z* 787.1949 (50%, $[M–H]^-$), calculated 787.1952.

Trifluoromethyl-substituted cyclometalated Ir(III)-Cp complex (**7c**)*

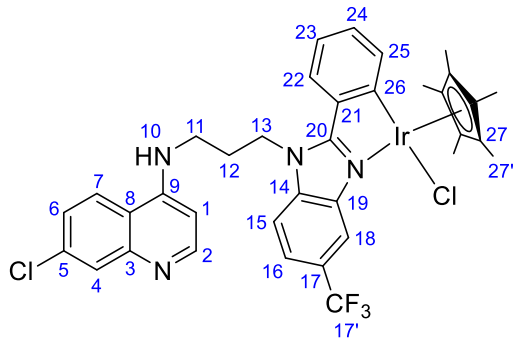

Sodium acetate (0.0259 g, 0.316 mmol), compound **4c** (0.0754 g, 0.157 mmol), $[Ir(Cp^*)Cl_2]_2$ (0.0624 g, 0.0784 mmol). Product: Yellow powder. Yield: 0.0683 g, 51.7%. **M.p.** 201.1 – 203.1 °C.**^{1}H NMR (600 MHz, DMSO-*d*$_6$):** δ 8.38 (d, $^{3}J_{HH}$ = 9.0 Hz, 1H, H-7), 8.35 (d, $^{3}J_{HH}$ = 5.5 Hz, 1H, H-2), 8.32 (d, $^{3}J_{HH}$ = 8.6 Hz, 1H, H-15), 7.99 (d, $^{3}J_{HH}$ = 7.8 Hz, 1H, H-25), 7.85 – 7.82 (overlapping m, 2H, H-16/22), 7.79 (d, $^{4}J_{HH}$ = 2.3 Hz, 1H, H-4), 7.75 (t, $^{3}J_{HH}$ = 5.5 Hz, 1H, H-10), 7.69 (m, 1H, H-18), 7.45 (dd, $^{3}J_{HH}$ = 9.0, $^{4}J_{HH}$ = 2.3 Hz, 1H, H-6), 7.29 (td, $^{3}J_{HH}$ = 7.8, $^{4}J_{HH}$ = 1.1 Hz, 1H, H-23), 6.89 (td, $^{3}J_{HH}$ = 7.8, $^{4}J_{HH}$ = 1.1 Hz, 1H, H-24), 6.47 (d, $^{3}J_{HH}$ = 5.5 Hz, 1H, H-1), 5.02 (m, 2H, H-13), 3.52 (m, 2H, H-11), 2.29 (m, 2H, H-12), 1.70 (s, 15H, H-27'). **$^{13}C\{^{1}H\}$ NMR (151 MHz, DMSO-*d*$_6$):** δ 164.3, 155.6, 152.3, 150.4, 149.6, 138.7, 138.2, 137.3, 133.9, 133.6, 132.3, 127.9, 127.52, 127.1, 125.3, 125.0, 124.8, 124.6, 121.4, 118.0, 114.6, 112.8, 99.2, 96.4 (5C), 43.8, 40.5, 28.2, 9.2 (5C). **FT-IR (ATR, cm^{-1}):** ν = 3274 (N–H), 1611 (C=N$_{quin}$), 1584 (C=C/C=N$_{benz}$), 1326 (C–F). **ESI-MS:** *m/z* 404.1064 (100%, $[M–Cl+H]^{2+}$), calculated 404.1066; *m/z* 807.2033 (70%, $[M–Cl]^-$), calculated 807.2053; *m/z* 841.1702 (100%, $[M\text{-}H]^-$), calculated 841.1669.

7.4.2 General method for synthesis of C^N-coordinated Rh(III)-Cp complexes (8a – 8b)*

Sodium acetate (2 eq.) was added to a stirring solution of ligand **4a** or **4b** (1 eq.) in dry methanol (15 ml) and the pale-yellow solution was stirred under N_2 for 30 minutes. Thereafter, a solution of pentamethylcyclopentadienylrhodium(III) chloride dimer (0.5 eq.) in dry DCM (20 ml) was added dropwise over 10 minutes and the red solution was refluxed under N_2 for 96 hours. The resulting red solution was cooled to room temperature and the solvent was removed to afford a red residue. This crude residue was purified by column chromatography (aluminium oxide) using $CHCl_3$:MeOH (19:1). Precipitation from DCM/pentane afforded the desired product as a dull orange powder, which was collected by suction filtration and dried *in vacuo*.

Unsubstituted cyclometalated Rh(III)-Cp complex (**8a**)*

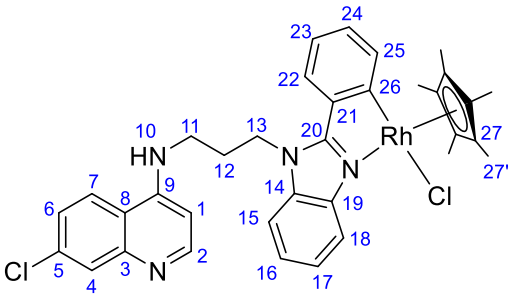

Sodium acetate (0.0217 g, 0.264 mmol), compound **4a** (0.0514 g, 0.124 mmol), $[Rh(Cp^*)Cl_2]_2$ (0.0382 g, 0.0618 mmol). Product: Dull orange powder. Yield: 0.0304 g, 35.9%. **M.p.** 186.8 °C (Decomp. w/o melting). **^{1}H NMR (300 MHz, DMSO-d_6):** δ 8.39 – 8.32 (overlapping m, 2H, H-2/7), 8.01 (dd, $^3J_{HH}$ = 6.9, $^4J_{HH}$ = 1.9 Hz, 1H, H-25), 7.93 (d, $^3J_{HH}$ = 7.5 Hz, 1H, H-22), 7.83 – 7.79 (overlapping m, 2H, H-4/15), 7.66 – 7.59 (overlapping m, 2H, H-10/18), 7.54 – 7.43 (overlapping m, 3H, H-6/16/17), 7.32 (t, $^3J_{HH}$ = 7.4 Hz, 1H, H-23), 6.90 (t, $^3J_{HH}$ = 7.2 Hz, 1H, H-24), 6.45 (d, $^3J_{HH}$ = 5.5 Hz, 1H, H-1), 4.92 (m, 2H, H-13), 3.47 (m, 2H, H-11), 2.26 (m, 2H, H-12), 1.64 (s, 15H, H-27'). **^{13}C{^{1}H} NMR (151 MHz, DMSO-d_6):** δ 158.4, 152.7, 151.1, 149.5, 139.2, 138.2, 136.8, 135.1, 134.8, 131.7, 128.0, 126.7, 126.0, 125.4, 125.3 (2C), 124.9 (2C), 118.3, 116.8, 113.2, 102.5 (2C), 102.4 (3C), 99.7, 43.7, 40.5, 28.6, 9.9 (5C). **FT-IR (ATR, cm^{-1}):** ν = 3266 (N–H), 1611 (C=N_{quin}), 1580 (C=C/C=N_{benz}). **ESI-MS:** *m*/*z* 325.0846 (100%, $[M–Cl+H]^{2+}$), calculated 325.0842; *m*/*z* 649.1589 (30%, $[M–Cl]^+$), calculated 649.1605.

Methyl-substituted cyclometalated Rh(III)-Cp complex (**8b**)*

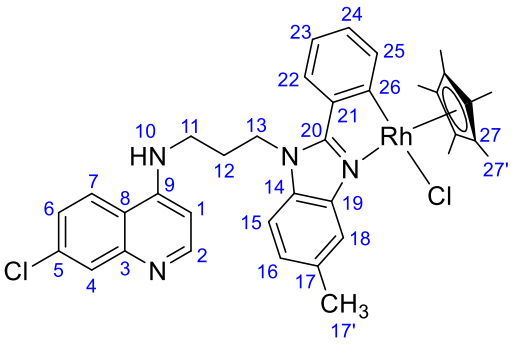

Sodium acetate (0.0320 g, 0.390 mmol), compound **4b** (0.0801 g, 0.188 mmol), $[Rh(Cp^*)Cl_2]_2$ (0.0580 g, 0.0938 mmol). Product: Dull orange powder. Yield: 0.0613 g, 46.8%. **M.p.** 194.2 °C (Decomp. w/o melting). **^{1}H NMR (600 MHz, DMSO-*d*$_6$):** δ 8.39 (d, $^3J_{HH}$ = 9.1 Hz, 1H, H-7), 8.34 (d, $^3J_{HH}$ = 5.4 Hz, 1H, H-2), 7.92 – 7.87 (overlapping m, 2H, H-15/25), 7.82 – 7.77 (overlapping m, 2H, H-4/22), 7.68 (t, $^3J_{HH}$ = 5.4 Hz, 1H, H-10), 7.47 (dd, $^3J_{HH}$ = 9.0, $^4J_{HH}$ = 2.3 Hz, 1H, H-6), 7.34 (m, 1H, H-18), 7.33 – 7.26 (m, 2H, H-16/23), 6.89 (td, $^3J_{HH}$ = 7.8, $^4J_{HH}$ = 1.0 Hz, 1H, H-24), 6.43 (d, $^3J_{HH}$ = 5.5 Hz, 1H, H-1), 4.88 (m, 2H, H-13), 3.46 (m, 2H, H-11), 2.54 (s, 3H, H-17'), 2.23 (m, 2H, H-12), 1.63 (s, 15H, H-27'). **^{13}C{^{1}H} NMR (151 MHz, DMSO-*d*$_6$):** δ 157.7, 152.3, 150.4, 149.6, 139.2, 137.6, 134.7, 134.6, 134.4, 133.9, 131.0, 127.9, 126.2, 126.1, 125.4, 124.8 (2C), 124.6, 118.0, 115.8, 112.6, 101.9 (3C), 101.8 (2C), 99.1, 43.3, 40.5, 28.3, 21.6, 9.5 (5C). **FT-IR (ATR, cm^{-1}):** ν = 3258 (N–H), 1611 (C=N$_{quin}$), 1580 (C=C/C=N$_{benz}$). **ESI-MS:** *m*/*z* 332.0920 (100%, $[M–Cl+H]^{2+}$), calculated 332.0920; *m*/*z* 663.1749 (28%, $[M–Cl]^+$), calculated 663.1761.

7.4.3 General method for synthesis of quinoline N-coordinated Ir(III)- and Rh(III)-Cp complexes (9a – 9c and 10a – 10c)*

Pentamethylcyclopentadienyliridium(III) chloride dimer (0.5 eq.) or pentamethyl-cyclopentadienylrhodium(III) chloride dimer (0.5 eq.) suspended in anhydrous MeOH (15 ml) was added dropwise to a stirring solution of ligand **4a**, **4b** or **4c** (1 eq.) in anhydrous methanol (5 ml) and the orange or red solution was stirred under N_2 at room temperature for 24 hours. The desired product precipitated as a yellow or orange powder, which was collected by suction filtration and washed with cold methanol, followed by diethyl ether and dried *in vacuo*.

Unsubstituted quinoline N-coordinated Ir(III)-Cp complex (**9a**)*

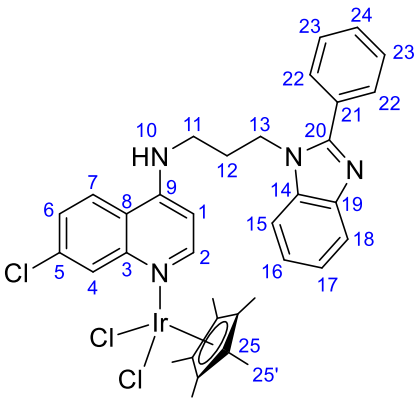

Compound **4a** (0.0509 g, 0.122 mmol), $[Ir(Cp^*)Cl_2]_2$ (0.0482 g, 0.0605 mmol). Product: Yellow powder. Yield: 0.0902 g, 91.9%. **M.p.** 241.8 °C (Decomp. with melting). **^{1}H NMR (300 MHz, DMSO-*d*$_6$):** δ 8.41 (d, *J* = 6.1 Hz, 1H, H-2), 8.23 (d, $^3J_{HH}$ = 9.1 Hz, 1H, H-7), 7.97 (t, $^3J_{HH}$ = 5.5 Hz, 1H, H-10), 7.85 (d, $^4J_{HH}$ = 2.1 Hz, 1H, H-4), 7.75 – 7.63 (overlapping m, 4H, H-15/18/22), 7.58 (dd, $^3J_{HH}$ = 9.1, $^4J_{HH}$ = 2.2 Hz, 1H, H-6), 7.34 – 7.21 (overlapping m, 5H, H-16/17/23/24), 6.46 (d, $^3J_{HH}$ = 6.1 Hz, 1H, H-1), 4.49 (t, $^3J_{HH}$ = 7.3 Hz, 2H, H-13), 3.28 (m, 2H, H-11), 2.1 (m, 2H, H-12), 1.63 (s, 15H, H-25'). **^{13}C{^{1}H} NMR (151 MHz, DMSO-*d*$_6$):** δ 153.8, 153.1, 148.6, 144.9, 143.2, 136.5, 136.2, 130.7, 130.3, 129.7 (2C), 129.3 (2C), 126.2, 125.4, 124.3, 123.5, 123.1, 120.0, 117.3, 111.7, 99.5, 93.0 (5C), 42.5, 40.5, 28.3, 9.0 (5C). **FT-IR (ATR, cm^{-1}):** ν = 3317 (N–H), 1613 (C=N), 1590 (C=C). **ESI-MS:** *m/z* 811.1723 ($[M+H]^+$), calculated 811.1708; *m/z* 775.1938 ($[M-Cl]^+$), calculated 775.1946.

Methyl-substituted quinoline N-coordinated Ir(III)-Cp complex (**9b**)*

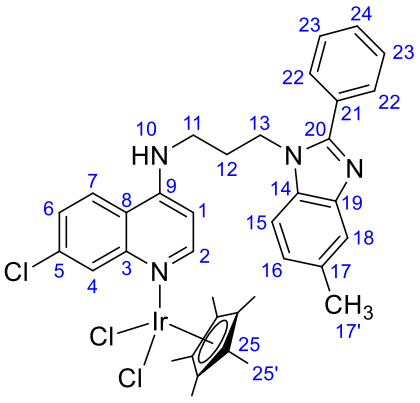

Compound **4b** (0.0521 g, 0.122 mmol), $[Ir(Cp^*)Cl_2]_2$ (0.0469 g, 0.0589 mmol). Product: Yellow powder. Yield: 0.0834 g, 96.2%. **M.p.** 253.6 °C (Decomp. with melting). **^{1}H NMR (300 MHz, DMSO-*d*$_6$):** δ 8.35 (d, $^3J_{HH}$ = 5.5 Hz, 1H, H-2), 8.13 (d, $^3J_{HH}$ = 9.0 Hz, 1H, H-7), 7.79 (d, $^3J_{HH}$ = 2.1 Hz, 1H, H-4), 7.67 (m, 2H, H-22), 7.57 (d, $^3J_{HH}$ = 8.2 Hz, 1H, H-15), 7.48 (m, 1H, H-18), 7.43 (dd, $^3J_{HH}$ = 9.0, $^4J_{HH}$ = 2.2 Hz, 1H, H-6), 7.40 – 7.27 (overlapping m, 3H, H-23/24), 7.21 (t, $^3J_{HH}$ = 5.2 Hz, 1H, H-10), 7.10 (d, $^3J_{HH}$ = 8.2 Hz, 1H, H-16), 6.29 (d, $^3J_{HH}$ = 5.5 Hz, 1H, H-1), 4.44 (t, $^3J_{HH}$ = 7.3 Hz, 2H, H-13), 3.18 (m, 2H, H-11), 2.44 (s, 3H, H-17'), 2.11 (m, 2H, H-12), 1.63 (s, 15H, H-25'). **^{13}C{^{1}H} NMR (101 MHz, DMSO-*d*$_6$):** δ 153.2, 152.2, 150.2, 149.4, 143.4, 134.2, 133.8, 131.4, 130.8, 129.7 (2C), 129.3 (2C), 128.9, 127.9, 124.4 (2C), 124.2, 119.3, 117.9, 110.8, 99.1, 92.5 (5C), 42.5, 40.5, 28.3, 21.6, 8.6 (5C). **FT-IR (ATR, cm^{-1})** ν = 3317 (N–H), 1611 (C=N), 1590 (C=C).

ESI-MS: *m/z* 789.2087 ([M–Cl]$^+$), calculated 789.2102; *m/z* 825.1714 ([M+H]$^+$), calculated 825.1864.

Trifluoromethyl-substituted quinoline N-coordinated Ir(III)-Cp complex (**9c**)*

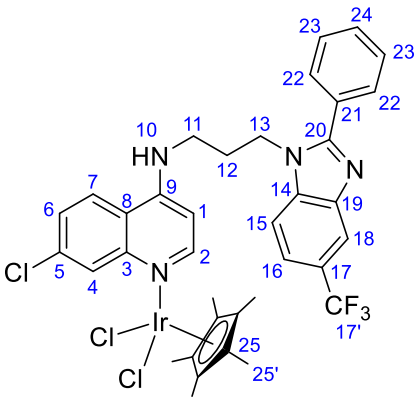

Compound **4c** (0.0508 g, 0.106 mmol), $[Ir(Cp^*)Cl_2]_2$ (0.0411 g, 0.0516 mmol). Product: Yellow powder. Yield: 0.0834 g, 88.6%. **M.p.** 267.4 °C (Decomp. with melting). **^{1}H NMR (600 MHz, DMSO-*d*$_6$):** δ 8.30 (d, $^3J_{HH}$ = 5.4 Hz, 1H, H-2), 8.04 (d, $^3J_{HH}$ = 9.1 Hz, 1H, H-7), 8.03 (m, 1H, H-18), 7.92 (d, $^3J_{HH}$ = 8.5 Hz, 1H, H-15), 7.79 (d, $^3J_{HH}$ = 2.2 Hz, 1H, H-4), 7.65 (m, 2H, H-22), 7.59 (dd, $^3J_{HH}$ = 8.6, $^4J_{HH}$ = 1.3 Hz, 1H, H-16), 7.41 (dd, $^3J_{HH}$ = 9.0, $^4J_{HH}$ = 2.2 Hz, 1H, H-6), 7.36 – 7.27 (overlapping m, 3H, H-23/24), 7.21 (t, $^3J_{HH}$ = 5.2 Hz, 1H, H-10), 6.27 (d, $^3J_{HH}$ = 5.4 Hz, 1H, H-1), 4.51 (t, $^3J_{HH}$ = 7.4 Hz, 2H, H-13), 3.18 (m, 2H, H-11), 2.11 (m, 2H, H-12), 1.61 (s, 15H, H-25'). **^{13}C{^{1}H} NMR (151 MHz, DMSO-*d*$_6$):** δ 156.1, 152.4, 150.8, 149.3, 142.6, 138.6, 134.4, 130.7, 130.1, 129.7, 129.4, 128.0, 127.8, 125.0 (2C), 124.7 (2C), 124.0, 119.9, 118.1, 117.2, 112.8, 99.4, 93.0 (5C), 43.1, 40.5, 28.3, 9.0 (5C). **FT-IR (ATR, cm^{-1}):** ν = 3321 (N–H), 1613 (C=N), 1590 (C=C), 1328 (C-F). **ESI-MS:** *m/z* 879.1503 ([M+H]$^+$), calculated 879.1582, *m/z* 843.1803 ([M–Cl]$^+$), calculated 843.1820.

Unsubstituted quinoline N-coordinated Rh(III)-Cp complex (**10a**)*

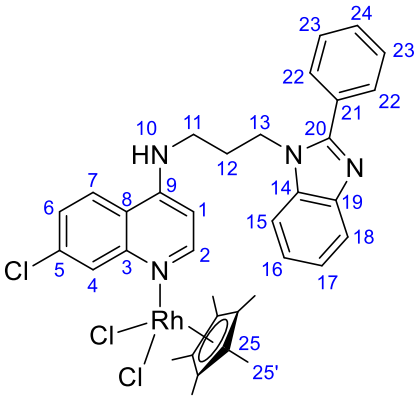

Compound **4a** (0.0521 g, 0.122 mmol), $[Rh(Cp^*)Cl_2]_2$ (0.0469 g, 0.0589 mmol). Product: Orange powder. Yield: 0.0786 g, 89.9%. **M.p.** 261.7 °C (Decomp. with melting). **^{1}H NMR (300 MHz, DMSO-*d*$_6$):** δ 8.42 (d, $^3J_{HH}$ = 6.1 Hz, 1H, H-2), 8.23 (d, $^3J_{HH}$ = 9.1 Hz, 1H, H-7), 8.04 (t, $^3J_{HH}$ = 5.5 Hz, 1H, H-10), 7.85 (d, $^3J_{HH}$ = 2.1 Hz, 1H, H-4), 7.77 – 7.63 (overlapping m, 4H, H-15/18/22), 7.59 (dd, $^3J_{HH}$ = 9.0, $^4J_{HH}$ = 2.1 Hz, 1H, H-6), 7.36 – 7.16 (overlapping m, 5H, H-16/17/23/24), 6.48 (d, $^3J_{HH}$ = 6.2 Hz, 1H, H-1), 4.49 (t, $^3J_{HH}$ = 7.3 Hz, 2H, H-13), 3.29 (m, 2H, H-11), 2.13 (m, 2H, H-12), 1.63 (s, 15H, H-25'). **^{13}C{^{1}H} NMR (151 MHz, DMSO-*d*$_6$):** δ 153.9, 153.5, 148.3, 144.5, 143.2, 136.8, 136.2,

130.7, 130.4, 129.8 (2C), 129.4 (2C), 126.5, 125.5, 124.1, 123.7, 123.3, 120.0, 117.3, 111.8, 100.0 (3C), 99.9 (2C), 99.5, 42.6, 40.5, 28.3, 9.5 (5C). **FT-IR (ATR, cm^{-1}):** ν = 3313 (N–H), 1613 (C=N), 1588 (C=C). **ESI-MS:** *m/z* 721.1142 ([M+H]$^+$), calculated 721.1134; *m/z* 685.1360 ([M–Cl]$^+$), calculated 685.1372.

Methyl-substituted quinoline N-coordinated Rh(III)-Cp complex (**10b**)*

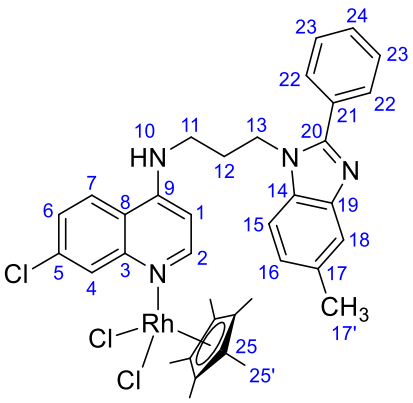

Compound **4b** (0.0516 g, 0.121 mmol), $[Rh(Cp^*)Cl_2]_2$ (0.0364 g, 0.0589 mmol). Product: Orange powder. Yield: 0.0692 g, 71.2%. **M.p.** 278.6 °C (Decomp. with melting). **^{1}H NMR (300 MHz, DMSO-*d*$_6$):** δ 8.35 (d, $^3J_{HH}$ = 5.4 Hz, 1H, H-2), 8.13 (d, $^3J_{HH}$ = 9.1 Hz, 1H, H-7), 7.79 (d, $^3J_{HH}$ = 1.9 Hz, 1H, H-4), 7.67 (m, 2H, H-22), 7.57 (d, $^3J_{HH}$ = 8.3 Hz, 1H, H-15), 7.48 (m, 1H, H-18), 7.43 (dd, $^3J_{HH}$ = 9.0, $^4J_{HH}$ = 2.1 Hz, 1H, H-6), 7.40 – 7.27 (overlapping m, 3H, H-23/24), 7.20 (t, $^3J_{HH}$ = 4.5 Hz, 1H, H-10), 7.10 (d, $^3J_{HH}$ = 7.3 Hz, 1H, H-16), 6.30 (d, $^3J_{HH}$ = 5.4 Hz, 1H, H-1), 4.44 (t, $^3J_{HH}$ = 7.3 Hz, 2H, H-13), 3.18 (m, 2H, H-11), 2.44 (s, 3H, H-17'), 2.11 (m, 2H, H-12), 1.63 (s, 15H, H-25'). **^{13}C{^{1}H} NMR (101 MHz, DMSO-*d*$_6$):** δ 153.3, 152.2, 150.3, 149.4, 143.4, 134.2, 133.8, 131.5, 130.8, 129.8 (2C), 129.3 (2C), 128.9, 127.8, 124.5, 124.4, 124.3, 119.4, 117.9, 110.8, 99.3 (2C), 99.2 (3C), 99.1, 42.5, 28.3, 21.6, 9.0 (5C). **FT-IR (ATR, cm^{-1}):** ν = 3306 (N-H), 1611 (C=N), 1588 (C=C). **ESI-MS:** *m/z* 735.1277 ([M+H]$^+$), calculated 735.1290; *m/z* 699.1505 ([M–Cl]$^+$), calculated 699.1528.

Trifluoromethyl-substituted quinoline N-coordinated Rh(III)-Cp complex (**10c**)*

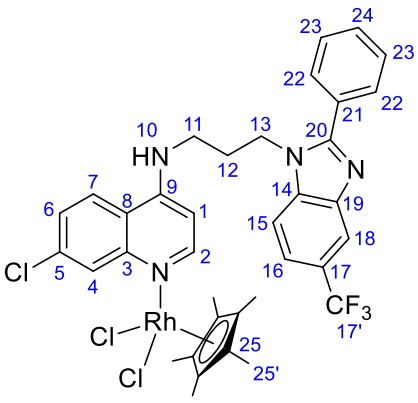

Compound **4c** (0.0513 g, 0.107 mmol), $[Rh(Cp^*)Cl_2]_2$ (0.0326 g, 0.0527 mmol). Product: Orange powder. Yield: 0.0544 g, 65.4%. **M.p.** 285.4 °C (Decomp. with melting). **^{1}H NMR (300 MHz, DMSO-*d*$_6$):** δ 8.31 (d, $^3J_{HH}$ = 5.5 Hz, 1H, H-2), 8.06 (d, $^3J_{HH}$ = 9.1 Hz, 1H, H-7), 8.03 (m, 1H, H-18), 7.92 (d, $^3J_{HH}$ = 8.5 Hz, 1H, H-15), 7.80 (d, $^4J_{HH}$ = 2.2 Hz, 1H, H-4), 7.65 (m, 2H, H-22), 7.59 (dd, $^3J_{HH}$ = 8.6 Hz, $^4J_{HH}$ = 1.5 Hz, 1H, H-16), 7.43 (dd, $^3J_{HH}$ = 9.1 Hz, $^4J_{HH}$ = 2.2 Hz, 1H, H-6), 7.36 – 7.27 (overlapping m, 4H, H-10/23/24), 6.29 (d,

$^3J_{HH}$ = 5.2 Hz, 1H, H-1), 4.52 (t, J = $^3J_{HH}$ = 7.4 Hz, 2H, H-13), 3.19 (m, 2H, H-11), 2.11 (m, 2H, H-12), 1.61 (s, 15H, H-25'). **^{13}C{^{1}H} NMR (151 MHz, DMSO-*d*$_6$):** δ 156.1, 151.9, 151.0, 148.8, 142.6, 138.5, 134.6, 130.7, 130.1, 129.7, 129.3, 128.4, 127.4, 125.1, 124.7, 123.9, 119.9, 118.0, 117.2, 112.8, 99.7 (3C), 99.6 (2C), 99.4, 43.1, 40.5, 28.3, 9.3 (5C). **FT-IR (ATR, cm^{-1}):** ν = 3310 (N-H), 1613 (C=N), 1588 (C=C). **ESI-MS:** *m/z* 789.1037 ([M+H]$^+$), calculated 789.1007; *m/z* 753.1227 ([M–Cl]$^+$), calculated 753.1245.

7.5 Cationic iridium(III) and rhodium(III) hybrid complexes

7.5.1 General method for synthesis of N^N-coordinated Ir(III)- and Rh(III)-Cp complexes (11a – 11c and 12a – 12c)*

Pentamethylcyclopentadienyliridium(III) chloride dimer (0.5 eq.) or pentamethyl-cyclopentadienylrhodium(III) chloride dimer (0.5 eq.) dissolved in DCM (10 ml) was added dropwise to a stirring solution of ligand **6a**, **6b** or **6c** (1 eq.) in EtOH (10 ml) and the orange solution was stirred at room temperature under N_2 for 16 – 24 hours. The DCM was then removed, NH_4PF_6 (1.2 eq.) was added and the solution was stirred at 0 °C for 2 hours, resulting in the precipitation of the product as a yellow or orange solid. Thereafter, the solvent was reduced and the mixture placed in the fridge overnight. The resulting precipitate was collected by suction filtration and washed with cold ethanol, followed by diethyl ether and dried *in vacuo*.

Unsubstituted N^N-coordinated Ir(III)-Cp complex (**11a**)*

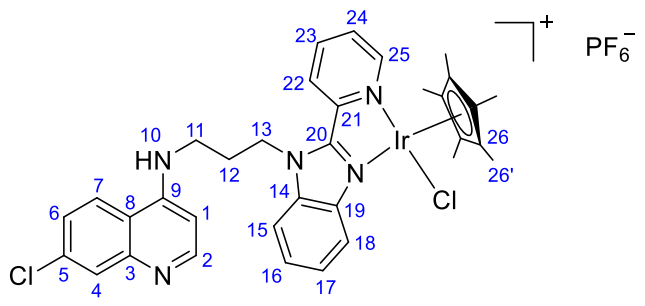

$[Ir(Cp^*)Cl_2]_2$ (0.0494 g, 0.0620 mmol), compound **6a** (0.0512 g, 0.124 mmol) and NH_4PF_6 (0.0255 g, 0.156 mmol). Product: Yellow powder. Yield: 0.0759 g, 66.4%. **M.p.** 189.3 – 192.3 °C. **^{1}H NMR (400 MHz, DMSO-*d*$_6$):** δ 9.12 (dd, $^3J_{HH}$ = 5.6 Hz, $^4J_{HH}$ = 1.0 Hz, 1H, H-25), 8.56 (d, $^3J_{HH}$ = 8.2 Hz, 1H, H-22), 8.40 (d, $^3J_{HH}$ = 5.7 Hz, 1H, H-2), 8.26 (d, $^3J_{HH}$ = 9.1 Hz, 1H, H-7), 8.11 – 8.06 (overlapping m, 2H, H-10/23), 7.86 – 7.82 (overlapping m, 2H, H-4/24), 7.76 (m, 1H, H-15), 7.66 – 7.58 (overlapping m, 3H, H-16/17/18), 7.53 (dd, $^3J_{HH}$ = 9.1, $^4J_{HH}$ = 2.2 Hz, 1H, H-6), 6.50 (d, $^3J_{HH}$ = 5.7 Hz, 1H,

H-1), 5.08 (m, 2H, H-13), 3.50 (m, 2H, H-11), 2.31 (m, 2H, H-12), 1.69 (s, 15H, H-26'). **^{13}C{^{1}H} NMR (101 MHz, DMSO-*d*$_6$):** δ 154.3, 151.2, 151.0, 150.9, 148.0, 145.6, 140.8, 137.7, 136.4, 134.6, 129.1, 126.9, 126.7, 126.0, 125.1, 125.0, 124.6, 117.8, 117.6, 113.4, 99.2, 89.1 (5C), 43.7, 40.5, 28.4, 9.3 (5C). **^{31}P{^{1}H} NMR (162 MHz, DMSO-*d*$_6$):** δ -144.2 (sep, ^{1}J = 711.2 Hz, PF_6^-). **FT-IR (ATR, cm^{-1}):** ν = 3333 (N-H), 1633 (sh, C=N$_{pyr}$), 1609 (C=N$_{benz/quin}$), 1580 (C=C). **ESI-MS:** *m/z* 388.5986 ($[M+H]^{2+}$), calculated 388.5986.

Methyl-substituted N^N-coordinated Ir(III)-Cp complex (**11b**)*

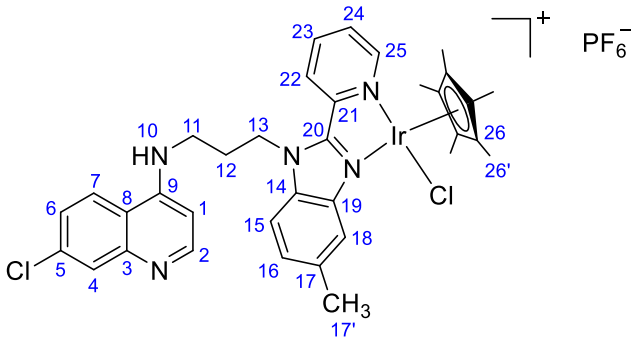

$[Ir(Cp^*)Cl_2]_2$ (0.0485 g, 0.0609 mmol), compound **6b** (0.0521 g, 0.122 mmol) and NH_4PF_6 (0.0255 g, 0.156 mmol). Product: Yellow powder. Yield: 0.0805 g, 70.7%. **M.p.** 200.8 – 202.5 °C. **^{1}H NMR (600 MHz, DMSO-*d*$_6$):** δ 9.10 (dd, $^{3}J_{HH}$ = 5.6, $^{4}J_{HH}$ = 1.3 Hz, 1H, H-25), 8.54 (d, $^{3}J_{HH}$ = 8.2 Hz, 1H, H-22), 8.43 (d, $^{3}J_{HH}$ = 6.0 Hz, 1H, H-2), 8.26 (d, $^{3}J_{HH}$ = 9.1 Hz, 1H, H-7), 8.11 (td, $^{3}J_{HH}$ = 8.2, $^{4}J_{HH}$ = 1.3 Hz, 1H, H-23), 7.99 (m, 1H, H-10), 7.95 (d, $^{3}J_{HH}$ = 8.6 Hz, 1H, H-15), 7.85 – 7.81 (overlapping m, 2H, H-4/24), 7.57 (dd, $^{3}J_{HH}$ = 9.1, $^{4}J_{HH}$ = 2.2 Hz, 1H, H-6), 7.45 (m, 1H, H-18), 7.43 (dd, $^{3}J_{HH}$ = 8.6, $^{4}J_{HH}$ = 1.1 Hz, 1H, H-16), 6.57 (d, $^{3}J_{HH}$ = 6.0 Hz, 1H, H-1), 5.04 (m, 2H, H-13), 3.52 (m, 2H, H-11), 2.56 (s, 3H, H-17'), 2.29 (m, 2H, H-12), 1.68 (s, 15H, H-26'). **^{13}C{^{1}H} NMR (151 MHz, DMSO-*d*$_6$):** δ 154.3, 152.1, 150.7, 149.6, 146.0, 145.7, 140.9, 138.0, 135.9, 135.5, 134.7, 129.1, 128.4, 125.6, 125.3, 124.9, 124.8, 117.3, 116.9, 113.2, 99.2, 89.1 (5C), 43.7, 40.5, 28.4, 21.6, 9.4 (5C). **^{31}P{^{1}H} NMR (162 MHz, DMSO-*d*$_6$):** δ -144.2 (sep, ^{1}J = 711.2 Hz, PF_6^-). **FT-IR (ATR, cm^{-1}):** ν = 3337 (N-H), 1633 (sh, C=N$_{pyr}$), 1613 (C=N$_{benz/quin}$), 1580 (C=C). **ESI-MS:** *m/z* 395.6066 ($[M+H]^{2+}$), calculated 395.6064.

Trifluoromethyl-substituted N^N-coordinated Ir(III)-Cp complex (**11c**)*

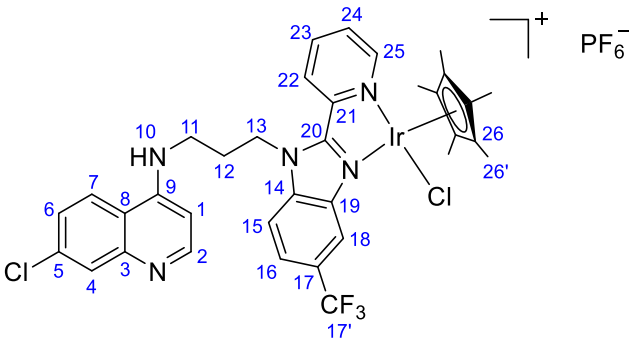

[Ir(Cp*)Cl$_2$]$_2$ (0.0436 g, 0.0547 mmol), compound **6c** (0.0526 g, 0.109 mmol) and NH_4PF_6 (0.0236 g, 0.145 mmol). Product: Yellow powder. Yield: 0.0573 g, 53.0%. **M.p.** 244.5 – 247.2 °C. **^{1}H NMR (400 MHz, DMSO-*d*$_6$):** δ 9.16 (dd, $^3J_{HH}$ = 5.6, $^4J_{HH}$ = 1.1 Hz, 1H, H-25), 8.63 (d, $^3J_{HH}$ = 8.2 Hz, 1H, H-22), 8.41 (d, $^3J_{HH}$ = 5.6 Hz, 1H, H-2), 8.35 (d, $^3J_{HH}$ = 9.2 Hz, 1H, H-15), 8.18 – 8.09 (overlapping m, 2H, H-7/23), 7.97 – 7.87 (overlapping m, 3H, H-16/18/24), 7.81 (d, $^4J_{HH}$ = 2.2 Hz, 1H, H-4), 7.60 (t, $^3J_{HH}$ = 5.5 Hz, 1H, H-10), 7.49 (dd, $^3J_{HH}$ = 9.0, $^4J_{HH}$ = 2.2 Hz, 1H, H-6), 6.52 (d, $^3J_{HH}$ = 5.7 Hz, 1H, H-1), 5.14 (m, 2H, H-13), 3.53 (m, 2H, H-11), 2.36 (m, 2H, H-12), 1.69 (s, 15H, H-26'). **^{13}C{^{1}H} NMR (151 MHz, DMSO-*d*$_6$):** δ 154.4, 153.7, 151.1, 151.0, 147.8, 145.1, 141.0, 138.9, 137.1, 134.6, 129.9, 126.1, 125.9, 125.8, 125.4, 125.1, 124.6, 123.0, 117.6, 115.5, 114.5, 99.3, 89.3 (5C), 44.4, 40.5, 28.2, 9.4 (5C). **^{31}P{^{1}H} NMR (162 MHz, DMSO-*d*$_6$):** δ -144.2 (sep, ^1J = 711.2 Hz, PF_6^-). **FT-IR (ATR, cm^{-1}):** ν = 3337 (N-H), 1633 (sh, C=N$_{pyr}$), 1611 (sh, C=N$_{benz/quin}$), 1582 (C=C), 1330 (C–F). **ESI-MS:** *m/z* 422.5920 ([M+H]$^{2+}$), calculated 422.5923.

Unsubstituted N^N-coordinated Rh(III)-Cp complex (**12a**)*

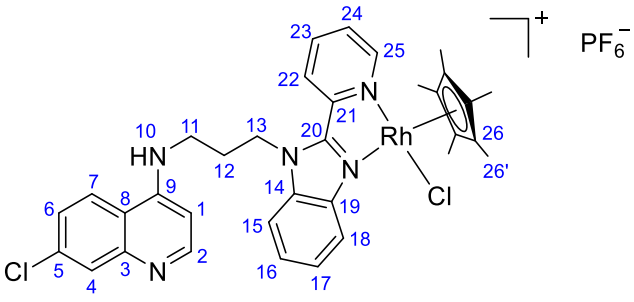

[Rh(Cp*)Cl$_2$]$_2$ (0.0382 g, 0.0618 mmol), compound **6a** (0.0512 g, 0.124 mmol) and NH_4PF_6 (0.0243 g, 0.149 mmol). Product: Orange powder. Yield: 0.0723 g, 70.2%. **M.p.** 194.9 – 197.0 °C. **^{1}H NMR (400 MHz, DMSO-*d*$_6$):** δ 9.12 (dd, $^3J_{HH}$ = 5.4, $^4J_{HH}$ = 0.9 Hz, 1H, H-25), 8.48 (d, $^3J_{HH}$ = 8.2 Hz, 1H, H-22), 8.41 (d, $^3J_{HH}$ = 5.8 Hz, 1H, H-2), 8.25 (d, $^3J_{HH}$ = 9.1 Hz, 1H, H-7), 8.11 – 8.04 (overlapping m, 2H, H-15/23), 7.87 (m, 1H, H-24), 7.85 – 7.80 (overlapping m, 2H, H-4/18), 7.73 (t, $^3J_{HH}$ = 5.5 Hz, 1H, H-10), 7.62 – 7.57 (overlapping m, 2H, H-16/17), 7.54 (dd, $^3J_{HH}$ = 9.1, $^4J_{HH}$ = 2.2 Hz, 1H, H-6), 6.53 (d, $^3J_{HH}$ = 5.8 Hz, 1H, H-1), 5.01 (m, 2H, H-13), 3.55 (m, 2H, H-11), 2.29 (m, 2H, H-12), 1.68 (s, 15H, H-26'). **^{13}C{^{1}H} NMR (101 MHz, DMSO-*d*$_6$):** δ 154.3, 151.4,

150.8, 148.3, 147.5, 145.7, 140.8, 138.5, 137.0, 134.9, 128.5, 126.5, 126.4, 125.7, 125.3, 124.9, 124.7, 118.3, 117.5, 113.3, 99.3, 97.1 (3C), 97.0 (2C), 43.8, 40.5, 28.3, 9.5 (5C). **^{31}P{^{1}H} NMR (162 MHz, DMSO-*d*$_6$):** δ -144.2 (sep, ^{1}J = 711.2 Hz, PF_6^-). **FT-IR (ATR, cm^{-1}):** ν = 3329 (N-H), 1633 (sh, C=N$_{pyr}$), 1609 (C=N$_{benz/quin}$), 1580 (C=C). **ESI-MS:** *m/z* 325.5818 ([M–Cl]$^{2+}$), calculated 325.5818.

Methyl-substituted N^N-coordinated Rh(III)-Cp complex (**12b**)*

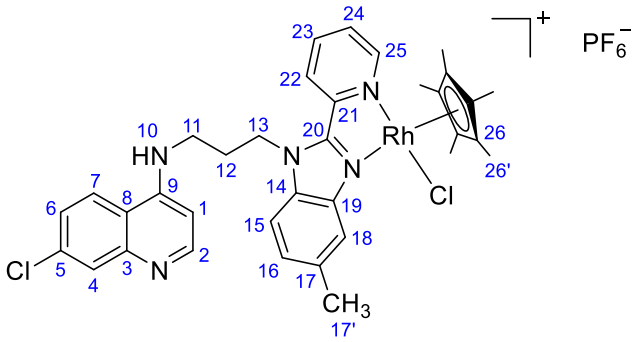

$[Rh(Cp^*)Cl_2]_2$ (0.0372 g, 0.0602 mmol), compound **6b** (0.0515 g, 0.120 mmol) and NH_4PF_6 (0.0253 g, 0.155 mmol). Product: Orange powder. Yield: 0.0842 g, 82.7%. **M.p.** 201.1 – 202.6 °C. **^{1}H NMR (600 MHz, DMSO-*d*$_6$):** δ 9.10 (dd, $^{3}J_{HH}$ = 5.5, $^{4}J_{HH}$ = 1.1 Hz, 1H, H-25), 8.45 (d, $^{3}J_{HH}$ = 7.9 Hz, 1H, H-22), 8.44 (d, $^{3}J_{HH}$ = 6.1 Hz, 1H, H-2), 8.24 (d, $^{3}J_{HH}$ = 9.1 Hz, 1H, H-7), 8.11 (td, $^{3}J_{HH}$ = 7.9, $^{4}J_{HH}$ = 1.1 Hz, 1H, H-23), 8.01 (m, 1H, H-10), 7.93 (d, $^{3}J_{HH}$ = 8.6 Hz, 1H, H-15), 7.86 (ddd, $^{3}J_{HH}$ = 7.9, $^{3}J_{HH}$ = 5.5, $^{4}J_{HH}$ = 1.0 Hz, 1H, H-24), 7.84 (d, $^{4}J_{HH}$ = 2.2 Hz, 1H, H-4), 7.58 (dd, $^{3}J_{HH}$ = 9.0, $^{4}J_{HH}$ = 2.2 Hz, 1H, H-6), 7.51 (dt, $^{3}J_{HH}$ = 1.5, $^{4}J_{HH}$ = 0.9 Hz, 1H, H-18), 7.39 (dd, $^{3}J_{HH}$ = 8.6, $^{4}J_{HH}$ = 1.5 Hz, 1H, H-16), 6.58 (d, $^{3}J_{HH}$ = 6.1 Hz, 1H, H-1), 4.97 (m, 2H, H-13), 3.52 (m, 2H, H-11), 2.55 (s, 3H, H-17'), 2.26 (m, 2H, H-12), 1.67 (s, 15H, H-26'). **^{13}C{^{1}H} NMR (151 MHz, DMSO-*d*$_6$):** δ 154.3, 152.3, 149.3, 148.0, 145.8 (2C), 140.8, 138.8, 135.6, 135.4, 135.2, 128.4, 128.1, 125.7, 125.1, 124.9, 124.8, 117.4, 117.2, 113.0, 99.2, 97.1 (2C), 97.0 (3C), 43.8, 40.5, 28.3, 21.6, 9.6 (5C). **^{31}P{^{1}H} NMR (162 MHz, DMSO-*d*$_6$):** δ -144.2 (sep, ^{1}J = 711.2 Hz, PF_6^-). **FT-IR (ATR, cm^{-1}):** ν = 3329 (N–H), 1633 (sh, C=N$_{pyr}$), 1613 (C=N$_{benz/quin}$), 1582 (C=C). **ESI-MS:** *m/z* 332.5899 ([M-Cl]$^{2+}$), calculated 332.5896.

Trifluoromethyl-substituted N^N-coordinated Rh(III)-Cp complex (**12c**)*

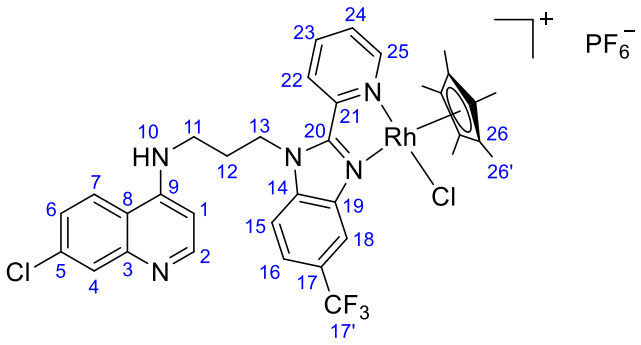

$[Rh(Cp^*)Cl_2]_2$ (0.0335 g, 0.0542 mmol), compound **6c** (0.0521 g, 0.108 mmol) and NH_4PF_6 (0.0211 g, 0.129 mmol). Product: Orange powder. Yield: 0.0805 g, 82.7%. **M.p.** 202.0 – 204.7 °C. **^{1}H NMR (400 MHz, DMSO-*d*$_6$):** δ 9.17 (d, $^3J_{HH}$ = 5.2 Hz, 1H, H-25), 8.56 (d, $^3J_{HH}$ = 7.9 Hz, 1H, H-22), 8.46 (d, $^3J_{HH}$ = 6.1 Hz, 1H, H-2), 8.30 (d, $^3J_{HH}$ = 8.8 Hz, 1H, H-15), 8.21 (t, $^3J_{HH}$ = 7.9 Hz, 1H, H-23), 8.11 (d, $^3J_{HH}$ = 9.1 Hz, 1H, H-7), 8.04 (m, 1H, H-10), 8.00 – 7.92 (overlapping m, 2H, H-18/24), 7.87 – 7.82 (overlapping m, 2H, H-4/16), 7.57 (dd, $^3J_{HH}$ = 9.1, $^4J_{HH}$ = 1.5 Hz, 1H, H-6), 6.62 (d, $^3J_{HH}$ = 6.1 Hz, 1H, H-1), 5.08 (m, 2H, H-13), 3.58 (m, 2H, H-11), 2.35 (m, 2H, H-12), 1.68 (s, 15H, H-26'). **^{13}C{^{1}H} NMR (101 MHz, DMSO-*d*$_6$):** δ 154.4, 152.6, 151.0, 148.7, 145.2, 141.0, 139.4, 137.8, 135.9, 129.2, 126.1, 125.9, 125.7, 125.1, 124.9, 124.4, 122.6, 116.9, 115.3, 115.0, 114.9, 99.2, 97.3 (3C), 97.2 (2C), 44.5, 40.4, 28.0, 9.5 (5C). **^{31}P{^{1}H} NMR (162 MHz, DMSO-*d*$_6$):** δ -144.2 (sep, ^1J = 711.2 Hz, PF_6^-). **FT-IR (ATR, cm^{-1}):** ν = 3341 (N–H), 1631 (sh, C=N_{pyr}), 1613 (C=$N_{benz/quin}$), 1582 (C=C), 1330 (C–F). **ESI-MS:** *m/z* 240.0528 ($[M–Cl+H]^{3+}$), calculated 240.0529.

7.5.2 General method for synthesis of N^N-coordinated Rh(III)-ppy complexes (13a – 13c)

Dichlorotetrakis(2-(2-pyridinyl)phenyl)dirhodium(III) (0.5 eq.) was added to a stirring solution of ligand **6a**, **6b** or **6c** (1 eq.) in dry DCM (10 ml) and MeOH (10 ml), and the orange mixture was refluxed under N_2 for 24 hours. Thereafter, the reaction mixture was cooled to room temperature, NH_4PF_6 (1.2 eq.) was added and the mixture was stirred for 1.5 hours. The solvent was then removed, DCM was added and the mixture was filtered through Celite®. The solvent of the filtrate was removed and the resulting residue was triturated in pentane to afford the product as a pale-yellow, beige or orange precipitate, which was collected by suction filtration and dried *in vacuo*.

*Unsubstituted N^N-coordinated Rh(III)-ppy complex (**13a**)*

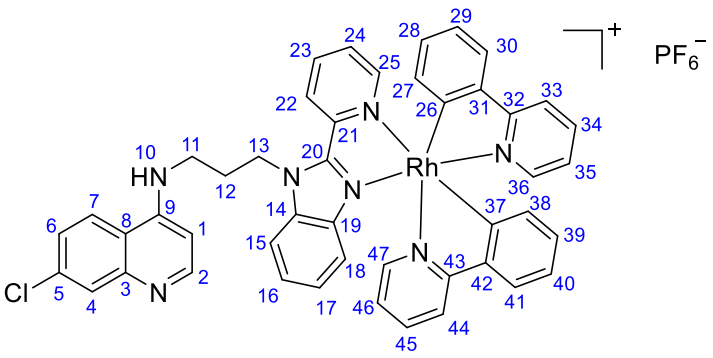

[Rh(ppy)$_2$Cl]$_2$ (0.0587 g, 0.0657 mmol), compound **6a** (0.0544 g, 0.131 mmol) and NH_4PF_6 (0.0278 g, 0.171 mmol). Product: Pale-yellow powder. Yield: 0.107 g, 84.3%. **M.p.** 227.6 – 230.0 °C. **^{1}H NMR (600 MHz, DMSO-*d*$_6$):** δ 8.57 (overlapping m, 2H, H-10/22), 8.46 (d, $^3J_{HH}$ = 6.4 Hz, 1H, H-2), 8.41 (d, $^3J_{HH}$ = 9.1 Hz, 1H, H-7), 8.27 (d, $^3J_{HH}$ = 8.2 Hz, 1H, H-44), 8.20 (d, $^3J_{HH}$ = 8.1 Hz, 1H, H-33), 8.07 (td, $^3J_{HH}$ = 8.0, $^4J_{HH}$ = 1.6 Hz, 1H, H-23), 8.03 – 7.89 (overlapping m, 6H, H-15/25/27/34/38/45), 7.88 (d, $^4J_{HH}$ = 2.2 Hz, 1H, H-4), 7.71 (d, $^3J_{HH}$ = 5.7 Hz, 1H, H-47), 7.69 – 7.65 (overlapping m, 2H, H-6/24), 7.61 (d, $^3J_{HH}$ = 5.7 Hz, 1H, H-36), 7.32 (ddd, $^3J_{HH}$ = 8.3, $^3J_{HH}$ = 7.3, $^4J_{HH}$ = 1.0 Hz, 1H, H-16), 7.18 – 7.13 (overlapping m, 2H, H-35/39/46), 7.10 (td, $^3J_{HH}$ = 7.6, $^4J_{HH}$ = 1.2 Hz, 1H, H-28), 7.03 – 6.96 (overlapping m, 3H, H-17/29/40), 6.64 (d, $^3J_{HH}$ = 6.4 Hz, 1H, H-1), 6.29 (d, $^3J_{HH}$ = 7.7 Hz, 1H, H-41), 6.21 (overlapping m, 2H, H-18/30), 5.02 (m, 2H, H-13), 3.58 (m, 2H, H-11), 2.37 (m, 2H, H-12). **^{13}C{^{1}H} NMR (151 MHz, DMSO-*d*$_6$):** δ 168.8, 168.6, 166.1, 165.9, 164.7, 164.6, 153.7, 151.2, 150.0, 149.8, 149.5, 147.2, 146.5, 144.7, 144.4, 140.4, 139.5, 139.3, 139.1, 137.0, 133.1, 132.5, 130.5, 129.9, 128.4, 126.4, 125.9, 125.5, 125.4, 125.3, 125.1, 125.0, 124.3, 124.2, 123.7, 123.6, 123.2, 120.6, 120.4, 117.8, 116.7, 112.8, 99.1, 43.8, 40.6, 28.4. **^{31}P{^{1}H} NMR (162 MHz, DMSO-*d*$_6$):** δ -144.2 (sep, ^1J = 711.2 Hz, PF_6^-). **FT-IR (ATR, cm^{-1}):** ν = 3340 (N-H), 1633 (sh, C=N$_{pyr}$), 1615 (sh, C=N$_{benz/quin}$), 1604 (C=N$_{ppy}$), 1581 (C=C). **ESI-MS:** *m/z* 824.1747 ([M]$^+$), calculated 824.1776.

*Methyl-substituted N^N-coordinated Rh(III)-ppy complex (**13b**)*

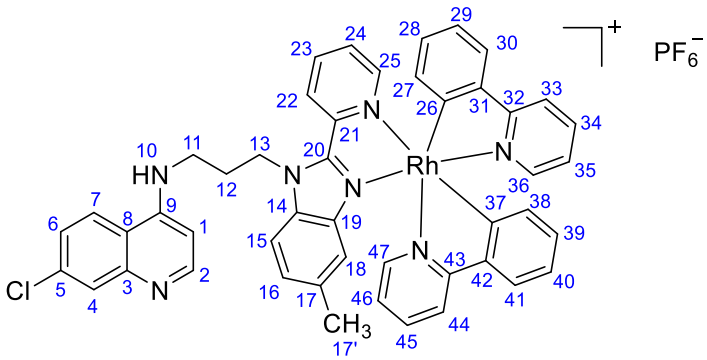

[Rh(ppy)$_2$Cl]$_2$ (0.0787 g, 0.0881 mmol), compound **6b** (0.0754 g, 0.176 mmol) and NH_4PF_6 (0.0328 g, 0.201 mmol). Product: Dark orange powder. Yield: 0.0154 g, 89.0%. **M.p.** 225.9 – 228.1 °C. **^{1}H NMR (600 MHz, DMSO-*d*$_6$):** δ 9.04 (m, 1H, H-10), 8.58 (d, $^3J_{HH}$ = 8.3 Hz, 1H, H-22), 8.52 (d, $^3J_{HH}$ = 9.2 Hz, 1H, H-7), 8.47 (d, $^3J_{HH}$ = 6.7 Hz, 1H, H-2), 8.27 (d, $^3J_{HH}$ = 8.2 Hz, 1H, H-44), 8.21 (d, $^3J_{HH}$ = 8.3 Hz, 1H, H-33), 8.12 (td, $^3J_{HH}$ = 8.0, $^4J_{HH}$ = 1.6 Hz, 1H, H-23), 8.03 – 7.91 (overlapping m, 6H, H-4/25/27/34/38/45), 7.78 (d, $^3J_{HH}$ = 8.6 Hz, 1H, H-15), 7.70 – 7.65 (overlapping m, 3H, H-6/24/47), 7.64 (d, $^3J_{HH}$ = 5.7 Hz, 1H, H-36), 7.19 – 7.16 (overlapping m, 3H, H-35/39/46), 7.13 (dd, $^3J_{HH}$ = 8.7, $^4J_{HH}$ = 1.4 Hz, 1H, H-16), 7.10 (td, $^3J_{HH}$ = 7.6, $^4J_{HH}$ = 1.1 Hz, 1H, H-28), 7.03 – 6.96 (overlapping m, 2H, H-40/29), 6.69 (d, $^3J_{HH}$ = 6.8 Hz, 1H, H-1), 6.30 (d, $^3J_{HH}$ = 7.7 Hz, 1H, H-41), 6.23 (d, $^3J_{HH}$ = 7.6 Hz, 1H, H-30), 5.85 (m, 1H, H-18), 5.00 (m, 2H, H-13), 3.63 (m, 2H, H-11), 2.36 (m, 2H, H-12), 2.02 (s, 3H, H-17'). **^{13}C{^{1}H} NMR (151 MHz, DMSO-*d*$_6$):** δ 168.9, 168.7, 166.3, 166.1, 164.7, 164.6, 154.6, 151.1, 149.8, 149.7, 149.5, 146.5, 145.6, 144.9, 144.4, 140.5, 139.6, 139.2, 139.1, 137.5, 135.2, 134.3, 133.3, 132.5, 130.4, 129.7, 128.2, 127.3, 126.7, 125.7, 125.3, 125.0, 124.3, 124.2, 123.7, 123.4, 121.6, 120.6, 120.4, 117.6, 116.4, 112.2, 99.0, 43.8, 40.5, 28.3, 21.5. **^{31}P{^{1}H} NMR (162 MHz, DMSO-*d*$_6$):** δ -144.2 (sep, ^1J = 711.2 Hz, PF_6^-). **FT-IR (ATR, cm^{-1}):** ν = 3345 (N–H), 1629 (sh, C=N$_{pyr}$), 1615 (sh, C=N$_{benz/quin}$), 1604 (C=N$_{ppy}$), 1580 (C=C). **ESI-MS:** *m/z* 838.1908 ([M]$^+$), calculated 838.1932.

*Trifluoromethyl-substituted N^N-coordinated Rh(III)-ppy complex (**13c**)*

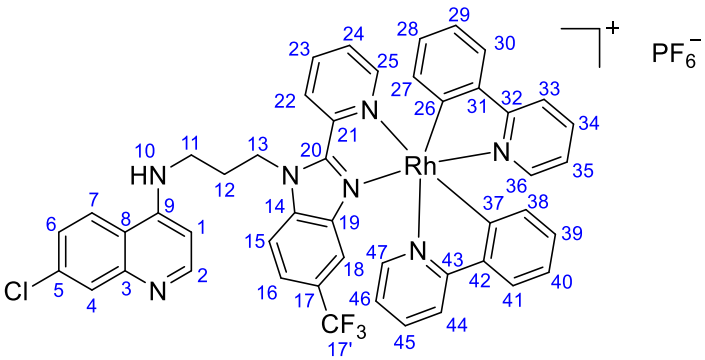

$[Rh(ppy)_2Cl]_2$ (0.0516 g, 0.0578 mmol), compound **6c** (0.0557 g, 0.116 mmol) and NH_4PF_6 (0.0237 g, 0.145 mmol). Product: Beige powder. Yield: 0.0849 g, 70.8%. **M.p.** 260.0 °C (Decomp. w/o melting). **^{1}H NMR (600 MHz, DMSO-*d*$_6$):** δ 8.60 (d, $^3J_{HH}$ = 8.3 Hz, 1H, H-22), 8.39 (d, $^3J_{HH}$ = 6.0 Hz, 1H, H-2), 8.30 – 8.27 (overlapping m, 2H, H-7/44), 8.22 (d, $^3J_{HH}$ = 8.3 Hz, 1H, H-33), 8.15 (d, $^3J_{HH}$ = 8.9 Hz, 1H, H-15), 8.08 – 7.92 (overlapping m, 7H, H-10/23/25/27/34/38/45), 7.83 (d, $^4J_{HH}$ = 2.2 Hz, 1H, H-4), 7.78 (d, $^3J_{HH}$ = 5.7 Hz, 1H, H-47), 7.71 (ddd, $^3J_{HH}$ *J* = 7.7, $^3J_{HH}$ = 5.3, $^4J_{HH}$ = 0.7 Hz, 1H, H-24), 7.65 (d, $^3J_{HH}$ = 5.7 Hz, 1H, H-36), 7.61 (dd, $^3J_{HH}$ = 8.9, $^4J_{HH}$ = 1.4 Hz, 1H, H-16), 7.55 (dd, $^3J_{HH}$ = 9.0, $^4J_{HH}$ = 2.2 Hz, 1H, H-6), 7.19 – 7.14 (overlapping m, 3H, H-35/39/46), 7.11 (td, $^3J_{HH}$ = 7.6, $^4J_{HH}$ = 1.1 Hz, 1H, H-28), 7.03 – 6.97 (overlapping m, 2H, H-29/40), 6.49 (d, $^3J_{HH}$ = 6.0 Hz, 1H, H-1), 6.44 (m, 1H, H-18), 6.31 (d, $^3J_{HH}$ = 7.7 Hz, 1H, H-41), 6.21 (d, $^3J_{HH}$ = 7.6 Hz, 1H, H-30), 5.06 (m, 2H, H-13), 3.51 (m, 2H, H-11), 2.39 (m, 2H, H-12). **^{13}C{^{1}H} NMR (151 MHz, DMSO-*d*$_6$):** δ 168.3, 168.1, 165.3, 165.1, 164.6, 164.5, 152.5, 152.3, 151.3, 150.1, 149.6, 149.3, 146.0, 144.8, 144.4, 140.4, 139.3, 139.3, 138.7, 135.6, 133.2, 132.5, 130.5, 129.9, 128.9, 127.0, 126.0, 125.7, 125.4, 125.2, 125.1, 124.8, 124.4, 124.3, 123.8, 123.8, 122.0, 120.6, 120.4, 117.2, 115.5, 115.5, 114.3, 99.1, 44.3, 40.5, 28.2. **^{31}P{^{1}H} NMR (162 MHz, DMSO-*d*$_6$):** δ -144.2 (sep, ^1J = 711.2 Hz, PF_6^-). **FT-IR (ATR, cm^{-1}):** ν = 3345 (N-H), 1629 (sh, C=N$_{pyr}$), 1615 (sh, C=N$_{benz/quin}$), 1606 (C=N$_{ppy}$), 1581 (C=C), 1330 (C–F). **ESI-MS:** *m/z* 892.1625 ($[M]^+$), calculated 892.1650.

7.6 *In vitro Plasmodium falciparum* assay

The samples were tested against the chloroquine-sensitive NF54 strain and chloroquine-resistant K1 strain of *P. falciparum*. Continuous *in vitro* cultures of asexual erythrocyte stages of *P. falciparum* were maintained using a modified method of Trager and Jensen.[9] The *in vitro* antiplasmodium activity was determined *via* the parasite lactate dehydrogenase (pLDH) assay using a modified method described by Makler *et al.*[10] The samples were prepared as 20 mg/ml stock solutions using dimethyl sulfoxide (DMSO) and sonicated to enhance solubility. Samples were tested as a suspension if not completely dissolved. Stock solutions were stored at -20 °C and further dilutions were prepared on the day of the experiment. Chloroquine was used as the reference drug in all experiments. A full dose-response measurement was performed for all compounds to determine the concentration inhibiting 50% of parasite growth (IC_{50} value). The samples were tested at a starting concentration of 10 µg/ml, which was then serially diluted 2-fold in complete medium to give 10 concentrations; with the lowest concentration being 0.02 µg/ml. The same dilution technique was used for all samples. The positive control drugs were tested at a starting concentration of 10 µg/ml. The highest concentration of solvent to which the parasites were exposed had no measurable effect on the parasite viability. The IC_{50} values were obtained using a non-linear dose-response curve fitting analysis *via* Graph Pad Prism v.5.0 software.

Formate study

For the formate co-administration experiments in the NF54 strain, medium containing 0, 5, 10 and 20 mM sodium formate was used instead of complete medium (after addition of the medium to the 96-well plates, the final sodium formate concentrations are 0, 5, 10 and 20 mM, respectively). The same procedure was followed as in the pLDH assay described above.

7.7 Isobologram analysis

Compound solution preparation

Stock solutions of the test compounds were prepared at 20 mg/ml using DMSO, and solutions were stored at -20 °C. Dilutions and combinations were made on the day of the experiment. Initially, dose response assays were performed to determine the IC_{50} values of compounds **B1** and **B2**. For the combination assay, test compound dilutions were made to allow the IC_{50} of compounds **B1** and **B2** to fall at the fourth 2-fold serial dilution. Dilutions of each compound were prepared in fixed ratios and volumes according to Table 7.1. The compounds were combined and tested according to a modified method described by Fivelman *et al*.[11]

Table 7.1 Combination ratios and volumes of test compounds **B1** and **B2**.

	Ratio		Volume (µl)	
Mixture	**B1**	**B2**	**B1**	**B2**
1	5	0	1000	0
2	4	1	800	200
3	3	2	600	400
4	1	1	500	500
5	2	3	400	600
6	1	4	200	800
7	0	5	0	100

Plate preparation

The compounds and combinations were tested against the NF54 strain of *P. falciparum* and the assays were carried out in 96-well plates. Complete medium (100 µl) was added into all wells except row A, column 3 to 11. Red blood cells (RBCs) at 2% haematocrit were prepared and 100 µl was added to column 1 as the blank. One hundred microlitres of parasitized red blood cells (pRBC) at 2% haematocrit and 2% parasitemia were added to rows A to H, column 2 and 12 as positive controls. Two hundred microlitres of the top concentration of each compound or compound combination was added in triplicate to row A, column 3 to 11. The combination solutions were serially diluted (2-fold) from row A to H, transferring 100 µl of compound solutions each after mixing and discarding the last 100 µl. One hundred microlitres of pRBC were added to all wells in rows A to H,

columns 3 to 11. The dose-response curves were used to determine IC_{50} and FIC_{50} values, which were used to construct an isobologram.

7.8 *In vitro* cytotoxicity assay

In vitro cytotoxicity of potent target compounds against the Chinese Hamster Ovarian (CHO) cells was determined using the 3-(4,5-dimethylthiazol-2-yl)-2,5-diphenyltetrazolium bromide (MTT) assay, which determines cellular growth and survival.[12, 13] For each test compound, a stock solution (2 mg/ml) was prepared in 10% DMSO, and then diluted with the assay medium to yield a starting concentration of a 100 µg/ml. This was then serially diluted (10-fold) to give six assay concentrations ranging from 100–0.001 µg/ml. The positive control drug, emetine, was subjected to similar dilutions. In all cases, samples were tested in triplicate. The highest concentration of DMSO used had no measurable effect on cell viability. A solution of MTT was then added after 44 hours of exposure of the cells to the test compound, followed by a further 4 hours of incubation at 37 °C. The supernatant was then separated from the cells by suction and the formazan crystals were dissolved by addition of DMSO to each well. The amount of formazan in each well was determined by measuring the absorbance at 540 nm. The IC_{50} values were obtained from dose-response curves, using a non-linear dose-response curve analysis *via* GraphPad Prism v.5.0 software.

7.9 *In vivo* antimalarial efficacy studies

In vivo efficacy against *Plasmodium berghei* was performed using mice (n = 3) which were infected with a GFP-transfected *P. berghei* ANKA strain (donated by A. P. Waters and C. J. Janse, Glasgow and Leiden Universities respectively). Parasitemia was determined using standard flow cytometry techniques. The detection limit was 1 parasite per 1000 erythrocytes (0.1%). Activity was calculated as the difference between the mean percentage parasitemia for the control and treated groups, expressed as a percentage relative to the control group. Compounds were dissolved or suspended in 90/10 Tween80/ethanol (v/v), diluted 10 times with water and administered orally as four consecutive daily doses (4, 24, 48 and 72 h after infection). Animals were considered

cured if there were no detectable parasites on day 30 post-infection as determined by light microscopy.

7.10 β-Haematin inhibition assay

The β-haematin formation assay was adapted from the method described by Sandlin *et al*.[14] Test compounds were prepared as a 10 mM stock solution in 100% DMSO. Compounds were tested at concentrations between 500 μM and 5 μM. The stock solution was serially diluted to give 12 concentrations in a 96 well flat-bottom assay plate. NP-40 detergent was then added to mediate the formation of β-haematin (30.55 μM, final concentration). A 25 mM stock solution of haematin was prepared by dissolving haemin (16.3 mg) in DMSO (1 ml). A 177.76 μl aliquot of haematin stock was suspended in 20 ml of a 2 M acetate buffer (pH 4.7). The haematin suspension was then added to the plate to give a final haematin concentration of 100 μM. The plate was then incubated for 16 hours at 37 °C. The assay was analysed using the pyridine ferrihaemochrome method developed by Ncokazi and Egan.[15] Thirty-two microlitres of a solution of 50% pyridine, 20% acetone, 20% water, and 10% 2 M HEPES buffer (pH 7.4) was added to each well. To this, 60 μl of acetone was then added to each well and mixed. The absorbance of the resulting complex was measured at 405 nm on a SpectraMax 340PC plate reader. The IC_{50} values were obtained using a non-linear dose-response curve fitting analysis *via* Graph Pad Prism v.5.0 software.

7.11 Cellular haem fractionation assay

Synchronized ring stage NF54 parasites (5% parasitemia and 2% haematocrit) were incubated with varying concentrations of test compounds and controls for 36 h. Trophozoites were isolated afterwards by saponin lysis, diluted to 1 ml, counted using a hemocytometer and then stored at −80 °C. For measurements, samples were thawed and 50 μl of water was added before sonication for 5 minutes. Fifty microlitres of 0.2 M HEPES buffer (pH 7.5) and 50 μl of water was added, followed by centrifugation at 3600 rpm for 20 min. Fifty microlitres of 4% SDS was added to the supernatant, which was sonicated and incubated at room temperature for 30 minutes. Fifty microliters of 0.3 M NaCl and 50

µl of 25% pyridine (v/v) were added and the UV−visible spectrum of this fraction (Hb) was recorded. Water (50 µl) was added to the pellet, followed by 50 µl of 4% SDS. After re-suspending the pellet, the solution was sonicated and incubated for 30 minutes. To the centrifuged sample, 50 µl of 0.2 M HEPES, 50 µl of 0.3 M NaCl, and 50 µl of 25% pyridine were added. The supernatant was diluted to 400 µl with water and the UV−visible spectrum of this fraction (haem) was recorded. To the pellet, 50 µl of water and 50 µl of 0.3 M NaOH was added, which was sonicated 15 minutes and incubated for 30 minutes. Fifty microliters of 0.2 M HEPES, 50 µl of 0.3 M HCl, and 50 µl of 25% pyridine were added and the supernatant was diluted to 300 µl. The UV−visible spectrum of this fraction (haemozoin) was recorded and percentages of the three haem species (haemoglobin, haem and haemozoin) were determined from the absorbance values.

7.12 DNA cleavage assay

All gel electrophoresis experiments were carried out using hand-cast 1.25% agarose gels dissolved in 1× TAE buffer (Sigma Aldrich) in a Mini-Sub-Cell GT® Agarose Gel Electrophoresis System (Bio-Rad). Compound-DNA interaction assays (EMSA) were performed in tubes containing 25 ng of pUC57 plasmid DNA (ThermoFisher) and an appropriate amount of the test compound dissolved in DMSO (to a final concentration of 10% DMSO) in 1× TAE buffer (Sigma-Aldrich, pH 8.3), for a total volume of 10 µl. The samples were incubated at 37 °C for 30 minutes. Four microlitres of loading dye (Sigma Aldrich, 0.25% bromophenol blue, 0.25% xylene cyanol, and 40% sucrose) was added to each sample and 6 µl aliquots were then loaded onto the gels and electrophoresed at a constant 75 V for 90 minutes in 1× TAE buffer. The DNA was stained with an Ethidium Bromide solution (0.5 mg/l in Type 1 ultrapure water) for 30 minutes, washed in Type 1 ultrapure water for 20 minutes and visualized using a G:Box Chemi XRQ gel doc system (Syngene) with midwave transillumination and a UV filter (GeneSys 1.4.6.0).

7.13 Transfer hydrogenation studies

^{1}H NMR study

Approximately 6 mg of the test complex, 20 mg of NAD^+ and 40 mg of sodium formate were weighed. The NAD^+ and sodium formate were each dissolved separately in 600 µl of D_2O. The complex was then suspended in a mixture of 100 µl of the sodium formate solution and 300 µl of the NAD^+ solution. To this, 300 µl of MeOD was added. The suspension was then mixed well, any solid matter that remained was filtered off and the pH of the resulting filtrate adjusted to 7.4 using a NaOH solution. The solution was then added to an NMR tube. The ^{1}H NMR spectrum was recorded prior to incubation at 37 °C. The tube was then incubated at 37 °C and the spectra recorded after 30 and 60 minutes.

Cell-free assay

The compounds were evaluated using a method described by Stringer *et al*.[16] An NAD^+ solution (50 ml) was prepared by dissolving sodium formate (0.310 g, 4.56 mmol), trizma base (0.330 g, 2.72 mmol) and NAD^+ (5.50 mg, 0.00829 mmol) in distilled water (25 ml). The pH was adjusted to pH 7.4 using HCl and the volume made up to 50 ml with distilled water. A tetrazolium (NBT) solution was prepared by dissolving nitroblue tetrazolium (0.080 g, 0.0978 mmol) and phenazine ethosulfate (0.004 g, 0.0120 mmol) in distilled water (50 ml). Stock solutions (6 mM) of each complex were prepared in DMSO (1 ml). In a 96-well plate (plate 1), 200 µl of the complex solution was added to column 3 in triplicate. DMSO (100 µl) was added to each well from column 4 to column 12. The compounds were serially diluted giving 10 concentrations (2250 µM to 4 µM). Seventy-five microlitres of the solution from each well was transferred into a second 96-well plate (plate 2) into the corresponding well (e.g. 75 µl C1 of plate 1 into C1 of plate 2). The NAD^+ solution (100 µl) was then added to each well. In column 1, 75 µl DMSO and 100 µl NAD^+ solution were added to each well only. In column 2, 175 µl DMSO was added to each well only. The plate was read at 600 nm to account for the absorbance of the compounds (pre-read). The plate was then covered with a foil plate cover to prevent evaporation and was incubated for 6-8 hours at 37 °C. After this time, 25 µl of the NBT solution was added and the plate incubated for a further 16 hours to aid plate developing. Thereafter, the absorbance was read at 600 nm again, the data from the pre-read accounted for, and the data plotted using Graph Pad Prism v.5.0 at the various concentrations.

7.14 *In vitro Mycobacterium tuberculosis* assay

The minimum inhibitory concentration (MIC) values were determined using the standard broth micro dilution method,[17] where a 10 ml culture of *Mycobacterium tuberculosis* H37Rv,[18] was grown to an absorbance (OD600) of 0.6 – 0.7. The media used were Middlebrook 7H9 media (Difco) supplemented with 0.2% Glucose, Middlebrook albumin-dextrose- catalase (ADC) enrichment (Difco) and 0.05% Tween,[19] as well as Middlebrook 7H9 supplemented with 0.03% casitone, 0.4% glucose, and 0.05% tyloxapol.[20] Cultures grown in these media were diluted 1:500, prior to inoculation of the MIC assay. The compounds to be tested were reconstituted to a concentration of 10 mM in DMSO. Duplicate 2-fold serial dilutions of the test compound were prepared across a 96-well micro titre plate, in a volume of 50 µl, after which, 50 µl of the diluted *M. tuberculosis* cultures was added to each well in the plate (including control wells). The final volume per well is 100 µl. The plate layout is a modification of the method previously described.[21] Controls used were a minimum growth control (rifampicin at 2 × MIC), and a maximum growth control (5% DMSO). The micro titre plates were sealed in a secondary container and incubated at 37 °C with 5% CO_2 and humidification. Alamar Blue reagent was added to each well of the assay plate, 24 hours prior to the assay end data, after which the assay is re-incubated for 24 hours. Relative fluorescence (excitation 485 nM; emission 520 nM) was measured using a plate reader (FLUOstar OPTIMA, BMG LABTECH), at day 7. The raw fluorescence data was archived and analysed using the CDD Vault from Collaborative Drug Discovery, in which, data was normalised to the minimum and maximum inhibition controls to generate a dose response curve (percentage inhibition), using the Levenberg-Marquardt damped least squares method, from which the MIC_{90} was calculated.[22] The lowest concentration of drug that inhibited growth of more than 90% of the mycobacterial population was considered to be the MIC_{90}.

7.15 References

1. C. C. Musonda, S. Little, V. Yardley and K. Chibale, *Bioorg. Med. Chem. Lett.*, 2007, **17**, 4733-4736.
2. C. White, A. Yates, P. Maitlis and D. Heinekey, *Inorg. Synth.*, 1992, 228-234.
3. M. S. Lowry, W. R. Hudson, R. A. Pascal and S. Bernhard, *J. Am. Chem. Soc.*, 2004, **126**, 14129-14135.
4. SAINT Version 7.60a, Bruker AXS Inc., Madison, WI, USA, 2006.
5. G. M. Sheldrick, SHELXS-97, SHELXL-2014, SHELXL-2018/3 and SADABS Version 2.05, University of Göttingen, Germany, 1997.
6. L. J. Barbour, *J. Supramol. Chem.*, 2001, **1**, 189-191.
7. J. L. Atwood and L. J. Barbour, *Cryst. Growth Des.*, 2003, **3**, 3-8.
8. http://www.povray.org (accessed 2017-2019).
9. W. Trager and J. B. Jensen, *Science*, 1976, **193**, 673-675.
10. M. Makler, J. Ries, J. Williams, J. Bancroft, R. Piper, B. Gibbins and D. Hinrichs, *Am. J. Trop. Med. Hyg.*, 1993, **48**, 739-741.
11. Q. L. Fivelman, I. S. Adagu and D. C. Warhurst, *Antimicrob. Agents Ch.*, 2004, **48**, 4097-4102.
12. T. Mosmann, *J. Immunol. Methods*, 1983, **65**, 55-63.
13. J. Carmichael, W. G. DeGraff, A. F. Gazdar, J. D. Minna and J. B. Mitchell, *Cancer Res.*, 1987, **47**, 936-942.
14. R. D. Sandlin, M. D. Carter, P. J. Lee, J. M. Auschwitz, S. E. Leed, J. D. Johnson and D. W. Wright, *Antimicrob. Agents Ch.*, 2011, **55**, 3363-3369.
15. K. K. Ncokazi and T. J. Egan, *Anal. Biochem.*, 2005, **338**, 306-319.
16. T. Stringer, D. R. Melis and G. S. Smith, *Dalton Trans.*, 2019.
17. J. H. Jorgensen and J. D. Turnidge, in *Manual of Clinical Microbiology, Eleventh Edition*, American Society of Microbiology, 2015, pp. 1253-1273.
18. T. R. Ioerger, Y. Feng, K. Ganesula, X. Chen, K. M. Dobos, S. Fortune, W. R. Jacobs, V. Mizrahi, T. Parish and E. Rubin, *J. Bacteriol.*, 2010, **192**, 3645-3653.
19. S. G. Franzblau, M. A. DeGroote, S. H. Cho, K. Andries, E. Nuermberger, I. M. Orme, K. Mdluli, I. Angulo-Barturen, T. Dick and V. Dartois, *Tuberculosis*, 2012, **92**, 453-488.

20. Y. J. Tang, W. Shui, S. Myers, X. Feng, C. Bertozzi and J. D. Keasling, *Biotechnol. Lett.*, 2009, **31**, 1233-1240.
21. J. Ollinger, M. A. Bailey, G. C. Moraski, A. Casey, S. Florio, T. Alling, M. J. Miller and T. Parish, *PloS one*, 2013, **8**, e60531.
22. The Collaborative Drug Discovery Database, www.collaborativedrug.com (accessed 2017-2019).